Université de Montréal

Molecular Tectonics: Supramolecular 2D Nanopatterning of Surfaces by Self-Assembly

Par

Hui Zhou

Département de chimie

Faculté des arts et des sciences

Thèse présentée à la Faculté des études supérieures

en vue de l'obtention du grade de

Philosophiae Doctor (Ph. D.)

en chimie

Février 2009

Université de Montréal

Faculté des études supérieures

Cette thése intitulée:

Molecular Tectonics: Supramolecular 2D Nanopatterning of Surfaces by Self-Assembly

Présentée par:

Hui Zhou

a été évaluée par un jury composé des personnes suivantes :

Andreea R. Schmitzer	Président-rapporteur
James D. Wuest	Directeur de recherche
Antonella Badia	Membre du jury
Dmitrii F. Perepichka	Examinateur externe
Jean-Yves Lapointe	Représentant du doyen de la FES

Sommaire

Au cours des dernières années, la tectonique moléculaire a été utilisée comme une stratégie efficace dans la construction d'architectures supramoléculaires en trois dimensions (3D). Les éléments de construction utilisés dans cette stratégie, qui ont été appelés tectons, ont des géométries bien définies et de multiples substituants qui contrôlent l'association intermoléculaire en formant des interactions directionnelles, comme les liaisons hydrogène. Une nouvelle opportunité existe maintenant d'adopter cette stratégie pour créer des réseaux moléculaires bien définis en 2D à la surface de divers substrats, tels que le graphite. Dans cette thèse, nous décrivons une nouvelle série de tectons qui ont été délibérément conçus et synthétisés pour faire le nanopatterning de la surface du graphite pyrolytique hautement orienté (HOPG).

Pour comprendre les détails de l'adsorption moléculaire, de multiples méthodes de caractérisation et d'analyse ont été utilisées dans ce travail, y compris 1) l'examen direct de l'adsorption par STM (microscopie de balayage à l'effet tunnel) ; 2) la modification systématique de la structure de l'adsorbate pour analyser les conséquences sur l'organisation en 2D ; 3) la comparaison de l'organisation observée en 2D avec celle favorisée dans les structures 3D déterminées par la cristallographie aux rayons X et 4) les calculs théoriques pour aider à révéler l'origine moléculaire de l'adsorption.

En particulier, notre étude a examiné l'effet de certains changements systématiques de la structure des molécules déposées, surtout la longueur, les groupes fonctionnels présents, la géométrie et la chiralité. Dans ces composés, des cœurs aromatiques comme le benzène,

le naphtalène et l'anthracène sont greffés à des espaceurs conjugués, y compris l'acétylène et arylacétylène, et sont liés également à divers groupes fonctionnels avec différentes capacités de s'engager dans des interactions intermoléculaires, notamment des groupes diaminotriazine, des acides carboxyliques et des esters correspondants. L'analyse des divers motifs d'assemblage obtenus a conduit à une compréhension plus profonde de l'interaction des adsorbates avec l'HOPG, des interactions inter-adsorbate et de l'importance relative des facteurs déterminant l'organisation observée.

Notre travail démontre les forces et les faiblesses de l'approche de la tectonique moléculaire pour régir l'assemblage moléculaire en 2D et en 3D. Certains aspects structuraux sont prévisibles, mais les interactions intermoléculaires que nous avons employées ne sont pas suffisantes pour positionner les adsorbates avec confiance, sans tenir compte de l'effet de la surface sous-jacente. Néanmoins, notre travail confirme que des molécules avec des structures bien définies, une forte affinité pour l'adsorption et une forte tendance de participer dans des interactions intermoléculaires directionnelles offrent une capacité importante pour structurer diverses surfaces à l'échelle du nanomètre.

Mots-clés: tectonique moléculaire, 2D nanopatterning, microscopie de balayage à effet tunnel (STM), l'auto-assemblage

Abstract

In recent years, molecular tectonics has been employed as an efficient strategy in the construction of supramolecular architectures in three dimensions (3D). The building blocks used in this strategy, which have been called tectons, have structures with well-defined geometries and multiple functional groups that control intermolecular association by forming directional interactions, such as hydrogen bonds. A new opportunity exists to adopt this strategy to create well-defined 2D molecular networks on the surfaces of various substrates, such as graphite. In this dissertation, a series of new tectons have been purposefully designed and synthesized for nanopatterning surfaces, and their adsorption on highly oriented pyrolytic graphite (HOPG) has been thoroughly examined by scanning tunneling microscopy (STM).

To understand the details of molecular adsorption, multiple methods of characterization and analysis have been used in this work, including 1) direct examination of adsorption by STM, 2) systematic alteration of the structure of the adsorbate to reveal how the self-assembled 2D nanopatterns changes, 3) comparison of the observed 2D nanopatterns with those seen in 3D structures by X-ray crystallography, and 4) theoretical calculations to help disclose the origin of molecular adsorption.

Specifically, the tectons investigated herein incorporate systematic changes of molecular length, cores, functional groups, and molecular geometries. The basic cores, which are aromatic systems such as benzene, naphthalene, and anthracene, are grafted to conjugated linkers, including acetylene and arylacetylene, and to various functional groups

with different abilities to engage in intermolecular interactions, including diaminotriazine groups, carboxylic acids, and related substituents. The observation of diverse nanopatterns has led to a deeper understanding of 1) how the basic backbone interacts with surfaces, 2) how the functional groups modify the behavior of the backbone, and 3) how the formation of interadsorbate interactions further influences adsorption.

Our work demonstrates that rational 2D and 3D molecular assembly can be achieved and analyzed by an integrated approach using the tools of STM, X-ray diffraction, computation, and molecular synthesis. Furthermore, our work confirms that molecules with well-defined shapes and multiple sites that engage in strong directional interactions are a consistently productive source of new materials with properties not previously observed.

Key words: Molecular tectonics, 2D nanopatterning, scanning tunneling microscopy (STM), self-assembly

Acknowledgment

First of all, I would like to thank my advisor, Professor James D. Wuest, for his support, guidance, and understanding. During the process of my research, he introduced me to the field of supramolecular chemistry and surface science, helped me work things out when they appeared complicated, and also gave me the freedom to develop my own ideas. He encouraged me not to give up when I failed my first pre-doctoral exam, and I will never forget his smiling face when he heard that I passed all the exams eventually.

I am grateful to Wuest group members who have shared their scientific thoughts and experimental know-how, in particular Dr. Hung Dang, Chengsong Hu, Dr. Kenneth E. Maly, Eric Gagnon, and Dr. Tao Tu. I would also like to thank Dr. Thierry Maris for his patient crystallographic analysis of my crystals, which were rarely as good as he wanted them to be.

I would like to thank Dr. Ji-Hyun Daniel Yi and Prof. Antonio Nanci, who provided me guidance and support to work in the Laboratoire de Recherche sur les Tissus Calcifiés et Biomatériaux, allowing me to finish all my nanopatterning experiments using scanning tunneling microscopy (STM). I am grateful to Dr. Alain Rochefort for his quantum chemical Density Functional Theory (DFT) calculations. I would also like to acknowledge the work of all the staff at the Laboratoire de RMN, the Centre Régional de Spectrométrie de Masse, and the Laboratoire d'Analyse Élémentaire at the Université de Montréal.

I also give great thanks to my mother, who came in 2005 to Montréal, so far away from China, and took care of my son and cooked for me. Many thanks to my sister and two

brothers for their concern. I would also like to thank my son Boming, who gives me the reason and strength to live well.

A very special thank you goes to my husband, Chengcan Wang, for his constant love, encouragement, and understanding. He gave up his career in China and decided to come to Montréal and start an entirely new life. With his company, I can never be alone or lost.

This dissertation is also dedicated to my father, who passed away in 1999. His love will be always with me.

Table of Contents

Table of Figures

Table of Schemes

Index of Tables

List of Abbreviations

Å	Ångstrom
BTA	3,3',5,5'-biphenyltetracarboxylic acid
CPK	molecular models by Corey, Pauling, and Koltun
°C	degree Celsius
DAT	4,6-diamino-1,3,5-triazinyl
DFT	density functional theory
DMF	*N*, *N*-dimethylformamide
2D	two dimensional
3D	three dimensional
DMSO	dimethyl sulfoxide
HOMO	highest-occupied molecular orbital
HOPG	highly-oriented pyrolytic graphite
HRMS	high-resolution mass spectrum
IR	infrared
LUMO	lowest-unoccupied molecular orbital
mL	millilitre
mg	milligram
mmol	millimole
m/z	mass per unit charge
mp	melting point

MS	mass spectrometry
nm	nanometer
nA	nanoampere
NMR	nuclear magnetic resonance
OPE	oligo(phenyleneethynylene)
ORTEP	Oak Ridge Thermal-Ellipsoid Plot Program
pA	picoampere
ppm	parts per million
SEM	scanning electronic microscopy
STM	scanning tunneling microscopy
TEM	transmission electron microscopy
THF	tetrahydrofuran
TMA	benzene-1,3,5-tricarboxylic acid
TMS	trimethylsilyl
UHV	ultra-high vacuum
V	volt
δ	chemical shift in ppm relative to Me_4Si in NMR spectra

CHAPTER 1

Introduction

1.1 Supramolecular Chemistry and Self-Assembly

Beyond molecular chemistry, which is based on covalent bonds, lies the field of supramolecular chemistry, which studies how molecules can assemble into multi-molecular complexes held together by noncovalent interactions, such as hydrogen bonding, metal coordination, π-π stacking, hydrophobic effects, and van der Waals forces.[1-5] In biological systems, for example, combinations of multiple noncovalent interactions have provided excellent control of key interactions, such as protein-ligand and protein-protein association, for the assembly of proteins into functional complexes. Over the last 30 years, supramolecular chemistry has grown into a major field of investigation. A number of well-designed structural and functional building blocks, including cyclodextrins,[6-9] cucurbiturils,[10-12] crown ethers,[13-15] and porphyrins,[16-19] have been employed in the construction of large new architectures. Furthermore, with the emergence and flowering of nanotechnology, novel building blocks such as fullerenes,[20-24] nanoparticles,[25-28] and dendrimers[29-32] are now being readily used to build supramolecular architectures with fascinating properties in the area of molecular electronics, optics, magnetics, and sensing.

Molecular self-assembly is a key concept of supramolecular chemistry, wherein the association of molecules is directed by noncovalent interactions, without guidance or management from external sources. The process is essential and well-established in biological systems, such as in the association of lipids to form self-assembled membranes, the formation of double helical DNA linked by hydrogen bonding of the individual strands, and the association of proteins to produce complex aggregates.

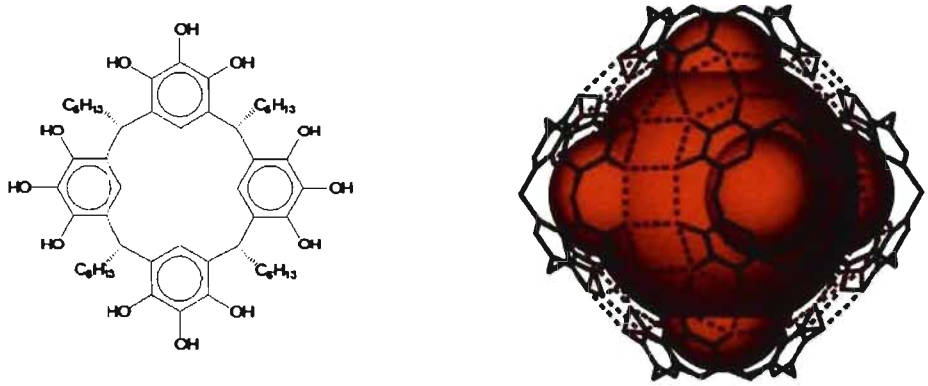

1

Figure 1.1 Hexameric hydrogen-bonded capsules built from molecule **1**.[34]

Currently, self-assembly plays an important role not only in the supramolecular systems of nature, but also in new bottom-up approaches to artificial nanoscale objects for use in nanotechnology.[33] Unlike making new molecules via complex chemical reactions, the process of self-assembly allows large architectures to be readily made by the spontaneous association of small molecules requiring fewer steps to synthesize. Noncovalent interactions are known to be far weaker than covalent bonds; however, multiple noncovalent interactions, such as multiple hydrogen bonds, can produce remarkably stable structures. As shown in Figure 1.1, C-hexylpyrogallo[4]arene (**1**) is a typical example which can form hexameric hydrogen-bonded capsules that enclose 1200 to 1500 $Å^3$ of space.[34-36] These capsules are stable in solution in polar and nonpolar solvents and can host a variety of ionic and molecular guests.[37-39]

1.2 Crystal Engineering and Surface Nanopatterning

Molecular crystal engineering is a subdivision of supramolecular chemistry that aims at the design and synthesis of periodic molecular structures with desired properties, based on the understanding and exploitation of intermolecular interactions. The two main strategies currently in use for positioning molecules in crystal engineering are based on hydrogen bonding and coodination to metals. During the past decades, the control of crystallization in three dimensions (3D) by using molecular self-assembly directed by noncovalent interactions has been extensively studied with the aid of X-ray crystallography.[40-45] In principle, it is also possible to envisage the control of molecular organization in 2D by using analogous strategies to position the molecular components. This possibility links the fields of crystal engineering and surface science. Unlike 3D crystal engineering, which has been explored for decades, 2D crystal engineering involving supramolecular nanopatterning at liquid-solid interfaces or under ultra-high vacuum (UHV) is a new area of research with opportunities that have not yet been fully exploited. The field has begun to attract great interest, particularly since the invention of scanning tunnelling microscopy (STM).[46-50] In the study summarized in this thesis, we have blended 3D and 2D crystal engineering. In particular, we have focused on the use of hydrogen bonding to direct crystallization in 2D to nanopattern surfaces, and we have increased our understanding by carrying our related studies of 3D crystallization as well.

1.2.1 Hydrogen Bonding

Hydrogen bonding is defined as a special type of dipole-dipole force that exists between an electronegative atom and a hydrogen atom bonded to another electronegative atom.[51-53] The classical type of hydrogen bond can be represented as D–H···A, where D is considered the hydrogen-bond donor and A the acceptor. Both D and A are electronegative atoms, such as O, N, F, S, C, Cl, and Br. The strength of a hydrogen bond varies from very weak (1~2 kJ/mol) to extremely strong (>155 kJ/mol), depending on the identity of D and A. For example, the F–H···F hydrogen bond has a strength of 155 kJ/mol, but the N–H···O hydrogen bond has a strength of only 8 kJ/mol.

In addition to classical hydrogen bonds, such as O–H···O, related interactions exist in which C-H bonds can be considered to act as hydrogen-bond donors.[54] Such interactions are normally weaker than conventional hydrogen bonds, but they are thought to be crucial in molecular complexes and crystal structures. Other types of hydrogen bonds involving aromatic rings or triple bonds, such as O–H···π, N–H···π, C–H···π, are also of great interest.[55-56]

Hydrogen bonds are the most commonly used noncovalent interactions to build either 3D or 2D crystal structures by design, largely because they have an attractive combination of properties, including high directionality, modest strength, and reversible formation. As a result, supramolecular assemblies directed by hydrogen bonding can be entirely or partially predicted, and they usually have strong collective stability. A number of hydrogen bonding motifs have been well-studied and applied extensively to the construction of

supramolecular architectures.[57-61] In particular, carboxyl (-COOH), diaminotriazine (DAT), and hydroxyl (-OH) are functional groups widely used to generate predictable hydrogen bonds, as will be discussed in detail below.

1.2.1.1 Carboxyl Groups

Carboxyl groups (-COOH) are widely used in crystal engineering because they self-associate reliably to form cyclic hydrogen-bonded dimers.[62] As shown in Figure 1.2, 1,3,5-benzenetricarboxylic acid (trimesic acid, or TMA) is a typical example. Self-association of all carboxyl groups according to the normal motif yields 2D hexagonal sheets, which then interpenetrate to generate the 3D crystal.[63] STM investigations have revealed that the 2D crystallization of trimesic acid at the liquid-solid interface of heptanoic acid and graphite occurs in an analogous way, and the 2D arrangement is consistent with the structure found in 3D.[64] In addition, derivatives of isophthalic and terephthalic acids, which have the same benzene core but only two carboxyl groups, behave similarly, and they have been

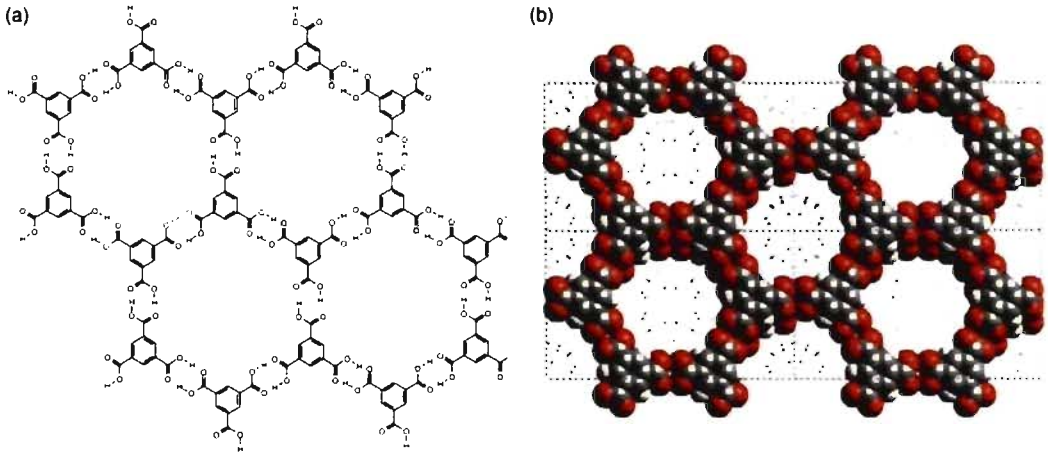

Figure 1.2 Schematic (a) and space-filling (b) views of the open-framework phase of trimesic acid.[63]

used as building blocks to produce well-ordered 2D networks on graphite surfaces (Figure 1.3).[46]

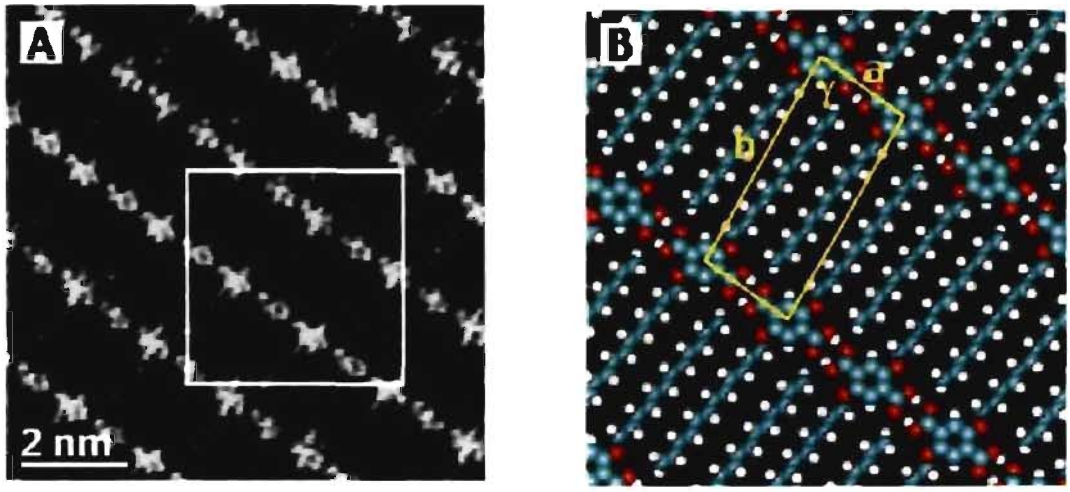

Figure 1.3 (a) STM image and (b) molecular model of a monolayer of 2,5-bis(dodecyloxy) terephthalic acid on graphite (I_{set} = 1 nA, V_{bias} = -0.6 V).[46]

1.2.1.2 Diaminotriazine Groups

4,6-Diamino-1,3,5-triazinyl (DAT) groups can be used to generate a variety of hydrogen-bonding motifs because they incorporate multiple sites that act as hydrogen-bond donors and acceptors. As depicted in Figure 1.4, hydrogen-bonded pairs can be formed in three different modes, which have been called face-to-face, face-to-side, and side-to-side, respectively.[65] Because of this complexity, supramolecular assemblies directed by DAT groups are not entirely predictable; however, they can still be confidently predicted to obey one of the three fundamental hydrogen-bonding patterns shown in Figure 1.4, particularly in their 3D structures.[65-71]

DAT groups are easy to introduce into molecular structures, and they are therefore of

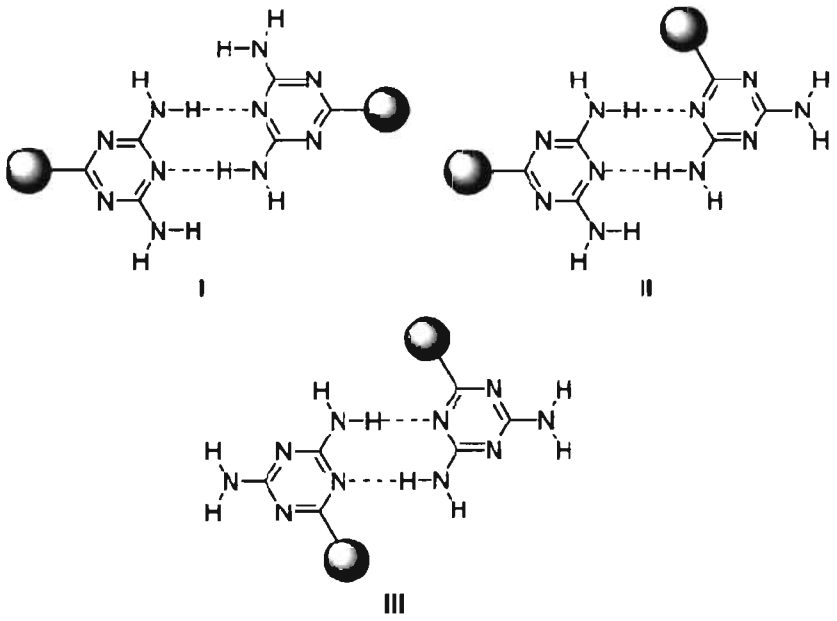

Figure 1.4 Fundamental hydrogen-bonding motifs of DAT pairs. I. Face-to-face. II. Face-to-side. III. Side-to-side.[65]

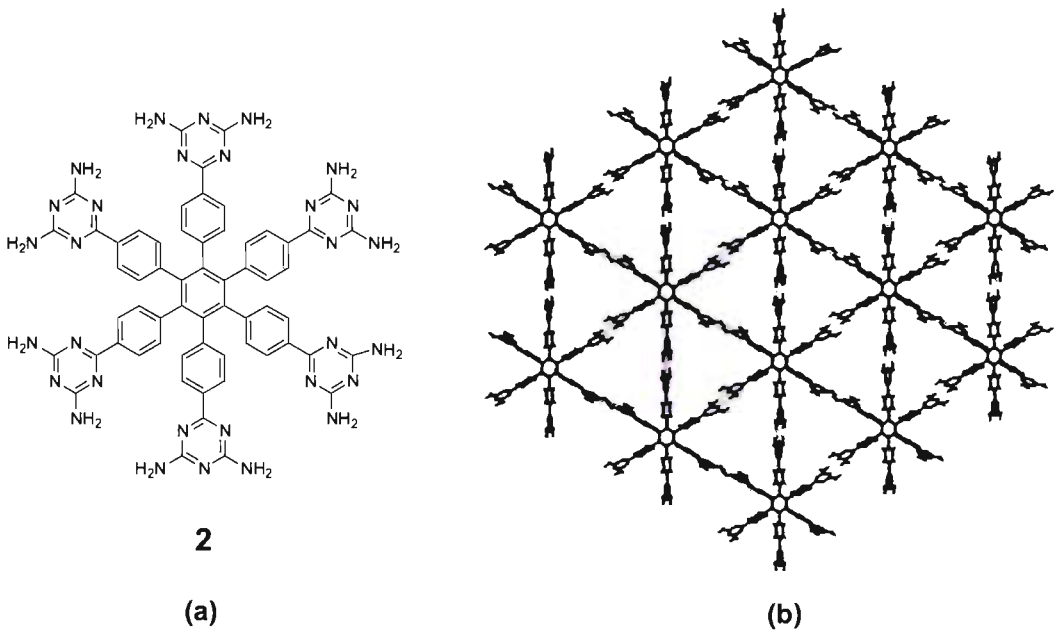

2

(a) **(b)**

Figure 1.5 (a) Molecular structure of hexakis[4-(2,4-diamino-1,3,5-triazin-6-yl) phenyl]benzene (**2**). (b) Hexagonal sheets formed by hydrogen bonding of DAT groups according to motif I.[71]

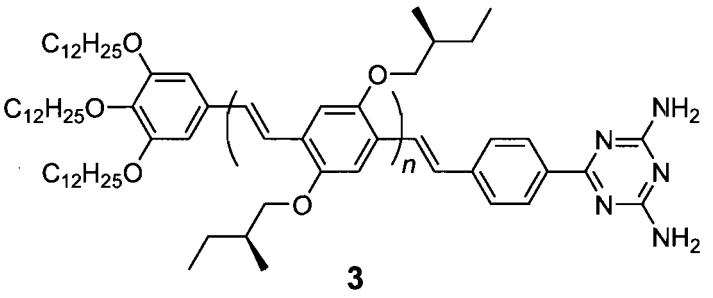

3

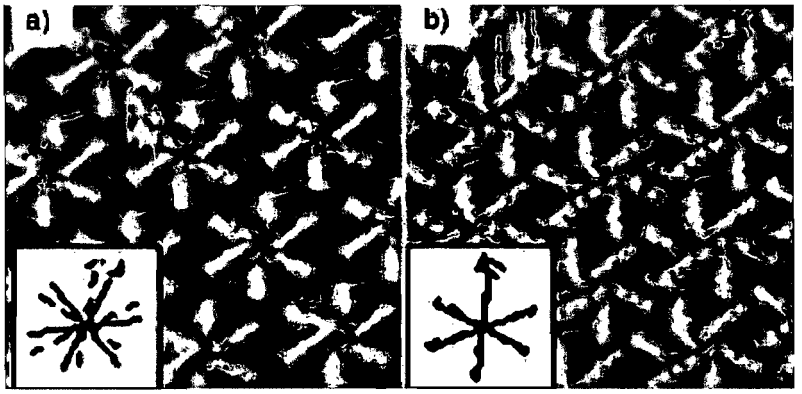

Figure 1.6 STM images showing rosettes formed by adsorption of compound **3** on graphite. Insets show the propagation direction of rosette lattices (solid line) and the main symmetry axes of the graphite substrate (dashed line). (a) Monolayers of **OPVT3** (compound **3**, n = 3). (b) Monolayers of **OPVT4** (compound **3**, n = 4). The relative orientation of rows of rosettes with respect to the main crystallographic axes of graphite shows opposite 2D chirality (+ 17.7 ± 1.7° and -2.3 ± 0.8° for **OPVT3** and **OPVT4**, respectively).[74]

great interest in engineering hydrogen-bonded supramolecular architectures. The Wuest group has developed a number of molecules with well-designed crystal structures based on the application of this functional group.[65-71] Recently, hexakis[4-(2,4-diamino-1,3,5-triazin-6-yl)phenyl]benzene (**2**), which incorporates a disc-shaped hexaphenylbenzene core and six peripheral DAT groups, was shown to crystallize to give non-interpenetrated 3D networks built from hexagonal sheets (Figure 1.5).[71] Each molecule associates with six

neighbors by forming typical hydrogen-bonded DAT pairs according to the face-to-face motif. Although DAT groups have been widely used to build up 3D crystals, only a few examples of their use in 2D surface nanopatterning have been reported.[72-75] For example, melamine (1,3,5-triazine-2,4,6-triamine) was coadsorbed with perylenetetracarboxylic diimide to form heteromolecular hydrogen-bonded networks on silver surfaces.[72,73] De Feyter and co-workers have investigated oligo(p-phenylenevinylene) diaminotriazine (OPVT) derivatives (**3**), which generate homochiral rosette structures on graphite surfaces directed by self-complementary hydrogen bonds between adjacent triazine moieties (Figure 1.6).[74]

1.2.1.3 Hydroxyl Groups

Hydroxyl groups might appear to be able to generate straightforward patterns of hydrogen bonding. However, molecules grafted with multiple hydroxyl groups can produce extremely complex hydrogen-bonded networks.[34,76-78] For example, tetrakis(3,5-dihydroxyphenyl)silane (**4**) was found to crystallize as a porous hydrogen-bonded network with submaximal interpenetration and novel bicontinuous systems of channels (Figure 1.7).[78] The central molecule (red) interacts with 14 neighbors via a complex array of 20 hydrogen bonds and aryl-aryl interactions. In 2D crystallization, hydroxyl groups can also play a key role in producing supramolecular networks. Many alkanols, such as 1-tetradecanol, 1-dodecanol, 1-decanol, 1,12-dodecanediol, and 1,14-tetradecanediol, have been found to form lamellae of herringbone structures when deposited on graphite (Figure 1.8). This observation is consistent with the hypothesis that adsorption is driven in

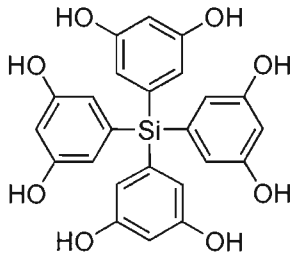

4

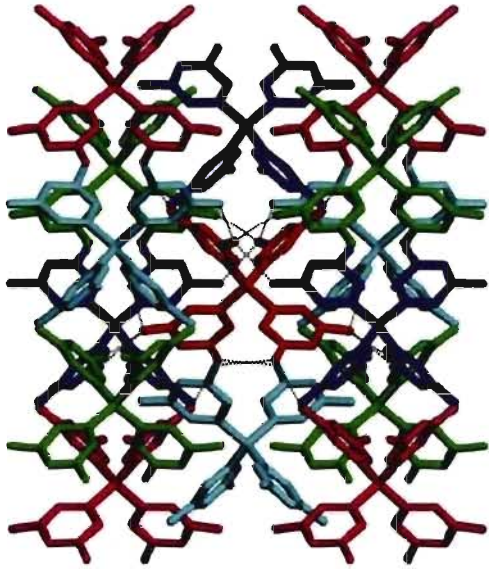

Figure 1.7 Tetrakis(3,5-dihydroxyphenyl)silane (**4**) crystallized from methyl propionate as a porous hydrogen-bonded network with submaximal interpenetration.[78]

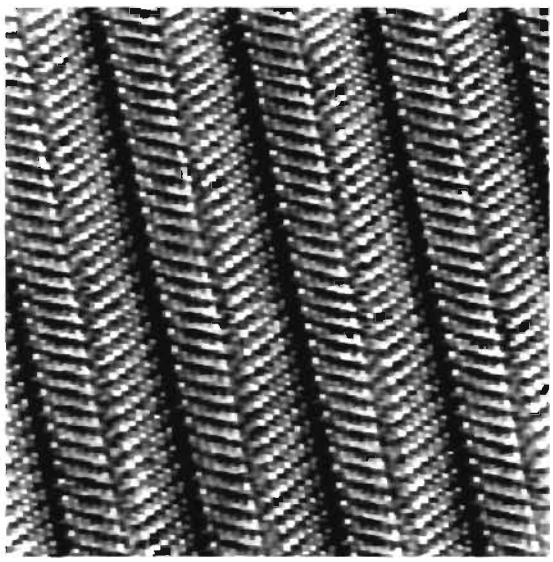

Figure 1.8 STM image of a monolayer of 1-tetradecanol ($C_{14}H_{29}OH$) adsorbed on graphite (V_{bias} = 1.127 V, I_{set} = 650 pA).[79]

part by close packing of extended alkyl chains to form characteristic tapes, and hydrogen bonding of hydroxyl headgroups then determines the interaction of the tapes and their detailed angular geometries.[79]

1.2.2 Metal Coordination

Besides hydrogen bonding, metal coordination is a powerful strategy for building supramolecular architectures, and this strategy has been widely used in recent years. A variety of metals can be coordinated to organic ligands, such as alkali metals, alkaline earth metals, transition metals, lanthanides, and actinides. Many supramolecular metal-organic coordination assemblies have been constructed, including metal-containing cages, macrocyles, interlocked species (such as catenanes and rotaxanes), and helicates.[80-85]

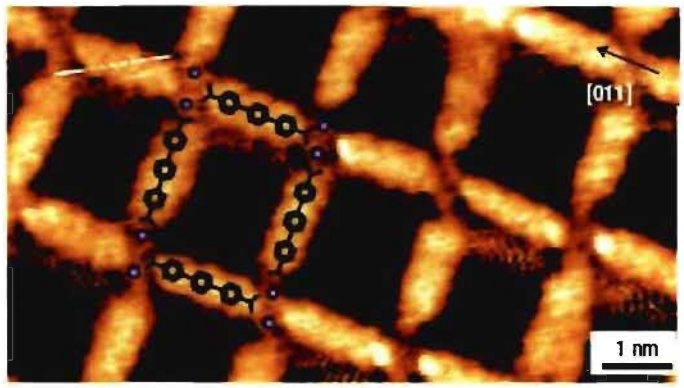

Figure 1.9 High-resolution STM image of reticulated Fe-TDA open network with rectangular nanocavities on Cu(100) substrate.[86]

In surface nanopatterning, metal-ligand coordination offers a new way to build open 2D networks on metal surfaces under UHV.[86-90] Figure 1.9 shows an STM image of open

networks with rectangular nanocavities formed by 4,1',4',1''-terphenyl-1,4''-dicarboxylic acid (TDA) coordinated with Fe on a Cu(100) surface.[86]

1.2.3 Van der Waals Interactions

Van der Waals interactions are a sum of long-range inductive and dispersive intermolecular forces.[91] Classic inductive forces include permanent dipole-dipole and induced dipole-dipole interactions. Such interactions have a magnitude that varies as the separation of the interacting species. Dispersion forces are quantum mechanical in nature and result from momentary fluctuations of the electron density within molecules. Van der Waals forces are relatively weak compared with normal chemical bonds, but their collective effects are not negligible, thus leading to a fundamental role in many fields, such as supramolecular chemistry and surface science. A number of well-designed molecules with long akyl chains have been found to self-assemble into highly-ordered patterns at surfaces by van der Waals interactions among molecules, as well as between adsorbed molecules and substrates.[46,47]

1.3 Molecular Tectonics

Molecular tectonics provides a powerful strategy for engineering three dimensional (3D) crystal structures, based on molecular self-assembly of building subunits which have been called tectons. Tecton is the Greek word for builder, and it describes *any molecule whose interactions are dominated by particular associative forces that induce the*

self-assembly of an organized network with specific architectural or functional features.[92] A typical tecton can be considered to have a core, which can be a simple central atom or a more complex structure. The cores can be varied freely to change various properties of the tecton, such as its geometry, size, reactivity, and physical properties. Functional groups are then connected to the core to provide sticky sites that control intermolecular association and lead to the formation of extended supramolecular networks held together by directional noncovalent interactions, such as hydrogen bonds. The sticky sites can include those

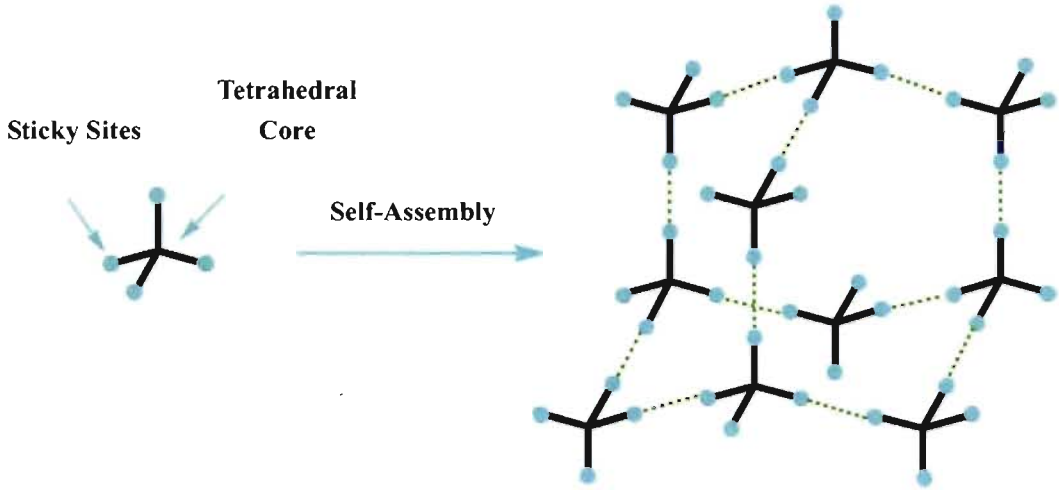

Figure 1.10 Self-assembly of a hypothetic diamondoid network by the association of a tetrahedral tecton directed by non-covalent interactions.[92]

described above, such as carboxyl, diaminotriazine (DAT), pyridone, and hydroxyl groups. Figure 1.10 shows the directed self-association of a theoretical tecton. The presence of four sticky sites that participate in non-covalent interactions, as well as the tetrahedral geometry of the molecule, should drive the system to form a diamondoid network.[92]

The crystallization of most small molecules produces close-packed structures in order to maximize intermolecular contact. This minimizes free space in molecular structures but

does not entirely eliminate it, because molecules have definite three-dimensional structures that can never be packed with perfect efficiency. In typical molecular crystals, the efficiency of packing is about 70%, which is the fraction of the volume of the unit cell actually occupied by the constituent molecules.[93] The strategy of molecular tectonics introduces important additional constraints that result from the presence of multiple directional intermolecular interactions. These constraints make close packing even more difficult to achieve. As a result, the crystallization of tectons can be used to produce open networks that contain large pores or channels. In such cases, the fraction of volume occupied by the tectons themselves can be as small as 30% or less, far below the typical values normally seen in molecular crystals (70%). Often, the space inside open networks formed by the crystallization of tectons is accessible from the surface of the crystal, and included guest molecules can be partially removed or completely exchanged without interrupting the integrity of the crystal. This key strategy has been applied to create a large number of well-designed 3D crystal structures that are permeable to outside agents.[65-71, 92, 94-96]

Shown in Figure 1.11 is a typical tecton **5**, which is a simple molecule with a tetrahedral core and four DAT groups.[66] Single crystals were obtained by allowing dioxane to diffuse into a solution of tecton **5** in formic acid. X-ray crystallography showed that the resulting 3D hydrogen-bonded network is highly porous (46%) and extremely robust, because each tecton is held in position by 16 intermolecular hydrogen bonds. During the exchange of guests or even during their partial removal by exposure to vacuum ranging from 3.5 h to 66 h, the network was found to remain the same and the unit cell parameters only showed small changes. Individual hydrogen bonds are known as weak interactions,

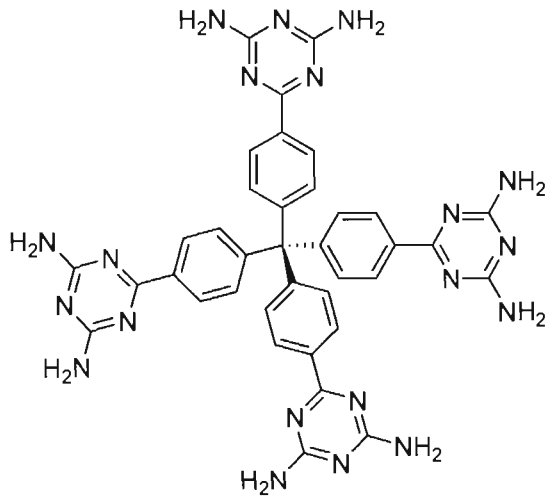

5

(a)

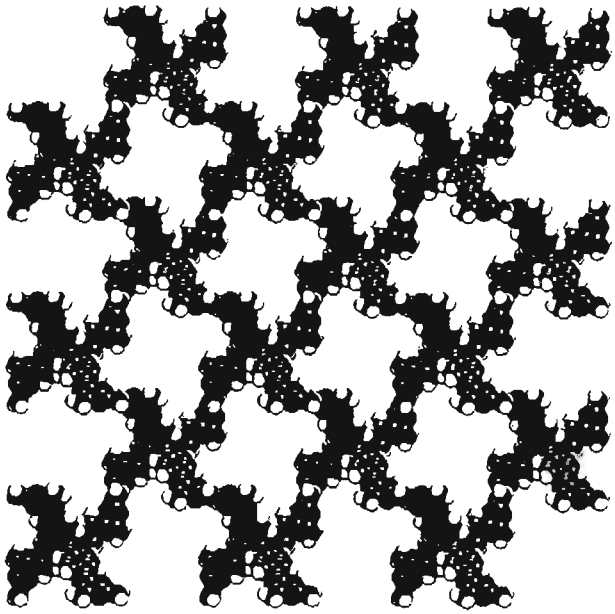

(b)

Figure 1.11 a) Molecular structure of tecton **5**. b) View (along c) of the crystal structure parallel to the channel axes, showing the cross sections of adjacent channels. Guest molecules of formic acid and dioxane are omitted for clarity.[66]

but when tectons are oriented in networks by suitably large numbers of hydrogen bonds, their collective effect can approach or even exceed that of strong covalent bonds.

1.4 Purpose of This Study

The strategy of molecular tectonics has been successfully used to build robust 3D crystal structures by design. Our goal is to extend this strategy to the 2D construction of supramolecular architectures on surfaces. Our initial surface study was inspired by the behavior of trimesic acid (TMA), which is a prototypic tecton with trigonally directed sticky sites (Figure 1.12). Directed by the association of the three –COOH groups as cyclic hydrogen-bonded pairs, trimesic acid forms hexagonal 2D porous networks, which can accommodate different guests, such as coronene and C_{60}.[97, 98] Expanded versions of the network can be built from molecules derived from TMA by inserting spacers between the –COOH groups and the 1,3,5-trisubstituted phenyl core.[99, 100]

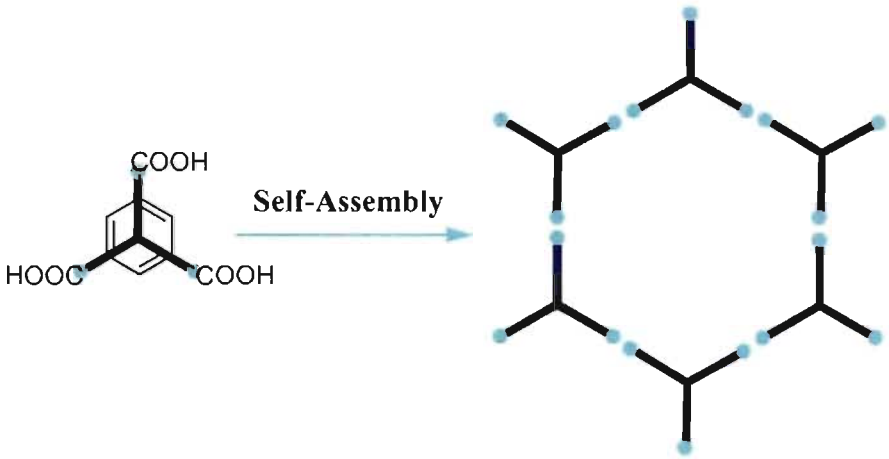

Figure 1.12 Schematic illustration of a hexagonal network built from trimesic acid.

However, the utility of this trigonal tecton and its extended analogues is limited by (1) the inability of normal pair-wise association of the –COOH groups to program the construction of networks other than hexagons and (2) the small number of hydrogen bonds (six) in which each molecule can participate.

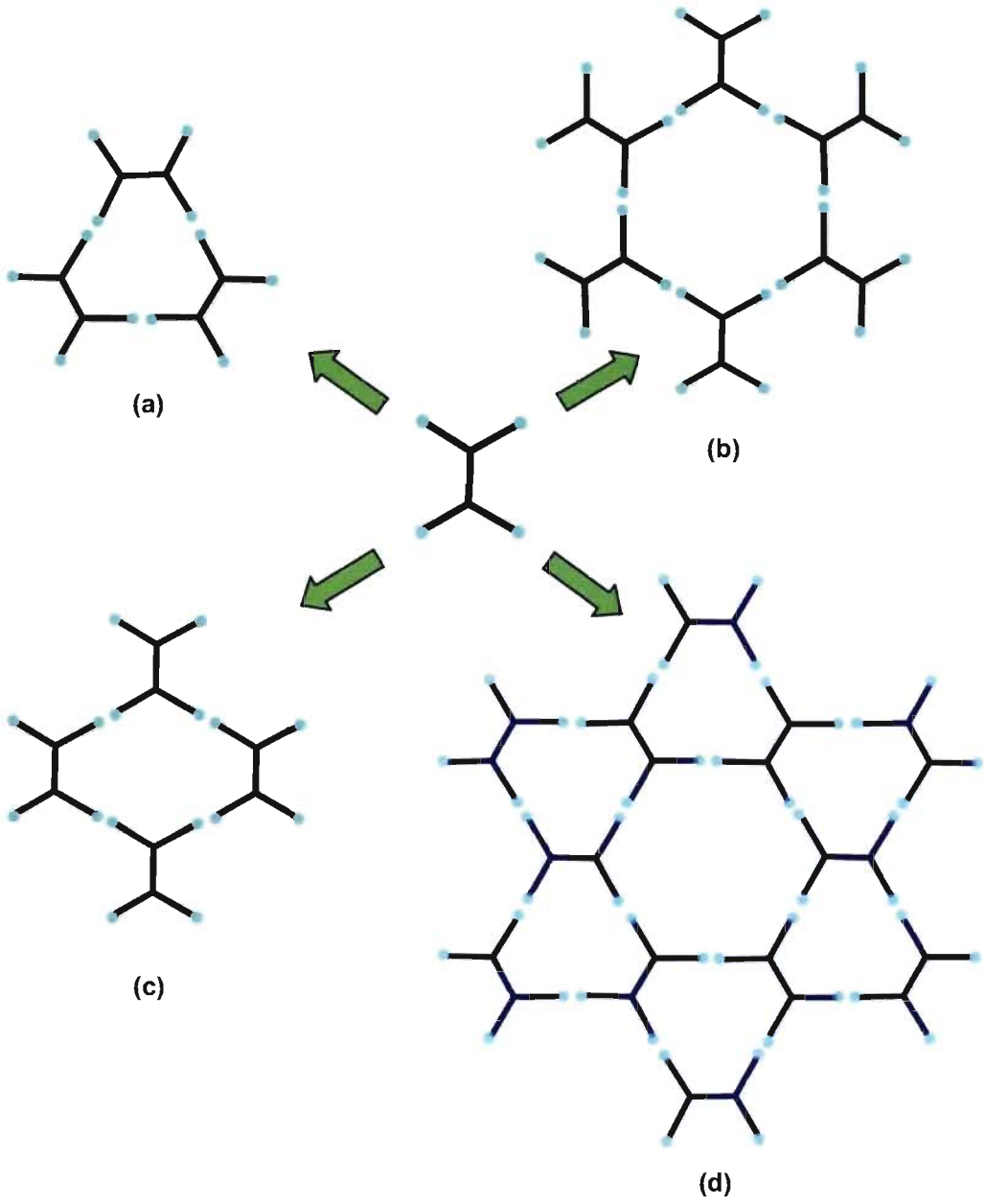

Figure 1.13 Schematic illustration of the formation of ordered 2D networks by directed molecular self-assembly of a planar tecton with four sticky sites. (a) Trigonal network. (b) Hexagonal network. (c) Parallel network. (d) Kagomé network.

To expand the diversity of 2D networks built from tectons, we were led rationally to the design of new planar analogues with four sticky sites (Figure 1.13). Compared with simple trigonal tectons, the new analogues can be expected to create supramolecular architectures that are not only richer in variety but also more robust. As shown in Figure 1.14,

self-assembly can form four types of networks, including the trigonal, parallel, hexagonal, and Kagomé networks. In particular, these networks can be held together by hydrogen bonding, using directed interactions between adjacent functional groups such as carboxyl, DAT, pyridone, and hydroxy, as described above.

In this dissertation, we report the systematic design and synthesis of a series of new tectons of this type, and we describe their adsorption at the liquid-solid interface of heptanoic acid and HOPG by STM. Specifically, tectons of the type shown in Figure 1.14 have been designed with a variety of linear backbones, such as biphenyl, 1,2-diphenylacetylene, 1,4-bis(2-phenylethynyl)benzene, 1,4-bis(2-phenylethynyl) naphthalene, and 1,4-bis(2- phenylethynyl)anthracene. Tectons of this type have been studied with diverse sticky sites, including DAT groups (Chapter 3), carboxyl groups (Chapter 4), and ester groups (Chapter 5). STM investigations of these tectons have revealed that surface nanopatterns can be controlled logically by changing the backbone, cores, functional groups, and molecular geometries. We have found that the resulting 2D networks are only partially predictable, due to the complex nature of the intermolecular interactions involved and the important contributions of the underlying surface. Even though some surface nanopatterns were generated unexpectedly, they could still be interpreted using simple molecular models.

Simultaneously, the structures of many tectons used in 2D studies have also been determined in 3D by X-ray crystallography. Comparison of 2D and 3D crystallizations shows that the resulting structures can sometimes have quite different features, due in part to the effect of confinement on surfaces. STM studies of 2D chirality are discussed

separately in Chapter 6. Tectons were specifically chosen to create 2D chiral nanopatterns based on rational considerations of molecular symmetry. As expected, well-designed tectons showed interesting 2D chiral behavior on the surface of graphite.

Overall, this dissertation describes initial steps toward the goal of developing the strategy of molecular tectonics as a reliable source of predictable 2D supramolecular nanopatterns. We have systematically examined various factors that can control the adsorption of tectons, including the identity of the backbone, core, sticky functional groups, and molecular symmetry. The results of our research provide a deeper understanding of how molecules can be used to nanopattern surfaces by design. Our work illustrates the special value of interdisciplinary studies that combine synthesis, theory, surface science, and X-ray crystallography to probe crystallization in both 2D and 3D.

References

1. Lehn, J.-M. *Rep. Prog. Phys.* **2004**, *67*, 249-265.
2. Lawrence, D. S.; Jiang, T.; Levett, M. *Chem. Rev.* **1995**, *95*, 2229-2260.
3. Lehn J.-M. *Science* **1993**, *260*, 1762-1763.
4. Emsley, J. *Chem. Soc. Rev.* **1980**, *9*, 91-124
5. Chandler, D. *Nature* **2005**, *437*, 640-647.

6. Naray-Szabo, G.; Ferenczy, G. G. *Chem. Rev.* **1995**, *95*, 829-847.

7. Szejtli, J. *Chem. Rev.* **1998**, *98*, 1743-1753.

8. Deng, W.; Yamguchi, H.; Takashima, Y.; Harada, A. *Angew. Chem. Int. Ed.* **2007**, *46*, 5144-5147.

9. Villalonga, R.; Cao, R.; Fragoso, A. *Chem. Rev.* **2007**, *107*, 3088-3116.

10. Gerasko, O. A.; Samsonenko, D. G.; Fedin, V. P. *Russ. Chem. Rev.* **2002**, *71*, 741-760.

11. Kim, K.; Selvapalam, N.; Ko, Y. H.; Park, K. M.; Kim, D.; Kim, J. *Chem. Soc. Rev.* **2007**, *36*, 267-279.

12. Zhang, Y.-Q.; Zhen, L.-M.; Yu, D.-H.; Zhao, Y.-J.; Xue, S.-F.; Zhu, Q.-J.; Tao, Z. *J. Mol. Struct.* **2008**, *875*, 435-441.

13. Akutagawa, T.; Endo, D.; Noro, S.-I.; Cronin, L.; Nakamura, T. *Coord. Chem. Rev.* **2007**, *251*, 2547-2561.

14. Illescas, B. M.; Santos, J.; Diaz, M. C.; Martin, N.; Atienza, C. M.; Culdi, D. M. *Eur. J. Org. Chem.* **2007**, *30*, 5027-5037.

15. Fedorova, O. A.; Fedorov, Y. V.; Vedernikov, A. I.; Yescheulova, O. V.; Gromov, S. P.; Alfimov, M. V.; Churakov, A. V. *New J. Chem.* **2002**, *26*, 543-553.

16. Khairutdinov, R. F.; Hurst, J. K. *Langmuir* **2004**, *20*, 1781-1785.

17. Nishiyama, F.; Yokoyama, T.; Kamikado, T.; Yokoyama, S.; Mashiko, S. *Appl. Phys. Lett.* **2006**, *88*, 253113/1-253113/3.

18. Drain, C. M.; Russell, K. C.; Lehn, J.-M. *Chem. Commun.* **1996**, *262*, 471-475.

19. Hu, J.-S.; Guo, Y.-G.; Liang, H.-P.; Wan, L.-J.; Jiang, L. *J. Am. Chem. Soc.* **2005**, *127*, 17090-17095.

20. Diederich, F.; Gómez-López, M. *Chem. Soc. Rev.* **1999**, *28*, 263-277.

21. Hahn, U.; Cardianli, F.; Nierengarten, J.-F. *New J. Chem.* **2007**, *31*, 1128-138.

22. Sun, D.-Y.; Tham, F. S.; Reed, C. A.; Chaker, L.; Boyd, P. W. *J. Am. Chem. Soc.* **2002**, *124*, 6604-6612.

23. Bonifazi, D.; Enger, O.; Diederich, F. *Chem. Soc. Rev.* **2007**, *36*, 390-414.

24. Figueira-Duarte, T. M.; Gegout, A.; Nierengarten, J.-F. *Chem. Commun.* **2007**, *46*, 1265-1269.

25. Binder, W. H.; Sachsenhofer, R.; Straif, C. J.; Zirbs, R. *J. Mater. Chem.* **2007**, *17*, 2125-2132.

26. Drain, C. M.; Smeureanu, G.; Patel, S.; Gong, X.-C. ; Garno, J.; Arijeloye, J. *New J. Chem.* **2006**, *30*, 1834-1843.

27. Daniel, M.-C.; Astruc, D. *Chem. Rev.* **2004**, *104*, 293-346.

28. Schemhar, R.; Rotello, V. M. *Acc. Chem. Res.* **2003**, 36, 549-561.

29. Radowski, M. R.; Shukla, A.; von Berlepsch, H.; Boettcher, C.; Pickaert, G.; Rehage, H.; Haag, R. *Angew. Chem. Int. Ed.* **2007**, *46*, 1265-1269.

30. Bury, I.; Heinrich, B.; Bourgogne, C.; Guillon, D.; Donnio, B. *Chem. Eur. J.* **2006**, *12*, 8396-8413.

31. Dykes, G. M.; Smith, D. K. *Tetrahedron* **2003**, *59*, 3999-4009.

32. Gittins, P. J.; Twyman, L. J. *Supramol. Chem.* **2003**, *15*, 5-23.

33. Balzani, V.; Credi, A.; Venturi, M. *Chem. Eur. J.* **2002**, *8*, 5524-5532.

34. Dalgarno, S. J.; Tucker, S. A.; Bassil, D. B.; Atwood, J. L. *Science* **2005**, *309*, 2037-2039.

35. MacGillivray, L. R.; Atwood, J. L. *Nature* **1997**, *389*, 469-472.

36. Cave, G. W. V.; Anterberger, J.; Barbour, L. J.; McKinlay, R. M.; Atwood, J. L. *Angew. Chem. Int. Ed.* **2004**, *43*, 5263-5266.

37. Palmer, L. C.; Rebek, J. Jr. *Org. Lett.* **2005**, *7*, 787-789.

38. Shivanyuk, A.; Rebek, J. Jr. *Chem. Commun.* **2001**, *11*, 2374-2375.

39. Avram, L.; Cohen, Y. *J. Am. Chem. Soc.* **2003**, *125*, 16180-16181.

40. Desiraju, G. R. *Acc. Chem. Res.* **2002**, *35*, 565-573.

41. Evans, O. R.; Lin, W. *Acc. Chem. Res.* **2002**, *35*, 511-522.

42. Desiraju, G. R. *J. Mol. Struct.* **2003**, *656*, 5-15.

43. Brammer, L. *Chem. Soc. Rev.* **2004**, *33*, 476-489.

44. Blake, A. J.; Champness, N. R.; Hubberstey, P.; Li, W.-S.; Withersby, M. A.; Schröder, M. *Coord. Chem. Rev.* **1999**, *183*, 117-138.

45. Shan, N.; Bond, A. D.; Jones, W. *Cryst. Eng.* **2002**, *5*, 9-24.

46. De Feyter, S.; Gesquière, A.; Abdel-Mottalev, M. M.; Grim, P. M.; De Schryver, F. C. *Acc. Chem. Res.* **2000**, *33*, 520-531.

47. De Feyter, S.; De Schryver, F. C. *Chem. Soc. Rev.* **2003**, *32*, 139-150.

48. Plass, K. E.; Grzesiak, A. L.; Matzger, A. J. *Acc. Chem. Res.* **2007**, *40*, 287-293.

49. Eichhorst-Gerner, K.; Stabel, A.; Moessner, G. Declerq, D.; Valiyaveettil, S.; Enkelmann, V.; Müllen, K.; Rabe, J. P. *Angew. Chem. Int. Ed.* **1996**, *35*, 1492-1495.

50. Yablon, D. G.; Giancarlo, L. C.; Flynn, G. W. *J. Phys. Chem. B* **2000**, *104*, 7627-7635.

51. Emsley, J. *Chem. Soc. Rev.* **1980**, *9*, 91-124.

52. Jeffrey, G. A. *An Introduction to Hydrogen Bonding (Topics in Physical Chemistry)*,

Oxford University Press, USA, **1997**.

53. Beijer, F. H.; Kooijman, H.; Spek, A. L.; Sijbesma, R. P.; Meijer, E. W. *Angew. Chem. Int. Ed.* **1998**, *37*, 75-78.

54. a) Kuduva, S. S.; Craig, D. C.; Nangia, A.; Desiraju, G. R. *J. Am. Chem. Soc.* **1999**, *121*, 1936-1944. b) Desiraju, G. R. *Acc. Chem. Res.* **1996**, *29*, 441–449. c) Hobza, P.; Havlas, Z. *Chem. Rev.* **2000**, *100*, 4253-4264.

55. a) Hanton, L. R.; Hunter, C. A.; Purvis, D. H. *Chem. Commun.* **1992**, 1134-1136. b) Allen, F. H.; Howard, J. A.; Hoy, V. J.; Desiraju, G. R.; Reddy, D. S.; Wilson, C. C. *J. Am. Chem. Soc.* **1996**, *118*, 4081-4084.

56. Muehldorf, A. V.; Engen, D. V.; Warner, J. C.; Hamilton, A. D. *J. Am. Chem. Soc.* **1988**, *110*, 6561-6562.

57. Sherrington, D. C.; Taskinen, K. A. *Chem. Soc. Rev.* **2001**, *30*, 83-93.

58. Bernstein, J.; Davis, R. E.; Shimoni, L.; Chang, N.-L. *Angew. Chem. Int. Ed.* **1995**, *34*, 1555-1573.

59. Du, M.; Zhang, Z.-H.; Zhao, X.-J. *Cryst. Growth Des.* **2005**, *5*, 1199-1208.

60. Munakata, M.; Wu, L. P.; Yamamoto M.; Kuroda-Sowa, T.; Maekawa, M. *J. Am. Chem. Soc.* **1996**, *118*, 3117-3124.

61. Yokoyama, T.; Yokoyama, S.; Kamikado, T.; Okuno, Y.; Mashiko, S. *Nature* **2001**, *413*, 619-621.

62. Schrier, E. E.; Pottle, M.; Scheraga, H. A. *J. Am. Chem. Soc.* **1964**,*86*, 3444-3449.

63. Zaworotko, M. J. *Chem. Commun.* **2001**, 1-9.

64. Griessl, S.; Lackinger, M.; Edelwirth, M.; Hietschold, M.; Heckl, W. M. *Single Mol.*

2002, *3*, 25-31.

65. Sauriat-Dorizon, H.; Maris, T.; Wuest, J. D. *J. Org. Chem.* **2003**, *68*, 240-246.

66. Brunet, P.; Simard, M.; Wuest, J. D. *J. Am. Chem. Soc.* **1997**, *119*, 2737-2738.

67. Laliberté, D.; Maris, T.; Sirois, A.; Wuest, J. D. *Org. Lett.* **2003**, 5, 4787-4790.

68. Laliberté, D.; Maris, T.; Wuest, J. D. *J. Org. Chem.* **2004**, *69*, 1776-1787.

69. Fournier, J.-H.; Maris, T.; Wuest, J. D. *J. Org. Chem.* **2004**, *69*, 1762-1775.

70. Malek, N.; Maris, T.; Simard, M.; Wuest, J. D. *J. Am. Chem. Soc.* **2005**, *127*, 5910-5916.

71. Maly, K. E.; Gagnon, E.; Maris, T.; Wuest. J. D. *J. Am. Chem. Soc,* **2007**, *129*, 4306-4322.

72. Theobaid, J. A.; Oxtoby, N. S.; Phillips, M. A.; Champness, N. R.; Beton, P. H. *Nature* **2003**, *424*, 1029-1031.

73. (a) Zhang, H.-M.; Xie, Z.-X.; Long, L.-S.; Zhong, H.-P. ; Zhao, W.; Mao, B.-W. ; Xu, X.; Zheng, L.-S. *J. Phys. Chem. C* **2008**, *112*, 4209-4218. (b) Xu, W.; Dong, M.-D.; Gersen, E. R.; Vázquez-Campos, S.; Crego-Calama, M.; Reinhoudt, D. N.; Stensgaard, I.; Laegsgaard, E.; Linderoth, T. R.; Besenbacher, F. *Small* **2007**, *3*, 854-858.

74. Jonkheijm, P.; Miura, A.; Zdanowska, M.; Hoeben, J. M.; De Feyter, S.; Schenning, A. P. H. J.; De Schryver, F. C.; Meijer, E. W. *Angew. Chem. Int. Ed.* **2004**, *43*, 74-78.

75. Caňas-Ventura, M. E.; Xiao, W.; Wasserfallen, D.; Müllen, K.; Brune, H. *Angew. Chem. Int. Ed.* **2007**, *46*, 1814-1818.

76. Atwood, J. L.; Barbour, L. J.; Jerga, A. *Proc. Natl. Acad. Sci. USA* **2002**, *99*, 4837-4841.

77. Cave, G. W. V.; Ferrarelli, M. C.; Atwood, J. L. *Chem. Commun.* **2005**, 2787-2789.

78. Saied, O.; Maris, T.; Wang, X.; Simard, M. Wuest, J. D. *J. Am. Chem. Soc.* **2005**, *127*, 10008-10009.

79. Claypool, C. L.; Faglioni, F.; Goddard III, W. A.; Gray, H. B.; Lewis, N. S.; Marcus, R. A. *J. Phys. Chem. B* **1997**, *101*, 5978-5995.

80. Gimeno, N.; Vilar, R. *Coord. Chem. Rev.* **2006**, *250*, 3161-3189.

81. Moussa, J.; Amouri, H. *Angew. Chem. Int. Ed.* **2008**, *47*, 1372-1380.

82. McKinlay, R. M.; Thallapally, P. K.; Cave, G. W. V.; Atwood, J. L. *Angew. Chem. Int. Ed.* **2005**, *117*, 5879-5882.

83. Seidel, S. R.; Stang, P. J. *Acc. Chem. Res.* **2002**, *35*, 972-983.

84. Fujita, M.; Tominaga, M.; Hori, A.; Therrien, B. *Acc. Chem. Res.* **2005**, *38*, 371-380.

85. (a) Habermehl, N. C.; Jennings, M. C.; McArdle, C. P.; Mohr, F.; Puddephatt, R. J. *Organometallics* **2005**, *24*, 5004-5014. (b) Loeb, S. J. *Chem. Soc. Rev.* **2007**, *36*, 226-235.

86. Stepanow, S.; Lingenfelder, M.; Dmitriev, A.; Spillmann, H.; Delvigne, E.; Lin, N.; Deng, X.-B.; Cai, C.-Z.; Barth, J. V.; Kern, K. *Nature Mat.* **2004**, *3*, 229-233.

87. Lin, N.; Stepanow, S.; Vidal, F.; Barth, J. V.; Kern, K. *Chem. Commun.* **2005**, 1681-1683.

88. Stepanow, S.; Lin, N.; Payer, D.; Schlickum, U.; Klappenberger, F.; Zoppellaro, G.; Ruben, M.; Brune, H.; Barth, J. V.; Kern, K. *Angew. Chem. Int. Ed.* **2007**, *46*, 710-713.

89. Dmitriev, A.; Spillmann, H.; Lin, N.; Barth, J. V.; Kern, K. *Angew. Chem. Int. Ed.* **2003**, *42*, 2670-2673.

90. Stepanow, S.; Lin, N.; Barth, J. V. Kern, K. *J. Phys. Chem. B* **2006**, *110*, 23472-23477.

91. Kipnis, A. K.; Yavelov, B. E.; Rowlinson, J. S. *Van der Waals and Molecular Science,* Clarendon Press, New York, **1996**.

92. Simard, M.; Su, D.; Wuest, J. D. *J. Am. Chem. Soc.* **1991**, *113*, 4696-4698.

93. Kitaigorodskii, A. I. *Molecular Crystals and Molecules*, Academic Press, New York, **1973**.

94. Ducharme, Y.; Wuest, J. D. *J. Org. Chem.* **1988**, *53*, 5787-5789.

95. Gallant, M.; Phan, M. T.; Wuest. J. D. *J. Org. Chem.* **1991**, *56*, 2284-2286.

96. Saied, O.; Maris, T.; Wuest, J. D. *J. Am. Chem. Soc.* **2003**, *125*, 14956-14957.

97. Griessl, S. J. H.; Lackinger, M.; Jamitzky, F.; Markert, T.; Hietschold, M.; Heckl, W. M. *J. Phys. Chem. B* **2004,** *108,* 11556-11560.

98. Griessl, S. J. H.; Lackinger, M.; Jamitzky, F.; Markert, T.; Hietschold, M.; Heckl, W. M. *Langmuir* **2004,** *20,* 9403-9407.

99. Kampschulte, L.; Lackinger, M.; Maier, A.-K.; Kishore, R. S. K.; Griessl, S.; Schmittel, M.; Heckl, W. M. *J. Phys. Chem. B* **2006**, *110*, 10829-10836.

100. Ruben, M.; Payer, D.; Landa, A.; Comisso, A.; Gattinoni, C.; Lin, N.; Collin, J.-P.; Sauvage, J.-P.; De Vita, A.; Kern, K. *J. Am. Chem. Soc.* **2006**, *128*, 15644-15651.

CHAPTER 2

Scanning Tunneling Microscopy

2.1 Introduction

A new technique known as scanning tunneling microscopy (STM) was first developed in 1982 by a group of scientists from the IBM Research Laboratory in Zurich.[1] These scientists finally invented a technique that can "see" (or at least "feel") individual atoms. Therefore, it is not surprising that the inventors, Binnig, Rohrer, and Herber, shared the Nobel Prize in physics in 1986. In 1990, scientists employed STM to position single atoms on surfaces for the first time (Figure 2.1).[2] Since its invention, STM has become a powerful technique for investigating surfaces at the atomic level. It has also played a key role in the recent development of many fields, such as nanotechnology, surface science, supramolecular chemistry, molecular electronics, and biochemistry. The initial applications of STM were focused on the imaging of semiconductor, inorganic, and metal surfaces. The first experiment on molecular monolayers was carried out under ultra-high vacuum (UHV).[3] In the late 1980s, STM was used to study physisorbed organic molecules at the

Figure 2.1 An STM image of a patterned array of xenon atoms on Ni (110).[2]

solid-liquid interface, thus allowing advantage to be taken of the versatility of STM to operate under ambient conditions.[4-6] STM has now been widely used to explore a broad field of topics, such as chirality,[7-12] reactivity,[13-17] and dynamics[18-23] at a molecular level.

2.2 Basic Principle of STM

The basic concept that presaged the birth of STM is quantum tunneling, which has been understood in principle since 1971.[24] Classically, an object hitting an impenetrable wall of infinite height will bounce back. It would be astonishing if the object were to simply pass through the wall rather than bounding back upon impact. However, for objects of very small mass, such as electrons, the wavelike nature has a more pronounced effect, so such an event, referred to as tunneling, has a much greater probability.

STM probes a conducting or semiconducting sample with a conducting tip. As shown in Figure 2.2a,[25] without a voltage bias applied between the tip and sample, they have the same energy levels in vacuum but different Fermi levels. When an electron is incident upon a vacuum barrier with a potential energy larger than the kinetic energy of the electron, there is a non-zero probability that it may traverse the forbidden region and reappear on the other side of the barrier. Its wavefunction will thus leak out. When a conducting tip is brought very close to a metallic or semiconducting surface (5-10 Å), their leak-out wavefunctions will overlap (Figure 2.2b). When a small voltage bias is applied between tip and sample, the overlapped electron wavefunction permits quantum mechanical tunneling, and a current will flow across the vacuum gap between them. At low voltage and temperature, the tunneling

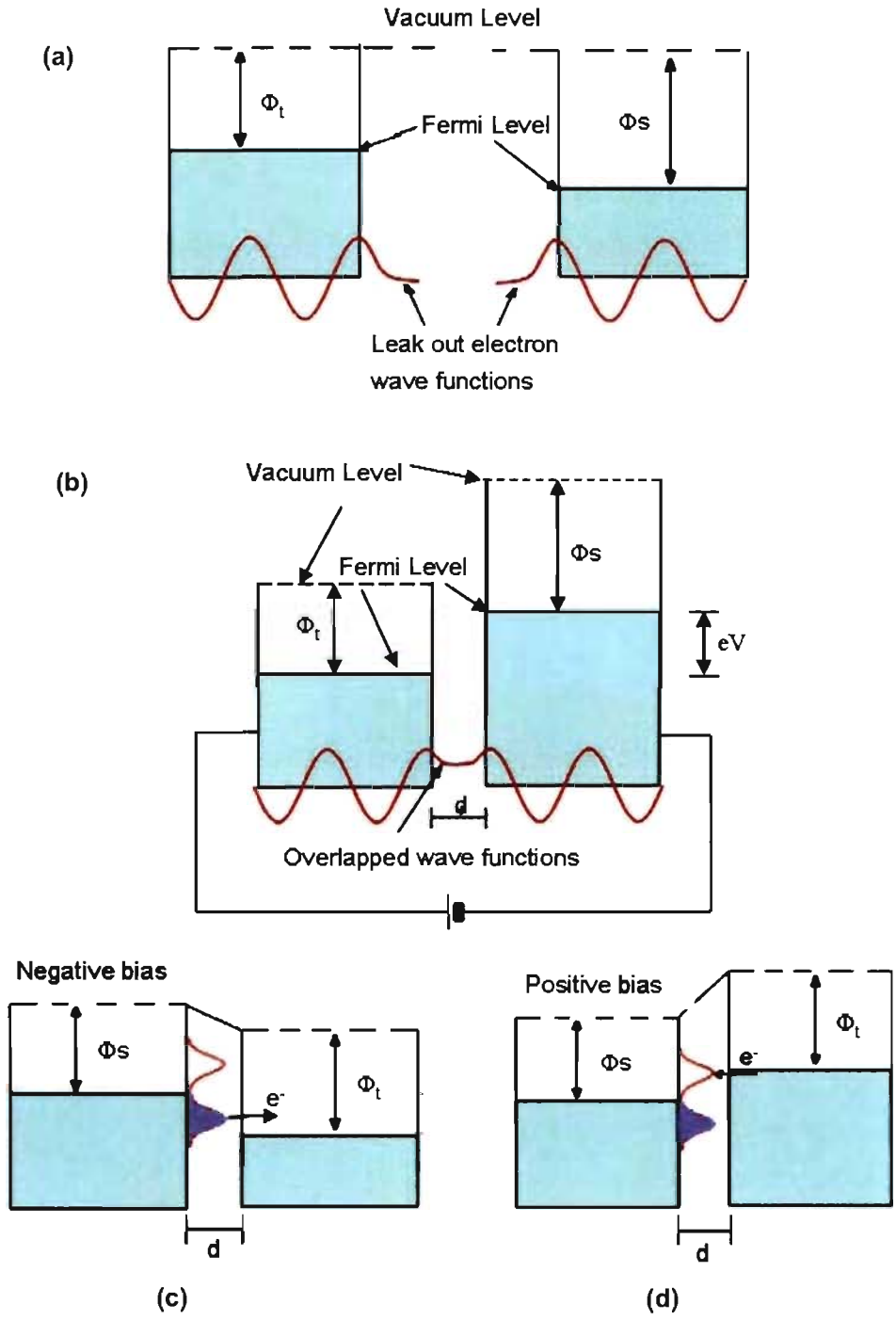

Figure 2.2 (a) Without bias applied, tip and sample have the same vacuum energy level but different Fermi levels. (b) When the distance, d, between tip and sample is close enough, and a small bias is applied, tunneling current flows across the vacuum gap. (c) When a negative bias is applied to the sample, tunneling current flows from sample to tip. (d) When a positive bias is applied to the sample, tunneling current flows from tip to sample.[25]

current, I, can be simply represented by equation 2.1, which shows the exponential dependence of tunneling current on the sample-tip separation.

$$I \propto \exp(-2Kd) \qquad (2.1)$$

where K is determined by equation (2.2) and d is the distance between the tip and the sample.

$$K = (2m\Phi)^{1/2}/h \qquad (2.2)$$

In equation (2.2), m is the mass of the electron, Φ is the local tunneling barrier height or the average work function of the tip and the sample, and h is Planck's constant.

Therefore, the remarkable atomic resolution of STM originates from the steep, exponential decay of the tunneling current with increasing tip-sample separation. Typically, an approach of only 1 Å from tip to sample can increase the tunneling current by almost one order of magnitude.

When the sample is negatively biased, as shown in Figure 2.2c, the tunneling current is dominated by electrons from the Fermi level of the sample, and the tunneling current flows from occupied states of the sample to unoccupied states of the tip. Reversibly, if the sample is positively biased (Figure 2.2d), the tunneling current is dominated by electrons from the Fermi level of the tip, and current flows from occupied states of the tip to unoccupied states of the sample.[25]

2.3 STM Instrumentation

As shown in Figure 2.3, a typical STM instrument requires 1) a sharp tip placed in a very close proximity to the sample and 2) a mechanism to control the location of the tip in the X-Y plane parallel to the sample surface (X-Y scan control), which includes a piezoelectric tube, current amplifier, feedback control electronics, and a data-processing and display system.[26] STM can work in two modes, constant current mode and constant height mode. In constant current mode (Figure 2.4, left), a feedback loop is enabled to maintain constant current while a fixed bias is applied between the tip and the sample. As the tip is rastered over the surface by X- and Y- piezo drivers, tunneling current between

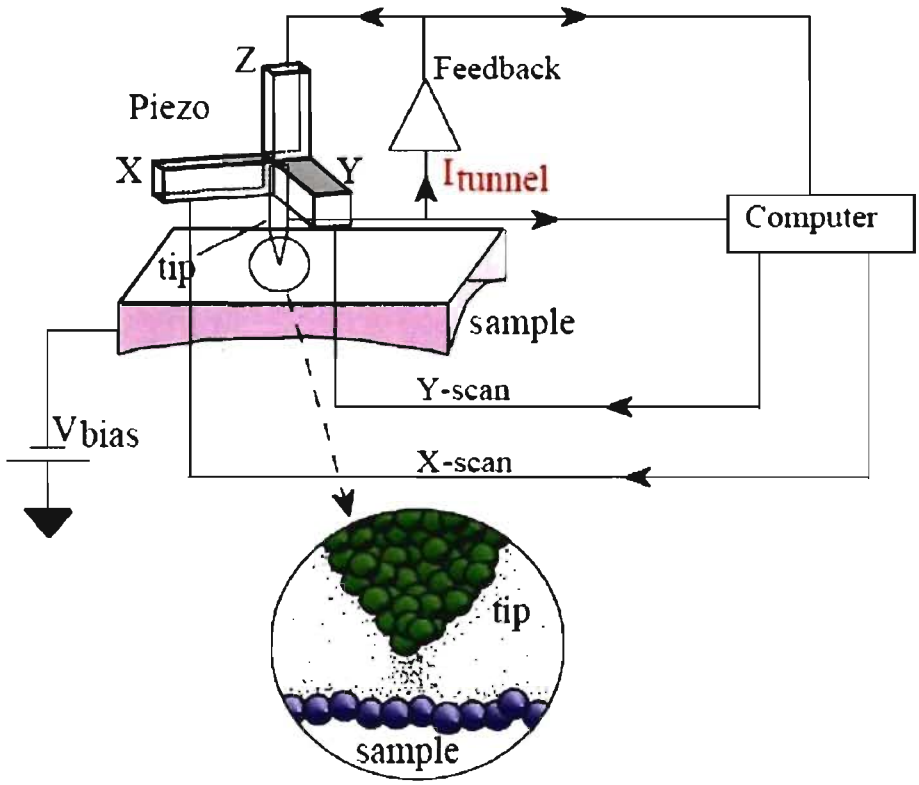

Figure 2.3 A schematic diagram of STM instrumentation.[26]

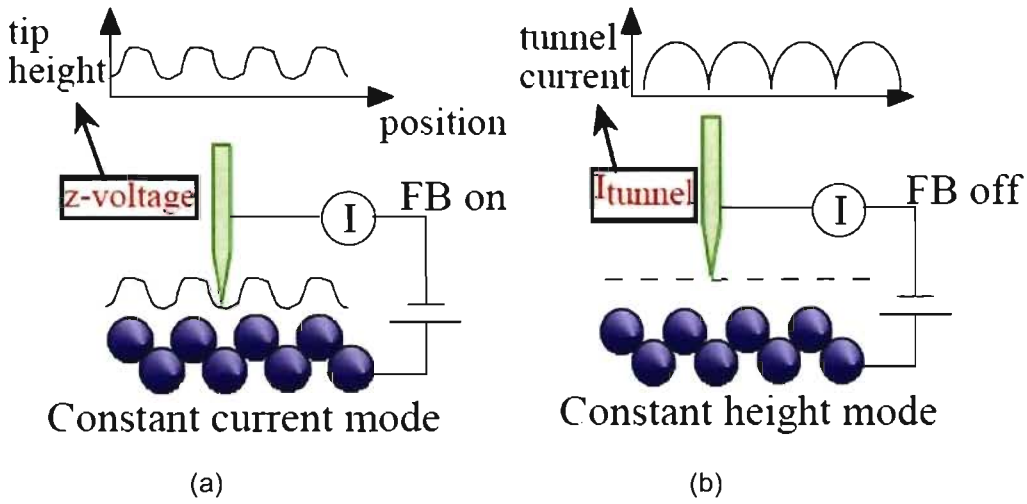

Figure 2.4 Two STM imaging modes. (a) Constant current mode. (b) Constant height mode.[26]

the tip and the sample is measured at each point of the raster. The vertical position (Z) of the tip is adjusted to maintain a constant current (the value of set tunneling current) throughout the scan.

Alternatively, in constant height mode (Figure 2.4, right), the vertical position of the tip is not changed, equivalent to a slow or disabled feedback. The tunneling current is measured as a function of the change of sample-tip separation, resulting from the topographic structure, such as steps of individual molecules. One of the advantages of this mode is that it can be used at high scanning frequencies (up to 20 kHz), since the tip does not need to be replaced by Z-piezo drivers. However, there is always a risk of crashing the tip into a tall feature on the surface. Constant current mode is most frequently used, whereas in this study, STM investigations were performed using constant height mode.

The STM instrument used to perform all the surface studies in this thesis is a JSPM-5200 instrument (Figure 2.5), which is a multipurpose, high resolution scanning-probe microscope (SPM) that allows the sample environment to be varied from

Figure 2.5 JSPM-5200 scanning-probe microscope.

ambient air, controlled atmosphere, fluids, or vacuum. In addition, the sample can be heated to 500 °C (773 K) or cooled to -143 °C (130 K).

2.4 Substrate Preparation

In our work, STM has primarily been used to image molecular monolayers. The molecules need to be deposited on an atomically flat, conductive surface. The substrate needs to be conductive to meet the requirements imposed by tunneling. An extended flat surface is also important because we want to be able to image deposited molecules over a large uniform area. It is hard to tell what is on the surface if it is bumpy. Two of the most common substrates used are gold and graphite. In certain cases, silver and copper are also sometimes used. All of these substrates are conductive and can be made atomically flat. Metal surfaces are usually prepared by repeated cycles of Ar^+ ion sputtering and subsequent annealing at ~800-900 K, which leads to an atomically flat and clean surface.[27]

2.4.1 Gold

Gold is a face-centered cubic metal (Figure 2.6a). The Au(111) plane is mostly used in STM studies under ultra-high vacuum (UHV) conditions, because in this plane the gold atoms are packed very tightly and are aligned at characteristic 60° angles (Figure 2.6b). Figure 2.7a shows an STM image of the surface of Au that has been flame annealed. Interestingly, the Au(111) 60° symmetry can be seen clearly through the entire image, which is one square micron.[28] For STM, we need to create a piece of gold that has large flat islands. A really good sample will have reconstruction lines on the flat islands (Figure 2.7a). The 3D view in Figure 2.7b shows that these lines are about 60-70 nm wide and 0.7 nm high. The gold is made by a process called vacuum deposition. If the gold does not

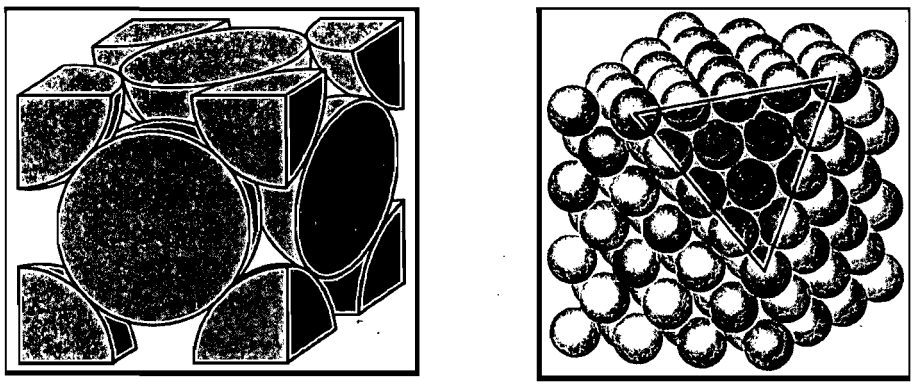

(a) (b)

Figure 2.6 (a) Face-centered cubic structure formed by Au. (b) Au(111) surface.

have large flat islands when it comes out of the vacuum chamber, it needs to be flame-annealed with a hydrogen torch. If this is done properly, the islands will increase in size, and reconstruction lines will form. Otherwise, bumps and pits will form on the gold.

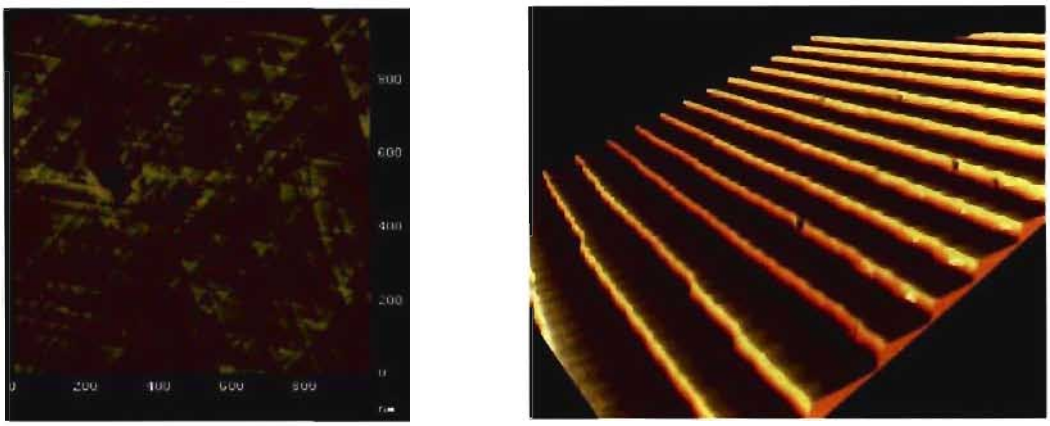

(a) (b)

Figure 2.7 (a) STM image of the surface of flame-annealed Au. (b) 3D representation highlighting the reconstruction lines perpendicular to the step edges.[28]

2.4.2 Graphite

Precious metals are used as substrates due to their low chemical reactivity, whereas the use of copper as a substrate can facilitate the adsorption of molecules via coordination interactions between molecules and the underlying metal.[29] Many reported STM studies on metal surfaces have been performed under UHV conditions. Because our experiments have involved the deposition of molecules of low volatility, we have opted to use studies at the liquid-solid interface. Specifically, we have chosen heptanoic acid as solvent and highly-oriented pyrolytic graphite (HOPG) as the substrate. Heptanoic acid is a reasonably good solvent for the relatively polar molecules featured in our study, and its volatility is low enough to prevent rapid evaporation. HOPG offers an attractive combination of good conductivity, good chemical stability, high affinity for organic molecules, and low cost.

Graphite has a layered structure, with each graphene layer composed of a planar

arrangement of fused hexagonal benzene rings (Figure 2.8a). As a result, graphite is highly anisotropic and hydrophobic. The trigonal bonding in each graphene sheet involves overlap of carbon sp^2 hybrid orbitals in the plane, whereas the overlap of carbon $2p_z$ orbitals produces delocalized rings of π electrons lying above and below each benzene ring, which makes graphite a good electrical conductor. The graphene layers are bonded to each other by weak van der Waals forces, so that they can easily slide over one another, which is why graphite is soft and slippery. As shown in Figure 2.8b, the positional relationship between two identical adjacent graphene planes displays two different positions of carbon atoms, one with a neighboring atom in the plane below (atom A) and one without a neighbor in the lattice below (atom B). Consequently the electrical conductivity of the graphite surface varies locally slightly (different electronic density of states).[30] As a result, carbon atom B above the hollow of the second graphene layer corresponds to the bright spot seen in STM images of HOPG (Figure 2.9a). Figure 2.9b shows a high-resolution STM image of HOPG obtained during our studies, showing the quality of our instrumentation, methods of sample preparation, and underlying HOPG.

Exposing a fresh layer of graphite requires cleavage. This is very simply achieved by sticking a piece of tape to the surface of a sample of graphite, then pulling up the tape, which takes off the top layer of graphite and leaves a new flat surface behind. This process also helps remove impurities on the surface. Graphite (SPI-1 grade) used in our STM experiments is commercially available from Structure Probe, Inc.

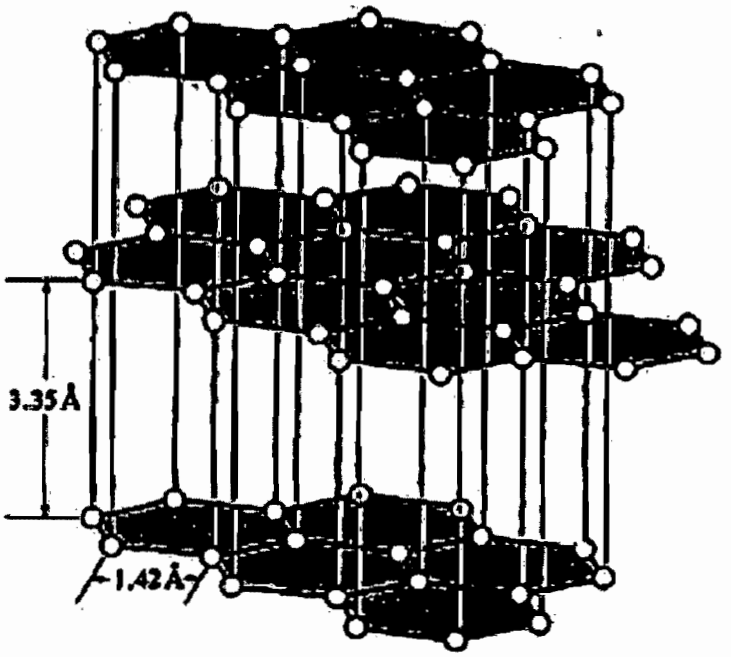

(a)

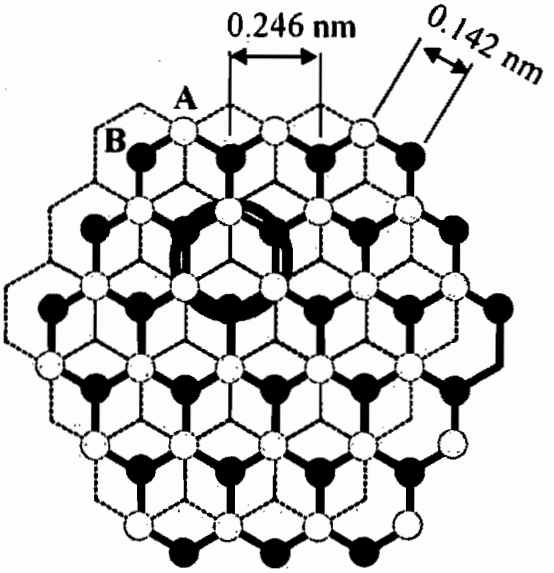

(b)

Figure 2.8 (a) Graphite layered structures. (b) Positional relationship between two identical graphene planes, showing the two different positions of carbon atoms A and B.[30]

(a)

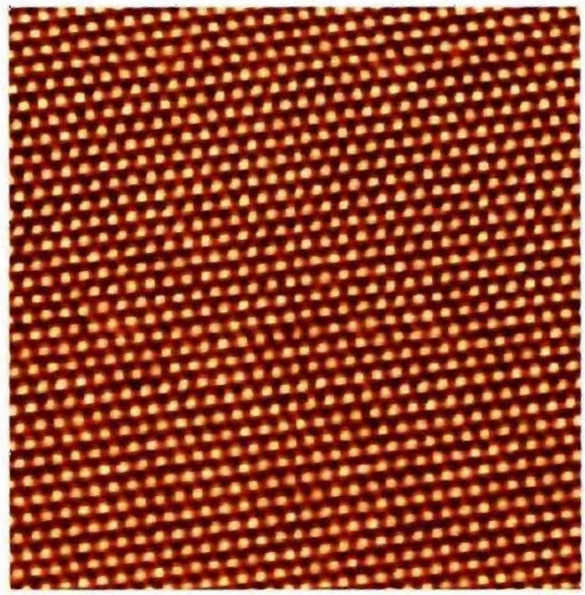

(b)

Figure 2.9 (a) Typical STM image of the HOPG surface, with a model of the corresponding fragment of graphene superimposed. (b) High-resolution STM image of HOPG (10×10 nm^2). V_{bias} = - 0.1V, I_{set} = 0.5 nA.

2.5 STM Tip

The STM tip is one of the most crucial factors for attaining high-resolution images. It is usually made of W (tungsten) or Pt/Ir (platinum-iridium). Tungsten wire is most commonly used as heating wires under UHV conditions. Pt/Ir wires are preferred for use in air because platinum does not easily oxidize. The tiny fraction of iridium in the alloy makes it much harder, and a tip made with pure platinum would naturally become blunt in a short time.

Generally, tips for STM scanning can be prepared by either mechanical cutting or electric etching. Cutting is simple and very effective. Sharp STM tips can be easily made by cutting Pt/Ir wire with a clean cutter. The standard technique uses a wire cutter (diagonal cutters) and a pair of pliers. The wire is held with the pliers, the cutters are placed at an acute angle to the wire, and the wire is pulled with the pliers as it is cut. Ideally, this ensures that as the wire is cut, it will weaken and break at the end of the point. The idea here is that because the wire breaks apart under tension, the tip is never touched by the cutters, avoiding possible contamination. The overall shape of cut tips may not be well defined, but the end can be very sharp. Previous TEM and SEM studies of mechanically cut tips have shown that there are often very sharp protrusions called micro-tips at the end of the main tip. Some of these micro-tips have a diameter of a few angstroms at their ends. High-resolution STM images can be obtained if the tunneling process mainly occurs via one of these micro-tips that is closest to the sample.

Tips made by electric etching are mainly used in UHV STM for good reproducibility.

The preparation of etched platinum or gold tips is feasible, but not often performed due to concern related to the use of highly concentrated solutions of cyanide. Tungsten (W) wire tips are commonly prepared by electronic etching in a typical solution of 3M KOH, which etches away the W atoms of the wire when a voltage is applied. The etched tips usually have a good shape with a radius of 40-150 nm.

In the process of scanning at the liquid-solid interface, tips are probably contaminated by the solution or adsorbates, thus leading to poorly resolved images. When this happens, the tip needs to be cleaned. Based on experience, we have used the following protocol for cleaning tips: (1) Retract the tip, and then move it to a corner of the scan area; (2) set up bias ± 1.0 ~ 5.0 V, tunneling current 0.5 nA, and scan rate 10 ~ 16.67 seconds per scan; (3) start scanning alternately under negative and positive bias for one scan each, and then move the tip to a different area and check the STM image of HOPG (10×10 nm^2) under normal set-up parameters (bias -0.5 V, tunneling current 0.5 nA, and scan rate 6.67 seconds per scan) to see if the image is clear or not (if not, keep scanning until the HOPG image shows good resolution, which means the tip is cleaned); and (4) if this cleaning procedure does not work efficiently even after extended scanning, abandon the current tip and replace it with a newly cut one.

2.6 Sample Preparation

Because our STM experiments are performed at the liquid-solid interface between organic solutions and HOPG, careful preparation of solutions of the target adsorbate is important to get high-resolution images. Typically, a small amount of the compound is

dissolved or dispersed in the selected solvent. The solvent should meet various requirements. It should dissolve the compound somewhat, but the solubility does not have to be high because the quantities of material needed to cover a surface are tiny. Sometimes even solvents in which solubility is poor can provide STM images with high resolution. In our studies, heptanoic acid is the most frequently used solvent, even though the compounds we have worked with typically show low solubility. However, even suspensions can give high-resolution images. Typically, 3-5 mg samples of the compound of interest were dispersed in 2-5 mL of heptanoic acid by sonication, and then the mixtures were deposited on HOPG.

In addition, solvents should be non-conducting unless they are to be used for electrochemical STM. The solvent must not corrode the substrate or any of the components of the STM instrument in contact with it. The vapor pressure of the solvent should be low enough to allow the solution or suspension to remain on the substrate for scanning for a few hours without extensive evaporation. In addition, the solvent itself should not adsorb on the solid substrate as strongly as the compound of interest, unless the solvent is to be used as one of the components of co-assembly.

Few solvents are commonly used for STM studies, and common choices include 1-phenyloctane,[31-35] 1-octanol,[36] 1,2,4-trichlorobenzene, [37-39] and heptanoic acid.[40-42] Different solvent systems can induce organic molecules to form different surface nanopatterns.[43,44] 1-Phenyloctane has been a widely used solvent because it can dissolve many nonpolar organic molecules, particularly with long alkyl chains, and has a relatively low affinity for HOPG. In our experiments, the compounds of interest have multiple polar

functional groups to control intermolecular interaction, including DAT and -COOH groups. As a result, we found that a polar solvent, 1-heptanoic acid, was particularly suitable for our STM investigations.

In a typical experiment, a drop of ~1.0 μL of the solution was deposited on HOPG via syringe by a very gentle physical touch of a droplet to the surface of the substrate, followed by spreading. Normally, 5 to 10 minutes was long enough to allow for most of the compounds of interest to form well-ordered monolayers on HOPG. For some compounds, such as TMA itself, scanning was started immediately after the deposition. Formation of long-lived monolayers on the surface by molecular self-assembly is a prerequisite for obtaining STM images of high quality. In our experience, adsorptions of tectons that yielded highly resolved images with long-range order tended to produce good images within minutes after deposition, and they were generally also stable enough to last for a few hours during the scanning.

2.7 Imaging Parameters

The proper choice of parameters such as bias voltage and tunneling current is also an important factor in obtaining high-resolution STM images. Typically, before depositing a solution on HOPG, we have examined the quality of the STM tip by scanning the untreated clean HOPG surface. The trial scan is performed using the following standard parameters: bias -0.5 V, tunneling current 0.5 nA, scan area 10 nm, and scan rate 6.67 seconds per scan. After about ten scans, if the image of HOPG is satisfactory, the solution can be deposited, and the experiment can begin. However, if the control images of HOPG are not good, then

the tip must be cleaned using the aforementioned procedure.

In our experience, the parameters needed to ensure high-quality STM images (in particular, the bias voltage and tunneling current) depend primarily on the solvent, not on the solute. For example, using heptanoic acid as the solvent, the optimized bias voltage was found to be from -1.5 V to -1.8 V, and the corresponding tunneling current in the range 0.03-0.1 nA, whatever the adsorbate used. However, if 1-phenyloctane was used as the solvent and the solute remained the same, the tunneling current had to be set higher than that in the case of heptanoic acid; otherwise, no signal could be observed because of the loss of contact. On the contrary, if the same solvent is used and the solutes are varied (for example, compounds with DAT groups, -COOH groups, or the corresponding esters), the parameters required to obtain high-resolution images varied only slightly. It therefore appears that dielectric constant is an important factor in determining tunneling parameters, especially when observing molecules with similar structures.

2.8 STM Image Analysis

To analyze STM images, it is important to understand the origin of image contrast. In the constant height mode, the image contrast reflects the changes of tunneling current at a constant bias voltage recorded during scanning of the sample. White corresponds to the highest measured tunneling current and black to the lowest. In the constant current mode, however, the image contrast is attributed to the voltage signal required to modulate the vertical tip position to maintain constant current during the scan.

In general, variations in both topography and electronic coupling properties of a

molecular overlayer will influence the contrast of an STM image. Claypool *et al.*[45] studied a series of alkanes and alkanols, and they found that topographic factors dominated the image contrast. However, for alkanes and alkanols substituted with various functional groups, including halides, disulfides, thioethers, ethers, amines, alkenes, and alkynes, the authors proposed a simple way to predict the image contrast based on ionization potential: if the electronic tip-sample coupling is dominated by the HOMO, functional groups with lower ionization potentials than that of the corresponding alkane should appear bright, whereas functional groups with higher ionization potentials should appear dark. This approach correlates remarkably well with most of the functional groups studied, and it fails only for alkyl bromides and when topographic factors dominate. The same authors also developed a theoretical model based on perturbation theory, and computations suggest that the highly diffuse unoccupied orbitals of the adsorbed molecules, despite being much farther in energy from the Fermi level of the graphite than the occupied orbitals, also play an important role.

STM images can be effectively used to identify the structure and conformation of adsorbed molecules at interfaces, including molecular 2D chirality.[46-50] Gimzewski and co-workers[51] found that changes in the conformation of a porphyrin occur predominantly by rotations around the bonds of tertiary butyl appendages, which occur differently on different metal substrates. Schneider and co-workers[52] investigated 5,6,11,12-tetraphenylnaphthacene (rubrene) adsorbed on Au(111) surfaces and found three unequally shaped features in each molecule, which revealed the helically chiral conformation of the molecule in gas phase. Zimmt and co-workers[53] disclosed the adsorption of a

1,5-substituted anthracene on HOPG showing "six dominos" corresponding to the six lobes of the HOMO of anthracene, which suggested that tunneling at anthracene is mediated primarily by its HOMO. However, STM images of anthracene on Ag(110) in UHV at positive sample bias resemble the molecule's LUMO.[54]

In summary, the ability to attain high-resolution STM images depends on many factors, including the sharpness of the tip, the atomic flatness of the substrate (HOPG), the solvent, and most important of all, the rapid formation of stable monolayers of target molecules. Of course, experience, perseverance, and good luck are always helpful.

References

1. Binning, G.; Rohrer, H.; Gerber, Ch.; Weibel, E. *Phys. Rev. Lett.* **1982**, *49*, 57-61.

2. Eigler, D. M.; Schweizer, E. K. *Nature* **1990**, *344*, 524-526.

3. Ohtani, H.; Wilson, R. J.; Chiang, S.; Mate, C. M. *Phys. Rev. Lett.* **1988**, *60*, 2398-2401.

4. Foster, J. S.; Frommer, J. E. *Nature* **1988**, *333,* 524-545.

5. McGonigal, G. C.; Bernhardt, R. H.; Thomson, D. *J. Appl. Phys. Lett.* **1990**, *57*, 28-30.

6. Rabe, J.; Buchholz, S. *Science* **1991**, *253*, 424-427.

7. Kuhnle, A.; Lindertoh, T. R.; Hammer, B.; Besenbacher, F. *Nature* **2002**, *415*, 891-893.

8. Steven, F.; Dyer, D. J.; Walba, D. M. *Angew. Chem. Int. Ed.* **1996**, *35*, 900-901.

9. Lopinski, G. P.; Moffatt, D. J.; Wayner, D. D. M.; Wolkow, R. A. *Nature* **1998**, *392*, 909-911.

10. Fasel, R.; Parschau, M.; Ernst, K.-H. *Nature* **2006**, *439*, 449-452.

11. Vidal, F.; Delvigne, E.; Stepanow, S.; Lin, N.; Barth, J. V.; Kern, K. *J. Am. Chem. Soc,* **2005**, *127*, 10101-10106

12. Mu, Z. C.; Wang, Z. Q.; Zhang, X.; Ye, K. Q.; Wang, Y. *J. Phys. Chem. B.* **2004**, *108*, 19955-19959.

13. Heinz, R.; Stabel, A.; Rabe, J. P.; Wegner, G.; De Schryver, F. C.; Corens, D.; Dehaen, W.; Süling, C. *Angew. Chem. Int. Ed. Engl.* **1994**, *33*, 2080-2082.

14. Grim, P. C. M.; De Feyter, S.; Gesquière, A.; Vanoppen, P.; Rüker, M.; Valiyaveettil, S.; Moessner, G.; Müllen, K.; De Schryver, F. C. *Angew. Chem. Int. Ed. Engl.* **1997**, *36*, 2601-2603.

15. Hossain, M. Z.; Kato, H. S.; Kawai, M. *J. Am. Chem. Soc.* **2005**, *127*, 15030-15031.

16. Xu, L.-P.; Wan, L.-J. *J. Phys. Chem. B* **2006**, *110*, 3185-3188.

17. Mezhenny, S.; Sorescu, D. C.; Maksymovych, P.; Yates, J. T. *J. Am. Chem. Soc.* **2002**, *124*, 14202-14209.

18. Nath, K. G.; Ivasenko, O.; Macleod, J. M.; Miwa, J. A.; Wuest, J. D.; Nanci, A.; Perepichka, D. F.; Rosei, F. *J. Phys. Chem. C* **2007**, *111*, 16996-17007.

19. Dang, H.; Maris, T.; Yi, J.-H.; Rosei, F.; Nanci, A.; Wuest, J. D. *Langmuir* **2007**, *23*, 11980-11985.

20. Lackinger, M.; Griessl, S.; Kampschulte, L.; Jamitzky, F.; Heckl, W. M. *Small* **2005**, *1*, 532-539.

21. Gesquiere, A.; Abdel-Mottaleb, M. M.; De Feyter, S.; De Schryver, F. C.; Sieffert, M.; Mullen, K.; Calderone, A.; Lazzaroni, R.; Bredas, J.-L. *Chem. Eur. J.* **2000**, *6*, 3739-3746.

22. Stevens, F.; Beebe, T. P. *Langmuir* **1999**, *15*, 6884-6889.

23. Wakayama, Y.; Hill, J. P.; Ariga, K. *Surf. Sci.* **2007**, *601*, 3984-3987.

24. Hamers, R. J.; Tromp. R. M.; Demuth, J. E. *Phys. Rev. Lett.* **1986**, *56*, 1972-1975.

25. *http://www.chembio.uoguelph.ca/educmat/chm729/STMpage/stmdet.htm [You haven't added the dates as requested by Antonella Badia]*

26. *http://www.iap.tuwien.ac.at/www/surface/STM_gallery/stm_schematic.html [See above]*

27. Lin, N.; Stepanow, S.; Vidal, F.; Kern, K.; Alam, M. S.; Strömsdörfer, S.; Dremov, V.; Müller, P.; Ruben, M. *Dalton Trans.* **2006**, 2794-2800.

28. Repain, V.; Berroir, J. M.; Rousset, S.; Lecoeur, J. *Appl. Surf. Sci.* **2000**, *162-163*, 30-36.

29. Messina, P.; Dmitriev, A.; Lin, N.; Spillmann, H.; Abel, M.; Barth, J. V.; Kern, K. *J. Am. Chem. Soc.* **2002**, *124*, 14000-14001.

30. Batra, I. P.; Garcia, N.; Rohrer, H.; Salemink, H.; Stoll, E.; Ciraci, S. *Surf. Sci.* **1987**, *181*, 126-138.

31. Jonkheijm, P.; Miura, A.; Zdanowska, M.; Hoeben, J. M.; De Feyter, S.; Schenning, A. P. H. J.; De Schryver, F. C.; Meijer, E. W. *Angew. Chem. Int. Ed.* **2004**, *43*, 74-78.

32. De Feyter, S.; Gesquière, A.; Abdel-Mottalev, M. M.; Grim, P. M.; De Schryver, F. C. *Acc. Chem. Res.* **2000**, *33*, 520-531.

33. Katsonis, N.; Minoia, A.; Kudernac, T.; Mutai,T.; Xu, H.; Uji-i, H.; Lazzaroni, R.; De Feyter, S.; Feringa, B. L. *J. Am. Chem. Soc.* **2008**, *130*, 386-387.

34. De Feyter, S., Miura, A.; Yao, S.; Chen, Z.; Wüthner, F.; Jonkheijm, P.; Schenning, A. P. H. J.; Meijer, E. W.; De Schryver, F. C. *Nano Lett.* **2005**, *5*, 77-81.

35. Wei, Y.; Tong, W.; Zimmt, M. B. *J. Am. Chem. Soc.* **2008**, *130*, 3399-3405.

36. De Feyter, S.; Gesquière, A.; Klapper, M.; Müllen, K.; De Schryver, F. C. *Nano Lett.* **2003**, *3*, 1485-1488.

37. Tahara, K.; Furukawa, S.; Uji-I, H.; Uchino, T.; Ichikawa, T.; Zhang, J.; Mamdouh, W.; Motohiro, S.; De Schryver, F. C.; De Feyter, S.; Tobe, Y. *J. Am. Chem. Soc.* **2006**, *128*, 16613-16625.

38. Latterini, L.; Pourtois, G.; Moucheron, C.; Lazzaroni, J.-L. B.; Mesmaeker, A. K.-De; De Schryver, F. C. *Chem. Eur. J.* **2000**, *6*, 1331-1336.

39. Tahara, K.; Lei, S.; Mamdouh, W.; Yamaguchi, Y.; Ichikawa, T.; Uji-i, H.; Sonoda, M.; Hirose, K.; De Schryver, F. C.; De Feyter, S.; Tobe, Y. *J. Am. Chem. Soc.* **2008**, *130*, 6666-6667.

40. Kampschulte, L.; Lackinger, M.; Maier, A.-K.; Kishore, R. S. K.; Griessl, S.; Schmittel, M.; Heckl, W. M. *J. Phys. Chem. B* **2006**, *110,* 10829-10836.

41. Nath, K. G.; Ivasenko, O.; Miwa, J. A.; Dang, H.; Wuest, J. D.; Nanci, A.; Perepichka, D. F.; Rosei, F. *J. Am. Chem. Soc.* **2006**, *128*, 4212-4213.

42. Zhou, H.; Dang, H.; Yi, J.-H.; Nanci, A.; Rochefort, A.; Wuest, J. D. *J. Am. Chem. Soc.* **2007**, *129*, 13774-13775.

43. Mamdouh, W.; Uji-I, H.; Ladislaw, J. S.; Dulcey, A. E.; Percec, V.; De Schryver, F. C.; De Feyter, S. *J. Am. Chem. Soc.* **2006**, *128*, 317-325.

44. Lackinger, M.; Griessl, S.; Heckl, W. M.; Hietschold, M.; Flynn, G. W. *Langmuir* **2005**, *21*, 4984-4988.

45. Claypool, C. L.; Faglioni, F.; Goddard III, W. A.; Gray, H. B.; Lewis, N. S.; Marcus, R. A. *J. Phys. Chem. B* **1997**, *101*, 5978-5995.

46. Weigelt, S.; Busse, C.; Petersen, L.; Rauls, E.; Hammer, B.; Bothelf, K. V.; Besenbacher, F.; Linderoth, T. R. *Nature Mater.* **2006**, *5*, 112-117.

47. Moresco, F.; Meyer, G.; Tang, H.; Gourdon, A.; Joachim, C. *Phys. Rev. Lett.* **2001**, 86, 672-675.

48. Loppacher, C.; Guggisberg, M.; Pfeiffer, O.; Meyer, E.; Bammerlin, M.; Lüthi, R.; Schlittler, R.; Gimzewski, J. K.; Tang, H.; Joachim, C. *Phys. Rev. Lett.* **2003**, *90*, 066107.

49. Liu, N.; Sam, H.; Darling, G. R.; Raval, R. *Angew. Chem. Int. Ed.* **2007**, *46*, 7613-7616.

50. Fasel, R.; Parschau, M.; Ernst, K.-H. *Nature* **2006**, *439*, 449-452.

51. Jung, T. A.; Schlittler, R. R.; Gimzewski, J. K. *Nature* **1997**, *386*, 696-698.

52. Blüm, M.-C.; Ćavar, E.; Pibetta, M.; Patthey, F.; Schneider, W.-D. *Angew. Chem. Int. Ed.* **2005**, *44*, 5334-5337.

53. Wei, Y.-H.; Kannappan, K.; Flynn, G. W.; Zimmt, M. B. *J. Am. Chem. Soc.* **2004**, *126*, 5318-5322.

54. Böhringer, M.; Schneider, W.-D.; Berndt, R. *Surf. Sci.* **1998**, *408*, 72-85.

CHAPTER 3

STM Study of the Adsorption of Tectons Bearing Diaminotriazine Substituents

3.1 Introduction

The adsorption of many organic molecules on surfaces has been investigated by STM in recent years, but most of the compounds have contained long-chain alkyl substituents.[1-7] Many studies have revealed that such chains play a very important role in molecular physisorption at surfaces by forming van der Waals interactions between the adsorbate and the substrate. Thermodynamic studies confirm that compounds with long alkyl chains have high affinities for graphite.[8-10] STM studies have demonstrated that they adsorb on graphite with their carbon skeletons parallel to the surface, and they produce highly ordered patterns by self-assembly.[11,12] Well-studied molecules of this type include alkanes,[13-17] alkanols,[18-22] fatty acids,[23-27] carboxylic esters, [28-31] and other derivatives.[32-37]

In this thesis, we focus on the adsorption of molecules without long-chain alkyl substituents. This is a potentially important new area of investigation, because it substantially changes the balance of forces involved in adsorption. Specifically, it reduces the importance of diffuse interactions between the surface and the adsorbate, such as van der Waals interactions, and it creates an opportunity to increase the importance of directional forces between the adsorbates, thereby offering a new way to control the architecture of the nanopatterns formed by adsorption. Our work addresses the following question: Can tectons be designed to produce specific 2D nanopatterns that are controlled more by directional interadsorbate interactions than by orientational preferences of the underlying surface? Like related work of the group in 3D crystallization, our studies of directed 2D assembly have emphasized the use of tectons bearing functional groups that can direct molecular association by hydrogen bonding. In this chapter, we discuss the

Scheme 3.1 Molecular structures of tectons **DAT-1**, **DAT-2**, **DAT-3**, and **DAT-4**.

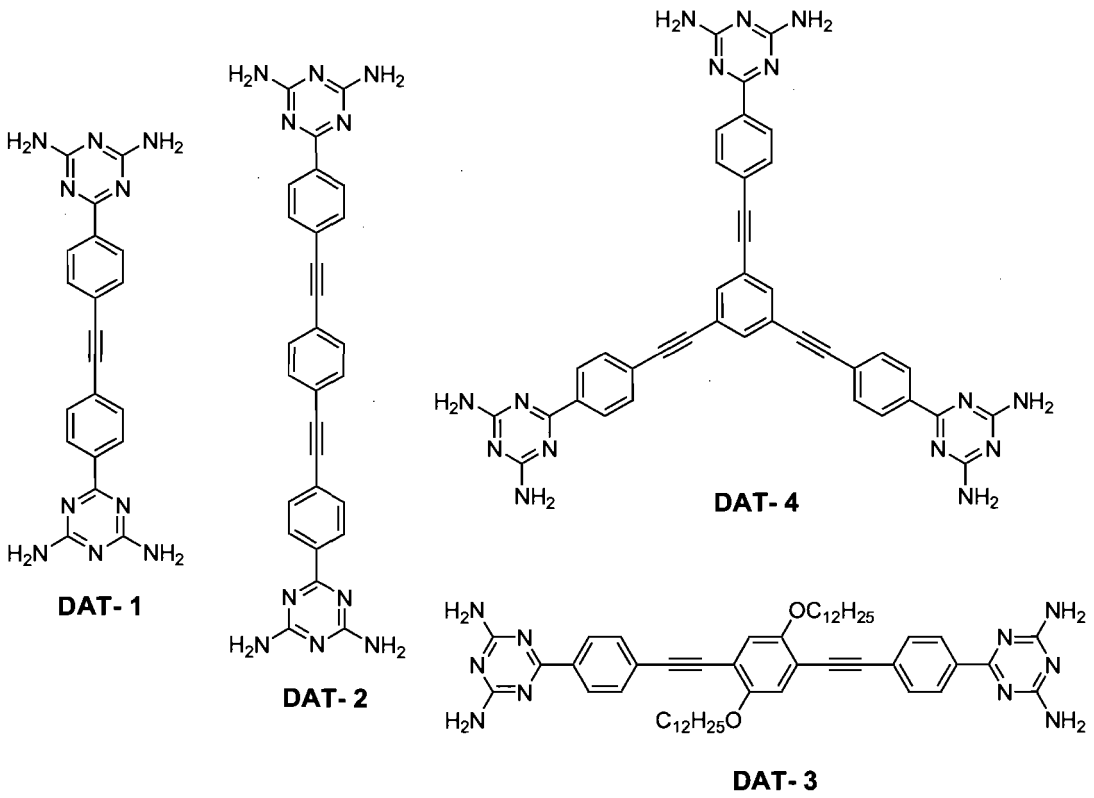

behavior of tectons with multiple diaminotriazine groups (DAT). As summarized in Chapter 1, DAT groups induce the formation of characteristic patterns of hydrogen bonds and have therefore found wide use in engineering 3D crystals [38, 39] and 2D nanopatterns.[40, 41]

The target tectons are designed to have π-conjugated linear backbones, such as oligo(phenyleneethynylene) cores (OPE). Due to their unique electronic properties, π-conjugated oligomers and polymers of this type have a wide range of applications in optoelectronics and photonics.[42-46] *p*-Phenyleneethynylene derivatives have shown a remarkable stiffness and linearity along the conjugated skeleton, which allow them to organize into well-defined nanostructures and become candidates for molecular nanowires in molecular-scale electronic devices.[47-50] The adsorption of several OPEs substituted with

long-chain alkyl groups has already been investigated by STM at solid-liquid interfaces.[51-53] To extend these studies in a promising new direction, we have investigated the adsorption of a series of OPEs without long alkyl chains but with DAT substituents, which have a proven ability to direct intermolecular association. Even relatively simple molecules of this type, as illustrated in Scheme 3.1, produce interesting supramolecular nanopatterns, and their behavior has yielded a more profound understanding of 2D self-assembly directed by noncovalent interactions.

3.2 Design and Synthesis of Tectons

3.2.1 Synthesis of Tecton DAT-1

Tecton **DAT-1**[54] is constructed from a 1,2-diphenylethyne core bearing two DAT groups. In principle, it can adopt a planar conformation, and it is clearly well suited for studies of 2D assembly directed by hydrogen bonding. Compound **DAT-1** was prepared in two steps by standard methods (Scheme 3.2). The reaction of commercially available bis(4-bromophenyl)acetylene with CuCN in DMF gave the known compound bis(4-cyanophenyl)acetylene (**6**)[55] in 74% yield, which was converted into the corresponding diaminotriazine derivative **DAT-1** in 70% yield using dicyandiamide and KOH in 2-methoxyethanol.[56]

Scheme 3.2 Synthesis of compound **DAT-1**.

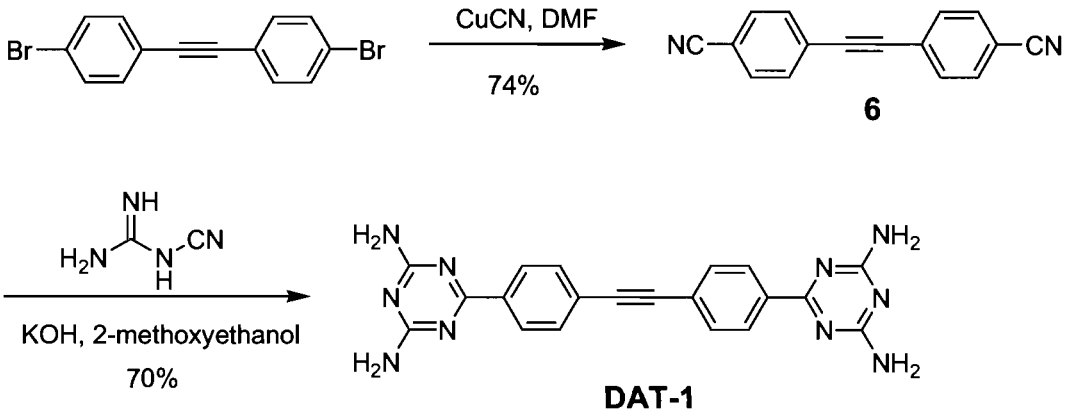

3.2.2 Synthesis of Tecton DAT-2

The structure of tecton **DAT-1** was extended by replacing its core with 1,4-bis(2-phenylethynyl)benzene, giving tecton **DAT-2.** This compound was synthesized as shown in Scheme 3.3. Coupling of commercially available 1,4-diethynylbenzene with 4-bromobenzonitrile under Sonogashira conditions in the presence of catalytic dichlorobis(triphenylphosphine)palladium(II) and copper(I) iodide provided dinitrile intermediate **7** in 90% yield,[57] which was then converted into the target tecton **DAT-2** in 78% yield by the standard reaction with dicyandiamide and KOH in 2-methoxyethanol.

3.2.3 Synthesis of Tecton DAT-3

Tecton **DAT-3** was designed to probe the effect of adding long alkyl chains to the structure of simple analogue **DAT-2**. In substituted derivative **DAT-3**, two alkyl chains with

Scheme 3.3 Synthesis of compound **DAT-2**.

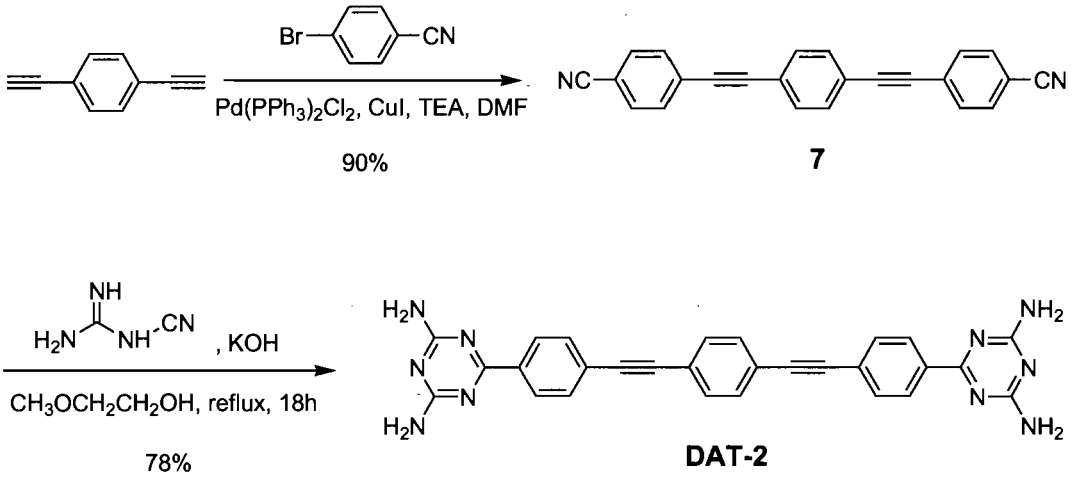

12 carbons were introduced in the central benzene ring, thereby producing a hybrid molecule in which van der Waals interactions with the underlying surface and intermolecular hydrogen bonding of the DAT groups will presumably compete to determine how adsorption occurs and what 2D nanopattern will emerge. Despite their structural similarity, compounds **DAT-2** and **DAT-3** are expected to adsorb in different ways if the alkyl groups can play a decisive role. As shown in Scheme 3.4, tecton **DAT-3** was synthesized from hydroquinone, which was alkylated to give known compound **8** in 87% yield.[58] Intermediate **8** was then subjected to iodination to produce the known 1,4-bis(dodecyloxy)-2,5-diiodobenzene (**9**) in 81% yield,[59] which was coupled with 2-methyl-3-butyn-2-ol under Sonogoshira conditions to give intermediate **10** in 80% yield, followed by deprotection to provide 1,4-bis(dodecyloxy)-2,5-diethynylbenzene (**11**) in 90% yield.[60] Palladium-catalyzed coupling of **11** with 4-iodobenzonitrile yielded dinitrile **12** in 65% yield, which was subjected to subsequent conversion of the nitrile groups into DAT groups by the standard method to provide target **DAT-3** in 78% yield.

Scheme 3.4 Synthesis of compound **DAT-3**.

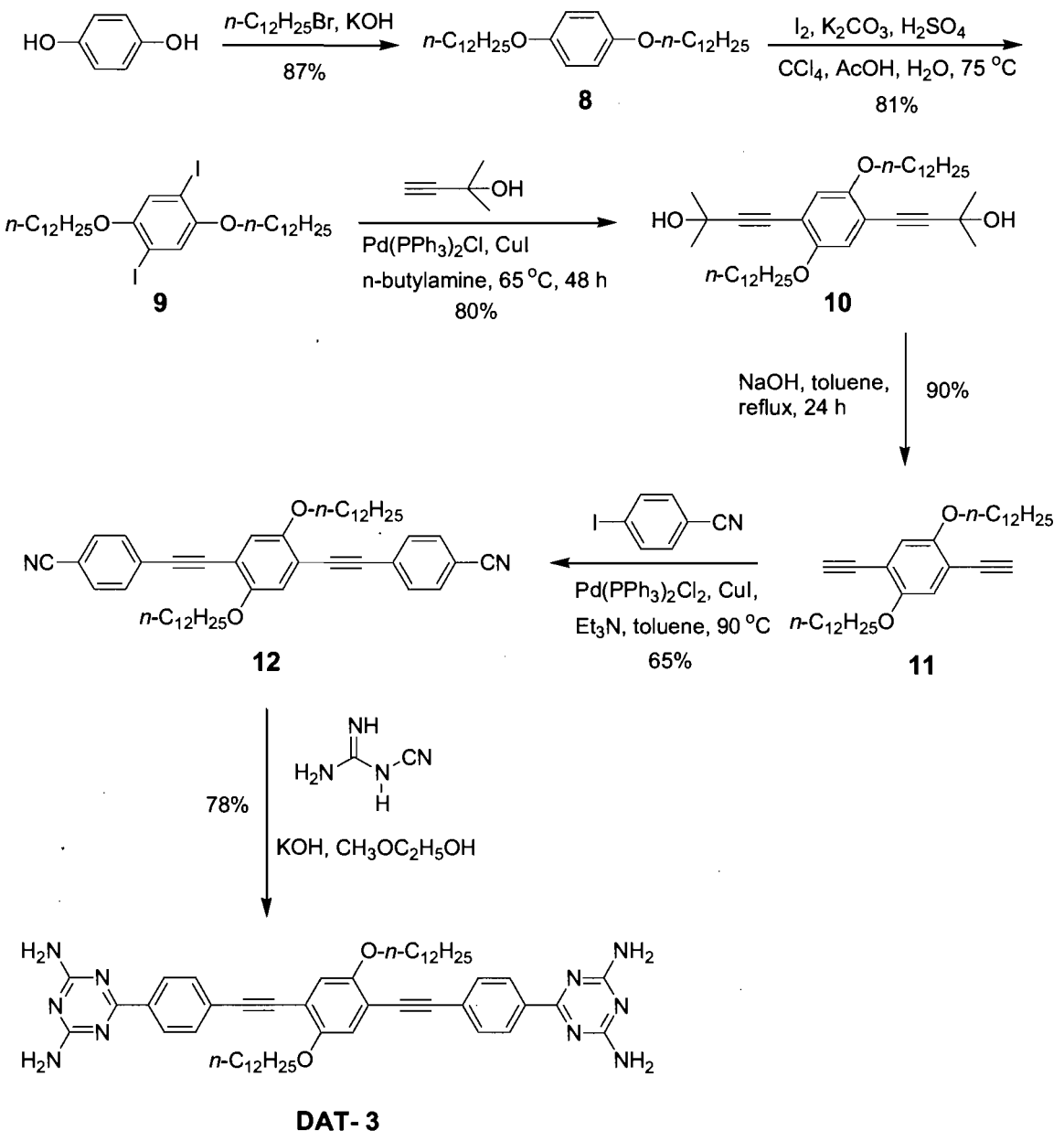

3.2.4 Synthesis of Tecton DAT-4

Tecton **DAT-4** alters the linear geometry of tectons **DAT-1**, **DAT-2**, and **DAT-3** to create a structure with three trigonally directed sticky sites. Its three-fold symmetry is

compatible with that of graphite, so we expected compound **DAT-4** to produce well-defined 2D networks when deposited on the surface. Synthesis of compound **DAT-4** is shown in Scheme 3.5. Sonogashia coupling of 1,3,5-tribromobenzene with (trimethylsilyl)acetylene produced intermediate **13** in 92% yield,[61] followed by deprotection to give known 1,3,5-triethynylbenzene (**14**) in 98% yield.[61] Coupling with 4-iodobenzonitrile under standard palladium-catalyzed conditions then gave intermediate trinitrile **15**[62] in 65% yield. The target tecton **DAT-4** was then produced by converting the nitrile groups into DAT groups by the standard method in 75% yield.

Scheme 3.5 Synthesis of compound **DAT-4.**

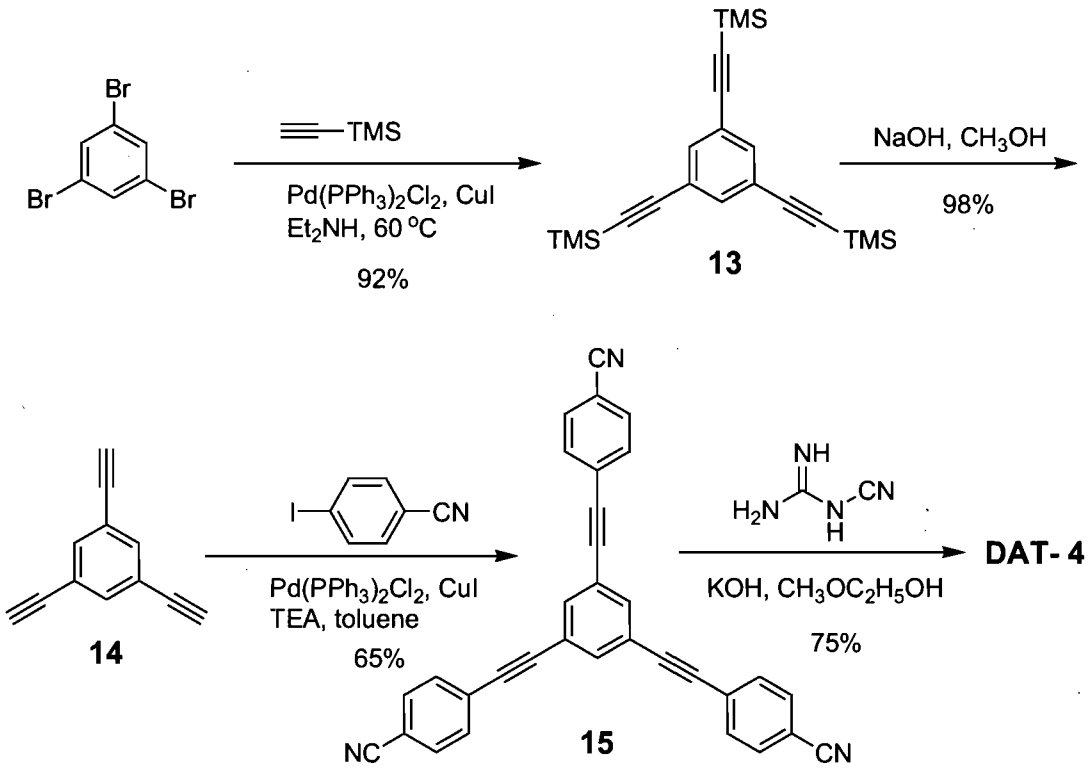

3.3 STM Investigations and X-Ray Crystallography of Tectons DAT-1, DAT-2, DAT-3, and DAT-4

3.3.1 2D Nanopatterns Formed by Tecton DAT-1

The ability of tecton **DAT-1** to create nanopatterns on the surface of HOPG was investigated by STM. The basic 1,2-diphenylethynyl core is expected to be planar, and the two DAT groups can participate in multiple hydrogen bonds according to well-established motifs. In addition, phenyl-substituted DAT groups are known to favor conformations in which the DAT group and the phenyl substituent are approximately coplanar.[63] For all of these reasons, tecton **DAT-1** is likely to favor a planar, highly aromatic structure that is particularly well designed to adsorb on the surface of graphite and create 2D networks held together by multiple hydrogen bonds. In a general procedure, a droplet of a well-dispersed suspension of tecton **DAT-1** in heptanoic acid ($\sim 10^{-5}$ mol/L) was deposited on the surface of freshly cleaved HOPG. Imaging was performed after a few minutes under constant height mode. After scanning for a short time, we observed that the images became stable, and they were automatically grabbed and saved in the computer.

Figure 3.1a shows an STM image of well-ordered arrays of tecton **DAT-1**. Each bright protrusion has an average size of 1.8 nm, which is consistent with the molecular length of **DAT-1**. The bright contrast originates from the higher tunneling current of π-conjugated aromatic rings due to their higher electronic density of states. Figure 3.1b shows the self-assembled networks with submolecular resolution, in which the molecules are found to employ two alternating orientations (highlighted in green and blue) with an angle (β)

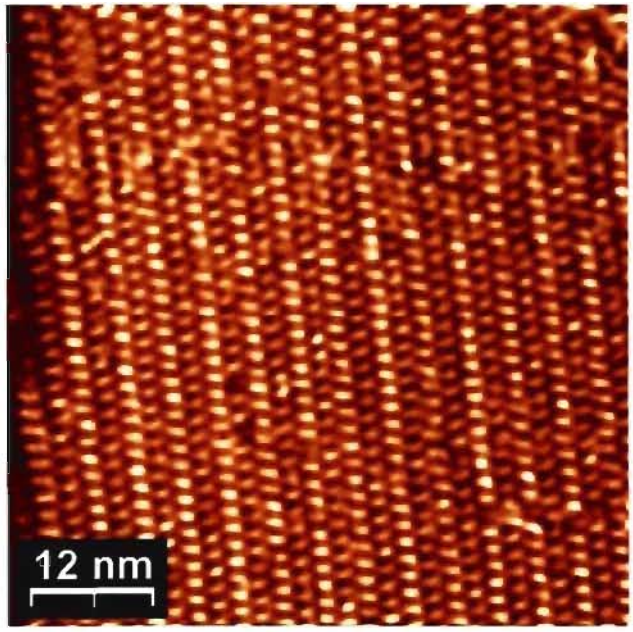

(a)

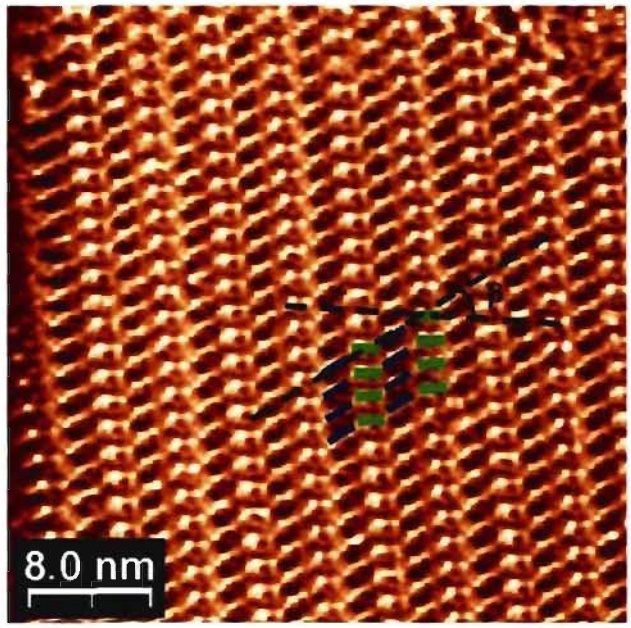

(b)

Figure 3.1 STM images of 2D nanopatterns created by adsorption of tecton **DAT-1** on HOPG (deposition from heptanoic acid, with V_{bias} = -1.5 V, I_{set} = 100 pA). (a) Image showing well-ordered networks covering large areas of surface in a single domain. (b) Higher-resolution image in which the tectons highlighted in blue and green have non-parallel or parallel orientations, respectively, relative to the underlying surface. The angle between the two types of tectons is $\beta = \sim 40°$.

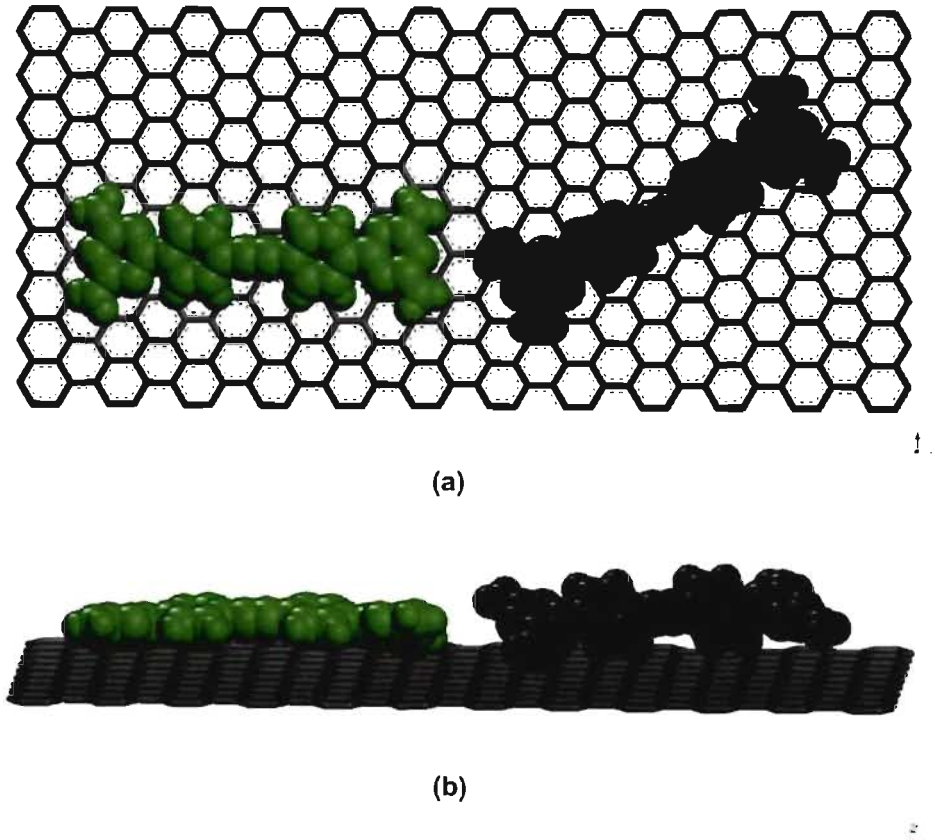

Figure 3.2 CPK models for the two proposed orientations of tecton **DAT-1** with respect to the underlying surface of HOPG. (a) View along *c* axis. (b) View along *a* axis.

of about 40° between each other.

Figure 3.2 shows the proposed CPK models of the two orientations: the green one lies flat, with the backbone parallel to the underlying graphite, and the blue one is tilted about 50°. The two orientations are observed more clearly in Figure 3.3, in which molecule A (adopting the co-parallel orientation) shows brighter contrast, and molecule B (tilted orientation) shows darker contrast. The unit cell parameters were determined to be a = ~1.46 nm, b = ~4.32 nm, and γ = ~68°. Molecule B is proposed to retain an essentially planar structure, with both the DAT groups and the diphenylethynyl core tilted relative to the surface. This hypothesis explains why the width of molecule A is greater than that of molecule B in the

(a)

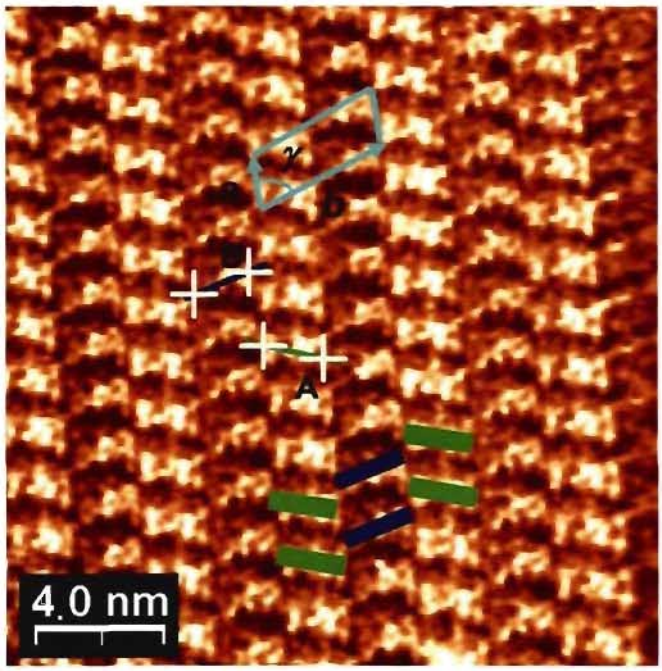

(b)

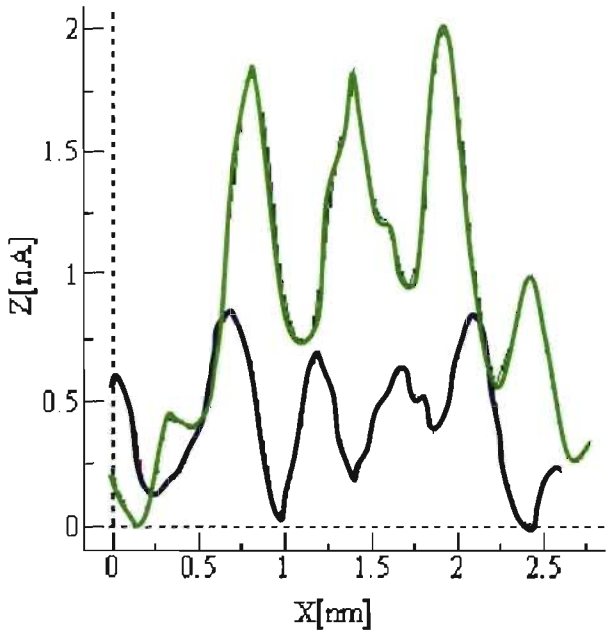

Figure 3.3 (a) Higher-resolution STM image of 2D nanopatterns created by depositing tecton **DAT-1** on HOPG (20 nm × 20 nm) in heptanoic acid. Molecules A (co-parallel orientation) and B (non-parallel orientation) are shown in green and blue, respectively. The unit cell is highlighted in light blue. (b) Profile of molecule A, which shows higher tunneling current (green curve), and the profile of molecule B, which shows lower tunneling current (blue curve).

images in Figures 3.1 and 3.3. Surface profiles (Figure 3.3b) indicate that the two molecular orientations produce different tunneling currents, with molecule A showing higher tunneling current than molecule B due to their different orientations with respect to the surface. The well-precedented co-parallel orientation of molecule A can be attributed to π-π interactions between the aromatic systems of the adsorbed molecule and graphite. The tilted orientation of molecule B is more unusual, and it can probably be ascribed to specific stabilizing interactions between the NH_2 groups and graphite.[64] Similar observations have been made in other cases. For example, trimesic acid was reported to interact with Au surfaces either via the lone electron pairs of its carboxyl groups (tilted or perpendicular orientation) or via the π-electrons of its aromatic core (planar orientation).[65]

It is hard to find a detailed molecular model for the adsorption of tecton **DAT-1** that is consistent with the observation of two distinct orientations and simultaneously is in agreement with the established hydrogen-bonding patterns formed by DAT groups. The typical hydrogen-bonding motifs of DAT groups,[56] combined with the extended linear geometry of tecton **DAT-1**, would normally be expected to favor the formation of planar networks such as those represented by the three models shown in Scheme 3.6. In model (a), the hydrogen bonding between DAT groups follows a side-to-side motif; in model (b), the hydrogen bonding is face-to-face, which creates parallel chains; and in model (c), the chains are displaced, allowing hydrogen bonds to be formed between them and creating a network with both face-to-face and side-to-side motifs. In all three cases, the long molecular axes of the tectons are aligned. The network shown in model (c) would appear to be highly attractive, because it offers a large number of hydrogen bonds per tecton (8), a coplanar

Scheme 3.6 Molecular models showing potential intermolecular hydrogen bonding in 2D nanopatterns formed by tecton **DAT-1** on HOPG.

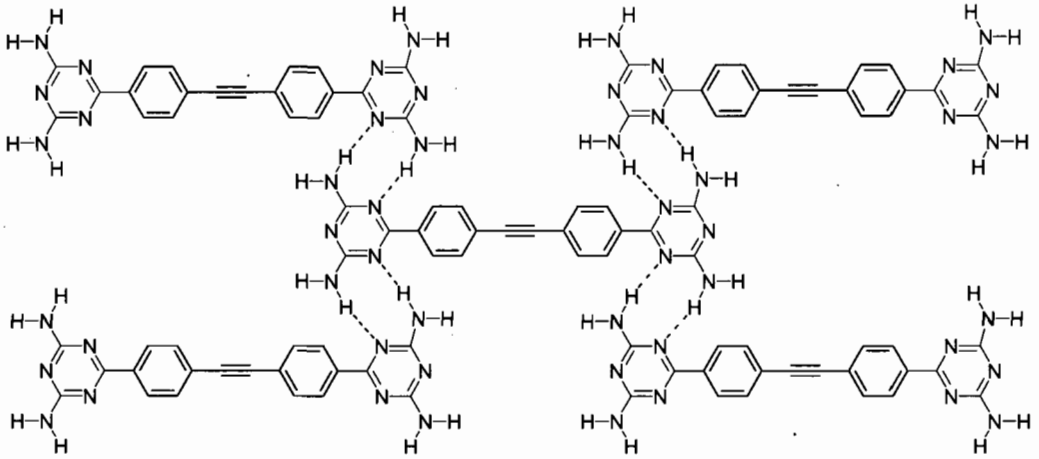

(a)

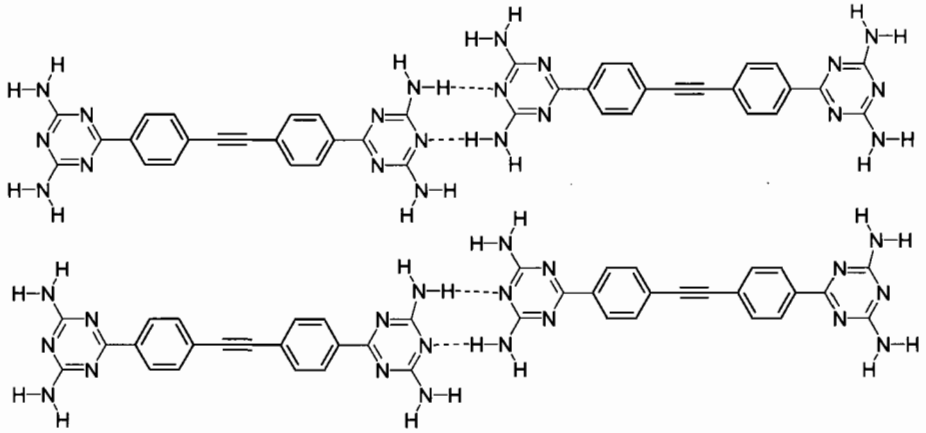

(b)

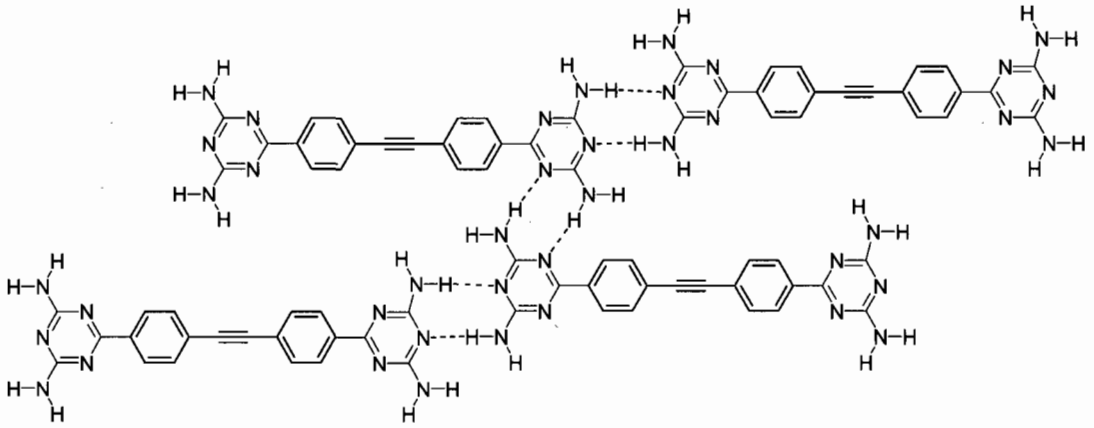

(c)

orientation with respect to the surface, and a relatively dense packing. However, none of the three models fits the observed surface nanopatterns formed by tecton **DAT-1**, which show two distinct orientations, with non-parallel tectons.

A recent publication reports the coassembly of melamine with different carboxylic acids, including heptanoic acid, to form hexagonal structures.[66] We have considered the possibility that a similar coassembly may occur in the case of diaminotriazine **DAT-1**. A new model based on this possibility is shown in Figure 3.4. In this model, In addition to the typical face-to-face hydrogen bonding between DAT groups, with an average H···N distance of 2.20 Å, closely packed pairs of heptanoic acid molecules in fully extended conformations interact with DAT groups in the normal manner to form N-H···O and O-H···N hydrogen bonds, with average H···O and H···N distances expected to be 2.15 Å and 1.95 Å, respectively. As a result, the unit cell parameters are determined to be a = ~1.36 nm, b = ~3.43 nm, and γ = ~68°, which is clearly inconsistent with those obtained from the STM image (Figure 3.3a).

We are therefore forced to propose that the well-ordered arrays of tecton **DAT-1** are not strictly 2D patterns. They have some 3D character, presumably to increase the density of coverage, and the intertectonic hydrogen bonds may not fully respect the ideal preferences expressed by the models in Scheme 3.6, in which hydrogen-bonded DAT groups are constrained to lie in the same plane. Although it is not often commented on, hydrogen-bonded DAT groups in 3D crystals frequently fail to be coplanar, and significant distortions from coplanarity are often observed in X-ray crystallographic studies. The crystal structure of tecton **DAT-3** provides an excellent example, which will be discussed

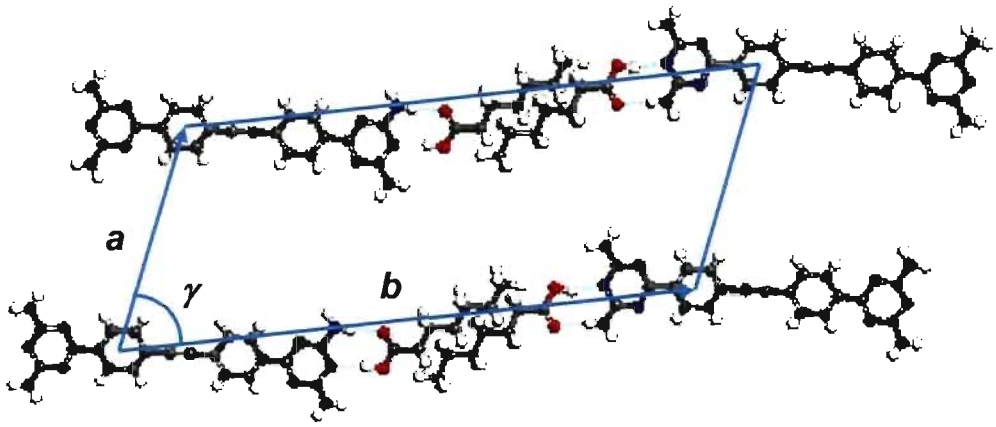

Figure 3.4 Proposed molecular model for the 2D coassembly of tecton **DAT-1** with heptanoic acid molecules mediated by hydrogen bonds (shown as broken lines).

later in this chapter (see Figure 3.13c). For these reasons, we propose a partially non-planar model for the adsorption of tecton **DAT-1** on HOPG as shown in Figure 3.5. The two tectons in green are coplanar with respect to the underlying graphite, whereas the central tecton in blue is tilted. Single N-H···N hydrogen bonds are still possible, with H···N distances of 2.35 and 2.28 Å (calculated from the models shown in Figure 3.5a) between the DAT groups of the green and blue tectons; however, such interactions will not be as strong as those formed between coplanar DAT groups. Similar single hydrogen bonds can also be observed in the crystal structure of tecton **DAT-3** (Figure 3.13c). The unit cell parameters are therefore determined to be $a = \sim 1.38$ nm, $b = \sim 4.17$ nm, and $\gamma = \sim 68°$, which are very close to those obtained by analysis of the STM image (Figure 3.3a).

The energetic disadvantages of this arrangement are obvious, but there are compensating advantages. In particular, twisting alternating tectons partially out of the plane increases the density of packing, and it also allows the NH_2 and CH groups to have a direct interaction with the surface.[64] The unexpected arrangement underscores the subtleties of adsorption on

surfaces and shows clearly that strong interadsorbate hydrogen bonding cannot always dictate what pattern is ultimately favored. Other factors must also be taken into account.

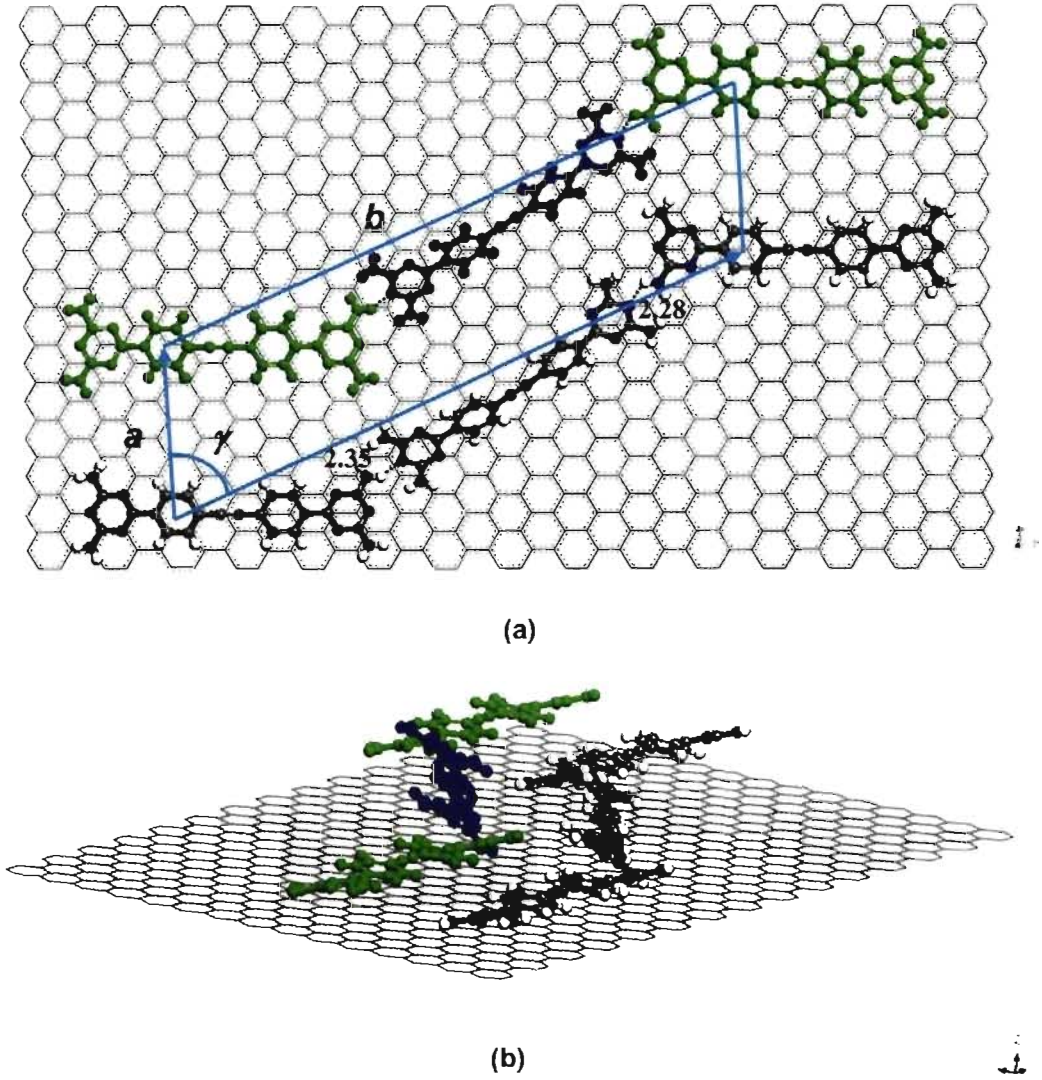

Figure 3.5 Proposed 3D molecular model for surface nanopatterns formed by the adsorption of tecton **DAT-1** on HOPG. Two orientations, parallel and tilted, are shown in green and blue, respectively. (a) View along the *c* axis, with possible hydrogen bonds between DAT groups shown as broken lines. The unit cell is highlighted in light blue. (b) Side view showing the 3D character of the proposed adsorption.

3.3.2 3D Crystal Structure of Tecton DAT-1

To provide deeper understanding of the behavior of tecton **DAT-1** and its ability to self-associate, we elected to study its structure by X-ray crystallography. Although it is not always standard practice in the field of surface science, we believe that the study of 3D assembly by X-ray crystallography is an essential complement to the study of 2D assembly using STM, and both should be carried out in the course of the analysis. Suitable single crystals of compound **DAT-1** were formed by allowing vapors of chloroform to diffuse into a solution in DMSO. The crystals were found to belong to the monoclinic space group $P21$ and to have the composition 2**DAT-1** • 2DMSO. Views of the structure appear in Figure 3.6. The unit cell parameters are a = 10.678(4) Å, b = 13.419(5) Å, c = 15.856(5) Å, α = 90°, β = 103.129(17)°, and γ = 90°. The unit cell reveals the presence of two distinct conformers (red and blue) with different torsional angles (21.8° and -29.1° in one case, versus 18.1° and -27.9° in the other) between the benzene and triazine rings (Figure 3.6b).

As shown in Figure 3.7a, the crystal is composed of alternating layers, each containing a single conformer (red or blue). Within each layer, each tecton interacts with four neighboring molecules by forming hydrogen bonds according to model (c), as shown in Scheme 3.6. As noted above, this model offers a highly plausible combination of 1) parallel orientation of the principal molecular axis, 2) extensive hydrogen bonding according to the well-established preferences of DAT groups, and 3) effective packing, with only a small percentage of volume (21%) available for the inclusion of guests. The percentage of volume accessible to guests is estimated by a standard method.[67,68] In this method, the accessible volume is defined by the volume that can be occupied by a spherical probe of

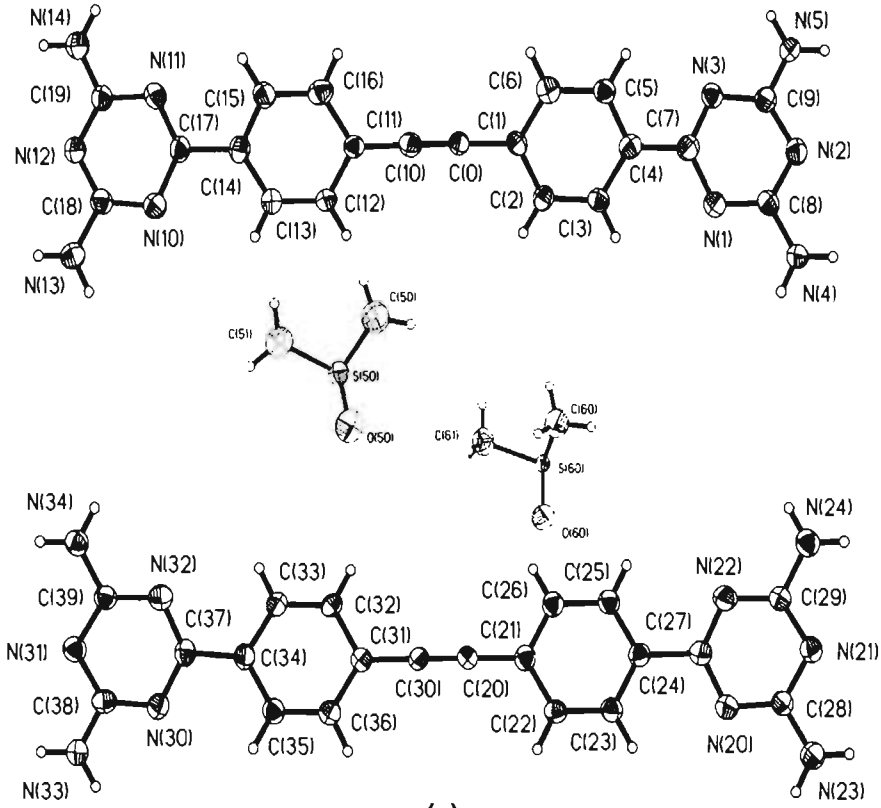

(a)

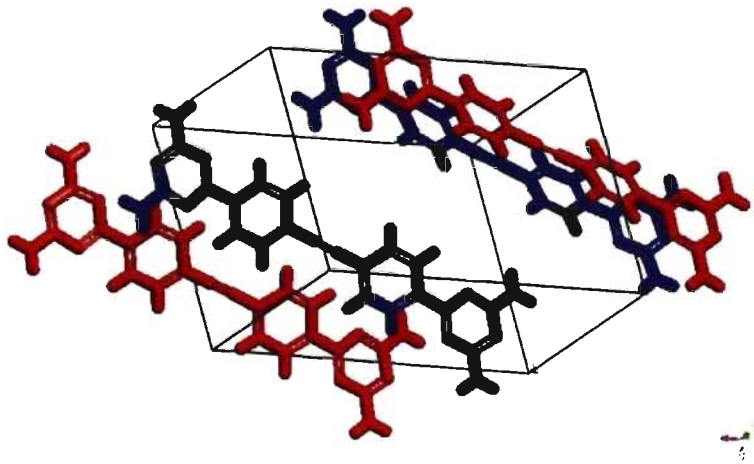

(b)

Figure 3.6 (a) ORTEP view of the structure of crystals of tecton **DAT-1** grown from $CHCl_3$/DMSO, with the numbering scheme adopted. Ellipsoids are drawn at the 30% probability level. Hydrogen atoms are represented by spheres of arbitrary size. (b) Unit cell showing two conformers with different torsional angles (red and blue). Guest molecules of DMSO are removed for clarity.

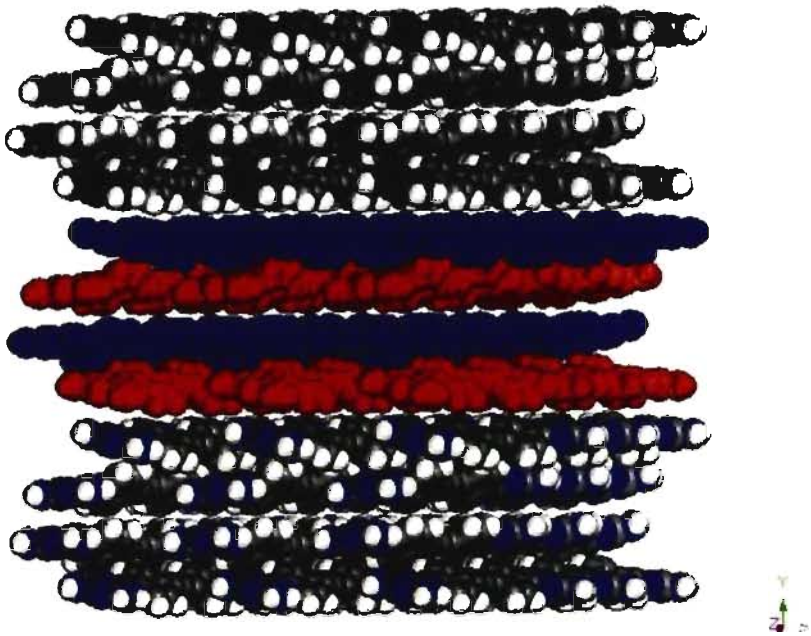

(a)

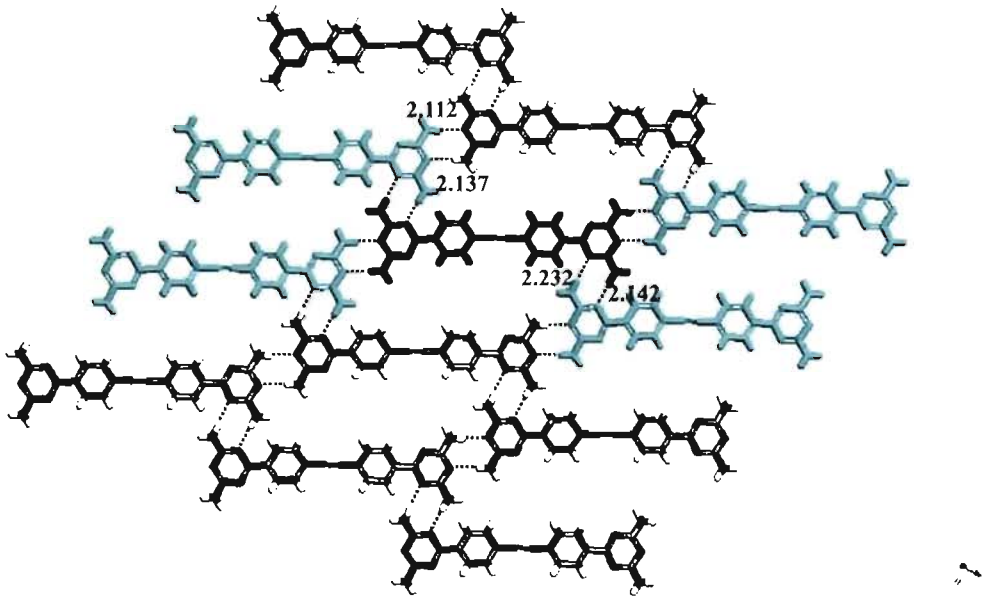

(b)

Figure 3.7 The structure of crystals of tecton **DAT-1** grown from $CHCl_3$/DMSO, showing (a) 2D hydrogen-bonded sheets composed of a single conformer (red or blue) and (b) a central molecule (blue) forming hydrogen bonds with four neighboring molecules (light blue). Guest molecules of DMSO are omitted for clarity. Hydrogen bonds are represented by broken lines.

radius *r* constrained to move in a way that its center must remain at a distance no less than *r* from closest point on the van der Waals surface of the ordered network. As a result, the crystallization of tecton **DAT-1** occurs essentially as expected. Because hydrogen bonding in the observed structure involves both face-to-face and side-to-side motifs, different N-H···N geometries are found, with H···N distances of 2.112 and 2.137 Å for face-to-face hydrogen bonds and with distances of 2.232 and 2.142 Å for side-to-side hydrogen bonds. Side-to-side hydrogen bonds of DAT groups are typically longer, which is a consequence of steric effects. The resulting hydrogen-bonding arrangement extends in two dimensions to form extensively hydrogen-bonded sheets (Figure 3.7b).

In its 3D crystallization, tecton **DAT-1** was found to behave essentially as expected, based on extensive precedents in the literature, and the compound revealed no structural surprises that would immediately account for the unusual features of its 2D assembly on HOPG. The stark differences between the association in 2D and 3D must therefore be attributed to the combined effects of interadsorbate interactions and interactions between the adsorbate and the underlying substrate.

3.3.3 2D Nanopatterns Formed by Tecton DAT-2

The assembly of extended tecton **DAT-2** on HOPG was investigated by STM under conditions similar to those used in the study of analogue **DAT-1**. The adsorbate was again deposited in heptanoic acid. STM images are provided in Figure 3.8. Figure 3.8a shows well-ordered linear structures with occasional defects. The bright bar-like protrusions

correspond to individual molecules of compound **DAT-2**.

Figure 3.8b shows an enlarged image of the light blue area with superimposed molecular models. The unit cell parameters are determined to be a = ~1.97 nm, b = ~2.89 nm, and γ = ~68°. In this model, the individual molecules each associate by participating in the formation of four hydrogen bonds according to the face-to-face motif preferred by DAT groups, thereby producing linear tapes. A surface profile (Figure 3.8c) indicates that the repeat distance along the direction of the tapes corresponds to the molecular length, which is about 2.5 nm. Unexpectedly, the tapes are not closely packed, and they are not displaced to allow the formation of intertape side-to-side hydrogen bonds of the type observed in the 3D crystal structure of shortened analogue **DAT-1** (Figure 3.7b). The measured distance between neighboring tapes is ΔL = ~ 1.82 nm.

To account for the unexpectedly large separation, we suggest that molecules of heptanoic acid may be adsorbed in the intervening spaces between adjacent tapes.[66] This coadsorption accounts plausibly for the distinct difference in contrast between neighboring tapes in the STM images. A new model is therefore proposed as shown in Figure 3.9. In addition to the typical face-to-face hydrogen bonding between DAT groups, with an average H···N distance of 2.20 Å, heptanoic acid associates with DAT groups by forming N-H···O and O-H···N hydrogen bonds, with average H···O and H···N distances of 2.15 Å and 1.95 Å, respectively. As a result, the unit cell parameters are determined to be a = ~1.97 nm, b = ~2.76 nm, and γ = ~68°, which are consistent with those obtained by analysis of the STM images (Figure 3.8b). The angle defined by the direction of the tapes and by the direction of alignment of molecules in adjacent tapes is ~120°, which corresponds to the

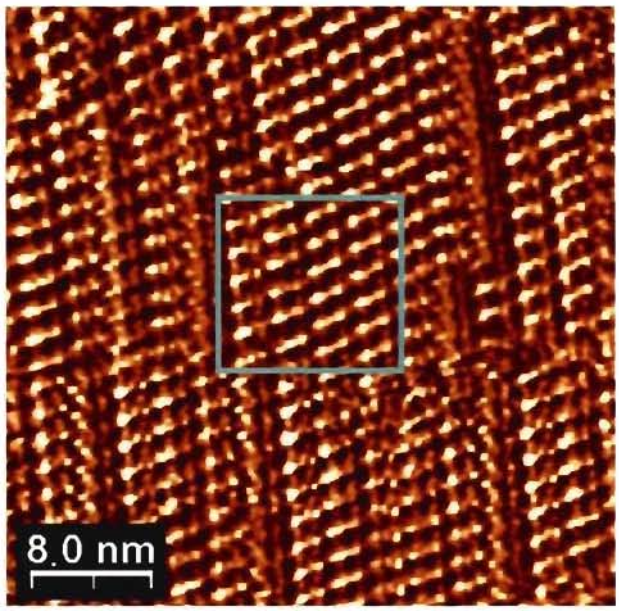

(a)

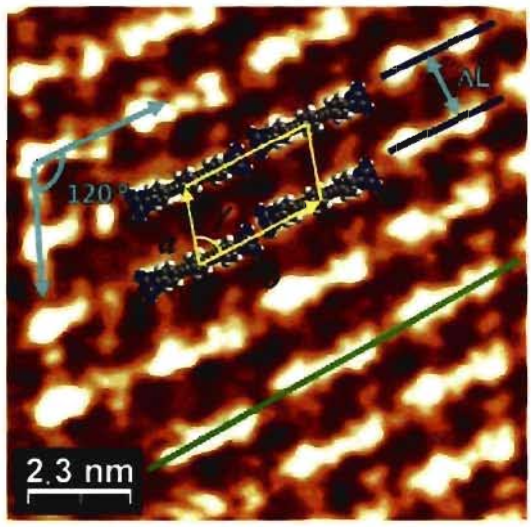

(b)

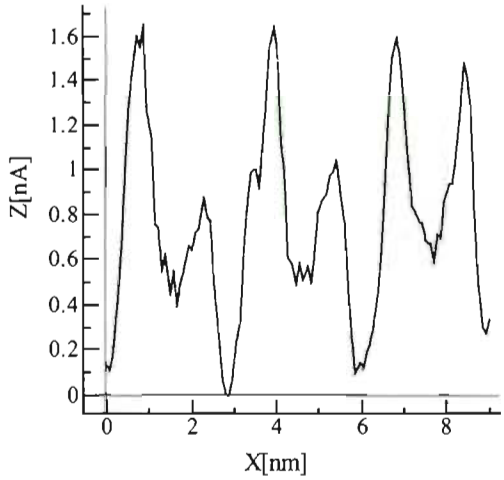

(c)

Figure 3.8 STM topographs showing the patterns produced by depositing tecton **DAT-2** on HOPG in heptanoic acid (V_{bias} = -1.5 V, I_{set} = 100 pA). (a) Well-ordered nanopatterns over an area of 40 nm × 40 nm. (b) Enlarged image of the area highlighted in light blue, with superimposed space-filling models showing the face-to-face hydrogen bonding of DAT groups. The unit cell is highlighted in yellow. (c) Profile along the direction of the green line in (b), showing that the repeat distance is consistent with the molecular length of tecton **DAT-2**.

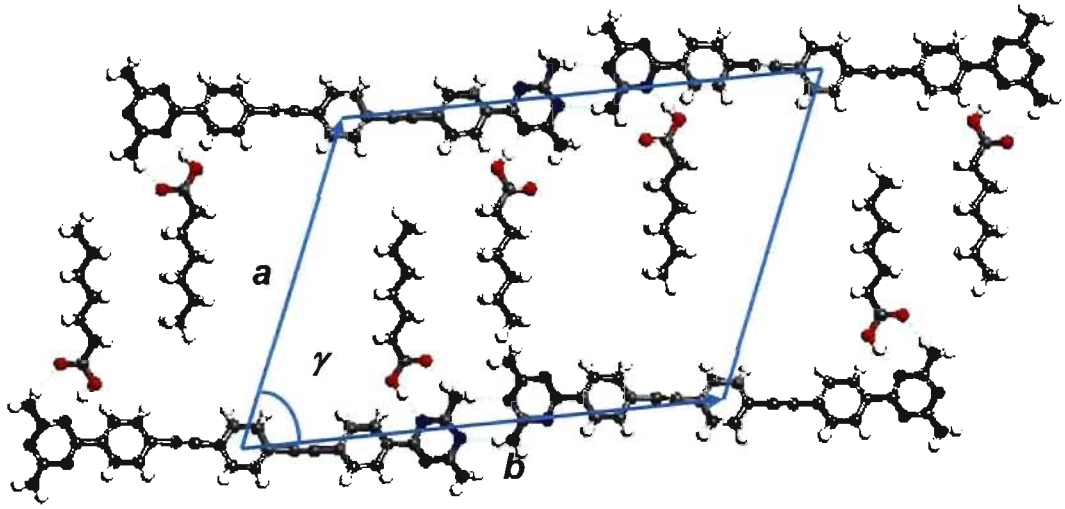

Figure 3.9 Proposed molecular model of tecton **DAT-2** coadsorbed with heptanoic acid. The unit cell is highlighted in light blue.

symmetry of the underlying HOPG (Figures 3.8b). This appears to maximize interactions between the adsorbate and the surface, including π-π stacking and van der Waals forces.

3.3.4 3D Crystal Structure of Tecton DAT-2

Crystals of tecton **DAT-2** were grown by slow evaporation of a solution in DMSO, and the structure was determined by X-ray diffraction. Views of the structure are provided in Figures 3.10 and 3.11. The crystals were found to have the composition **DAT-2** • 6DMSO (Figure 3.10a) and to belong to the monoclinic space group *P*21, with unit cell parameters a = 9.2111(11) Å, b = 10.7204(14) Å, c = 25.078(3) Å, α = 90°, β = 97.413(6)°, and γ = 90° (Figure 3.10b). The percentage of volume available for the inclusion of guest molecules was calculated to be 58%,[67,68] which reveals that tecton **DAT-2** crystallizes to form a highly open structure.

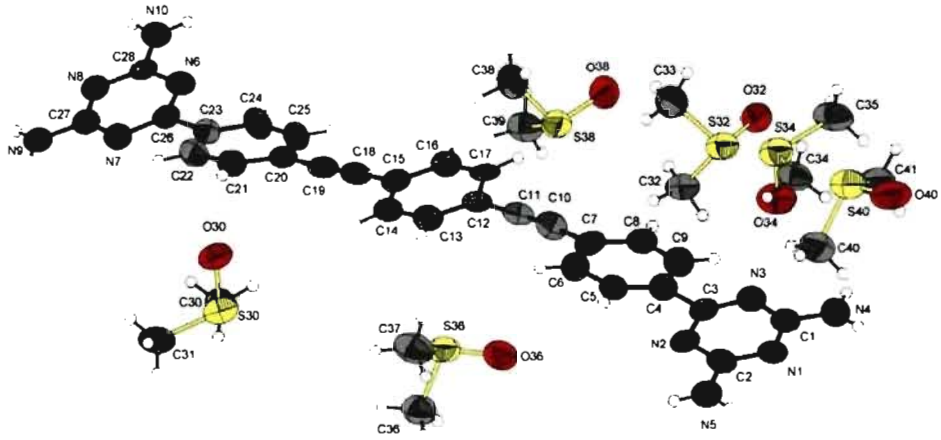

(a)

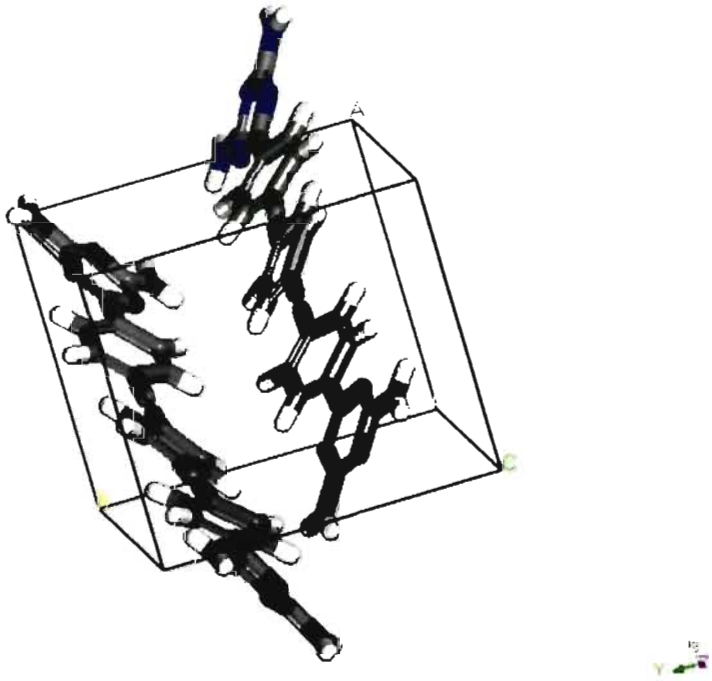

(b)

Figure 3.10 (a) ORTEP view of the structure of crystals of tecton **DAT-2** grown from DMSO, with the numbering scheme adopted. Ellipsoids are drawn at the 50% probability level. Hydrogen atoms are represented by a sphere of arbitrary size. (b) View of the unit cell, with DMSO removed for clarity.

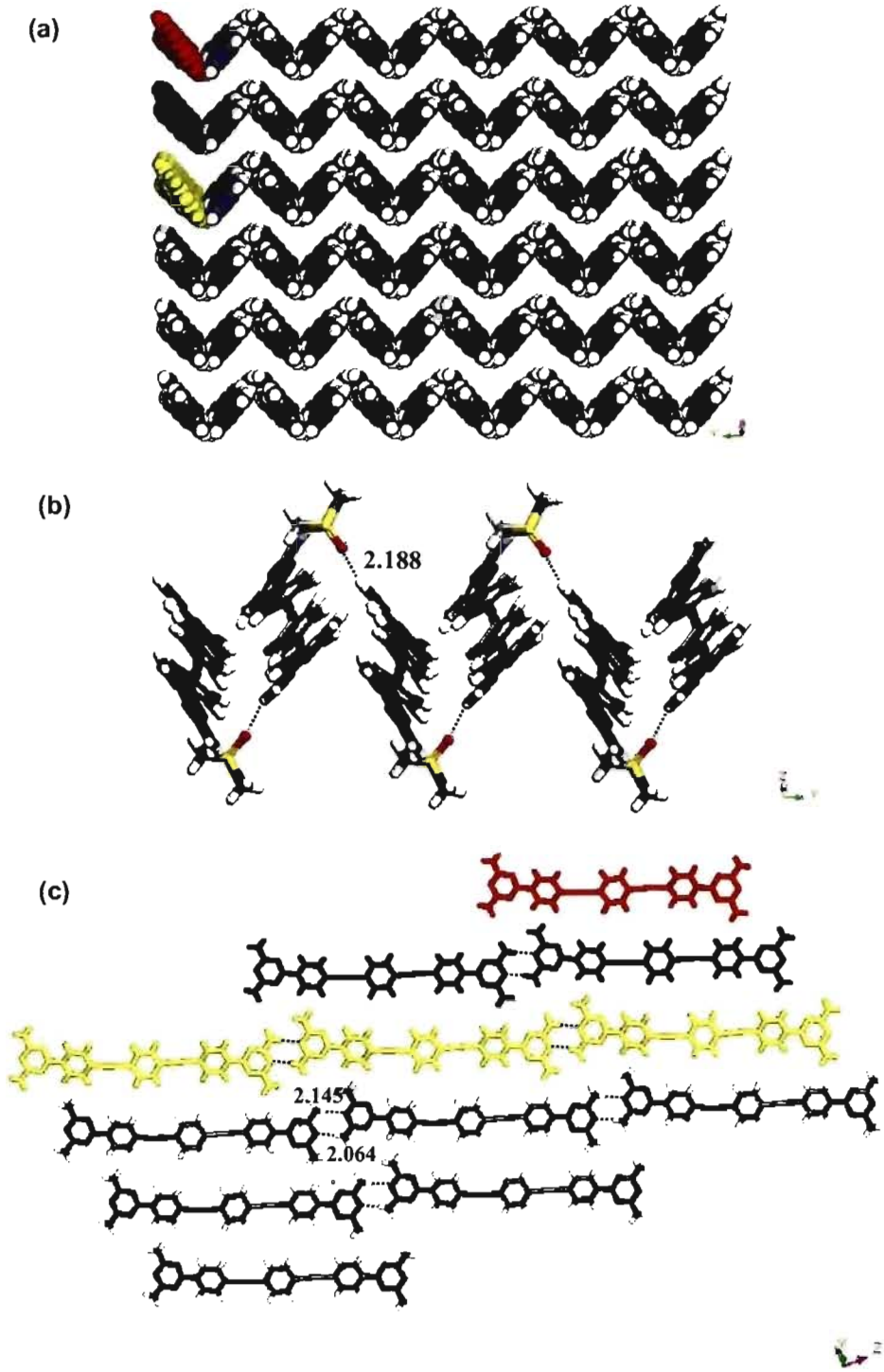

Figure 3.11 Structure of crystals of tecton **DAT-2** grown from DMSO. (a) View along the *a* axis showing the corrugated layers. (b) Within a single layer, no direct hydrogen bonds are found between neighboring tapes, which are associated with molecules of DMSO by hydrogen bonding. (c) View along the *b* axis showing neighboring molecules in six adjacent layers. Hydrogen bonds are represented by broken lines. Tectons are highlighted in red, blue, and yellow to show the relationship between views (a) and (c).

Figure 3.11a shows that the crystals of tecton **DAT-2** can be considered to be built from corrugated layers. Each layer is composed of linear tapes of tectons held together by the typical face-to-face hydrogen bonding of DAT groups, with H···N distances of 2.145 and 2.064 Å. Within a single layer, no strong interactions can be found between neighboring tapes, which are associated with molecules of DMSO by hydrogen bonding, with an H···O distance of 2.188 Å (Figure 3.11b). In this way, the 3D crystal structure and the 2D nanopattern formed by adsorption on HOPG (Figures 3.8 and 3.11) are closely analogous, despite the important effects of solvent and surface confinement. Both structures reveal an unwillingness of the tectons to form a rigorously planar layer in which the characteristic tapes engage in additional side-to-side intertape hydrogen bonding, as observed in the 3D crystal structure of analogue **DAT-1**. It is possible that such structures are disfavored because their more extensive hydrogen bonding enforces a higher degree of openness, leading to less effective molecular packing in both 3D and 2D.

3.3.5 2D Nanopatterns Formed by Tecton DAT-3

To evaluate the relative ability of interadsorbate hydrogen bonding and diffuse adsorbate-surface interactions to control molecular nanopatterning, we were eager to compare the behavior of tectons **DAT-1** and **DAT-2** with that of analogues bearing long alkyl chains. We designed tecton **DAT-3** to serve this purpose, because it is identical to tecton **DAT-2** except for the addition of two dodecyloxy chains to the central core. We expected to attain more stable 2D hydrogen-bonded networks with the added assistance of

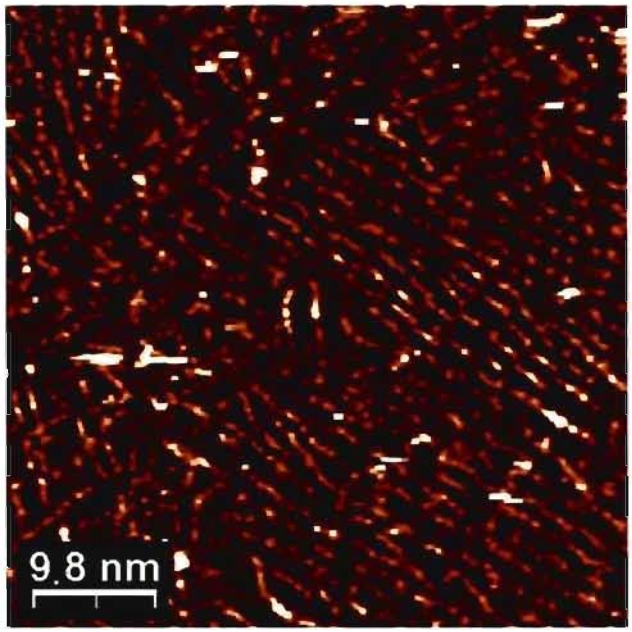

Figure 3.12 STM image of 2D nanopattern created by depositing tecton **DAT-3** on HOPG under the standard conditions (heptanoic acid, V_{bias} = -1.5 V, I_{set} = 100 pA).

the chains in immobilizing tecton **DAT-3** on the underlying surface via the formation of van der Waals interactions.

Figure 3.12 shows an STM image of tecton **DAT-3** adsorbed on HOPG under our standard conditions. Unlike the well-ordered nanopatterns formed by analogues **DAT-1** and **DAT-2,** the 2D patterns produced by substituted tecton **DAT-3** are not periodic over large areas, although small regions of local organization are visible. Most of the adsorbed tectons are found to assemble randomly, without a specific orientation of each molecule relative to its neighbors. It is noteworthy that individual molecules can be imaged clearly, even though the pattern does not enjoy the energetic benefits of periodic organization. We suggest that the long alkyl chains increase the strength of binding to the surface as planned, thereby increasing the degree of immobilization, retarding exchange, and facilitating

imaging. At the same time, however, the alkyl chains presumably interfere with the self-assembly of specific molecular aggregates directed by hydrogen bonding. This may result from steric effects that oppose suitable hydrogen bonding, or from kinetic effects that slow the rate of 2D crystallization. Indeed, strong adsorbate-surface interactions are not necessarily conducive to the formation of highly structured monolayers. Self-organization requires that deposited molecules be able to desorb, rotate, and translate to find themselves in a proper position to form stable periodic nanopatterns.[69]

3.3.6 3D Crystal Structure of Tecton DAT-3

Crystals of tecton **DAT-3** were grown by allowing vapors of chloroform to diffuse into a solution in DMSO, and their structure was determined by X-ray diffraction. Views of the structure are provided in Figures 3.13 and 3.14. The crystals proved to have the composition **DAT-3** • DMSO and to belong to the *P*21/C space group, with unit cell parameters a = 26.700(14) Å, b = 8.692(5) Å, c = 12.737(7) Å, α = 90°, β = 101.379(8)°, and γ = 90°. The percentage of volume available for the inclusion of guest molecules was calculated to be 19%,[66,67] which reveals that tecton **DAT-3** is able to form a structure that is more closely packed than the one derived from unsubstituted analogue **DAT-2** (58%). The three phenyl rings in the linear core of the compound are oriented approximately parallel to each other, as in the core of the tecton **DAT-2**. The dodecyloxy side chains adopt a conformation that is extended although not entirely all-trans.[53] As in the case of both analogues **DAT-1** and **DAT-2**, the structure of tecton **DAT-3** can be considered to be built from linear tapes in which the molecules are linked end-to-end by typical face-to-face

hydrogen bonds of DAT groups, with H···N distances of 2.165 Å (Figure 3.14b). The repeated appearance of this motif in all three structures underscores the primacy of forming face-to-face hydrogen bonds of DAT groups. This organization allows each tecton to form a total of four hydrogen bonds with the two adjacent tectons in the same tape.

In the structures of tectons **DAT-1** and **DAT-2**, the resulting tapes either interact by the formation of side-to-side intertape hydrogen bonds (**DAT-1**) or simply pack in a way that optimizes other interactions (**DAT-2**). In contrast, the alkyl substituents of tecton **DAT-3** prevent tapes from approaching each other in the same plane. Instead, adjacent tapes lie at an angle that allows the alkyl groups of adjacent tectons to interdigitate (Figure 3.14). In this way, the DAT groups each engage in the formation of two additional intertape hydrogen bonds (Figure 3.13c).

Because of geometric constraints imposed by the relative inclination of adjacent tapes, these intertape hydrogen bonds are not the normal cyclic side-to-side pairs seen in the structure of tecton **DAT-1**, but rather single N-H···N hydrogen bonds with an H···N distance of 2.276 Å (Figure 3.13c). As expected, these hydrogen bonds are longer than those of the primary face-to-face motif that holds the individual tapes together (H···N distance of 2.165 Å). Overall, each tecton in the observed structure participates in a total of eight hydrogen bonds, which is the same as in the structure of tecton **DAT-1** and is greater than that in the structure of tecton **DAT-2**. Although the number of hydrogen bonds per tecton is the same in the structures of compounds **DAT-1** and **DAT-3**, each molecule **DAT-1** forms hydrogen bonds with four neighbors, whereas analogue **DAT-3** has six hydrogen-bonded neighbors.

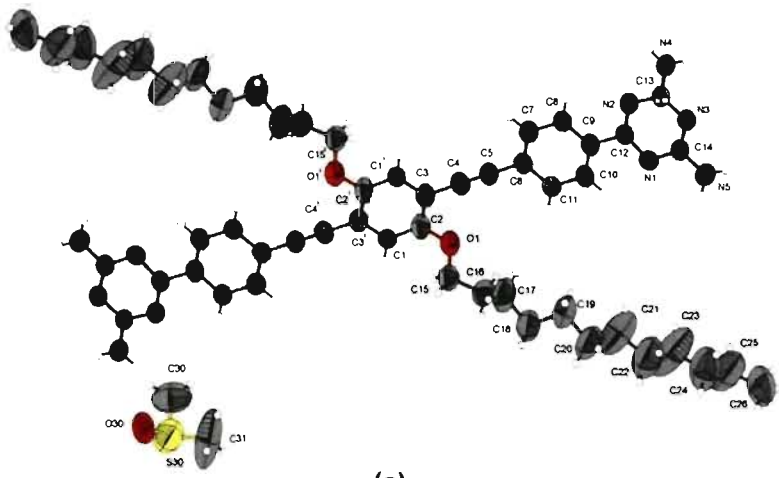

(a)

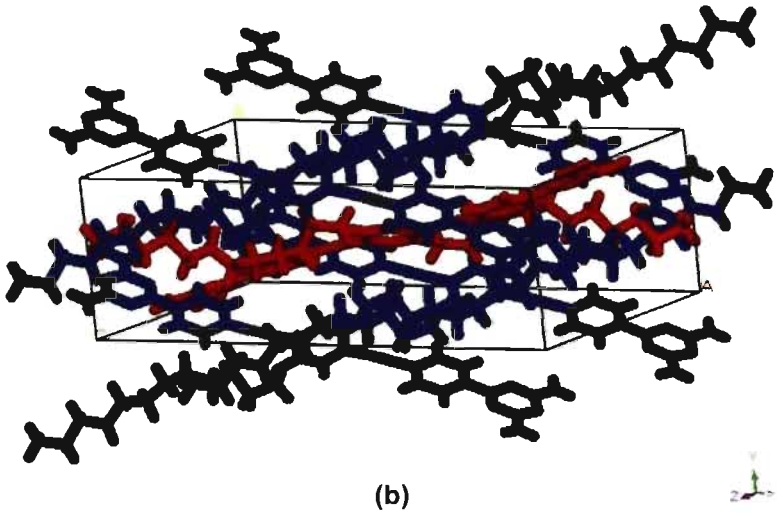

(b)

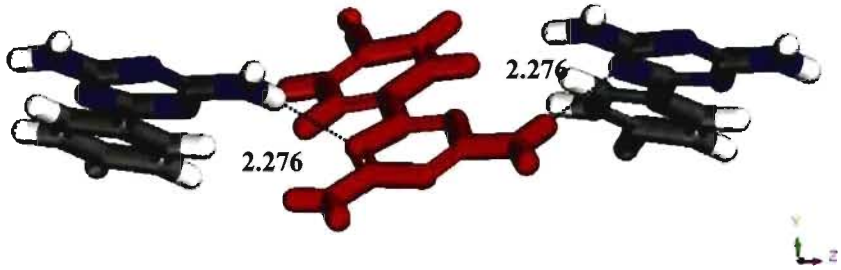

(c)

Figure 3.13 (a) ORTEP view of the structure of crystals of tecton **DAT-3** grown from $CHCl_3$/DMSO, with the numbering scheme adopted. Ellipsoids are drawn at the 50% probability level, and hydrogen atoms are represented by a sphere of arbitrary size. (b) Unit cell with guest molecules of DMSO removed for clarity. (c) Single hydrogen bonds between the DAT groups of tectons in adjacent non-parallel tapes.

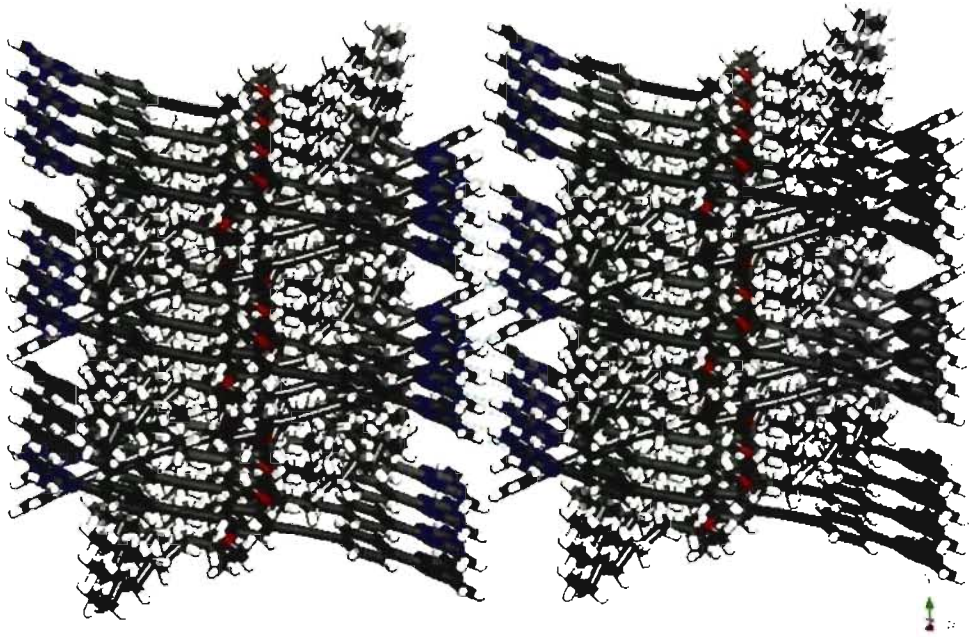

(a)

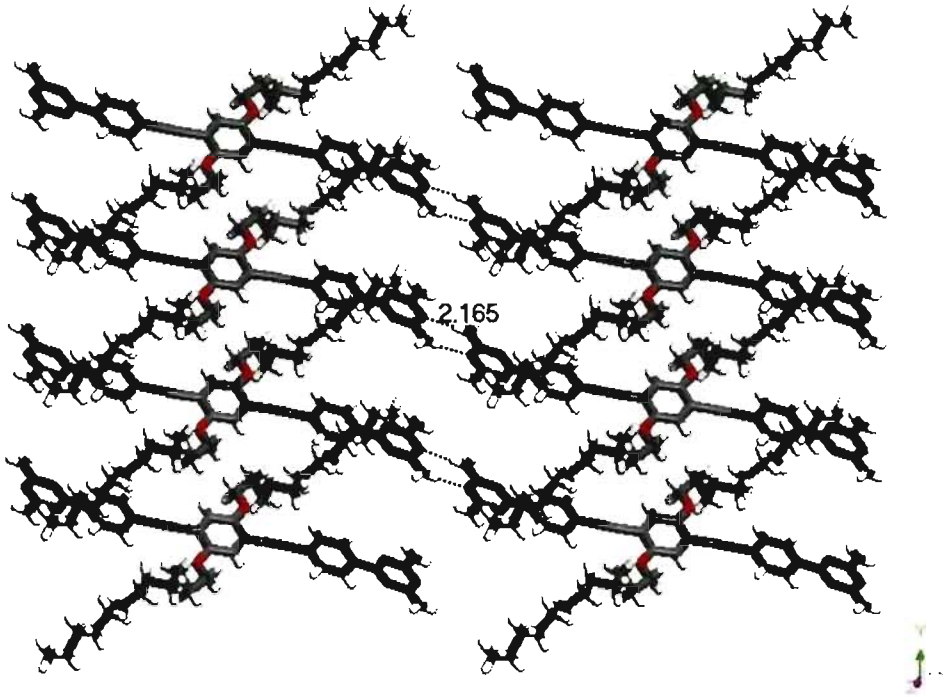

(b)

Figure 3.14 Views of the structure of crystals of tecton **DAT-3** grown from $CHCl_3$/DMSO Hydrogen bonds are represented by broken lines. (a) View along the *c* axis showing parallel hydrogen-bonded tapes cut by tapes lying at an angle. (b) Face-to-face hydrogen bonds with single tapes.

It is interesting to note that the dodecyloxy side chains of tecton **DAT-3** do not prevent 3D crystallization, although they lead to a structure in which hydrogen bonding is not optimized. In contrast, 2D crystallization is thwarted, at least on the normal time scale of STM experiments. This striking difference appears to be due to constraints imposed by confinement to a surface. The core of analogue **DAT-2** has a planar topology and an elongated axis that together favor sheet structures in which molecules have their long axes aligned. As a result, both 2D and 3D crystallization yield periodic structures with predictable features. In contrast, the alkyl substituents of tecton **DAT-3** inhibit the formation of periodic structures when the molecules are confined to a surface; however, attractive new opportunities for accommodating both alkyl groups and hydrogen bonding are created by moving to three dimensions. It is possible that a deeper understanding of such effects may provide new ways to engineer the properties of molecular films that are intermediate in thickness between 2D monolayers and 3D crystals. Of particular interest would be films that have some of the attractive features of amorphous materials, such as ease of formation by spin coating, transparency, and flexibility, yet also have some of the features of crystalline materials, such as local control of molecular positions and orientations.

3.3.7 2D Nanopatterning by Tecton DAT-4

Tecton **DAT-4** has three trigonally-directed DAT groups and was designed to adsorb on HOPG to form the 2D nanopattern shown in Figure 3.15. In this model, each tecton associates with three neighbors by forming a total of 12 hydrogen bonds of the face-to-side

type characteristic of paired DAT groups. A key feature of the network is the creation of rosettes consisting of cyclic aggregates of six DAT groups.[40] Unfortunately, we have not been able to obtain STM images showing how tecton **DAT-4** is adsorbed on graphite, although we tried many times and used a variety of solvents, including heptanoic acid, 1-phenyloctane, and 1-octanol.

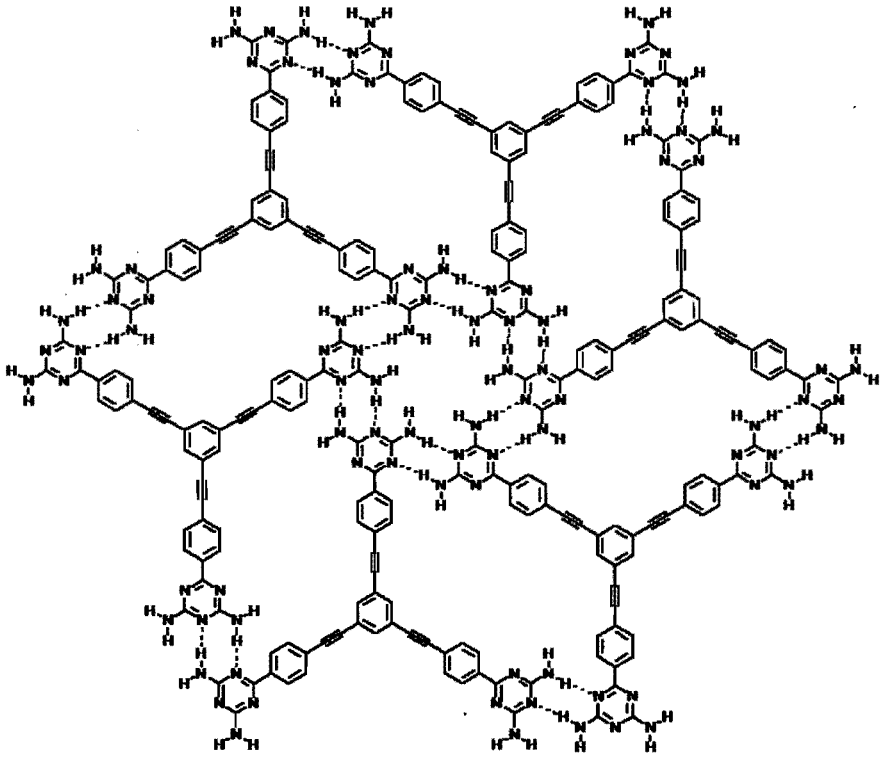

Figure 3.15 Proposed molecular model for 2D nanopatterns built from tecton **DAT-4**.

3.3.8 3D Crystal Structure of Tecton DAT-4

To test our hypotheses about how tecton **DAT-4** is predisposed to behave, we turned to an analysis of its 3D crystal structure. Crystals suitable for X-ray diffraction could be grown from DMSO. Views of the structure are shown in Figures 3.16, 3.17, and 3.18, and they show that the compound crystallizes essentially as expected. The crystals proved to have the composition 2**DAT-3** • 7DMSO and to belong to the *P*1 space group, with unit cell parameters a = 9.9203(7) Å, b = 21.3106(16) Å, c = 24.5546(18) Å, α = 104.402(2)°, β = 99.017(2)°, and γ = 92.955(2)°. The unit cell contains tectons with two conformations (Figure 3.16b), which differ somewhat in the torsional angles of the 1,3,5-tris(phenylethynyl)benzene core and the attached DAT groups.

As proposed in Figure 3.15, crystallization of trigonal tecton **DAT-4** generates sheets that are extensively hydrogen-bonded. Equal numbers of two distinct conformers are present, and each tecton is hydrogen bonded to three neighbors of the other conformational type. These conformational intrincacies are not easily rationalized in detail, but they presumably improve the packing of adjacent sheets or help accommodate included molecules of DMSO. Each DAT group participates in a total of four hydrogen bonds with N···H distances of 2.150, 2.404, 2.171, and 2.145 Å. The interaction of neighboring tectons in a single sheet can be described as an embracing motif involving face-to-side hydrogen bonding of two DAT groups provided by each partner (Figure 3.18a). The different lengths of the four hydrogen bonds indicate that the hydrogen-bonded DAT pairs are not exactly coplanar.

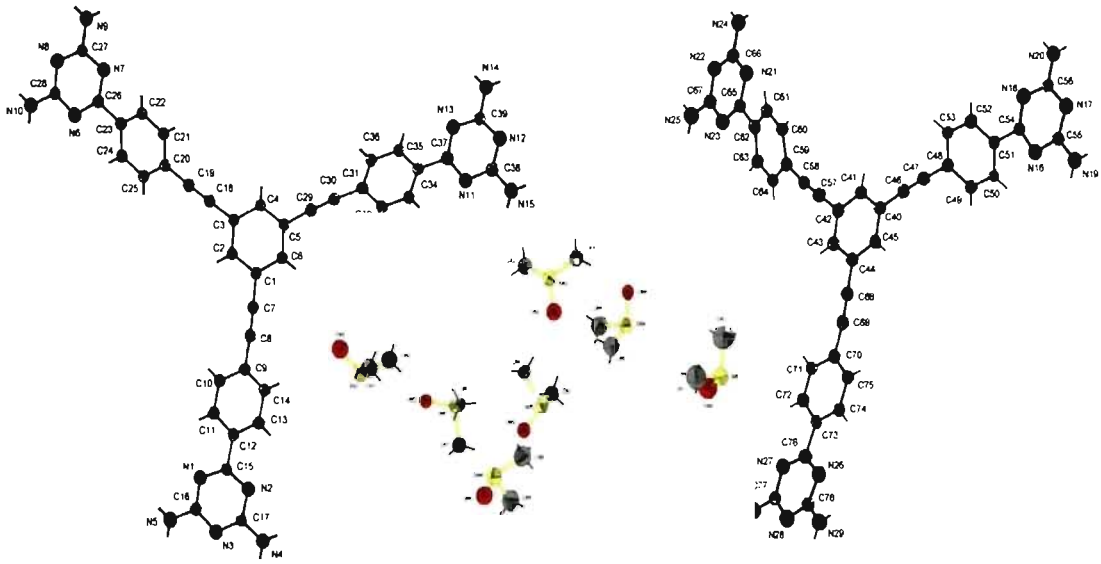

(a)

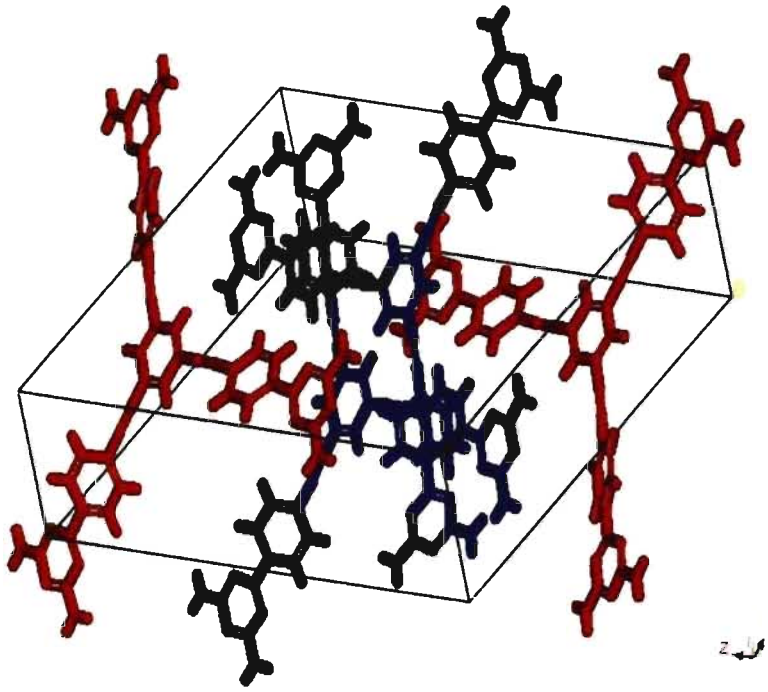

(b)

Figure 3.16 (a) ORTEP view of the structure of crystals of tecton **DAT-4** grown from DMSO, with the numbering scheme adopted. Ellipsoids are drawn at the 50% probability level, and hydrogen atoms are represented by a sphere of arbitrary size. (b) Unit cell with guest molecules of DMSO omitted for clarity. The two different conformers are highlighted in red and blue.

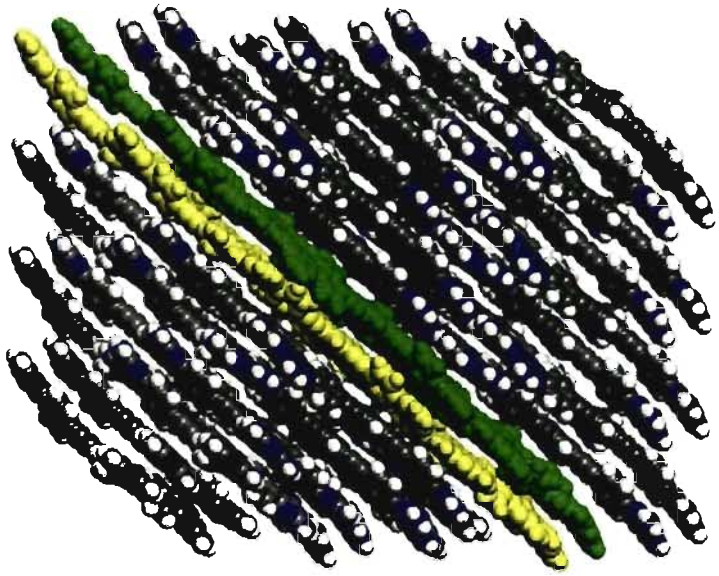

(a)

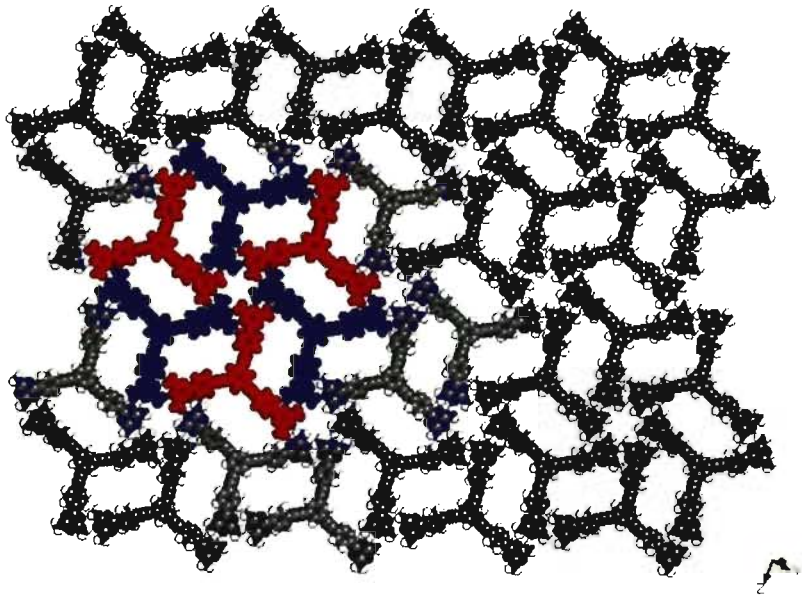

(b)

Figure 3.17 Views of the structure of crystals of tecton **DAT-4** grown from DMSO. Guest molecules of DMSO are removed for clarity. (a) View showing the stacking of sheets, with two adjacent layers highlighted in yellow and green. (b) View of a single sheet, with a rosette built from six tectons of alternating conformation highlighted in red and blue.

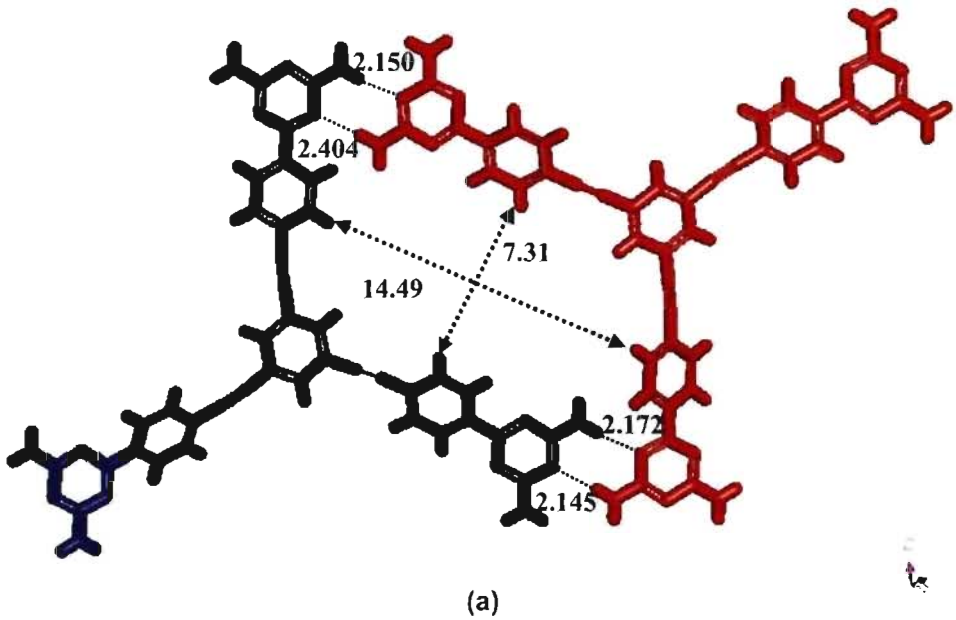

(a)

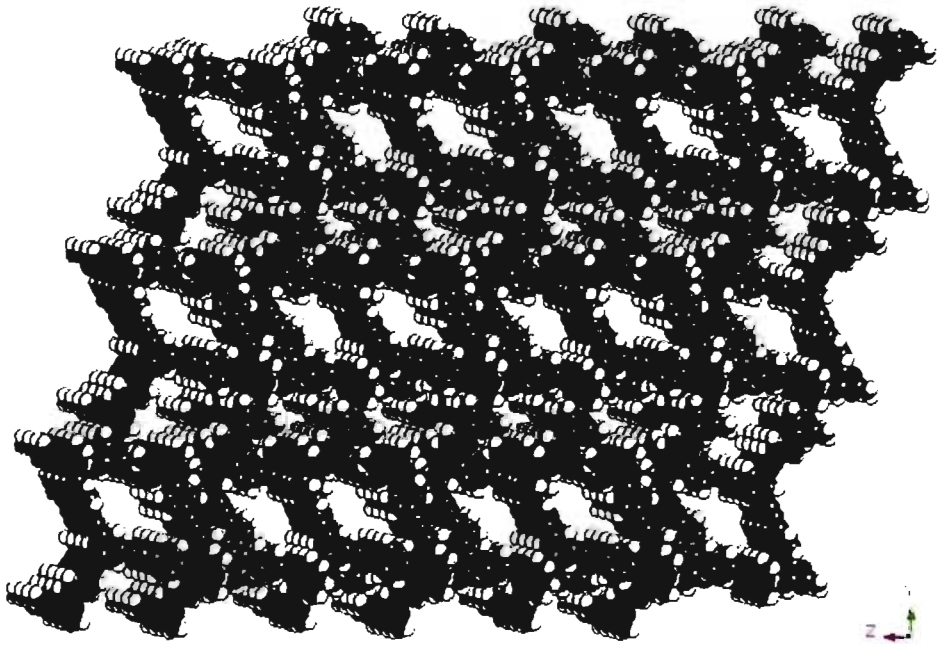

(b)

Figure 3.18 Additional views of the structure of crystals of tecton **DAT-4** grown from DMSO. Guest molecules of DMSO are removed for clarity. (a) The characteristic embracing motif of hydrogen bonding between two conformers of tecton **DAT-4** (shown in red and blue). Hydrogen bonds are represented by broken lines. (b) View along the *a* axis showing the cross section of channels.

A noteworthy feature of the structure is the formation of hexameric rosettes of DAT groups (Figure 3.17b). Although analogous rosettes have been proposed to result from various processes of supramolecular assembly, they have rarely been characterized unambiguously by X-ray crystallography.[69, 70] The internal diameter of the rosettes formed by tecton **DAT-4** (average transannular N···N distance = 7.7 Å) is identical to the value determined for the first DAT rosettes, which were generated by a metallotecton consisting of DAT groups grafted to a tris(dipyrrinato)cobalt(III) core.[70] Each sheet in the structure of tecton **DAT-4** therefore consists of an open hydrogen-bonded network, and the openings in adjacent sheets are aligned to create a system of parallel channels that lie along the *a* axis, with dimensions of 7.3 × 14.5 Å (Figure 3.18). The percentage of volume available for the inclusion of guest molecules was calculated to be 39%.[67,68]

3.4 Summary

In this chapter, we have presented the results of a study of four related compounds designed to adsorb on surfaces and to create specific hydrogen-bonded 2D nanopatterns. The four compounds have certain structural features in common, such as largely planar conjugated cores with phenylethynyl groups grafted to DAT groups as sticky sites. At the same time, the four compounds differ in ways that allow us to probe the effects of systematic structural alterations, such as lengthening the molecular core, changing its geometry, or altering the balance between hydrogen bonding and other intermolecular interactions. We attempted to analyze the ability of all four compounds to form periodic hydrogen-bonded networks, both in 2D (by adsorption on HOPG, using STM as the method

of analysis) and in 3D (by crystallization, followed by X-ray diffraction). Systematic structural variation, combined with analysis in both 2D and 3D, has made our study a rich source of new information about molecular association.

Tecton **DAT-1** and its elongated analogue **DAT-2** both generate periodic structures on HOPG with long-range order, when deposited from solution. In both cases, structural features seen in the solid state are also seen on the surface. In particular, both compounds reveal a general preference for forming sheets that can be considered to be composed of tapes in which the molecules are linked end-to-end by face-to-face hydrogen bonding of DAT groups. In neither case, however, are the structures observed in 2D and 3D fully homologous, and very important differences arise. In particular, the linear tapes formed by compounds **DAT-1** and **DAT-2** pack in 2D in unexpected ways, possibly to increase the density of packing on the surface.

Curiously, alkyl-substituted analogue **DAT-3** appears to adsorb strongly but failed to produce 2D nanopatterns with long-range periodicity, presumably because its dodecyloxy side chains cannot be packed efficiently when the molecules are confined to a surface and must simultaneously try to engage in extensive hydrogen bonding. The 3D crystals revealed expected features, including linear hydrogen-bonded tapes of the type also seen in the structures of compounds **DAT-1** and **DAT-2**.

Trigonal compound **DAT-4** failed to yield well-defined STM images when deposited on HOPG, but its 3D crystallization proceeded exactly as planned to produce a structure built from hydrogen-bonded sheets, featuring hexameric rosettes of DAT groups.

Together, our observations highlight the special ability of tectons to serve as sources of

periodic structures with predictable architectural features, both in 2D and in 3D. Although the 2D and 3D structures tend to have important similarities, firm predictions remain risky.

References

1. Plass, K. E.; Grzesiak, A. L.; Matzger, A. J. *Acc. Chem. Res.* **2007**, *40*, 287-293.
2. De Feyter, S.; Gesquière, A.; Abdel-Mottalev, M. M.; Grim, P. M.; De Schryver, F. C. *Acc. Chem. Res.* **2000**, *33*, 520-531.
3. De Feyter, S.; De Schryver, F. C. *Chem. Soc. Rev.* **2003**, *32*, 139-150.
4. Jonkheijm, P.; Miura, A.; Zdanowska, M.; Hoeben, F. J. M.; De Feyter, S.; Schenning, A. P. H. J.; De Schryver, F. C.; Meijer, E. W. *Angew. Chem. Int. Ed.* **2004**, *43*, 74-78.
5. Samorí, P.; Fechtenkötter, A.; Jäckel, F.; Böhme, T.; Müllen, K.; Rabe, J. P. *J. Am. Chem. Soc.* **2001**, *123*, 11462-11467.
6. Perronet, K.; Charra, F. *Surf. Sci.* **2004**, *551*, 213-218.
7. Lei, S.-B.; Pruigmartí-Luis, Minoia, A.; Der Auweraer, M. V.; Rovira, C.; Lazzaroni, R.; Amabilino, D. B.; De Feyter, S. *Chem. Commun.* **2008**, 703-705.
8. Groszek, A. J. *Proc. Roy. Soc. London A* **1970**, *314*, 473-494.
9. Findenegg, G. H. *J. Chem. Soc., Faraday Trans. 1* **1972**, *68*, 1799-1806.
10. Findenegg, G. H. *J. Chem. Soc., Faraday Trans. 1* **1973**, *69*, 1069-1078.
11. Rabe, J. P.; Buchholtz, S. *Science* **1991**, *253*, 424-427.
12. Cyr, D. M.; Venkataraman, B.; Flynn, G. W. *Chem. Mater.* **1996**, *8*, 1600-1615.

13. McGonigal, G. C.; Bernhadt, R. H.; Thomson, D. J. *Appl. Phys. Lett.* **1990**, *57*, 28-30.

14. Cyr. D. M.; Venkataraman, B.; Flynn, G. W.; Black, A.; Whitesides, G. M. *J. Phys. Chem.* **1996**, *100*, 13747-13759.

15. Watel, G.; Thibaudau, F.; Cousty, J. *Surf. Sci.* **1993**, *281*, L297-L302.

16. Venkataraman, B.; Breen, J. J.; Flynn, G. W. *J. Phys. Chem.* **1995**, *99*, 6608-6619.

17. Claypool, C. L.; Faglioni, F.; Goddard, W. A.; Gray, H. B.; Lewis, N. S.; Marcus, R. A. *J. Phys. Chem. B* **1997**, *101*, 5978-5995.

18. Claypool, C. L.; Faglioni, F.; Matzger, A. J.; Goddard, W. A.; Lewis, N. S. *J. Phys. Chem. B* **1999**, *103*, 9690-9699.

19. McGonigal, G. C.; Bernhardt, R. H.; Yeo, Y. H.; Thomson, D. *J. Vac. Sci. Technol. B* **1991**, *9*, 1107-1110.

20. Wintgens, D.; Yablon, D. G.; Flynn, G. W. *J. Phys. Chem. B* **2003**, *107*, 173-179.

21. Feng, C. L.; Zhang, Y.; Jin, J.; Song, Y.; Xie, L.; Qu, G.; Jiang, L.; Zhu, D. *Surf. Sci.* **2002**, *513*, 111-118.

22. Elbel, N.; Roth, W.; Günther, E.; von Seggern, H. *Surf. Sci.* **1994**, *303*, 424-432.

23. Hibino, M.; Sumi, A.; Tsuchiya, H.; Hatta, I. *J. Phys. Chem. B* **1998**, *102*, 4544-4547.

24. Fang, H. B.; Giancarlo, L. C.; Flynn, G. W. *J. Phys. Chem. B* **1999**, *103*, 5712-5715.

25. Yablon, D. G.; Guo, J.S.; Knapp, D.; Fang, H. B.; Flynn, G. W. *J. Phys. Chem. B* **2001**, *105*, 4313-4316.

26. Fang, H. B.; Giancarlo, L. C.; Flynn, G. W. *J. Phys. Chem. B* **1998**, *102*, 7421-7424.

27. Yablon, D. G.; Wintgens, D.; Flynn, G. W. *J. Phys. Chem. B* **2002**, *106*, 5470-5475.

28. Hoeppener, S.; Chi, L. F.; Wonnemann, J.; Erker, G.; Fuchs, H. *Surf. Sci.* **2001**, *487*, 9-14.

29. Stevens, F.; Dyer, D. J.; Müller, U.; Walba, D. M. *Langmuir* **1996**, *12*, 5625-5629.

30. Samorì, P.; Yin, X.; Tchebotareva, N.; Wang, Z.; Pakula, T.; Jäckel, F.; Watson, M. D.; Venturini, A.; Müllen, K.; Rabe, J. P. *J. Am. Chem. Soc.* **2004**, *126*, 3567-3575.

31. Giorgi, T.; Lena, S.; Mariani, P.; Bremonini, M. A.; Masiero, S.; Pieraccini, S.; Rabe, J. P.; Samori, P.; Spada, G. P.; Gottarelli, G. *J. Am. Chem. Soc.* **2003**, *125*, 14741-14749.

32. Stevens, F.; Dyer, D. J.; Walba, D. M. *Langmuir* **1996**, *12*, 436-440.

33. De Feyter, S.; Grim, P. C. M.; Rücker, M.; Vanoppen, P.; Meiners, C.; Sieffert, M.; Valiyaveettil, S.; Müllen, K.; De Schryver, F. C. *Angew. Chem. Int. Ed.* **1998**, *37*, 1223-1226.

34. Kalsani, V.; Ammon, H.; Jäckel, F.; Rabe, J. P.; Schmittel, M. *Chem.-Eur. J.* **2004**, *10*, 5481-5492.

35. Tomović, Ž.; van Dongen, J.; George, S. J.; Xu, H.; Pisula, W.; Leclère, P.; Smulers, M. M. J.; De Feyter, S.; Meijer, E. W.; Schenning, A. P. H. J. *J. Am. Chem. Soc.* **2007**, *129*, 16190-16196.

36. Tahara, K.; Furukawa, S.; Uji-i, H.; Uchino, T.; Ichikawa, T.; Zhang, J.; Mandouh, W.; Motohiro, S.; De Schryver, F. C.; De Feyter, S.; Tobe, Y. *J. Am. Chem. Soc.* **2006**, *128*, 16613-16625.

37. Tao, F.; Bernasek, S. L. *Chem. Rev.* **2007**, *107*, 1408-1453.

38. Malek, N.; Maris, T.; Simard, M.; Wuest, J. D. *J. Am. Chem. Soc.* **2005**, *127*, 5910-5916.

39. Maly, K. E.; Gagnon, E.; Maris, T.; Wuest. J. D. *J. Am. Chem. Soc,* **2007**, *129*, 4306-4322.

40. Jonkheijm, P.; Miura, A.; Zdanowska, M.; Hoeben, J. M.; De Feyter, S.; Schenning, A. P. H. J.; De Schryver, F. C.; Meijer, E. W. *Angew. Chem. Int. Ed.* **2004**, *43*, 74-78.

41. Caňas-Ventura, M. E.; Xiao, W.; Wasserfallen, D.; Müllen, K.; Brune, H. *Angew. Chem. Int. Ed.* **2007**, *46*, 1814-1818.

42. Garnler, F.; Hajlaoui, R.; Yassa, A.; Srivastava, P. *Science* **1994**, *265*, 1684-1686.

43. Burroughes, J. H.; Bradley, D. D. C.; Brown, A. R.; Marks, R. N.; Mackay, K.; Friend, R. H.; Burns, P. L.; Holmes, A. B. *Nature* **1990** *347*, 539-541.

44. Yu, G.; Gao, J.; Hummelen, J. C.; Wudl, F.; Heeger, A. J. *Science* **1995**, *270*, 1789-1791.

45. Stabel, A.; Herwig, P.; Müllen, K.; Rabe, J. P. *Angew. Chem. Int. Ed. Engl.* **1995**, *34*, 1609-1611.

46. Lidzey, D. G.; Bradley, D. D. C.; Alvarado, S. F.; Seidler, P. F. *Nature* **1997**, *386*, 135-137.

47. Kim, J.; Swager, T. M. *Nature* **2001**, *411*, 1030-1034.

48. McQuade, D. T.; Kim. J.; Swager, T. M. *J. Am. Chem. Soc.* **2000**, *122*, 5885-5886.

49. Bumm, L. A.; Arnold, J. J.; Cygan, M. T.; Dunbar, T. D.; Burgin, T. P.; Jones II, L.; Allara, D. L.; Tour, J. M.; Weiss, P. S. *Science* **1996**, *271*, 1705-1707.

50. Cygan, M. T.; Dunbar, T. D.; Arnold, J. J.; Bumm, L. A.; Shedlock, N. F.; Burgin, T. P.; Jones, L., II; Allara, D. L.; Tour, J. M.; Weiss, P. S. *J. Am. Chem. Soc.* **1998**, *120*, 2721-2732.

51. Gong, J.-R.; Zhao, J.-L.; Lei, S.-B.; Wan, L.-J.; Bo, Z.-S.; Fan, X.-L.; Bai, C.-L. *Langmuir* **2003**, *19*, 10128-10131.

52. Mu, Z.-C.; Yang, X.-Y.; Wang, Z.-Q.; Zhang, X. *Langmuir* **2004**, *20*, 8892-8896.

53. Samorí, P.; Francke, V.; Enkelmann, V.; Müllen, K.; Rabe, J. P. *Chem. Mater.* **2003**, *15*, 1032-1039.

54. This compound was first synthesized and crystallized in the group by Dr. K. E. Maly, and its structure was determined by Dr. Thierry Maris.

55. Zhang, W.; Kraft, S.; Moore, J. S. *J. Am. Chem. Soc.* **2004**, *126*, 329-333.

56. Sauriat-Dorizon, H.; Maris, T.; Wuest, J. D. *J. Org. Chem.* **2003**, *68*, 240-246.

57. Nguyen, P.; Yuan, Z.; Agocs, L.; Lesley, G; Marder, T. B. *Inorg. Chim. Acta* **1994**, *220*, 289-296.

58. Li, G.; Wang, X.; Wang, F. *Tetrahedron Lett.* **2006**, *47*, 723-725.

59. Ziessel, R.; Diring, S. *Tetrahedron Lett.* **2006**, *47*, 4687-4692.

60. Khatyr, A.; Ziessel, R. *J. Org. Chem.* **2000**, *65*, 3126-3134.

61. Weber, E.; Hecker, M.; Koepp, E.; Orlia, W.; Czugler, M.; Csoregh, I. *J. Chem. Soc. Perkin Trans. II* **1988**, *7*, 1251-1257.

62. Yamaguchi, Y.; Ochi, T.; Miyamura, S.; Tanaka, T. ; Kobayashi, S. ; Wakamiya, T. ; Matsubara, Y.; Yoshida, Z. *J. Am. Chem. Soc.* **2006**, *128*, 4504-4505.

63. Sauriat-Dorizon, H.; Maris, T.; Wuest, J. D. *J. Org. Chem.* **2003**, *68*, 240-246.

64. For related work showing the importance of interactions between graphite and the substituents of adsorbed aromatic compounds, see: Rochefort, A.; Wuest, J. D. *Langmuir* **2008**, *25*, 210-215. Unpublished results suggest that interactions with NH_2 groups may be particularly important.

65. Su, G.-J.; Zhang, H.-M.; Wan, L.-J.; Bai, C.-L.; Wandlowski, T. *J. Phys. Chem. B* **2004**,

108, 1931-1937.

66. Walch, H.; Maier, A. K.; Heckl, W. M.; Lackinger, M. *J. Phys. Chem. C* **2009**, *113*, 1014-1019.

67. The percentage of volume accessible to guests is estimated by a standard method. In this method, the accessible volume is defined by the volume that can be occupied by a spherical probe of radius r constrained to move in a way that its center must remain at a distance no less than r from the closest point on the van der Waals surface of the ordered network. The accessible volume is calculated by using the PLATON program,[68] which uses a default value of 1.20 Å for the radius of the probe. This value is an appropriate model for small guests such as water. The van der Waals radii used to define surfaces for these calculations are as follows: C: 1.70 Å, H: 1.20 Å, N: 1.55 Å, and O: 1.52 Å. If V is the volume of the unit cell and V_g is the guest-accessible volume per unit cell as calculated by PLATON, then the percentage of the volume accessible to guests is given by $100V_g/V$. Although this volume is typically occupied at least in part by included guests, it can be considered to provide a measure of potential porosity.

68. Spek, A. L. PLATON, A Multipurpose Crystallographic Tool; Utrecht University: Utrecht, The Netherlands, 2001. van der Sluis, P.; Spek, A. L. *Acta Crystallogr.* **1990**, *A46*, 194-201.

69. De Feyter, S.; De Schryver, F. C. *Chem. Soc. Rev.* **2003**, *32*, 139-150.

70. Telfer, S. G.; Wuest, J. D. *Chem. Commun.* **2007**, 3166-3168.

CHAPTER 4

STM Study of the Adsorption of Tetracarboxylic Acids Created by Connecting Isophthalic Acid Units to Linear Spacers

4.1 Introduction

The adsorption of benzene-1,3,5-tricarboxylic acid (TMA) has been extensively investigated by STM and shown to generate well-ordered 2D networks assembled by hydrogen bonding involving -COOH groups.[1a] Relatives of TMA, including isophthalic acid (benzene-1,3-dicarboxylic acid) and its derivatives, are also good candidates for producing 2D supramolecular nanopatterns on surfaces. For example, Heckl and co-workers have investigated the adsorption of isophthalic acid on graphite and found that it produces hydrogen-bonded zigzag chains with angles of 108°.[1b] This deviation from the ideal angle of 120°, which is set by the 1,3 positions of the carboxyl groups, is probably caused by interactions of the chains with their neighbors and with the substrate.

De Feyter and co-workers have investigated derivatives of isophthalic acid with long-chain alkyl substituents,[2] and these compounds have been revealed by STM to generate patterns at the liquid/graphite interface that can be controlled by varying the location and nature of the alkyl chains. Chiral derivatives of isophthalic acid have also been found to form chiral domains by coadsorption with achiral solvent molecules, such as 1-heptanol.[3] Similar STM observations of 2D chirality created by an achiral alkoxy-substituted isophthalic acid dissolved in 1-octanol or 1-undecanol have been made by Vanoppen *et al.*[4] Moreover, the adsorption of derivatives of isophthalic acid containing diyne units on the surface of graphite has been found to lead to polymerization under appropriate conditions, depending on intermolecular distance, irradiation with UV light, and stimulation by the STM tip.[5]

Most of the derivatives of isophthalic acid that have been investigated by STM have

had long-chain alkyl substituents, which can participate in van der Waals interactions that favor adsorption. As summarized in Chapter 3, we are interested in the possibility of achieving greater control over 2D assembly by using molecules in which the importance of diffuse adsorbate-surface interactions is reduced and the contribution of directional interadsorbate interactions is increased to ensure that the adsorbates are positioned predictably. The known behavior of TMA, isophthalic acid, and their derivatives suggested that it would be rewarding to examine the behavior of compounds in which multiple isophthalic acid units are connected to a central core. Such compounds would have multiple carboxyl groups and would therefore be expected to engage in the formation of extensively hydrogen-bonded networks, possibly leading to strong adsorption without the need to incorporate multiple alkyl chains.

In this chapter, we summarize our investigations of a series of well-designed tectons that are derived from isophthalic acid without long-chain alkyl substituents. The first molecule of this type that will be described is biphenyl-3,3',5,5'-tetracarboxylic acid (BTA), which incorporates two isophthalic acid groups that are coupled directly, without any intervening core or spacer. BTA is a known compound, and its crystallization from water has previously been shown to produce a 3D structure built from sheets.[6] Within a sheet, each molecule of BTA is linked to four neighbors by cyclic hydrogen-bonded pairs of -COOH groups (Figure 4.1a). In the 3D structure, tecton BTA resembles other biphenyls by adopting a non-planar conformation in which the torsional angle between the aryl rings is approximately 40°. For this reason, the hydrogen-bonded sheets are not planar but are instead corrugated and interpenetrating (Figure 4.1b). Nevertheless, the formation of sheets

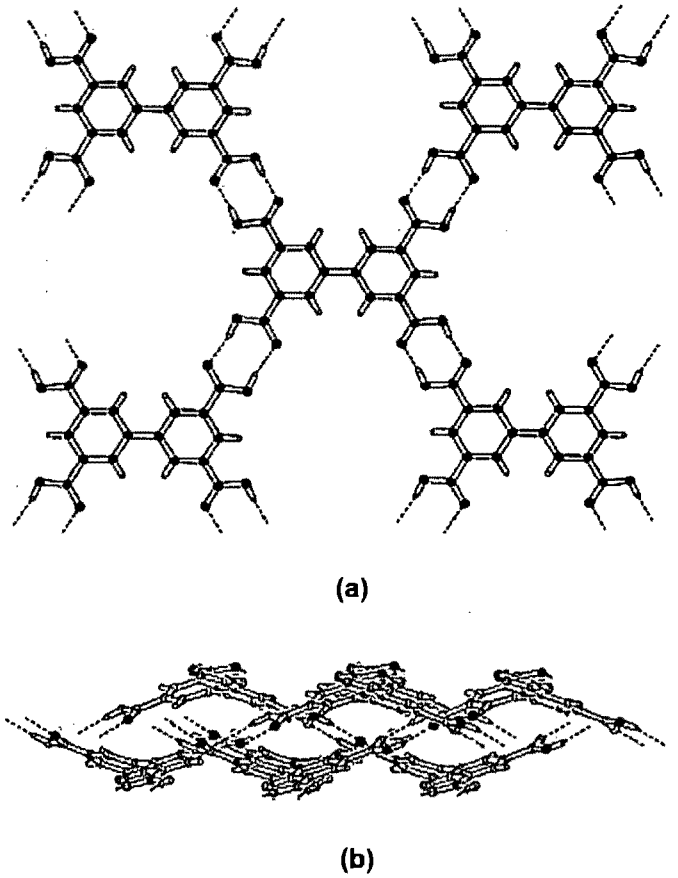

Figure 4.1 Views of the structure of crystals of benzene-3,3',5,5'-tetracarboxylic acid (BTA) grown from water. (a) View along the *a* axis showing a 2D hydrogen-bonded network. (b) View along the *c* axis showing interpenetrating corrugated sheets.[6]

indicates that BTA is a good candidate for producing well-organized nanopatterns on surfaces. As expected, STM images resulting from the adsorption of BTA on graphite have shown the formation of highly-ordered 2D arrays, which are discussed in detail below.

The related tectons illustrated in Scheme 4.1 are designed to have π-conjugated linear cores, such as those derived from 1,2-diphenylacetylene (**TA-5**) and 1,4-bis(phenylethynyl)benzene (**TA-6**). Such cores can easily be modified to create analogues containing other aromatic units, such as naphthalene (**TA-7**) and anthracene (**TA-8**). Systematic alteration of the molecular structures in such ways, including changing

Scheme 4.1 Molecular structures of tectons **TA-5**, **TA-6**, **TA-7**, and **TA-8.**

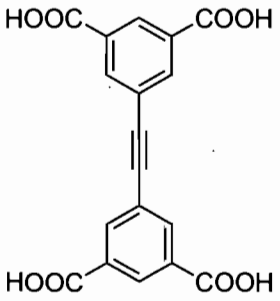

TA- 5

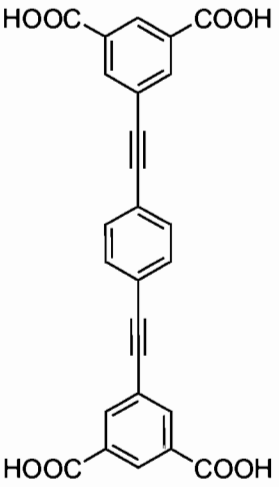

TA- 6

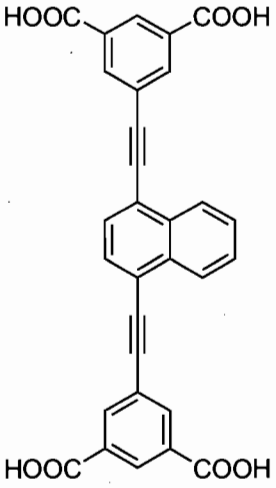

TA- 7

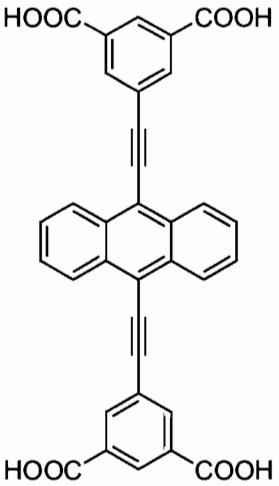

TA- 8

the molecular length and the core, is an important part of our effort to learn how to construct well-ordered 2D nanopatterns on surfaces. This approach allows us to vary the patterns systematically and to observe subtle changes in STM images that reveal more clearly how the molecules are organized.

4.2 Design and Synthesis of Tectons

4.2.1 Synthesis of Tecton TA-5

Tecton **TA-5** consists of two isophthalic acid units connected by an ethynyl spacer. Unlike BTA, in which two isophthalic acid units are coupled directly to produce a biphenyl, extended analogue **TA-5** can readily adopt a planar conformation. As a result, it was expected to yield 2D and 3D structures with features unlike those of BTA.

Compound **TA-5** is a simple molecule, and we were surprised to find that it had not previously been made. As shown in Scheme 4.2, it was synthesized in five steps by standard methods. Diazotization of commercially available 5-amino-1,3-benzenedicarboxylic acid and subsequent addition of iodide provided the known 5-iodo-1,3-benzenedicarboxylic acid (**16**)[7] in 73% yield, which was esterified to give the known diethyl 5-iodo-1,3-benzenedicarboxylate (**17**)[7] in 85% yield. Sonogashira coupling of intermediate **17** with (trimethylsilyl)acetylene in the presence of catalytic dichlorobis(triphenylphosphine)palladium(II) and copper(I) iodide, followed by the removal of trimethylsilyl groups, then gave diethyl 5-ethynylbenzene-1,3-dicarboxylate (**18**)[7] in 67% yield. Palladium-catalyzed coupling of intermediates **17** and **18** provided the tetraethyl ester of tecton **TA-5** in 82% yield. Because the adsorption of this tetraester and related compounds will be described later in the thesis, we have given it a special name (**TE-5**) to indicate that it belongs to a distinct family of compounds. Hydrolysis of the tetraester produced the target compound **TA-5** in 81% yield.[8]

Scheme 4.2 Synthesis of tecton **TA-5**.

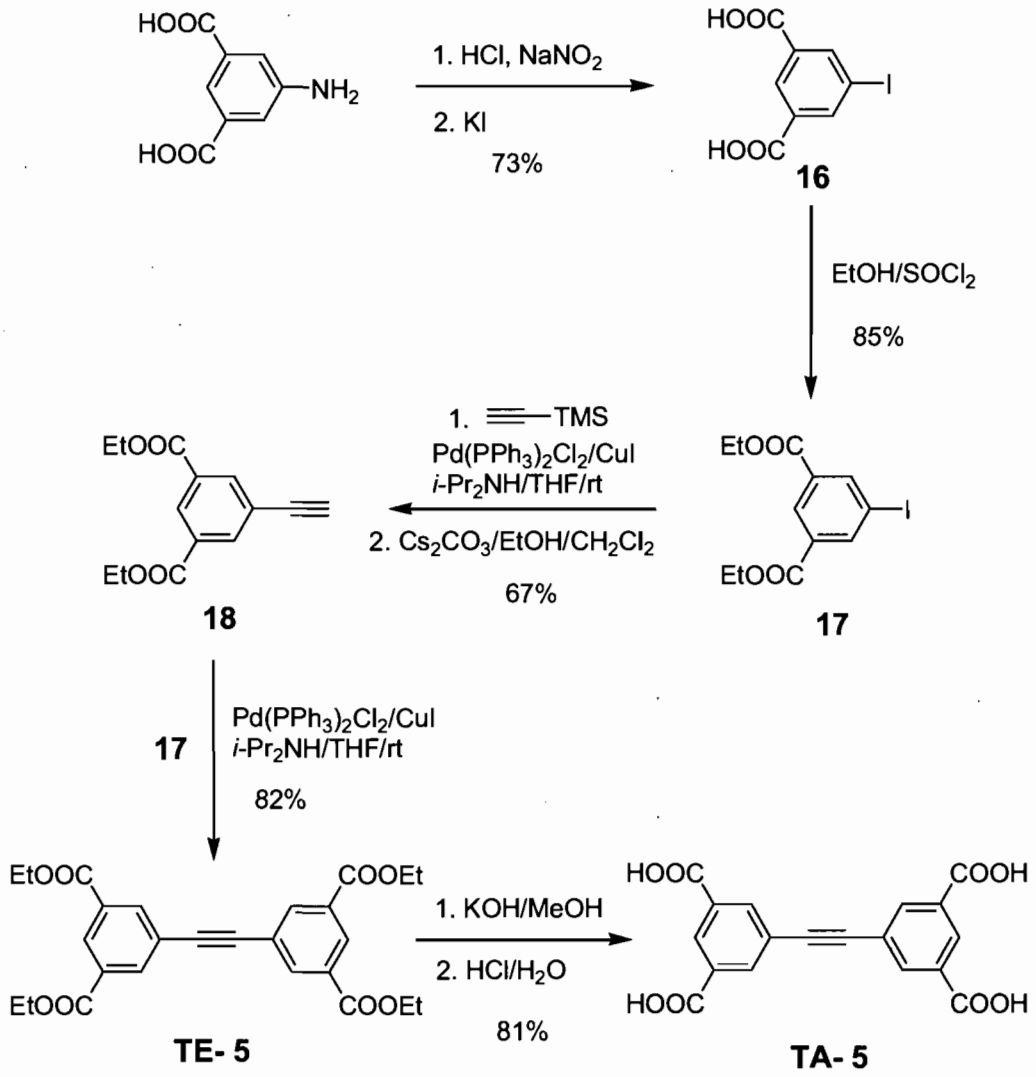

4.2.2 Synthesis of Tecton TA-6

Tecton **TA-5** was lengthened by replacing its core with 1,4-bis(2-phenylethynyl)benzene, giving tecton **TA-6** (Scheme 4.1). This compound was synthesized as shown in Scheme 4.3. Sonogashira coupling of commercial available 1,4-diethynylbenzene with diethyl 5-iodobenzene-1,3-dicarboxylate (**17**) in the presence of

catalytic dichlorobis(triphenylphosphine)palladium(II) and copper(I) iodide provided tetraester **TE-6** in 87% yield, which was then converted into the desired tecton **TA-6** in 78% yield by hydrolysis.[8]

Scheme 4.3 Synthesis of tecton **TA-6**.

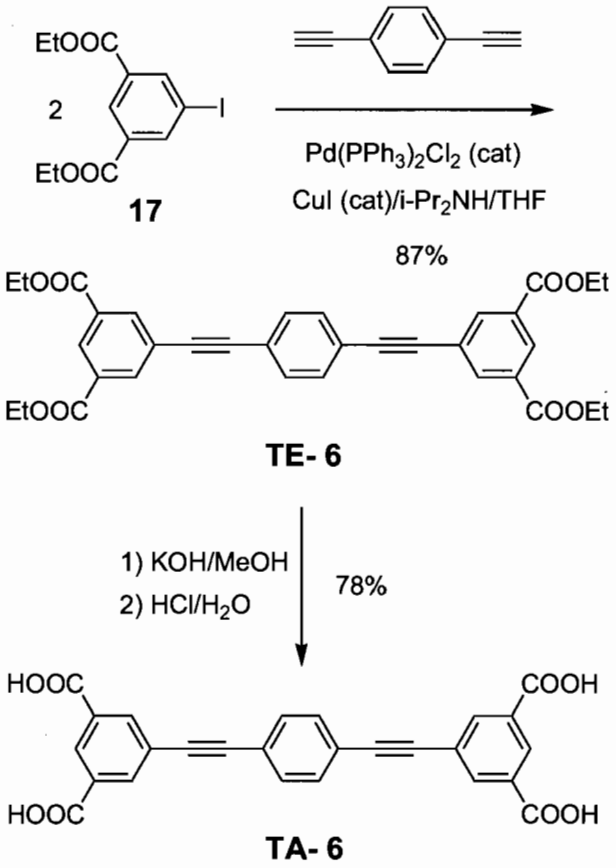

4.2.3 Synthesis of Tecton TA-7

Tecton **TA-7** (Scheme 4.1) was designed to probe the effect of replacing the benzene core of **TA-6** with naphthalene, which has greater affinity for the surface of graphite, arising from increased π-stacking interactions. This change, although subtle, was expected to alter the balance between interadsorbate interactions (hydrogen bonding of COOH

Scheme 4.4 Synthesis of tecton **TA-7**.

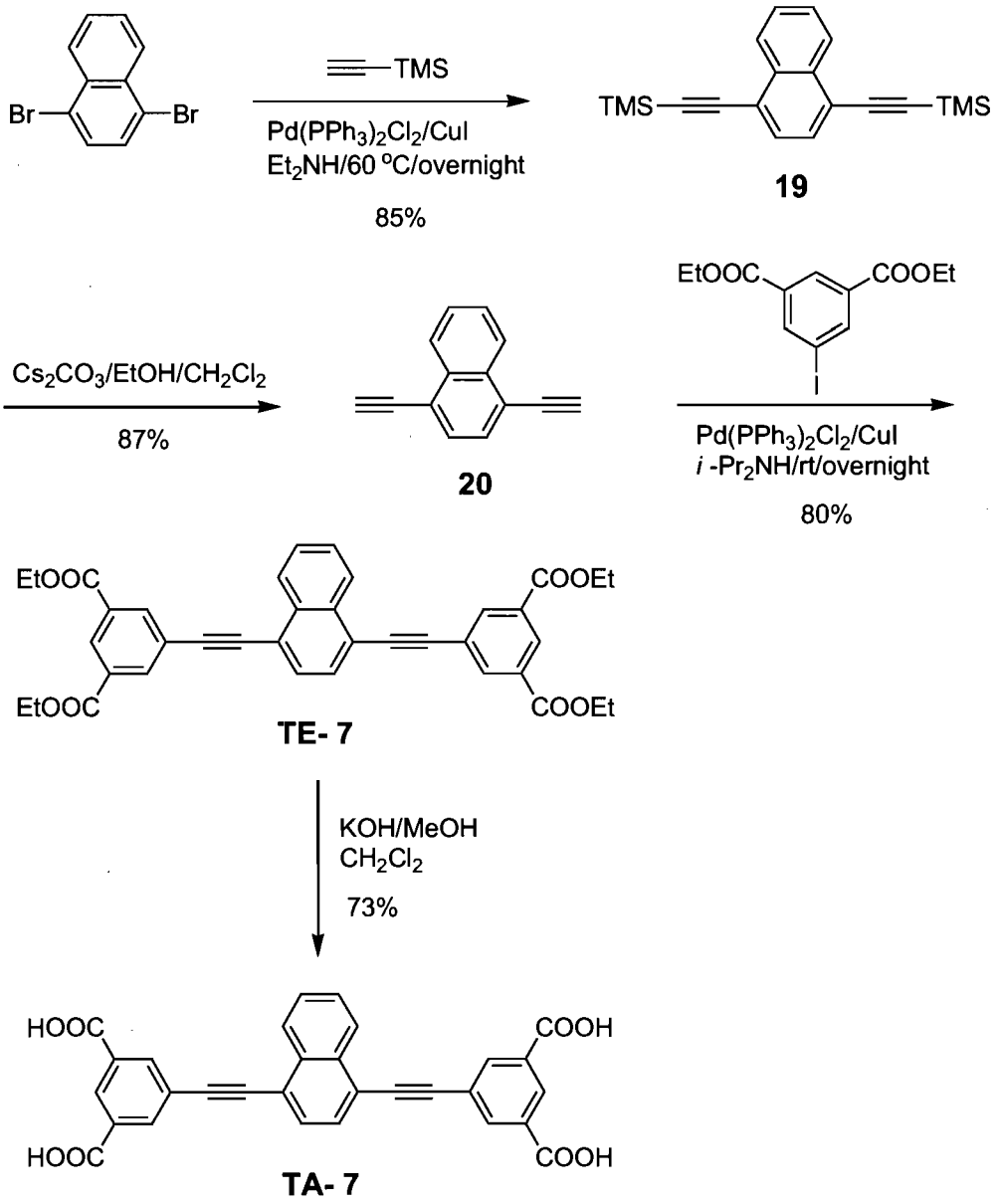

groups) and adsorbate-surface interactions, possibly inducing tecton **TA-7** to generate different 2D nanopatterns from those formed by analogue **TA-6**. Compound **TA-7** was synthesized in four steps as shown in Scheme 4.4. Sonogashira coupling of commercial available 1,4-dibromonaphthalene with (trimethylsilyl)acetylene in the presence of catalytic dichlorobis(triphenylphosphine)palladium(II) and copper(I) iodide provided

intermediate **19**[9] in 85% yield. Removal of the trimethysilyl groups then gave 1,4-diethynylnaphthalene (**20**)[9] in 87% yield. Palladium-catalyzed coupling of intermediate **20** with diethyl 5-iodo-1,3-benzenedicarboxylate (**17**) produced tecton **TE-7** in 80% yield. Subsequent hydrolysis provided the desired tecton **TA-7** in 73% yield.

4.2.4 Synthesis of Tecton TA-8

Tecton **TA-8** was derived from tecton **TA-7** by replacing the naphthalene core with anthracene, which has an even higher affinity for adsorption on the surface of graphite due to π-π stacking interactions. Compound **TA-8** was synthesized in four steps as shown in Scheme 4.5. Sonogashira coupling of commercially available 9,10-dibromoanthracene with (trimethylsilyl)acetylene in the presence of catalytic dichlorobis(triphenylphosphine)palladium(II) and copper(I) iodide produced the known intermediate **21**[9] in 76% yield, which was then deprotected to give 9,10-diethynylanthracene (**22**)[9] in 85% yield. Palladium-catalyzed coupling of intermediate **22** with diethyl 5-iodo-1,3-benzenedicarboxylate (**17**) produced tetraester **TE-8** in 88% yield, and subsequent hydrolysis afforded tecton **TA-8** in 70% yield.

Despite repeated efforts, we were unable to produce crystals of tectons **TA-5**, **TA-6**, **TA-7**, and **TA-8** that were suitable for structural analysis by X-ray diffraction. As a result, our evaluation of the self-association of these compounds is based on their patterns of adsorption, as determined by STM.

Scheme 4.5 Synthesis of tecton **TA-8**.

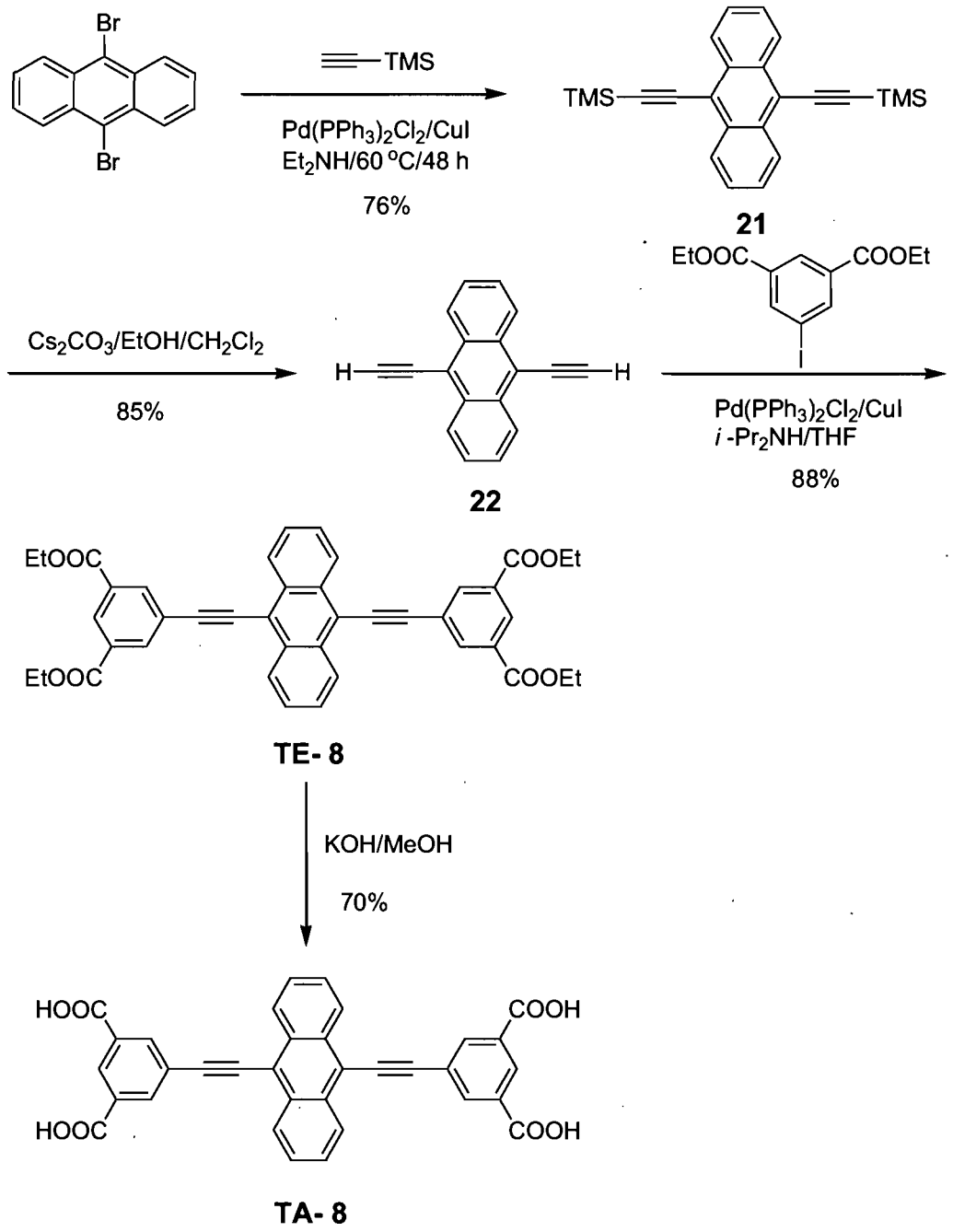

4.3 STM Investigation of the Adsorption of Tectons BTA, TA-5, TA-6, TA-7, and TA-8 on Graphite

4.3.1 2D Nanopatterns Formed by Tecton BTA[8]

The 2D self-association of biphenyl-3,3',5,5'-tetracarboxylic acid (BTA) was investigated by STM at the liquid/solid interface of heptanoic acid and HOPG. In a typical 2D crystallization, a droplet of a saturated solution of tecton BTA in heptanoic acid was placed on freshly cleaved graphite at room temperature, and the resulting physisorbed assembly was imaged by STM. STM images are provided in Figures 4.2, 4.3, and 4.4. Figure 4.2a shows well-ordered 2D nanopatterns composed of four domains (A-D) over a large area of 100 nm × 100 nm, and an isolated domain is shown in Figure 4.2b.

STM images with higher resolution display open parallel networks formed by tecton BTA (Figure 4.3). The bright protrusions represent the aromatic backbones, which have a higher tunnelling current due to their π-conjugated electron system. No adsorbed molecules of heptanoic acid could be resolved in these images.

A high-resolution STM image with superimposed CPK models (Figure 4.4a) reveals the formation of highly-ordered parallel networks, in which each tecton associates with four neighbors by the involvement of eight COOH groups in cyclic hydrogen-bonded pairs, with unit cell parameters $a = b = \sim 1.32$ nm and $\gamma = \sim 90°$. This interpretation is reinforced by the observation of homologous hydrogen-bonded sheets in the 3D crystal structure of BTA. In this structure, BTA resembles other biphenyls by adopting a nonplanar conformation, in which the torsional angle between the aryl rings is approximately 40°

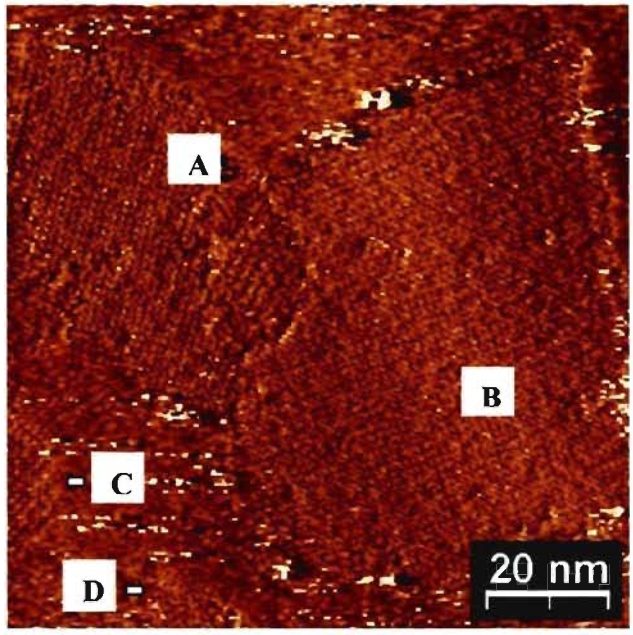

(a)

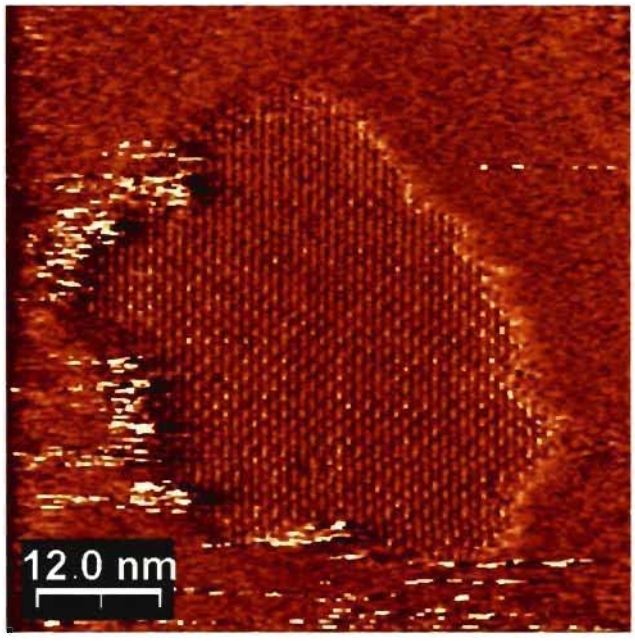

(b)

Figure 4.2 STM images of 2D nanopatterns created by the adsorption of tecton BTA on HOPG (deposition from heptanoic acid, with V_{bias} = -1.5 V, I_{set} = 100 pA). (a) Image showing four domains, labeled A-D, covering an area of 100 nm × 100 nm. (b) Image showing an isolated domain within an area of 60 nm × 60 nm.

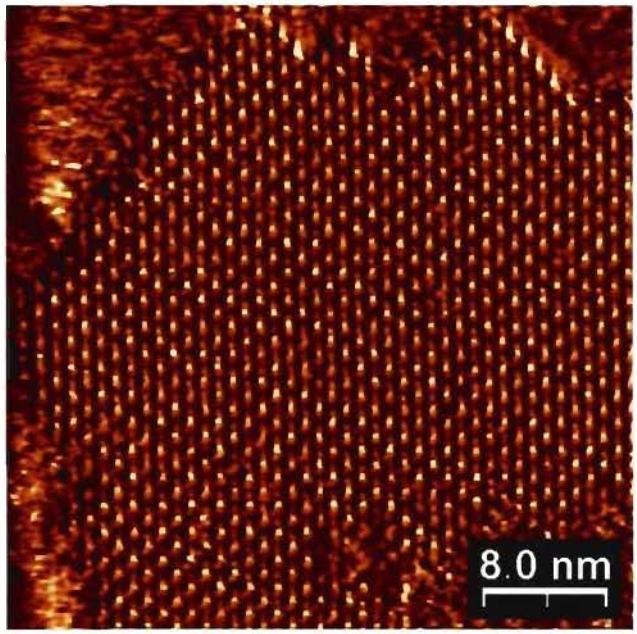

(a)

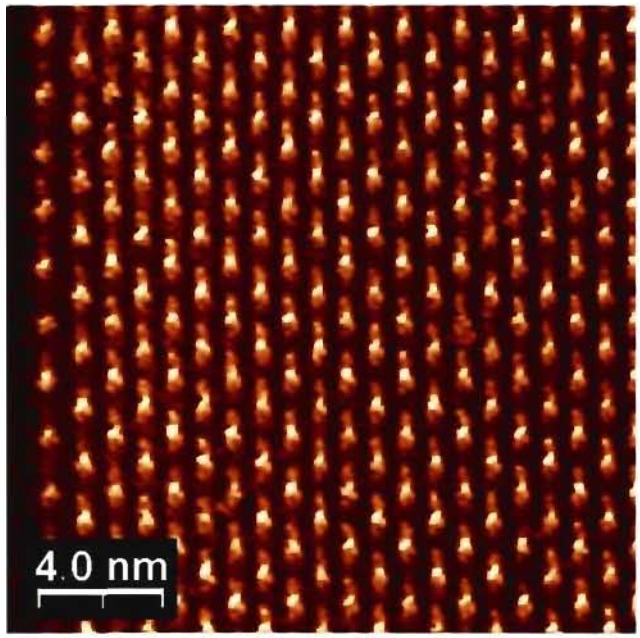

(b)

Figure 4.3 Higher-resolution STM images of 2D nanopatterns created by the adsorption of tecton BTA on HOPG showing open parallel networks (V_{bias} = -1.5 V, I_{set} = 100 pA). (a) Image covering an area of 40 nm × 40 nm. (b) Image covering an area of 20 nm × 20 nm.

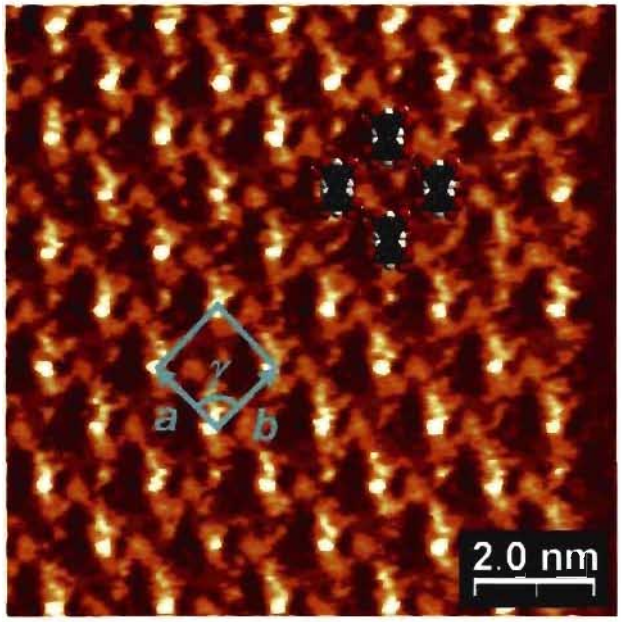

(a)

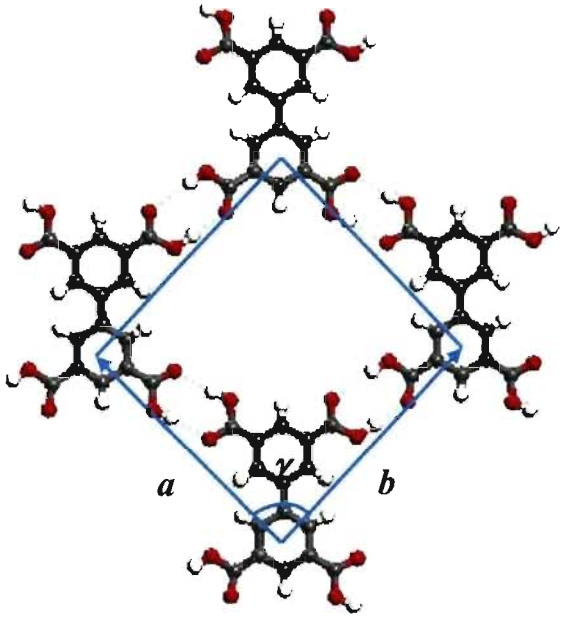

(b)

Figure 4.4 (a) Higher-resolution STM topograph showing the well-ordered parallel structure produced by depositing tecton BTA on HOPG, with superimposed space-filling models (V_{bias} = -1.5 V, I_{set} = 100 pA). (b) Tentative molecular model of the parallel structure, with unit cell highlighted in light blue.

(Figure 4.1). It is likely that adsorption on graphite reduces this angle, but it may not completely planarize BTA. Indeed, prominent differences of contrast within each molecule in the STM images may indicate that BTA also adopts a twisted conformation in its 2D crystals (Figure 4.4a). Despite a non-zero torsional angle between the phenyl rings of the core, the COOH groups can presumably retain an ability to form hydrogen-bonded pairs, although they may not be strictly coplanar and their strength may be reduced.

Recently published calculations[10] suggest that the adsorption of benzoic acids on graphite induces molecular deformations that bring the COOH group closer to the surface, thereby strengthening interactions between the COOH group and the surface while reducing π-π repulsion between the benzene ring and the surface. Such deformations make interadsorbate hydrogen bonding somewhat less strong, but it still makes an important contribution to the overall energy of the bound benzoic acid dimer. Clearly, however, conformational constraints prevent BTA from being an optimal adsorbate in which interadsorbate and adsorbate-surface interactions are optimized simultaneously. The proposed molecular model is shown in Figure 4.4b, with unit cell parameters $a = b = \sim 1.26$ nm and $\gamma = \sim 88°$, assuming O-H···O hydrogen bonding with an average H···O distance of 2.05 Å. The close similarity of the unit cell parameters estimated for the proposed model and those observed by STM provides strong support for the model.

4.3.2 2D Nanopatterns Formed by Tecton TA-6[8]

Before we present our STM study of the 2D crystallization of tecton **TA-5** on HOPG, we prefer to discuss the assembly of extended analogue **TA-6**, because the more

complicated 2D nanopatterns formed by tecton **TA-5** can be interpreted more clearly based on the assembled structures created by tecton **TA-6**.

Our STM investigation of tecton **TA-6** was performed under conditions similar to those used in the study of analogue BTA. Figure 4.5a shows an STM topograph of well-ordered arrays assembled by tecton **TA-6**. Each bright protrusion has an average size of 2.3 nm, which corresponds to the molecular length of compound **TA-6**. The bright contrast arises from the π-conjugated aromatic rings due to their higher electronic density of states. Figure 4.5b shows the arranged networks with submolecular resolution. Differences of contrast within each molecule indicate that the three benzene rings may not be exactly coplanar.

Figure 4.6a reveals a Kagomé network produced by tecton **TA-6,** with unit cell parameters $a = b = \sim 3.43$ nm and $\gamma = \sim 60°$. The superimposed CPK models highlight the structure of a cyclic hexamer, in which each tecton associates with four neighbors by forming eight hydrogen bonds involving COOH groups. The term Kagomé originates from a Japanese word referring to the particular pattern of holes in a traditional basket (Figure 4.6c). Among the great variety of crystal structures, Kagomé lattices are of particular interest due to their importance in the field of spin-frustrated magnetic materials.[11] Kagomé lattices have been the subject of many theoretical studies,[12-14] but there are few examples of molecular Kagomé lattices, and nanoscale versions have not been readily available to synthetic chemists until Zaworotko and co-workers built the first metal-organic Kagomé lattice,[15] with connected paramagnetic dicopper tetracarboxylate units derived from 1,3-benzenedicarboxylate. Recent examples of 2D Kagomé networks reported in the

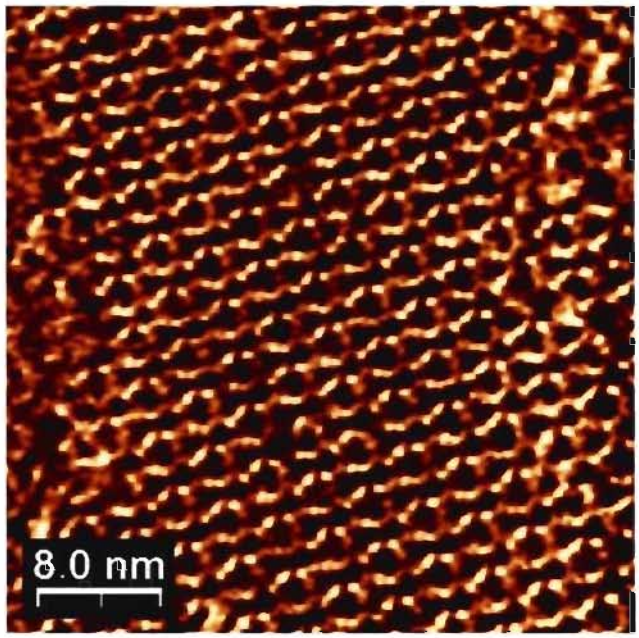

(a)

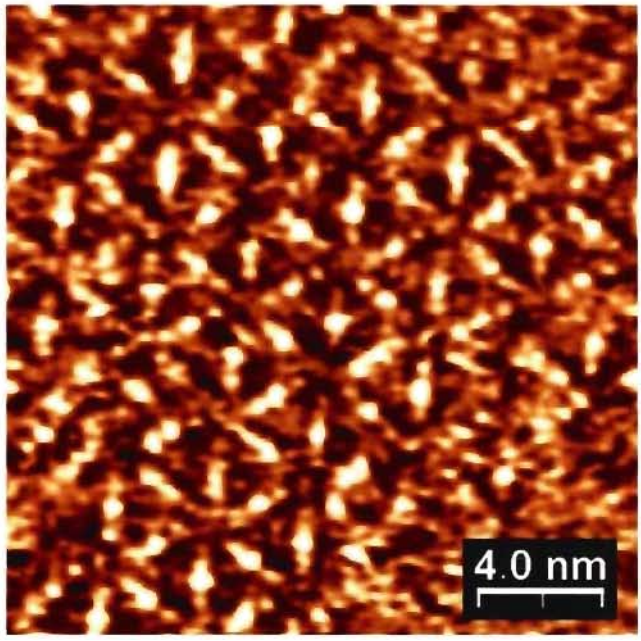

(b)

Figure 4.5 STM images of 2D nanopatterns formed by the adsorption of tecton **TA-6** on HOPG (deposition from heptanoic acid, with V_{bias} = -1.5 V, I_{set} = 100 pA). (a) Larger image showing well-ordered networks over an area of 40 nm × 40 nm. (b) Higher-resolution image showing bright protrusions which represent individual molecules.

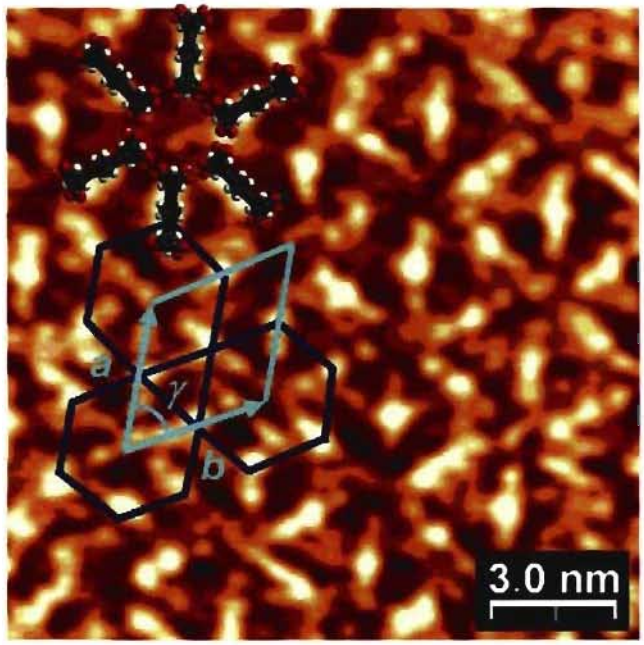

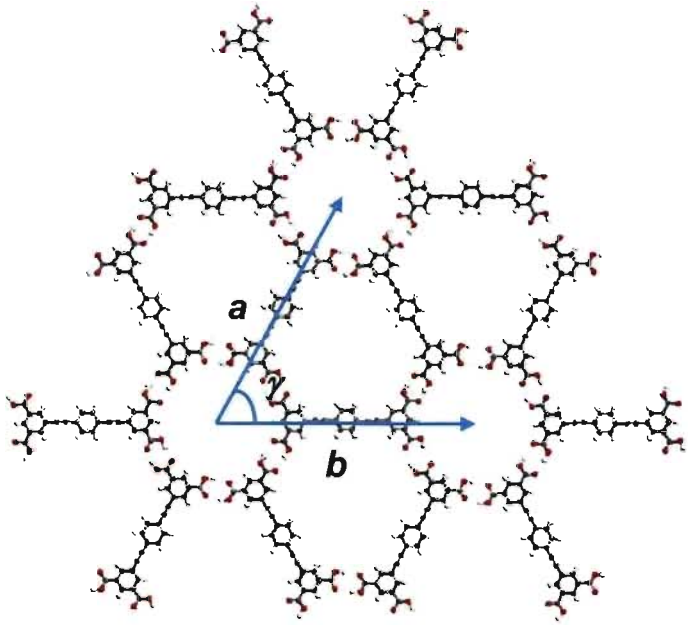

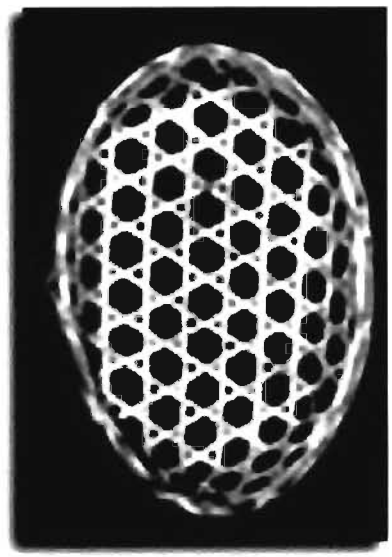

(b) (c)

Figure 4.6 (a) Higher-resolution STM image showing the Kagomé network created by tecton **TA-6**. The unit cell is highlighted in light blue, the Kagomé network is shown in dark blue, and molecular models are superimposed as an aid to visualization. (b) Tentative molecular models showing a cyclic hydrogen-bonded hexamer of tecton **TA-6**. The unit cell is highlighted in light blue. (c) An image of a Japanese Kagomé basket.

literature include those produced by thermal dehydrogenation of 4,9-diaminoperylenequinone-3,10-diimine (DPDI) on the surface of Cu(111),[16] alkyl-substituted dehydrobenzo[12]annulenes on graphite,[17] a linear aromatic tetracarboxylic acid directed by a coronene guest template,[18] linear aromatic dinitriles on graphite,[19] and oligonucleotides.[20]

The unit cell parameters corresponding to the molecular model in Figure 4.6b are calculated to be $a = b = \sim 3.38$ nm and $\gamma = \sim 60°$, assuming O-H···O hydrogen bonding with an average H···O distance of 2.05 Å. These data closely match the observed parameters. Clearly, the Kagomé network is optimal for following the three-fold symmetry of the underlying graphite to maximize adsorbate-substrate interactions, even though this may not be necessary due to the strong interadsorbate hydrogen bonding interactions. We suggest that the central benzene ring of tecton **TA-6** is parallel to the surface and that the other two benzene rings might be slightly tilted. This suggestion is based on the observation that the tunneling current of the central benzene ring is stronger than that of the other two benzene rings, thus leading to a brighter contrast at the centers of the molecules appearing in STM images in Figures 4.5b and 4.6a.

Unlike tecton BTA, which forms a parallel hydrogen-bonded structure when adsorbed on HOPG, analogue **TA-6** favors a Kagomé motif. This surprising difference in selectivity cannot be explained by differences in the density of packing (~ 0.29 molecules/nm^2 in both cases) or in the number of hydrogen bonds formed per tecton (8 in both cases), which are identical for both parallel and Kagomé motifs. Instead, the preferences must arise from small variations in the strengths of the hydrogen bonds between the adsorbates (see the

results of DFT calculations in Chapter 4.4), or from other subtle effects related to solvation or interactions of the adsorbates with each other and with the underlying surface.

4.3.3 2D Nanopatterns Formed by Tecton TA-5[8]

To help explain the prominent differences in the 2D nanopatterns formed by the structurally related tectons BTA and **TA-6,** we were eager to investigate the behavior of analogue **TA-5,** which has a molecular structure very similar to those of tectons BTA and **TA-6**, but its molecular length is intermediate. Initially, we expected the 2D nanopatterns built from **TA-5** to resemble those formed either by tectons BTA or **TA-6**.

An STM investigation of tecton **TA-5** was performed under conditions similar to those used in the study of analogues BTA and **TA-6.** Unexpectedly, the adsorption of tecton **TA-5** on HOPG generated a nanopattern strikingly unlike those produced by analogues **TA-6** and BTA (Figure 4.7). In the new pattern, individual molecules were again well resolved, presumably in part because they are held in place by multiple hydrogen bonds. Motifs characteristic of the parallel network (in yellow and light blue) and the Kagomé network (in green) can be clearly discerned in small areas of local order; however, large-scale periodicity apparently cannot be attained, possibly because the two motifs are closely matched in energy and can merge smoothly.

A higher-resolution image in Figure 4.8a shows again that large-scale ordered networks are unable to be achieved, with different structures highlighted in green (A) and blue (B), respectively. Figure 4.8b shows an enlarged image of area A with superimposed CPK models, which represent the parallel network. The models in Figure 4.8c, which

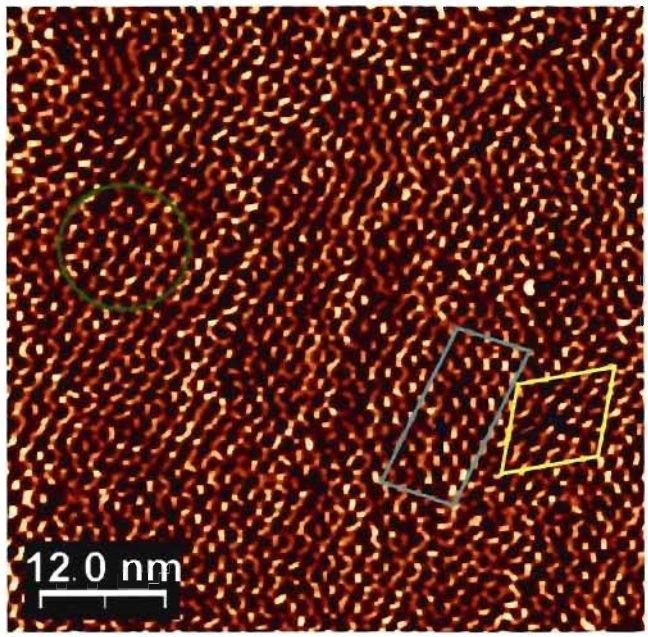

Figure 4.7 STM topograph of 2D nanopatterns formed by depositing tecton **TA-5** on HOPG in heptanoic acid (V_{bias} = -1.5 V, I_{set} = 50 pA). The image shows a structure with local order but no large-scale periodicity. Two small areas ordered according to the parallel network are highlighted in yellow and light blue, with blue arrows indicating the different directions of alignment. Another small area ordered according to the Kagomé network is highlighted in green.

corresponds to an enlarged image of area B, represent a hybrid structure composed of the two motifs (the parallel network and the Kagomé network), which can be seen to merge into each other smoothly without showing discontinuity. Despite the lack of long-range order the assembly shows a high degree of local order, and most molecules have specific orientations relative to their neighbors, resulting from the formation of hydrogen bonds according to the parallel structure and the Kagomé network. In a very recent publication,[21] the adsorption of *p*-terphenyl-3,5,3',5'-tetracarboxylic acid on graphite was reported to produce a similar random network that exhibits orientational symmetry but no translational order.

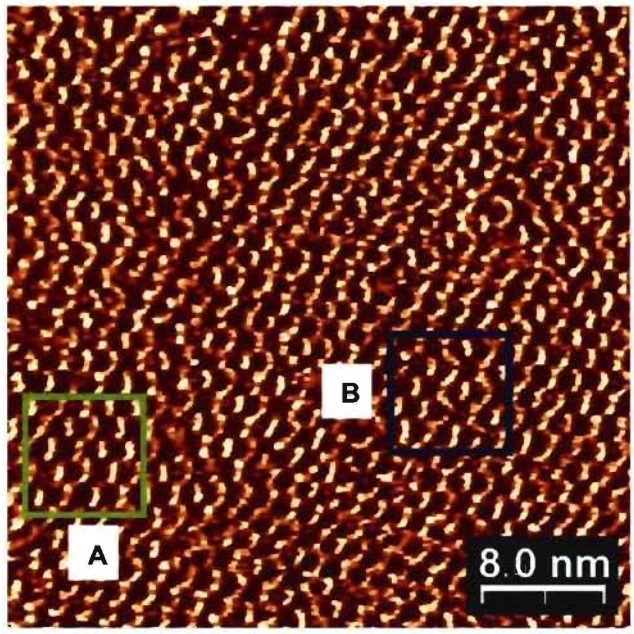

(a)

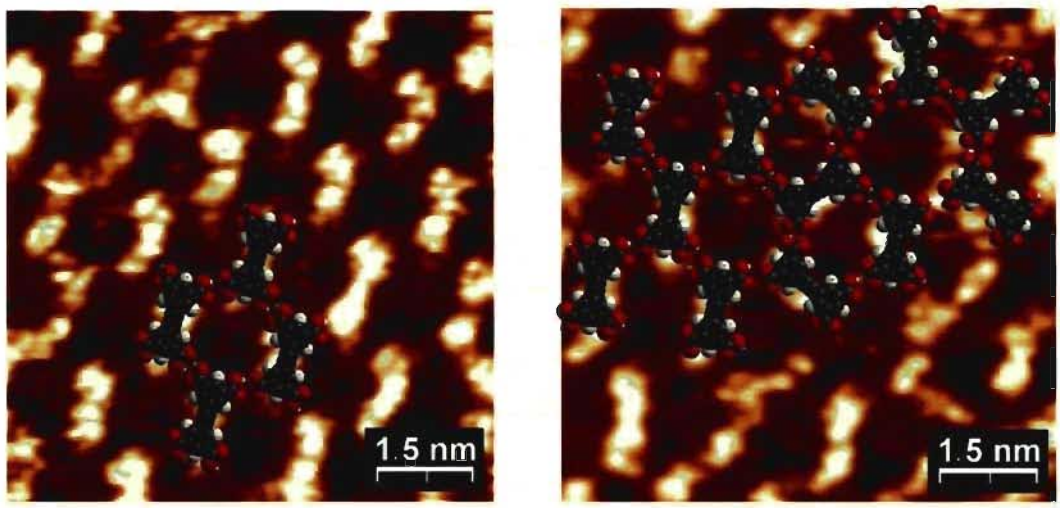

(b) (c)

Figure 4.8 (a) STM image of the assembly produced by the adsorption of tecton **TA-5**. (b and c) Higher-resolution images of the areas in Figure 4.8a highlighted in green and blue, respectively, with superimposed models. These images show regions of local order according to the parallel network and the Kagomé network, as well as the smooth transition between them.

In an earlier publication on 3D molecular glasses,[22] we concluded that directional molecular contacts can help maintain a degree of local order, but these interactions are sometimes detrimental to the creation of large-scale periodic order. Similarly, we suggest that Figure 4.8a provides a submolecularly resolved image of the organization of a 2D molecular glass. It is possible to imagine an alternative aperiodic arrangement in which the molecular components do not have preferred orientations with respect to their immediate neighbors. In this way, Figure 4.8a illustrates in 2D the possibility of polyamorphism, in which a single molecular material can exist as distinctly different amorphous phases.[23] The frustrated crystallization of tecton **TA-5** suggests that the 2D co-crystallization of mixtures of tectons **TA-6**, **TA-5**, and BTA will also prove to be difficult. This subject is discussed in greater detail in Section 4.5.

4.3.4 2D Nanopatterns Formed by Tecton TA-7

From the studies summarized above, we have learned that the series of analogues BTA, **TA-5**, and **TA-6** all have a prominent tendency to adsorb on HOPG to form hydrogen-bonded sheets. All three compounds are tetracarboxylic acids constructed by grafting two isophthalic acid groups to conjugated cores of variable length that can adopt planar or nearly planar conformations. As planned, analogues BTA and **TA-6** generate either a parallel network or a Kagomé network, respectively. Similarly, tecton **TA-5** produces a confused hybrid structure in which motifs are present. To further investigate the effects of the core on 2D molecular assembly on the surface of HOPG, we decided to examine the behavior of tecton **TA-7**, an analogue of tecton **TA-6** in which two isophthalic

acid groups are attached to a core containing a naphthalene ring in place of a benzene ring.

The adsorption of tecton **TA-7** on HOPG was investigated by STM under our standard conditions. The STM image in Figure 4.9a shows well-ordered monolayers with two domains over an area of 60 nm × 60 nm. Figure 4.9b shows a higher-resolution image of tecton **TA-7**, with superimposed CPK models representing the parallel network. The unit cell parameters are $a = b = \sim 2.21$ nm and $\gamma = \sim 53°$. In the parallel network, we believe that the naphthyl groups of neighboring tectons can have various relative orientations, so the specific models in Figure 4.9b should not be interpreted literally. Each tecton associates with four neighbors by forming a total of eight hydrogen bonds involving pairs of COOH groups. However, tecton **TA-7** does not form only parallel networks. In small areas, it was also found to produce a Kagomé network, with unit cell parameters $a = b = \sim 3.45$ nm and $\gamma = \sim 60°$ (Figure 4.10). Again, the superimposed models in Figure 4.10 suggest that the naphthalene core has no preferential orientation with respect to the surface.

Although naphthalene-substituted tecton **TA-7** was able to produce both the parallel network and the Kagomé network in separate areas on HOPG, the parallel network appeared to be dominant and covered a larger area. Despite having closely similar structures, tectons **TA-5**, **TA-6**, and **TA-7** are adsorbed on HOPG in distinctly different ways under essentially identical conditions. Analogue **TA-5** was shown to generate frustrated 2D nanopatterns in which elements of both the parallel network and Kagomé networks are present, but neither can be sustained to produce significant domains. In contrast, naphthalene-substituted extended tecton **TA-7** proved to yield both motifs, and the phenyl-substituted extended analogue **TA-6** was found to form only the Kagomé network.

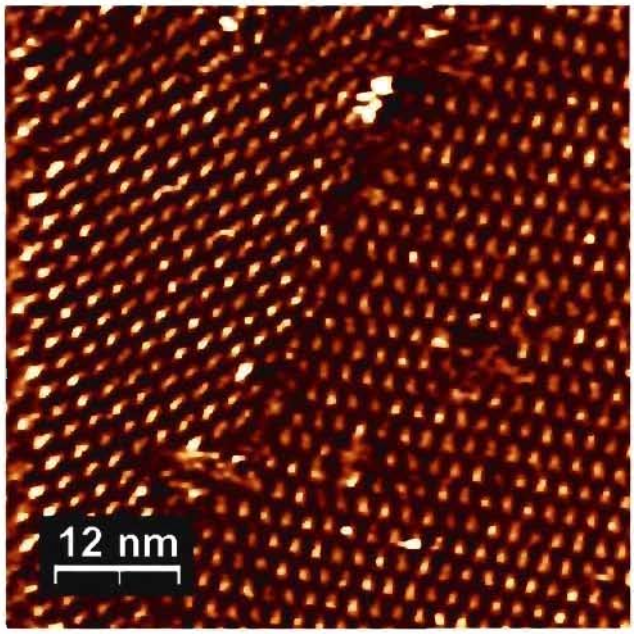

(a)

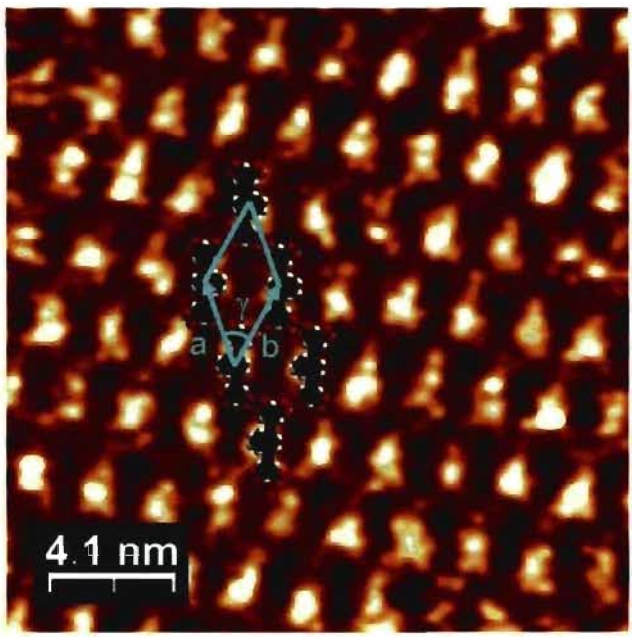

(b)

Figure 4.9 STM images of 2D nanopatterns created by the adsorption of tecton **TA-7** on HOPG (deposition from heptanoic acid, with V_{bias} = -1.5 V, I_{set} = 50 pA). (a) Image showing well-ordered monolayers with two domains. (b) Higher-resolution image showing a parallel network, with superimposed CPK models. The unit cell is highlighted in light blue.

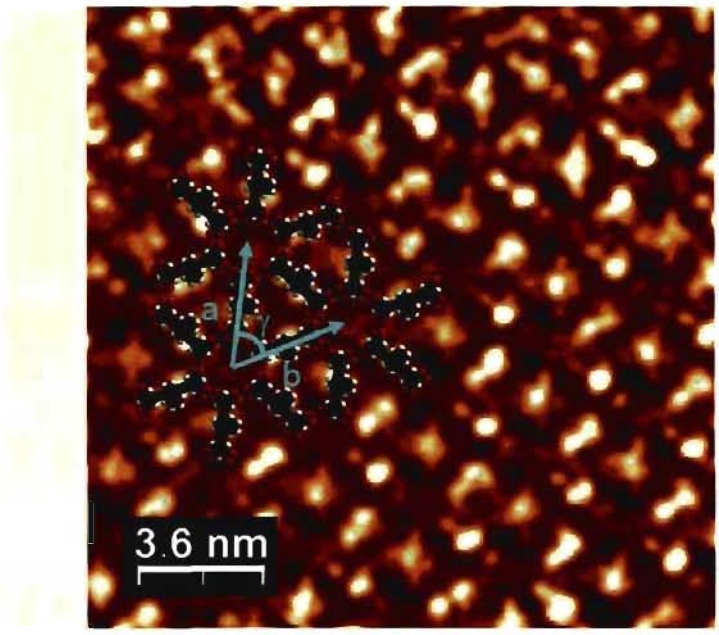

Figure 4.10 STM image of a Kagomé network formed by tecton **TA-7**, with superimposed space-filling models (heptanoic acid, V_{bias} = -1.5 V, I_{set} = 50 pA). The unit cell is highlighted in light blue.

The origin of these subtle differences is not clear, and the two observed networks cannot be distinguished on the basis of the density of packing and the number of hydrogen bonds per molecule, which are the same in both cases. We suggest that the motif ultimately formed is determined by a combination of effects, including the strength of the intermolecular interactions, the adsorbate-substrate interactions, and the possible role of co-adsorbed heptanoic acid. In particular, we note that in the case of the parallel network, all molecules are aligned along the long molecular axes. In contrast, molecules need to be arranged with three-fold symmetry in the Kagomé network, which may better match the symmetry of the underlying HOPG and lead to a commensurate relationship between the structure of the adsorbate and the structure of graphite. Deeper insights into the origin of the observed

preferences are provided below, in a discussion of a computational study of adsorption of a model graphene surface.

4.3.5 2D Nanopatterns Formed by Tecton TA-8

To provide further understanding of the baffling preferences of tectons **TA-5**, **TA-6**, and **TA-7**, and to probe the effect of their cores on the 2D nanopatterns formed, we elected to investigate analogue **TA-8,** which has a core derived from anthracene.

An STM investigation was performed under conditions similar to those used to study all the analogues discussed previously. The image in Figure 4.11a shows that 2D assembly of tecton **TA-8** produces well-ordered networks over a large area of 80 nm × 80 nm. Figure 4.11b shows a higher-resolution image with occasional defects. Figure 4.12a shows an enlarged image of the area highlighted in green in Figure 4.11b, with unit cell parameters $a = b = \sim 2.05$ nm and $\gamma = \sim 55°$. Figure 4.12b shows superimposed CPK models, which confirm that a parallel network is favored.

During the imaging, no Kagomé network was observed from analogue **TA-8**. Closely similar tecton **TA-7** forms primarily a parallel network with small regions of Kagomé network, and both motifs were found to coexist for extended periods. In contrast, anthracene analogue **TA-8** produces only the parallel network. Table 4.1 summarizes the 2D networks created by each tecton and reveals some interesting features: 1) Tectons BTA, **TA-5**, **TA-6**, **TA-7**, and **TA-8** all form either the parallel network or the Kagomé network, as programmed by their characteristic linear geometry and properly directed COOH groups; 2) increasing molecular length favors a change from parallel to Kagomé, as shown by the

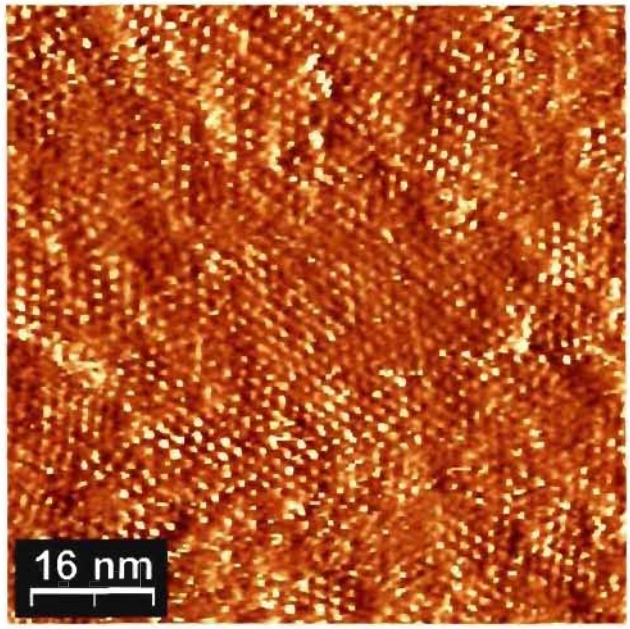

(a)

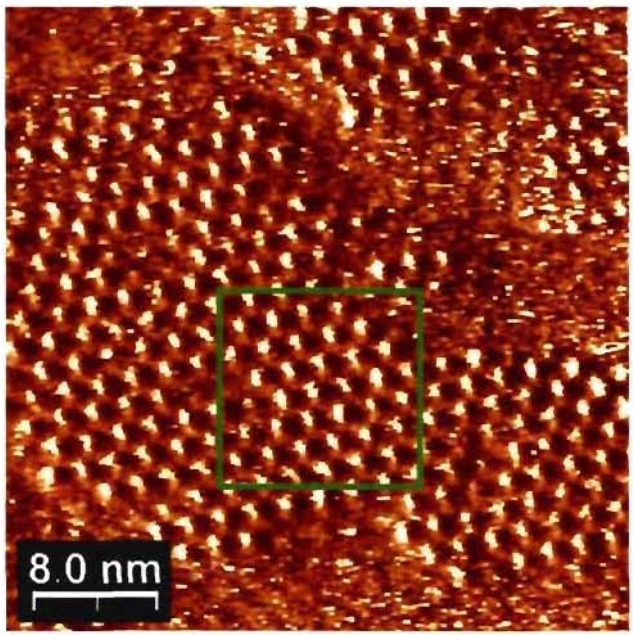

(b)

Figure 4.11 STM images showing 2D nanopatterns created by the adsorption of tecton **TA-8** on HOPG (deposition from heptanoic acid, with V_{bias} = -1.5 V, I_{set} = 50 pA). (a) Image showing well-ordered networks over an area of 80 nm × 80 nm. (b) Higher-resolution image with an ordered area highlighted in green.

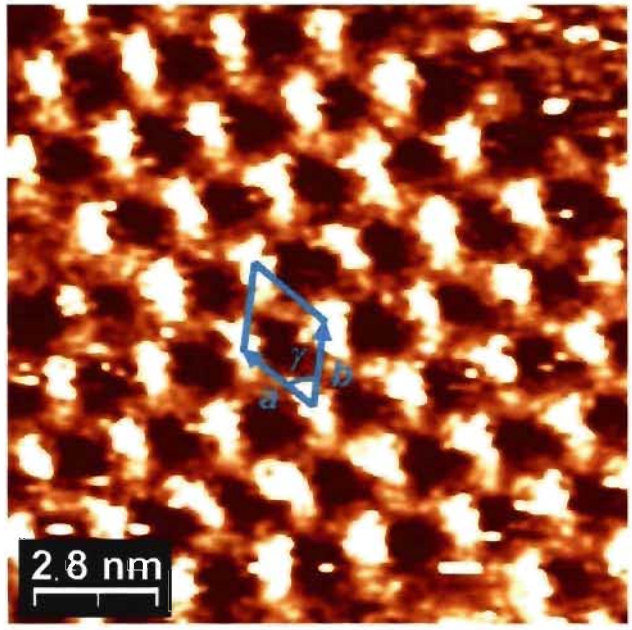

(a)

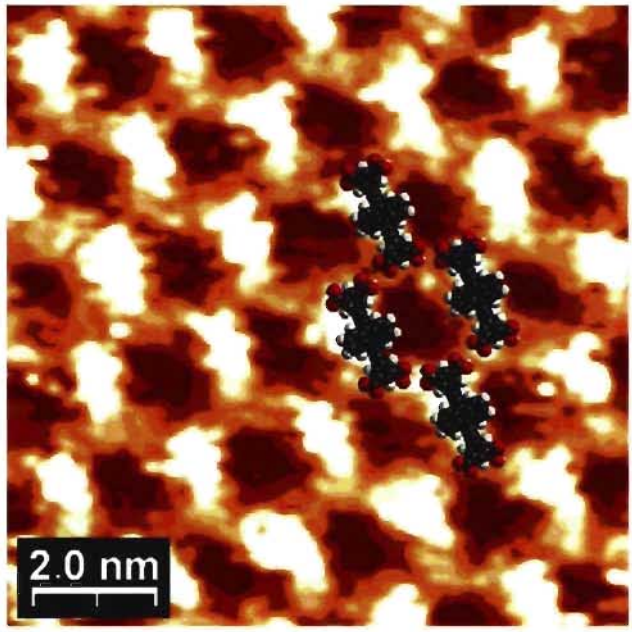

(b)

Figure 4.12 Higher-resolution STM images of the 2D assembly of tecton **TA-8** on HOPG. (a) Enlarged image of the area highlighted in green in Figure 4.11b, with a unit cell highlighted in light blue. (b) Superimposed CPK models showing the hydrogen-bonded parallel network.

Table 4.1 2D networks formed by tectons constructed by coupling two isophthalic acid units directly (BTA) or by connecting them to linear spacers, including ethyne (**TA-5**), 1,4-diethynylbenzene (**TA-6**), 1,4-diethynylnaphthalene (**TA-7**), and 9,10-diethynylanthracene (**TA-8**).

Tecton / Motif	BTA	TA-5	TA-6	TA-7	TA-8
Parallel	yes	yes	no	yes	yes
Kagomé	no	yes	yes	yes	no

series BTA (no spacer between the isophthalic acid units), **TA-5** (ethynyl spacer), and **TA-6** (diethynylphenyl spacer); and 3) increasing the size of the molecular core favors a change from Kagomé to parallel, as shown by the series **TA-6** (diethynylphenyl spacer), **TA-7** (diethylnaphthyl spacer), and **TA-8** (diethynylanthracenyl spacer). In each series, tectons **TA-5** and **TA-7** can be considered to be points where the factors favoring Kagomé and parallel networks are closely balanced. Based on the results of DFT calculations summarized below, we suggest that the observed preferences result in part from subtle differences in hydrogen bonding.[24]

4.4 DFT Calculations[8]

To help rationalize why the adsorption of these tectons on HOPG results in the selective formation of 2D nanopatterns, we carried out quantum chemical density functional theory (DFT) calculations using the NWChem software package.[25, 26] We used the 6-31G* basis set for hydrogen atoms and for oxygen atoms and an STO-3G basis set for carbon atoms in conjunction with the B3LYP functional. The use of the B3LYP

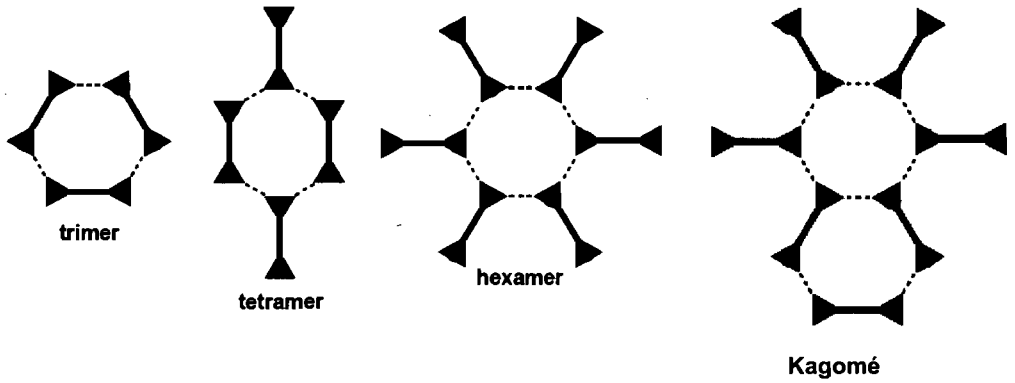

Figure 4.13 Schematic representation of molecular models.

Table 4.2 Calculated gas-phase stabilization energies (kcal/mol) per hydrogen bond for trimeric, tetrameric, and hexameric aggregates of tectons BTA, **TA-5** and **TA-6** as models of parallel and Kagomé networks.

Tecton	Δ E (trimer)	Δ E (tetramer)	Δ E (hexamer)	Δ E (Kagomé)[a]
BTA	9.86	10.75	9.74	9.80
TA-5	10.05	10.03	10.00	10.03
TA-6	9.89	9.43	9.81	9.85

[a]Average of Δ E (trimer) and Δ E (hexamer)

functional is motivated by its good performance in describing both intra- and intermolecular hydrogen bonds that occur in molecular structures.[27, 28] Structures were fully optimized without symmetry constraints using the quasi-Newton method until a gradient convergence factor better than 10^{-5} Hartree/Bohr was reached. The gas-phase stabilization energies reported in Table 4.2 were computed for the four distinct aggregates represented in Figure 4.13 (trimer, tetramer, hexamer, and Kagomé), using the relation $\Delta E = -[E_T(\text{complex})-x*E_T(\text{molecule})]/2x$, where E_T is the total DFT/B3LYP energy and x is the number of molecules in the aggregate. The tetrameric aggregate corresponds to the

parallel network, and the hexameric and trimeric aggregates appear in equal number in the Kagomé network. The calculated stabilization energies were normalized by reporting them per hydrogen bond formed. However, it is important to note that sources of differences in energy other than hydrogen bonding may also contribute to the overall stabilization. Such sources may include π-electron delocalization or structural deformations associated with formation of the networks.

DFT/B3LYP calculations have suggested that the contrasting preferences of tectons BTA and **TA-6** for parallel (tetramer) and Kagomé networks result in part from subtle differences in hydrogen bonding (Table 4.2). For short tecton BTA, the cyclic tetramer that generates a parallel network is estimated to be 0.95 kcal/mol more stable per hydrogen bond than the Kagomé alternative; in contrast, elongated analogue **TA-6** is estimated to favor the Kagomé structure by 0.42 kcal/mol. For intermediate compound **TA-5**, however, the two possible networks are predicted to have virtually identical energies.

4.5 Frustrated 2D Molecular Crystallization[8]

The frustrated 2D crystallization of tecton **TA-5** suggested that its cocrystallization with analogues BTA and **TA-6** might also prove to be difficult. Deposition of a 1:1 mixture of tectons **TA-5** and **TA-6** on HOPG under our standard conditions failed to yield large periodic domains, as determined by STM (Figure 4.14a). Again, the images showed clearly resolved molecules oriented locally according to the parallel and Kagomé motifs; however, sustained growth of single crystalline phases was not observed, despite the well-established tendency of extended tecton **TA-6** to produce Kagomé networks on its own. We attribute

the frustrated crystallization to a combination of two synergistic effects: (1) the feasibility of making a smooth transition from the parallel motif to the Kagomé motif without introducing defects and (2) the structural similarity of tectons **TA-5** and **TA-6**, which allows them to be interchanged without completely interrupting the growth of an extensively hydrogen-bonded network.

Deposition of a 1:4 mixture of tectons **TA-5** and **TA-6** on HOPG produced images showing similar hybrid structures involving both tectons engaged in the formation of parallel and Kagomé motifs (Figure 4.14b). Further experiments revealed that the 2D crystallization of tecton **TA-6**, which normally yields the Kagomé network, can be thwarted by the addition of less than 15% of compound **TA-5** (Figure 4.15a). Similar frustrated structures have also been achieved by changing the ratio of the mixture of **TA-5** and **TA-6** to 7:1 (Figure 4.15b).

Whenever less than 85% of **TA-6** is present in the mixed solution, all the STM images show the following characteristic features: (1) the lack of large-scale periodicity; (2) the mixed presence of both tectons **TA-5** and **TA-6**; (3) regions of local order according to the parallel and Kagomé motifs; and (4) smooth switching between these motifs.

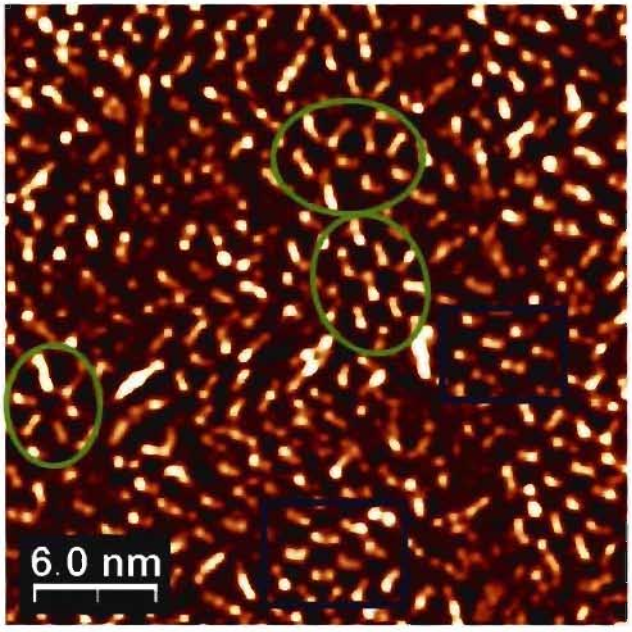

(a)

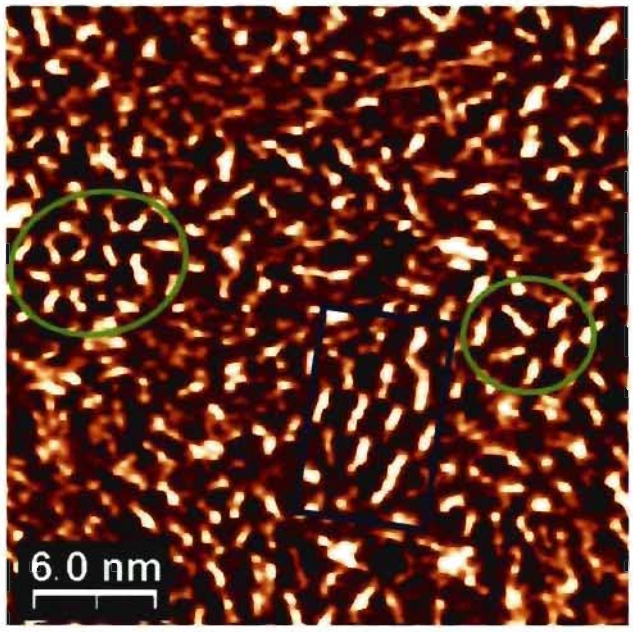

(b)

Figure 4.14 STM images of the assemblies produced by the co-adsorption of mixtures of tectons **TA-5** and **TA-6** (deposition from heptanoic acid, with V_{bias} = -1.5 V, I_{set} = 50 pA). (a) Co-adsorption of a 1:1 mixture. (b) Co-adsorption of a 1:4 mixture.

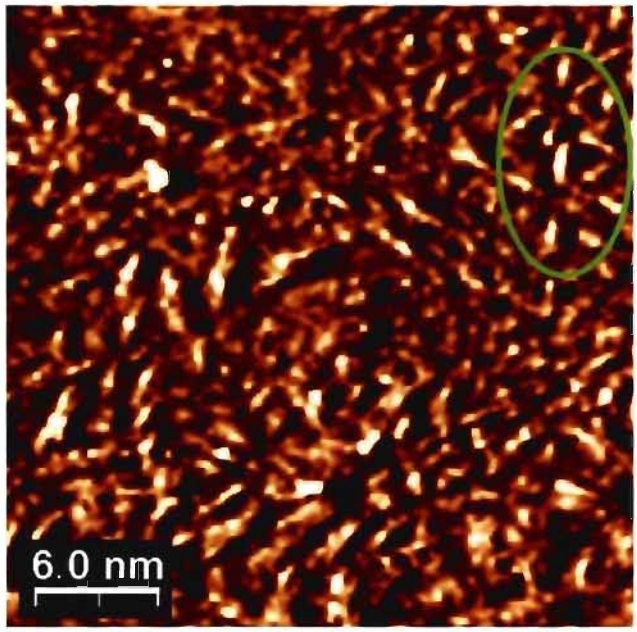

(a)

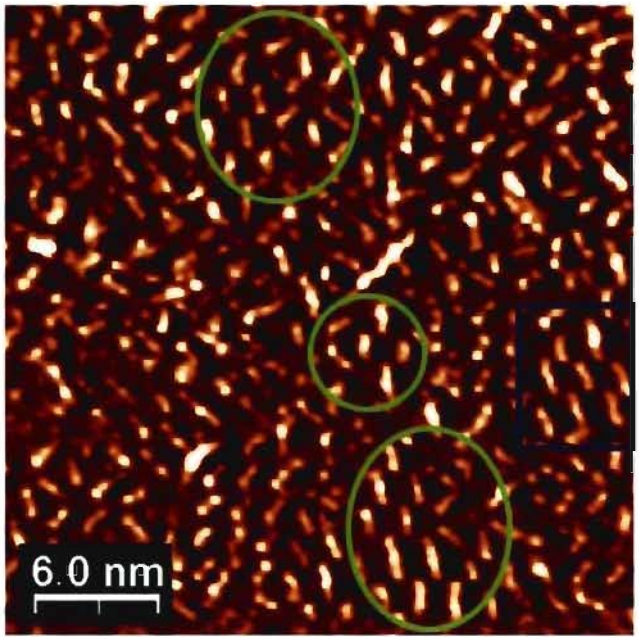

(b)

Figure 4.15 STM images of 2D nanopatterns produced by the co-adsorption of mixtures of tectons **TA-5** and **TA-6** (deposition from heptanoic acid, with V_{bias} = -1.5 V, I_{set} = 50 pA). (a) Co-adsorption of a 1:7 mixture. (b) Co-adsorption of a 7:1 mixture.

4.6 Summary

In this chapter, we have presented a series of studies of five related tectons designed to produce hydrogen-bonded 2D nanopatterns by adsorption on HOPG. The five compounds have various structural features in common. In particular, all have two isophthalic acid units coupled directly together (BTA) or grafted to linear spacers consisting of an ethynyl unit (**TA-5**) or diethynylaryl units (**TA-6**, **TA-7**, and **TA-8**). In this way, all five compounds can be considered to have a long, nearly flat molecular axis to which are attached four COOH groups, each held in an orientation designed to favor hydrogen bonding in a direction lying at an angle of 120° with respect to the principal molecular axis. As shown above, this well-defined geometry, combined with the presence of four properly oriented sticky sites, was expected to induce the formation of 2D hydrogen-bonded networks with only two possible architectures, the parallel or Kagomé structures. At the same time, systematic structural alterations within the family of five tectons allowed us to probe the effects of changing the molecular length and size of the core. In this way, we expected to be able to make fine adjustments of the geometries of the parallel and Kagomé networks, thereby bringing us closer to the goal of controlling 2D crystallization and surface assembly in a predictable way.

Many of these goals have been reached as planned. Although 2D nanopatterns formed by related tectons bearing DAT groups proved to be hard to foresee (see Chapter 3), the 2D nanopatterns shown in Chapter 4 have generally conformed to expectation and only two hydrogen-bonded motifs have emerged, the parallel network and the Kagomé network. Specifically, tectons BTA and **TA-8** produced only the parallel motif, tecton **TA-6**

generated only the Kagomè motif, and tectons **TA-5** and **TA-7** were found to form both motifs. Nanopatterns produced by tecton **TA-5** proved to be of special interest because they showed a lack of large-scale periodicity but revealed local order in small areas. This phenomenon provides an example of frustrated 2D crystallization and the formation of a 2D molecular glass, possibly because the two motifs are closely matched in energy and can merge smoothly. The selective formation of different motifs has been studied theoretically by DFT calculations, which suggest that the contrasting preferences of these tectons for different networks result partially from slight differences in hydrogen bonding. In addition, interactions between the adsorbates and HOPG may differ in subtle ways.

Overall, our work has demonstrated that a deeper understanding of 2D molecular assembly can be attained by an integrated approach using the tools of STM, computation, and molecular synthesis. In particular, our results provide new guidelines for designing 2D molecular glasses, as well as detailed models for their structures and the phenomenon of polyamorphism. Furthermore, our work confirms that molecules with well-defined shapes and multiple sites that engage in strong directional interactions are a consistently productive source of new materials with properties not previously observed.

References

1. a) Griessl, S.; Lackinger, M.; Edelwirth, M.; Hietschold, M.; Heckl, W. M. *Single Mol.* **2002**, *3*, 25-31. b) Lackinger, M.; Griessl, S.; Markert, T.; Jamitzky, F.; Heckl, W. M. *J.*

Phys. Chem. B **2004**, *108*, 13652-13655.

2. De Feyter, S.; Gesquière, A.; Klapper, M.; Müllen, K.; De Schryver, F. C. *Nano Lett.* **2003**, *3*, 1485-1488.
3. De Feyter, S.; Grim, P. C. M.; Rücker, M.; Vanoppen, P.; Meiners, C.; Sieffert, M.; Valiyaveettil, S.; Müllen, K.; De Schryver, F. C. *Angew. Chem. Int. Edit.* **1998** *37*, 1223-1226.
4. Vanoppen, P.; Grim, P. C. M.; Rücker, M.; De Feyter, S.; Moessner, G.; Valiyaveettil, S.; Müllen, K.; De Schryver, F. C. *J. Phys. Chem.* **1996**, *100*, 19636-19641.
5. Miura, A.; De Feyter, S.; Abdel-Mottaleb, M. M. S.; Gesquière, A.; Grim, P. C. M.; Moessner, G.; Sieffert, M.; Klapper, M.; Müllen, K.; De Schryver, F. C. *Langmuir* **2003**, *19*, 6474-6482.
6. Coles, S. J.; Holmes, R.; Hursthouse, M. B.; Price, D. J. *Acta Crystallogr.* **2002**, *E58*, o626-o628.
7. Aujard, I.; Baltaze, J.-P.; Baudin, J.-B.; Cogné, E.; Ferrage, F.; Jullien, L.; Perez, E.; Prévost, V.; Qian, L. M.; Ruel, O. *J. Am. Chem. Soc.* **2001**, *123*, 8177-8188.
8. Zhou, H.; Dang, H.; Yi, J.-H.; Nanci, A. ; Rochefort, A. ; Wuest, J. D. *J. Am. Chem. Soc.* **2007**, *129*, 13774-13775.
9. Khan, M. S.; Al-Mandhary, M. R. A.; Al-Suti, M. K.; Al-Battashi, F. R.; Al-Saadi, S.; Ahrens, B.; Bjernemose, J. K.; Mahon, M. F. *Dalton Trans.* **2004**, *15*, 2377-2385.
10. Rochefort, A.; Wuest, J. D. *Langmuir* **2008**, *25*, 210-215.
11. Atwood, J. L. *Nat. Mater.* **2002**, *1*, 91-92.
12. Ramirez, A. P. *Annu. Rev. Mater. Sci.* **1994**, *24*, 453-480.

13. Schröder, C.; Nojiri, H.; Schnack, J.; Hage, P.; Luban, M.; Kögerler, P. *Phys. Rev. Lett.* **2005**, *94*, 017205.

14. Grohol, D.; Matan, K.; Cho, J.-H.; Lee, S.-H.; Lynn, J. W.; Grocera, D. G.; Lee, Y. S. *Nat. Mater.* **2005**, *4*, 323-328.

15. Moulton, B.; Lu, J.; Hajndl. R.; Hariharan, S. ; Zaworotko, M. J. *Angew. Chem. Int. Ed.* **2002**, *41*, 2821-2824.

16. Stöhr, M.; Wahl, M.; Spillmann, H.; Gade, L. H.; Jung, T. A. *Small* **2007**, *3*, 1336-1340.

17. (a) Furukawa, S.; Uji-i, H.; Tahara, K.; Ichikawa, T.; Sonada, M.; De Schryver, F. C.; Tobe, Y.; De Feyter, S. *J. Am. Chem. Soc.* **2006**, *128*, 3502-3503. (b) Tahara, K.; Furukawa, S.; Uji-i, H.; Uchino, T.; Ichikawa, T.; Zhang, J.; Mamdouh, W.; Sonoda, M.; De Schryver, F. C.; De Feyter, S.; Tobe, Y. *J. Am. Chem. Soc.* **2006**, *128*, 16613-16625.

18. Blunt, M..; Lin, X.; Gimenez-Lopez, M. del C.; Schröder, M.; Champness, N. R.; Beton, P. H. *Chem. Commun.* **2008**, 2304-2306.

19. Schlickum, U.; Decker, R.; Klappenberger, F.; Zoppellaro, G.; Klyatskaya, S.; Auwärter, W.; Neppl, S.; Kern, K.; Brune, H.; Ruben, M.; Barth, J. V. *J. Am. Chem. Soc.* **2008**, *130*, 11778-11782.

20. Malo, J.; Mitchell, J. C.; Vénien-Bryan, C.; Harris, J. R.; Wille, H.; Sherratt, D. J.; Turberfield, A. J. *Angew. Chem. Int. Ed.* **2005**, *44*, 3057-3061.

21. Blunt, M. O.; Russell, J. C.; Giménez-López, M. del C.; Garrahan, J. P.; Lin, X.; Schröder, M.; Champness, N. R.; Beton, P. H. *Science* **2008**, *322*, 1077-1080.

22. Lebel, O.; Maris, T.; Perron, M.-È .; Demers, E.; Wuest, J. D. *J. Am. Chem. Soc.* **2006**, *128*, 10372-10373.

23. Poole, P. H.; Grande, T.; Sciortino, F.; Stanley, H. E.; Angell, C. A. *Comp. Mater. Sci.* **1995**, *4*, 373-382.

24. For a recent example of the use of DFT calculations to study hydrogen-bonded networks, see: Trolliet, C.; Poulet, G.; Tuel, A.; Wuest, J. D.; Sautet, P. *J. Am. Chem. Soc.* **2007**, *129*, 3621-3626.

25. Bylaska, E. J.; de Jong, W. A.; Kowalski, K.; Straatsma, T. P.; Valiev, M.; Wang, D.; Aprà, E.; Windus, T. L.; Hirata, S.; Hackler, M. T.; Zhao, Y.; Fan, P.-D.; Harrison, R. J.; Dupuis, M.; Smith, D. M. A.; Nieplocha, J.; Tipparaju, V.; Krishnan, M.; Auer, A. A.; Nooijen, M.; Brown, E.; Cisneros, G.; Fann, G. I.; Fruchtl, H.; Garza, J.; Hirao, K.; Kendall, R.; Nichols, J. A.; Tsemekhman, K.; Wolinski, K.; Anchell, J.; Bernholdt, D.; Borowski, P.; Clark, T.; Clerc, D.; Dachsel, H.; Deegan, M.; Dyall, K.; Elwood, D.; Glendening, E.; Gutowski, M.; Hess, A.; Jaffe, J.; Johnson, B.; Ju, J.; Kobayashi, R.; Kutteh, R.; Lin, Z.; Littlefield, R.; Long, X.; Meng, B.; Nakajima, T.; Niu, S.; Pollack, L.; Rosing, M.; Sandrone, G.; Stave, M.; Taylor, H.; Thomas, G.; van Lenthe, J.; Wong, A.; Zhang, Z. *NWChem, A Computational Chemistry Package for Parallel Computers, Version 5.0* (2006), Pacific Northwest National Laboratory, Richland, Washington 99352-0999, USA.

26. Kendall, R. A.; Aprà, E.; Bernholdt, D. E.; Bylaska, E. J.; Dupuis, M.; Fann, G. I.; Harrison, R. J.; Ju, J.; Nichols, J. A.; Nieplocha, J.; Straatsma, T. P.; Windus, T. L.; Wong, A.T. *Computer Phys. Comm.* **2000**, *128*, 260-283.

27. Zhao, Y.; Truhlar, D. G. *J. Chem. Theory Comput.* **2005**, *1*, 415-432.

28. Bayard, É.; Hamel, S.; Rochefort, A. *Org. Electr.* **2006**, *7*, 144-154.

CHAPTER 5

STM Study of the Adsorption of Tetraesters Created by Connecting Isophthalate Units to Linear Spacers

5.1 Introduction

Chapters 3 and 4 have described the behavior of well-designed tectons with conjugated linear planar cores bearing multiple sticky functional groups able to participate in extensive hydrogen bonding. As expected, these compounds can create ordered 2D nanopatterns on HOPG, resulting presumably from (1) their ability to engage in strong interadsorbate interactions leading to the formation of hydrogen-bonded networks and (2) their inherently strong affinity for adsorption on HOPG.

To provide a deeper understanding of the relative contributions of these two effects, we decided to study the adsorption of analogues with closely similar structures but no ability to form strong hydrogen bonds. The relatively simple adsorption of tetraacids produced by coupling isophthalic acid units to linear spacers suggested that the adsorption of analogous tetraesters would provide invaluable complementary information. With similar linear, conjugated, planar aromatic cores and substituents, the tetraesters and tetraacids would be expected to have comparable affinity for HOPG. However, by lacking the ability to position neighboring molecules through the formation of hydrogen bonds between COOH groups, the tetraesters were expected to construct unrelated nanopatterns held together by different interactions, including weak C–H···O hydrogen bonds and van der Waals interactions. As summarized below, these expectations have been confirmed by STM studies of a series of tetraesters.

Among a number of molecules investigated by STM, only a few esters decorated with long alkyl chains were reported to generate well-ordered surface nanopatterns.[1-7] Matzger and co-workers[1] found that isophthalates formed close-packed structures showing different

Scheme 5.1 Molecular structures of tetraesters **TE-5**, **TE-6**, **TE-7**, **TE-8**, and **TE-9**.

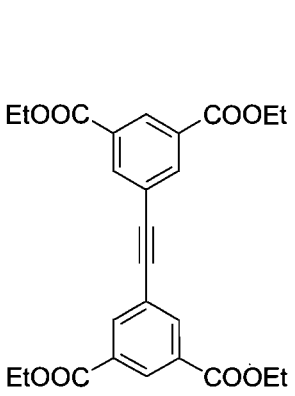

TE-5

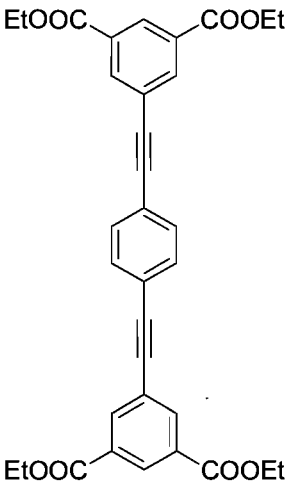

TE-6

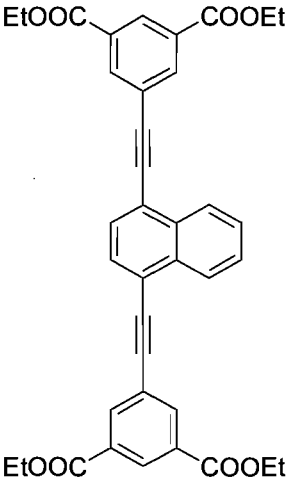

TE-7

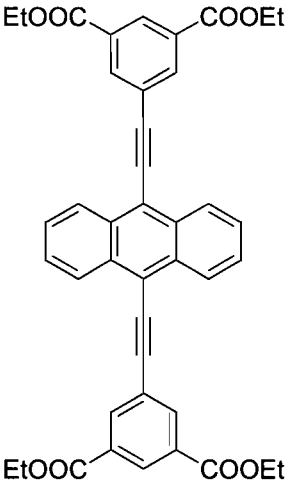

TE-8

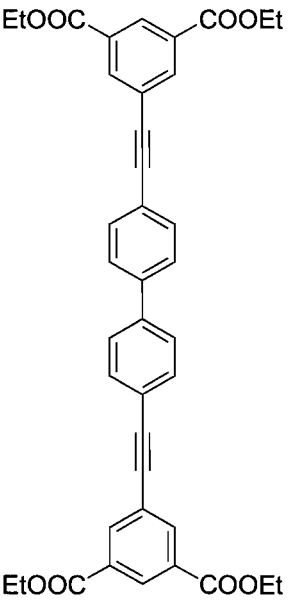

TE-9

motifs corresponding to the odd-even effect.[8,9] Müllen and co-workers[4] have developed complex esters containing hexa-peri-hexabenzocoronene as a electron donor and anthraquinone as an electron acceptor, which were then assembled into nanophase-separated structures both in 2D and 3D.

To allow comparison with the adsorption of the tetraacids reported in Chapter 4, we selected the ester analogues shown in Scheme 5.1. Esters **TE-5**, **TE-6**, **TE-7**, and **TE-8** are directly related to tetraacids **TA-5**, **TA-6**, **TA-7**, and **TA-8**, respectively, and tetraester **TE-9** is closely similar but further lengthens the core. As in other parts of our work, our study of these tetraesters features a combination of STM investigations and X-ray crystallography to provide a deeper understanding of molecular association, both in 2D and 3D.

5.2 Design and Synthesis of Tetraesters

The syntheses of tetraesters **TE-5**, **TE-6**, **TE-7**, and **TE-8** were previously shown in Schemes 4.2-4.5, respectively. Additional tetraester **TE-9** was synthesized by standard procedures in three steps as shown in Scheme 5.2. Sonogashira coupling of commercially available 4,4'-diiodobiphenyl with (trimethylsilyl)acetylene in the presence of catalytic dichlorobis(triphenylphosphine)palladium(II) and copper(I) iodide provided known intermediate **23**[10, 11] in 85% yield. Subsequent deprotection gave 4,4'-diethynylbiphenyl (**24**)[10,11] in 86% yield. Compound **24** reacted with diethyl 5-iodobenzene-1,3-dicarboxylate (**17**) under Sonogashira conditions to produce the desired tetraester **TE-9** in 65% yield.

Scheme 5.2 Synthesis of tetraester **TE-9.**

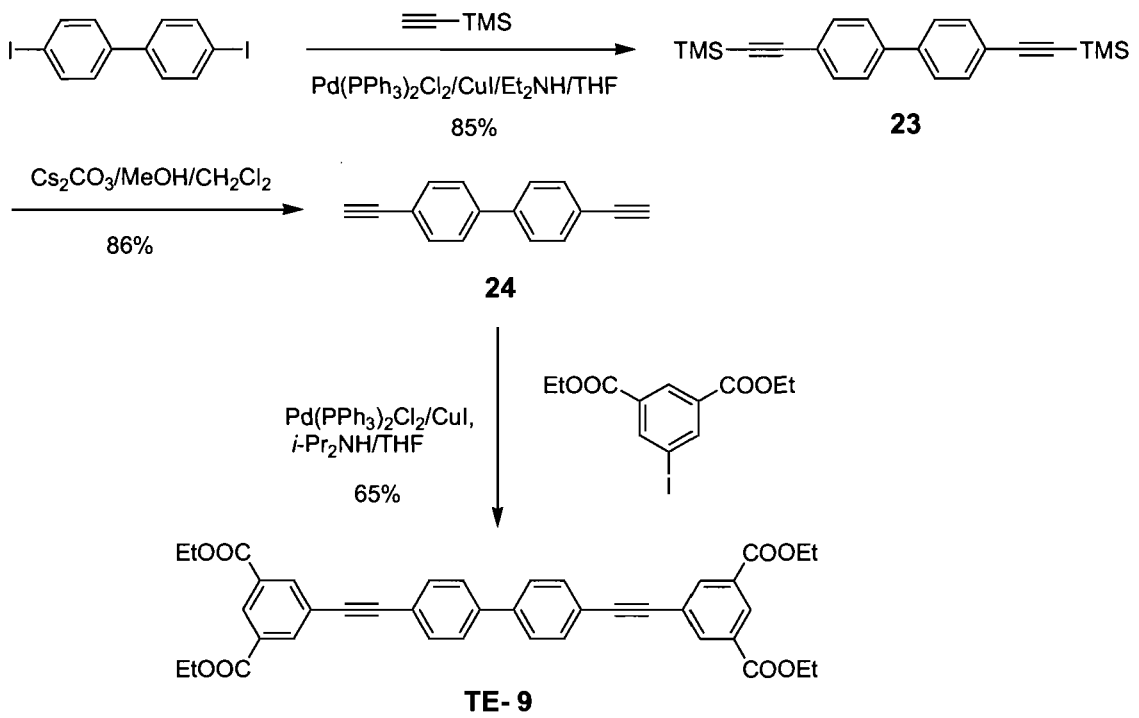

5.3 STM Investigations and X-ray Crystallography of Tetraesters TE-5, TE-6, TE-7, TE-8, and TE-9

5.3.1 2D Nanopatterns Formed by Tetraester TE-5

Tetraester **TE-5** is related to tetracid **TA-5**, which was shown to undergo frustrated 2D crystallization that produced confused hybrids of parallel motifs and Kagomé motifs directed by association of COOH groups as cyclic hydrogen-bonded pairs (Figure 4.9). Because tetraester **TE-5** is unable to engage in any reliable intermolecular interactions, the 2D nanopatterns resulting from its adsorption on HOPG are impossible to predict with

confidence. An STM investigation of compound **TE-5** was performed under our standard conditions by deposition on HOPG in heptanoic acid.

Figure 5.1a shows an STM image of remarkably well-ordered nanopatterns created by tetraester **TE-5**. A higher-resolution image in Figure 5.1b displays a periodic arrangement of bright protrusions, which correspond to individual molecules. The observation of well-resolved images is noteworthy, because it demonstrates that the tetraester has a strong affinity for HOPG despite the absence of long alkyl chains, which are frequently used to promote adsorption, and despite its inability to form an extended hydrogen-bonded network. Parallel networks or Kagomé networks are formed locally by tetraacid **TA-5**, but monolayers of tetraester **TE-5** exhibit a completely different architecture, which can be described as a butterfly structure (highlighted in blue and green in Figure 5.1b). The unit cell parameters are determined to be a = ~2.38 nm, b = ~3.42 nm, and γ = ~90°. A proposed molecular model is shown in Figure 5.2. The unit cell parameters are calculated to be a = ~2.34 nm, b = ~3.48 nm, and γ = ~90°, assuming C-H···O hydrogen bonding with an average H···O distance of 2.42 Å. The model suggests that two neighboring molecules associate by forming weak C–H···O hydrogen bonds, which are discussed below in greater detail. The angle defined by the direction of the two long axes of adjacent molecules within such aggregates is 60°, which is consistent with the angle observed in the STM image shown in Figure 5.1b. Adjacent pairs are probably connected by van der Waals interactions involving four ethyl groups, which may or may not lie in the plane of the monolayer.

A subtle feature of this model is that tetraester **TE-5** adopts a planar conformation in which each ester group adopts the normally favored s-*trans* geometry to minimize the

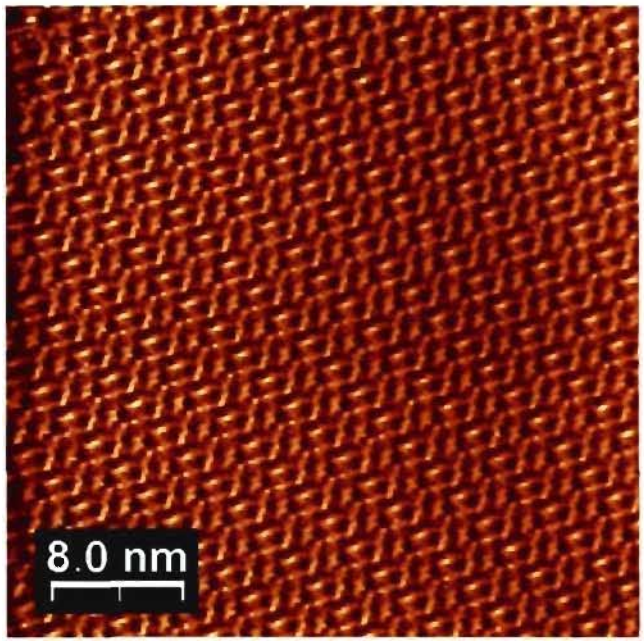

(a)

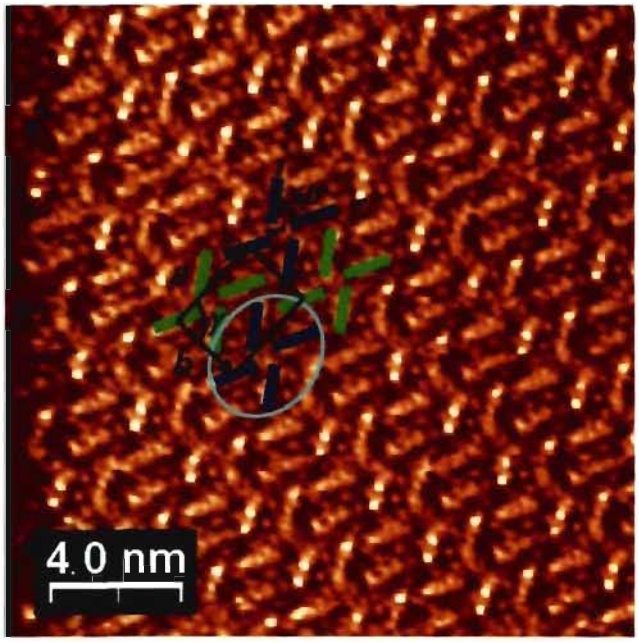

(b)

Figure 5.1 STM images of 2D nanopatterns produced by the adsorption of tetraester **TE-5** on HOPG (deposition from heptanoic acid, with V_{bias} = -1.5 V and I_{set} = 100 pA). (a) Well-ordered nanopatterns over an area of 40 nm × 40 nm. (b) Higher-resolution image with schematic representations of the butterfly structures highlighted in blue and green (the short bars indicate individual molecules). The unit cell is highlighted in black.

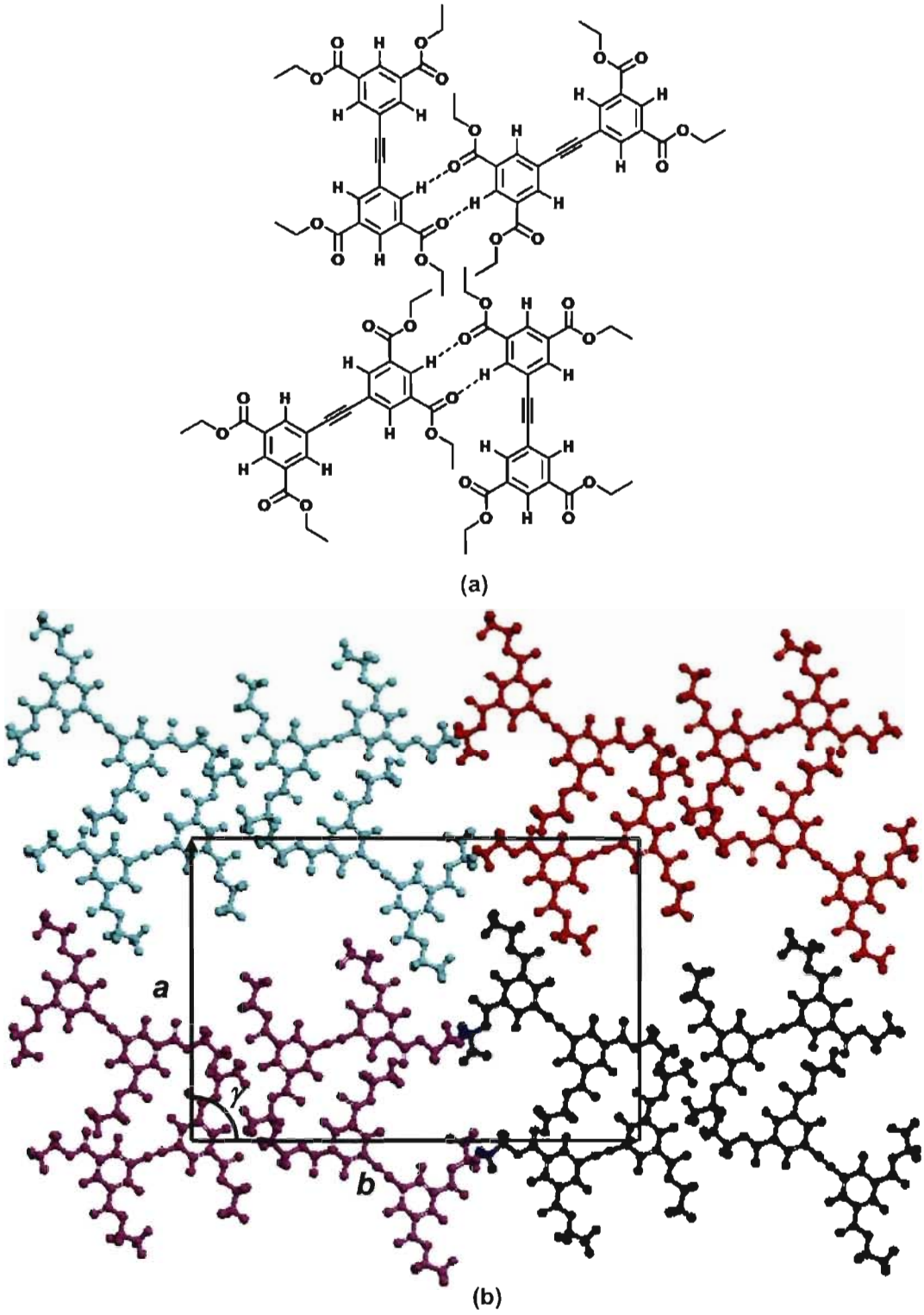

Figure 5.2 Proposed molecular models of the 2D network formed by the adsorption of tetraester **TE-5** on HOPG. a) C–H···O hydrogen bonds are represented by broken lines. b) The unit cell is highlighted in black.

dipole-dipole interaction between C=O and O-Et bonds, as well as to optimize stereoelectronic effects involving lone pairs and antibonding orbitals.[12] Conformations of tetraester **TE-5** other than the one shown in Figure 5.2 can also satisfy this condition, but the ethyl groups are then directed in ways that appear to lead to less efficient packing. The model shown in Figure 5.2 is therefore consistent with the observed 60° intermolecular angle, the established conformations of esters, and the normal preference for closely packed structures.

Although normally weaker than conventional hydrogen bonds between electronegative elements, C–H···O interactions and related bonds are thought to be crucial in a large number of molecular complexes and crystal structures.[13-17] These weak hydrogen bonds are known to have wide range of geometries and strengths. Although this means that they cannot be used effectively to position molecules in many applications, they are nevertheless of considerable importance in crystal engineering, biological assembly, and molecular recognition.[18-21] The tetracarboxylic acids described in Chapter 4 associate in 2D by forming conventional strong O–H···O hydrogen bonds. In contrast, analogous tetraester **TE-5** does not have the same opportunity, and it appears instead to rely on C–H···O interactions to produce well-ordered 2D nanopatterns. The particular aryl C–H···O hydrogen-bonding motif postulated in Figure 5.2 is plausible, although it is not well established in the 2D or 3D structures of benzoate esters. We therefore undertook an analysis of the 3D crystal structure of tetraester **TE-5** to find support for the hypothesis of Figure 5.2.

5.3.2 3D Crystal Structure of Tetraester TE-5

To further understand the self-association of tetraester **TE-5**, single crystals were grown by allowing vapors of hexane to diffuse into a solution in chloroform, and their structure was determined by X-ray diffraction. Views of the structure are provided in Figures 5.3 and 5.4. The crystals were found to contain only compound **TE-5** and to belong to the *P*-1 space group, with unit cell parameters a = 9.3227(1) Å, b = 10.6215(2) Å, c = 13.2099(2) Å, α = 76.492(1)°, β = 69.406(1)°, and γ = 78.765(2)°.

As shown in Figure 5.4a, the crystal is composed of layers. This observation is fully consistent with the highly aromatic character of the core of tetraester **TE-5** and with the ability of the molecule to adopt a planar or nearly planar conformation. The formation of sheets in the 3D structure confirms that the molecule is inherently well suited for deposition on HOPG. Within each layer, molecules are found to align parallel to the principal molecular axis and to be packed efficiently with many close contacts (average H···H and O···H distances of 2.382 and 2.696 Å). Adjacent sheets are associated by C–H···π interactions, with H···π distances of 3.128 Å. Unexpectedly, no aromatic C–H···O hydrogen bonds were found in the 3D structure of tetraester **TE-5**.

Overall, the 2D and 3D structures show distinct similarities, as well as important differences. In particular, both structures feature efficiently packed sheets with no space for guests. However, the particular conformations of all four ester groups postulated in the 2D assembly (Figure 5.2a) and observed in the 3D structure (Figure 5.4b) are not identical. As a consequence, the packing of molecules within the sheets is also different. Clearly, tetraacid **TA-5** and the analogous tetraester **TE-5** are both well designed for adsorption on

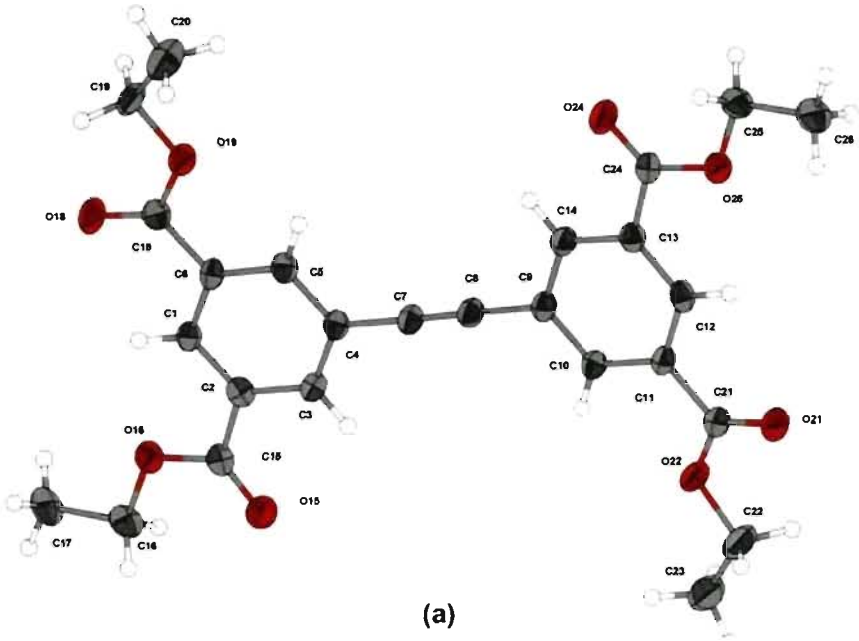

(a)

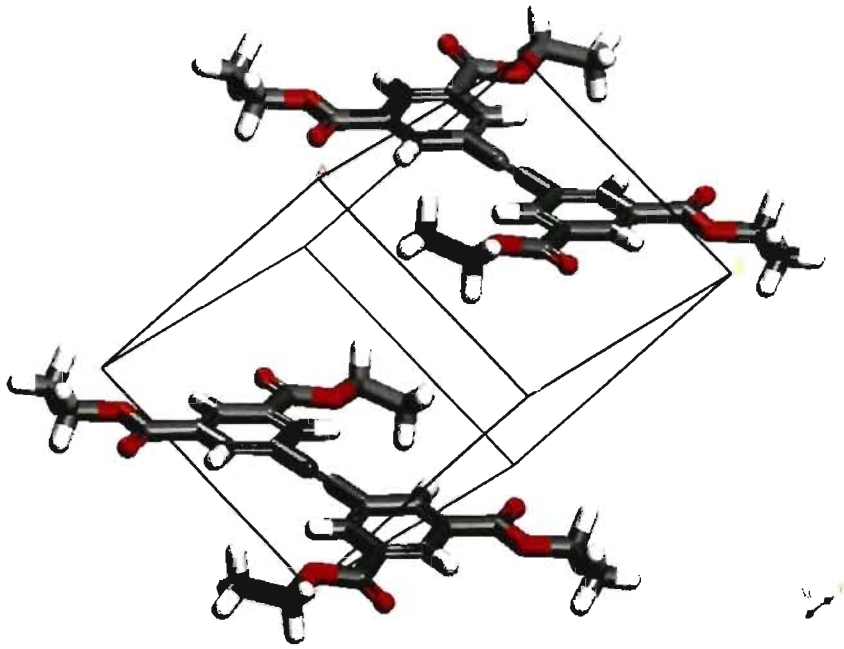

(b)

Figure 5.3 (a) ORTEP view of the structure of crystals of tetraester **TE-5** grown from hexane/$CHCl_3$, with the numbering scheme adopted. Ellipsoids are drawn at 50% probability level, and hydrogen atoms are represented by a sphere of arbitrary size. (b) Unit cell showing two parallel molecules.

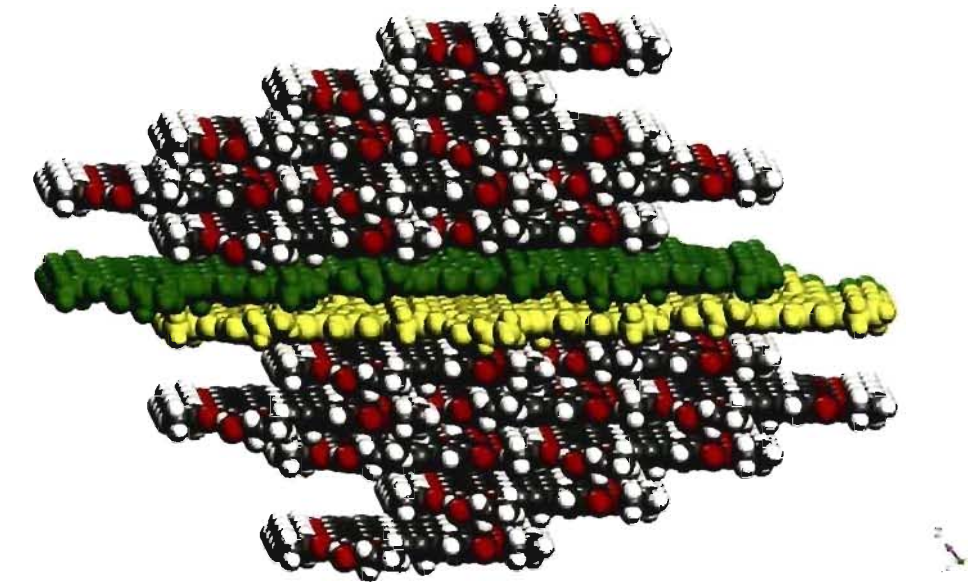

(a)

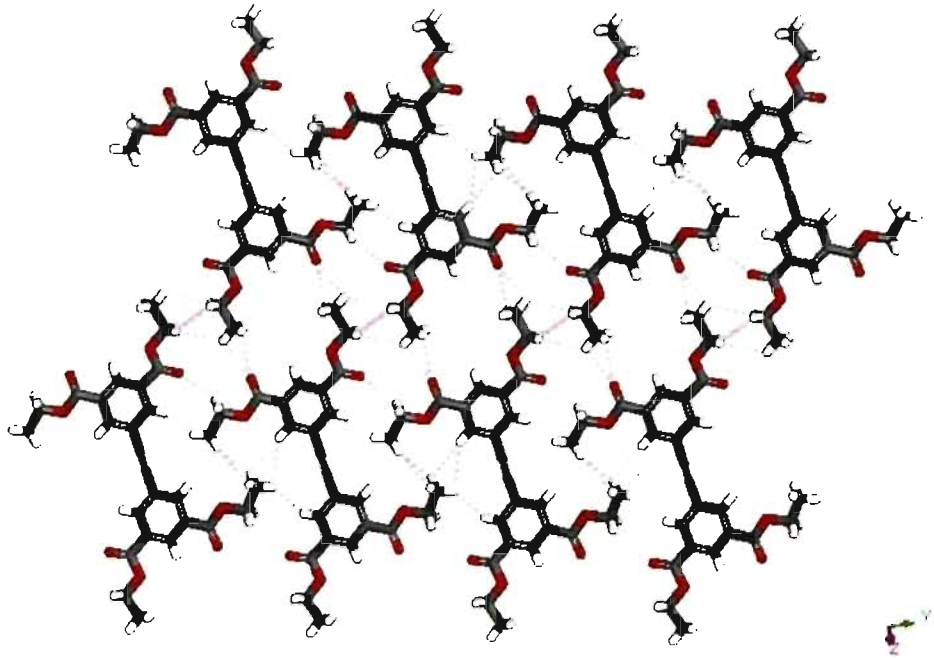

(b)

Figure 5.4 Views of the structure of crystals of tetraester **TE-5** grown from hexane/$CHCl_3$. (a) View showing the stacking of sheets, with two adjacent layers highlighted in green and yellow. (b) View of a single sheet, showing that the molecules are parallel and closely packed. Close contacts are represented by broken lines.

HOPG. However, the tetraester lacks substituents that can interact strongly and impose particular orientations on adjacent molecules. As a result, close homology between the 2D and 3D structures is not enforced. Under these circumstances, it is likely that subtle adsorbate-surface interactions may play a particularly important role in determining what 2D pattern ultimately emerges.

5.3.3 2D Nanopatterns Formed by Tetraester TE-6

The adsorption of extended tetraester **TE-6** on HOPG was investigated by STM under conditions similar to those used in the study of analogue **TE-5**. STM images are provided in Figure 5.5. Unlike the corresponding tetraacid **TA-6**, which was shown to favor Kagomé networks (Chapter 4), tetraester **TE-6** proved to produce completely different 2D nanopatterns. Figure 5.5a shows a notably well resolved open-framed square network with C_4 symmetry. The schematic representation in Figure 5.5b highlights the square structure, with unit cell parameters $a = b = \sim 2.05$ nm and $\gamma = \sim 90°$. Adjacent molecules forming the square are perpendicular to each other, with each end group pointing to the centre of a neighbor.

The proposed molecular model in Figure 5.6a suggests that the perpendicular coupling is mediated by two equivalent C–H···O hydrogen bonds between the oxygen atoms of two carbonyl groups and two C–H bonds of the central phenyl group of tetraester **TE-6** (see black dashed lines in Figure 5.6a). Each molecule thereby associates with four neighbors by forming a total of eight C–H···O hydrogen bonds, resulting in the formation of a 2D network. If the adsorbed molecules are coplanar with the underlying substrate, and if the

C–H···O distance is assumed to be approximately 2.42 Å, then the unit cell parameters are calculated to be $a = b = \sim 1.98$ nm and $\gamma = \sim 90°$ (Figure 5.6b), which are consistent with the observed unit cell parameters obtained from analysis of the STM image (Figure 5.5b). To our knowledge, this square hydrogen-bonding motif has not previously been observed in 3D structures. However, 4,4'-biphenyldicarboxylic acid has been reported to crystallize in 2D on Cu(100) by forming square networks held together by a similar hydrogen-bonding motif.[22]

Compared with the Kagomé network created by analogous tetraacid **TA-6**, the square network generated by tetraester **TE-6** might appear to be less stable thermodynamically, in part because it cannot respect the three-fold symmetry of the underlying HOPG, leading to adsorbate-substrate interactions that may be weaker, and in part because the interadsorbate interactions are also less strong. Nevertheless, tetraester **TE-6** displays an affinity for HOPG similar to that shown by the analogous tetraacid **TA-6**. As shown in Figure 5.7, an STM image was obtained from the co-adsorption of a 1:1 (mol/mol) mixture of compounds **TA-6** and **TE-6**. Five irregular domains with prominent boundaries are clearly resolved in the image. The square network assembled from tetraester **TE-6** is the only nanopattern observed over a large area of 80 × 80 nm^2. The absence of the characteristic Kagomé network of tecton **TA-6** indicates that adsorption of the corresponding tetraester is favored. A factor that might favor the adsorption of the tetraester is the presence of the ester groups, which add a total of eight carbon atoms and may thereby increase the adsorbate-substrate interaction through additional van der Waals interactions. These interactions may also help

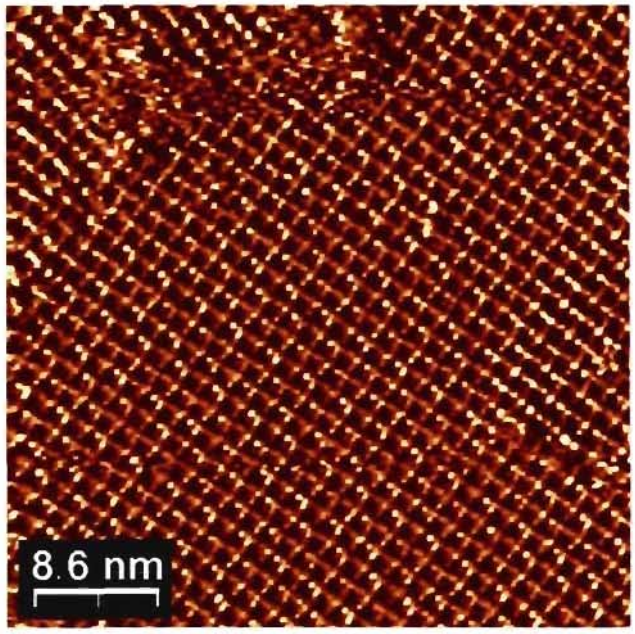

(a)

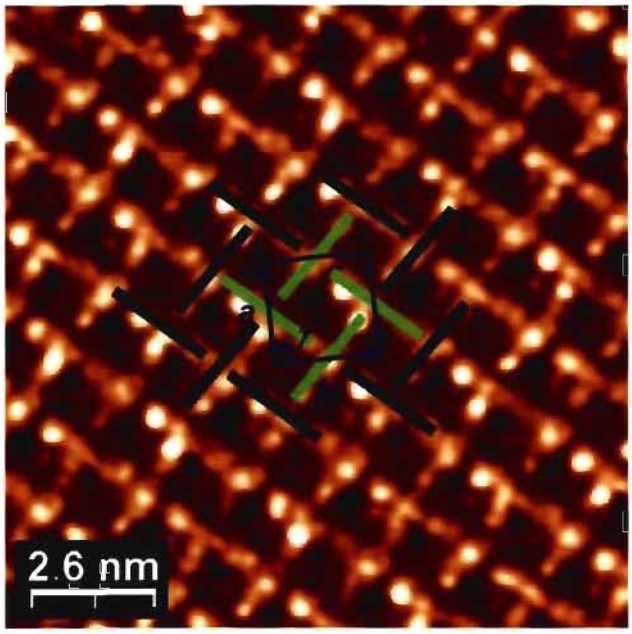

(b)

Figure 5.5 STM images of 2D nanopatterns created by the adsorption of tetraester **TE-6** on HOPG (deposition from heptanoic acid, with V_{bias} = -1.5 V and I_{set} = 100 pA). (a) Well-ordered monolayers over an area of 43 nm × 43 nm. (b) Schematic illustration showing the square network, with four adjacent individual molecules represented by green bars and surrounding molecules shown as black bars. The unit cell is highlighted in blue.

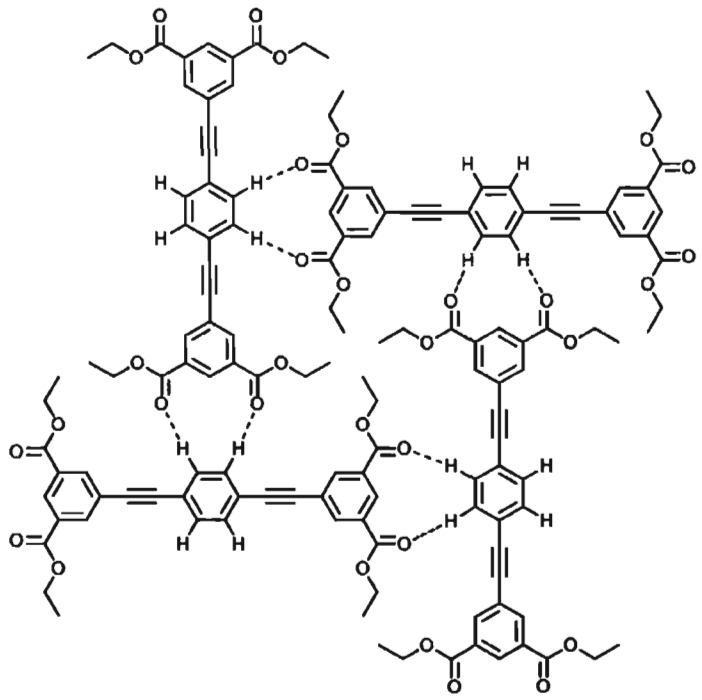

(a)

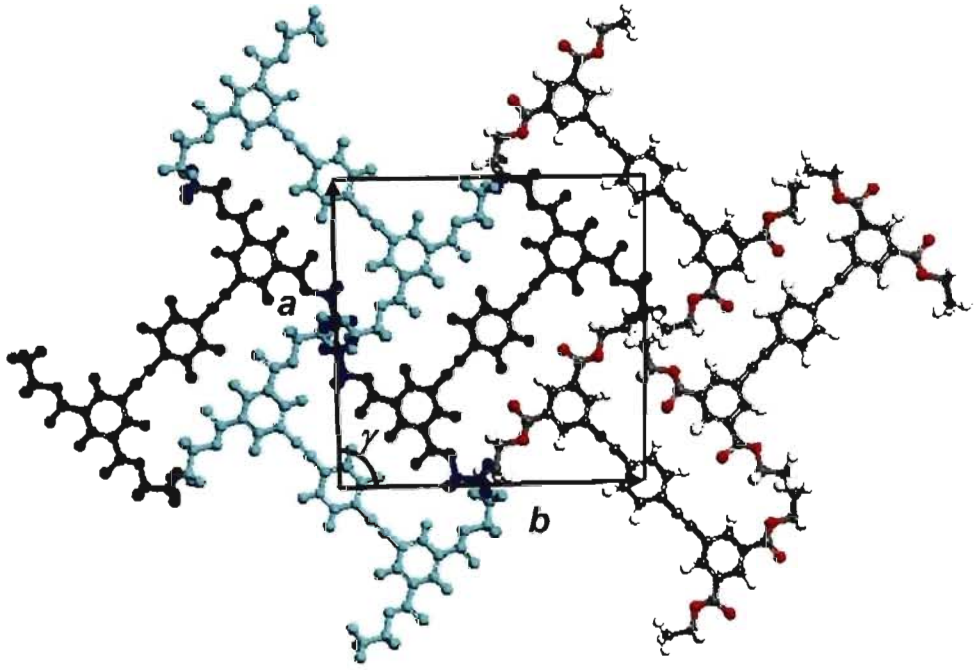

(b)

Figure 5.6 Proposed molecular models of the 2D network formed by tetraester **TE-6**. a) A tentative model showing a square hydrogen-bonding motif involving aromatic C-H···O interactions. b) The unit cell is highlighted in black. The molecules in blue and light blue represent two perpendicular orientations.

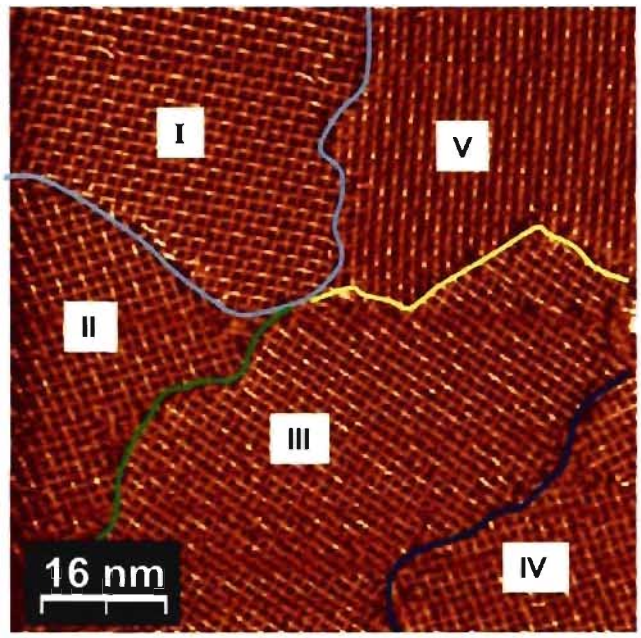

Figure 5.7 STM image of 2D nanopatterns formed by the adsorption of a 1:1 (mol/mol) mixture of tecton **TA-6** and tetraester **TE-6** on HOPG (deposition from heptanoic acid, with V_{bias} = -1.5 V and I_{set} = 50 pA). Five domains labelled I to V are highlighted in different colors.

compensate for the inability of the square structure to respect the symmetry of the underlying graphite.

5.3.4 3D Crystal Structure of Tetraester TE-6

To test the structural model set out in Figure 5.6, we decided to examine the 3D crystal structure of tetraester **TE-6**. Crystals were formed by allowing vapors of hexane to diffuse into a solution in chloroform, and their structure was determined by X-ray diffraction. Views of the structure are provided in Figures 5.8 and 5.9. The crystals were found to contain only compound **TE-6** and to belong to the *P*-1 space group, with unit cell parameters a = 9.0092(2) Å, b = 9.5914(2) Å, c = 10.1026(1) Å, α= 70.319(2)°, β= 66.113(1)°,

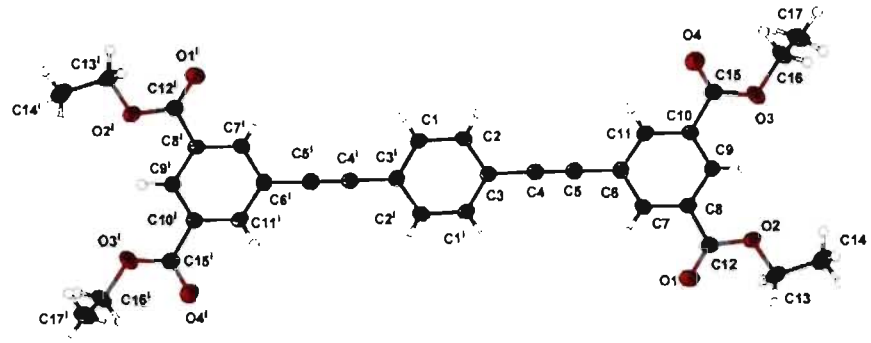

(a)

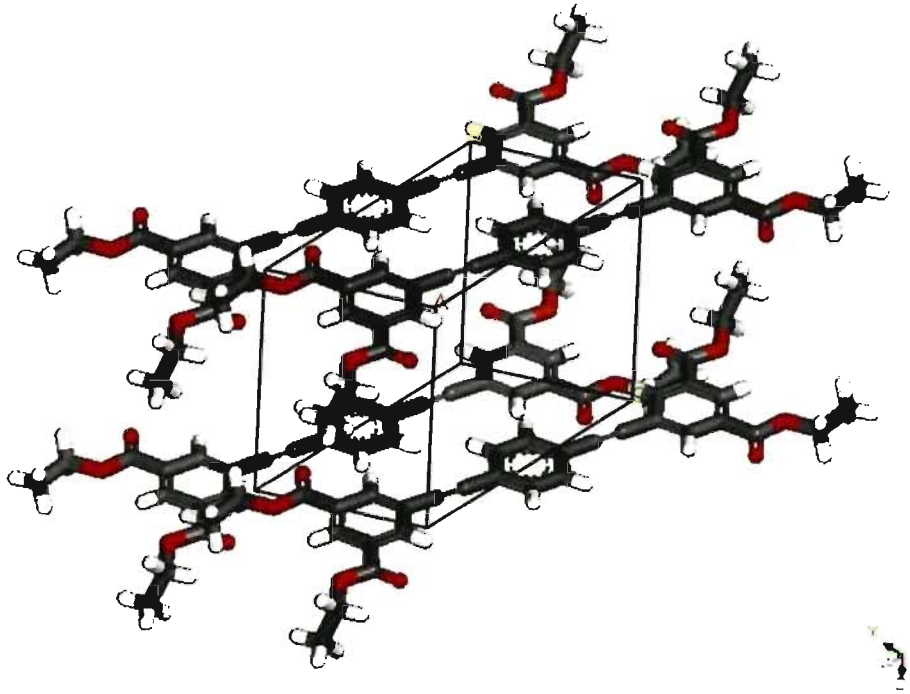

(b)

Figure 5.8 (a) ORTEP view of the structure of crystals of tetraester **TE-6** grown from hexane/$CHCl_3$, with the numbering scheme adopted. Ellipsoids are drawn at 50% probability level, and hydrogen atoms are represented by a sphere of arbitrary size. (b) Unit cell showing four parallel molecules.

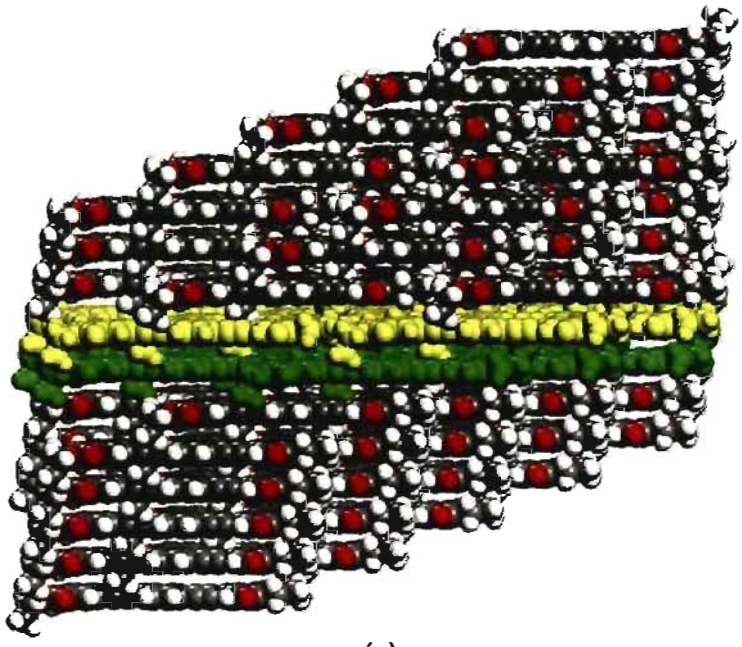

(a)

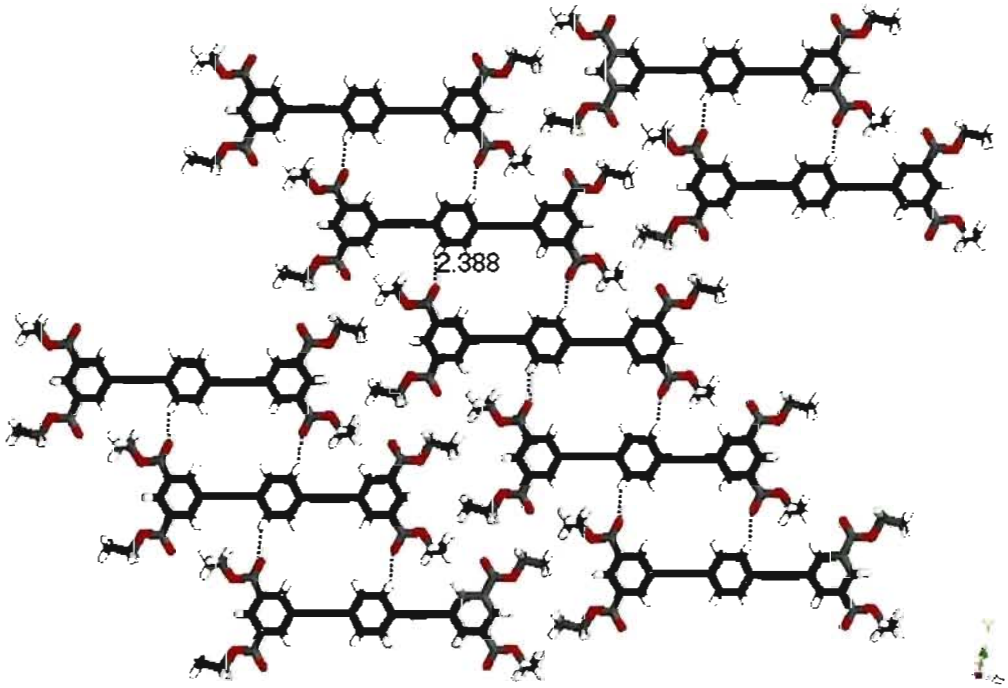

(b)

Figure 5.9 Views of the structure of crystals of tetraester **TE-6** grown from hexane/$CHCl_3$. (a) View along the *a* axis showing the stacking of sheets, with two adjacent layers highlighted in yellow and green. (b) View of a single sheet, with molecules parallel and closely packed. C-H···O hydrogen bonds are represented by broken lines.

and $\gamma = 65.792(1)°$ (Figure 5.8).

As in the case of shorter analogue **TE-5**, tetraester **TE-6** is designed to have a flat, linear, highly aromatic core that fosters crystallization in sheets. Figure 5.9 confirms this expectation. The three phenyl rings in the core of tetraester **TE-6** are found to be essentially coplanar, and molecules within each sheet have an approximately parallel orientation. The molecules are weakly associated by weak C–H···O hydrogen bonds (H···O distance of 2.388 Å) involving carbonyl oxygen atoms and the C–H bonds of aromatic rings. Adjacent layers are separated by 3.529 Å, which suggests the presence of π-stacking interactions. As in the case of tetraester **TE-5**, the ester groups of extended analogue **TE-6** adopt an s-*trans* geometry. Overall, tetraester **TE-6** adopts a maximally extended amphiphilic conformation in which all four ethyl groups are extended along the long molecular axis, creating two aliphatic head groups and a conjugated aromatic core. The resulting high aspect ratio and the segregation of aliphatic and aromatic regions undoubtedly promotes crystallization of the type observed in Figure 5.9b, which shows that parallel molecules are aligned end-to-end to form sheets with interdigitated alkyl groups.

Again, the observed 3D structure and the postulated 2D nanopattern produced by the adsorption of tetraester **TE-6** on HOPG (Figure 5.5) show certain similarities. In particular, sheets are favored in the 3D structure; packing is efficient and excludes guests, and molecular positioning in controlled in part by C–H···O hydrogen bonds. However, the 2D and 3D structures also reveal significant differences, particularly in the conformations of the ester groups in compound **TE-6**, the relative orientations of the long molecular axis (parallel in 3D and perpendicular in 2D), and both the number and nature of the

intermolecular C–H···O interactions.

5.3.5 2D Nanopatterns Formed by Tetraester TE-9

Tetraester **TE-6** differs from analogue **TE-5** by having an extended linear core containing an additional aryl ring. Further extension was achieved by creating tetraester **TE-9**, in which two isophthalate units are linked to a diethynylbiphenyl core, thereby increasing the molecular length from 1.9 nm to 2.3 nm. STM investigation of compound **TE-9** was performed under our standard conditions, and the adsorbate was again deposited in heptanoic acid. Figure 5.10a shows an STM image of tetraester **TE-9** adsorbed on HOPG. Unlike the remarkably well-ordered nanopatterns formed by analogues **TE-5** and **TE-6**, the 2D nanopatterns created by tecton **TE-9** are poorly ordered over large areas, although local regions of organization are visible (highlighted in blue in Figure 5.10a). Longer delays before recording the images did not change their appearance. Most of the adsorbed molecules can be solved clearly, and some of them do not have regular orientations relative to their neighbors. This suggests that the molecules have a strong affinity for HOPG, but it may be difficult to form extensive periodic domains. Figure 5.10b shows an enlarged image of the area highlighted in blue in Figure 5.10a, with unit cell parameters $a = b = \sim 2.48$ nm and $\gamma = \sim 90°$. The schematic illustration highlights a square network similar to that formed by tetraester **TE-6**.

As shown in Figure 5.11a, the square motif is proposed to be generated by C–H···O hydrogen bonds between carbonyl oxygen atoms and C–H bonds of biphenyls. The unit

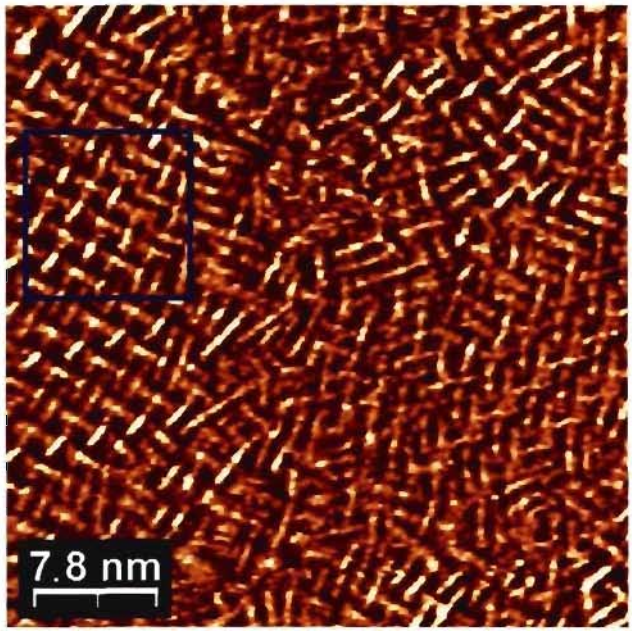

(a)

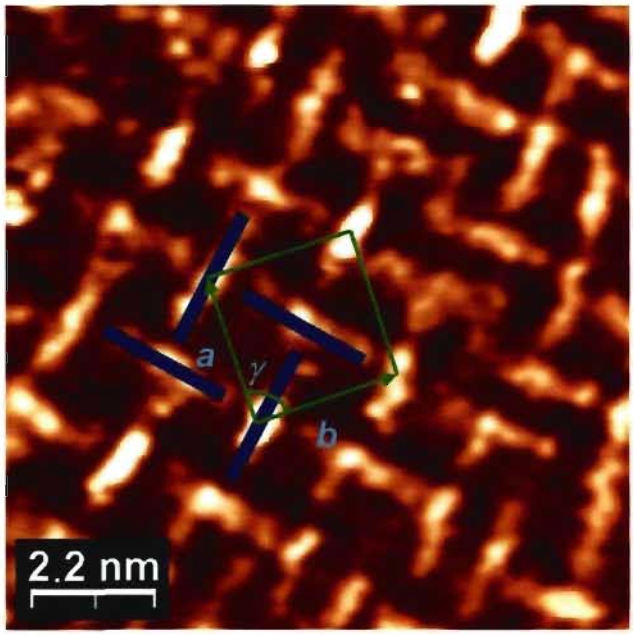

(b)

Figure 5.10 STM images of 2D nanopatterns formed by the adsorption of tetraester **TE-9** on HOPG (deposition from heptanoic acid, with V_{bias} = -1.5 V and I_{set} = 50 pA). (a) A large-scale image showing poorly ordered nanopatterns. (b) An enlarged image of the blue area in Figure 6.10a, with the unit cell highlighted in green. The individual molecules are represented by blue bars.

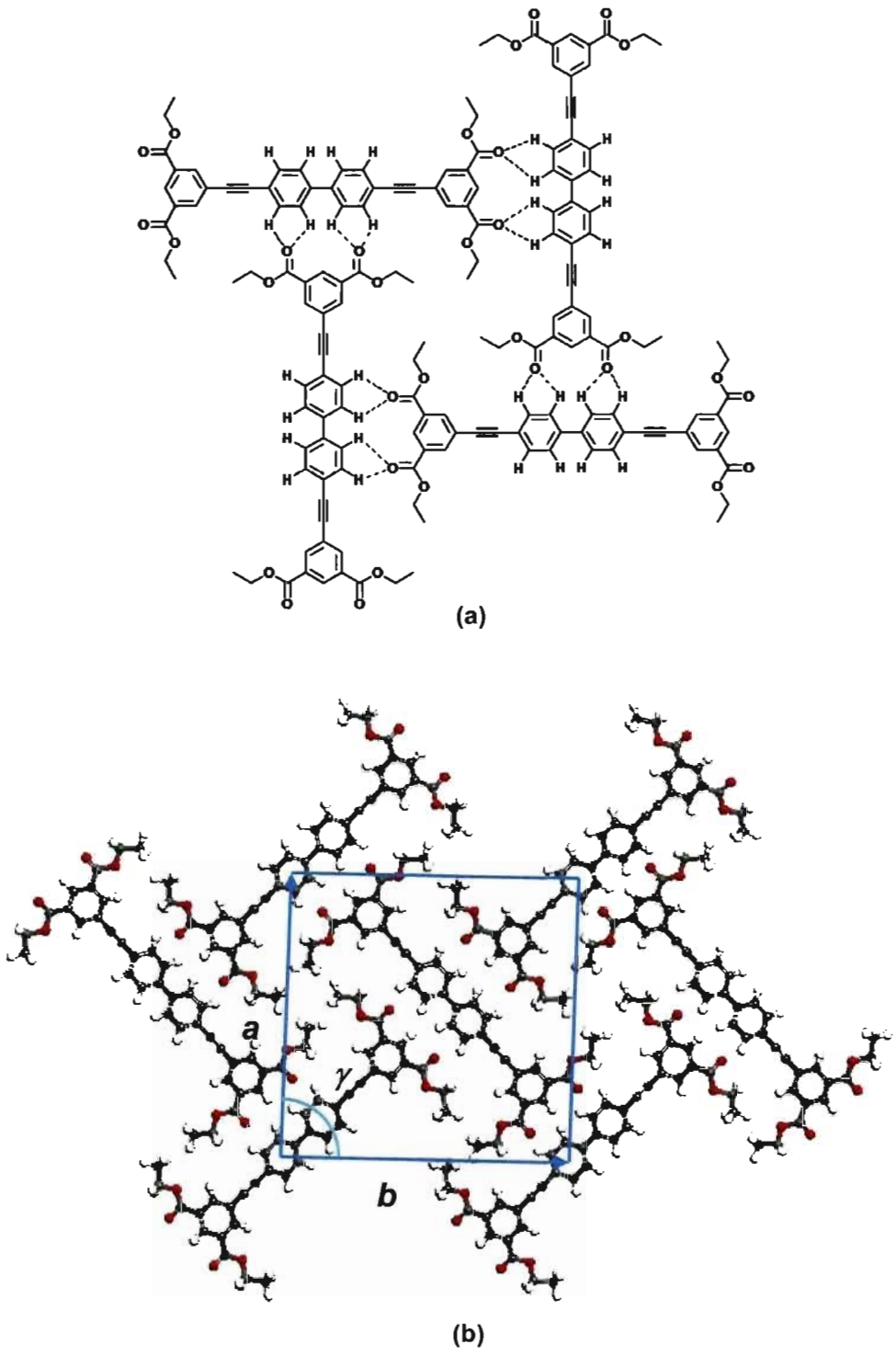

Figure 5.11 Proposed molecular model for the 2D nanopatterns formed by the adsorption of tetraester **TE-9**. a) The square network is assembled by C-H···O interactions, represented by broken lines. b) The unit cell is highlighted in light blue.

cell shown in Figure 5.11b is calculated to have parameters $a = b = \sim 2.36$ nm and $\gamma = \sim 90°$, assuming C-H···O hydrogen bonding with an average H···O distance of 2.42 Å.To facilitate the formation and adsorption of this structure, tetraester **TE-9** must adopt a planar or nearly planar conformation, whereas biphenyls normally favor twisted conformations. Flattening of the structure may be induced by adsorption, but tetraester **TE-9** is not optimally designed for creating extended periodic 2D structures. Nevertheless, we suggest that the increased length of tetraester **TE-9** leads to a higher degree of immobilization on HOPG than that observed for shortened analogues **TE-5** and **TE-6**, thereby retarding 2D crystallization by inhibiting movements needed to allow desorption, readsorption, and migration on the surface.

5.3.6 3D Crystal Structure of Tetraester TE-9

To acquire further understanding, we grew crystals of tetraester **TE-9** by allowing vapors of hexane to diffuse into a solution in chloroform, and their structure was determined by X-ray diffraction. Views of the structure are shown in Figures 5.12-5.14. The crystals were found to have the composition **2TE-9** • $2CHCl_3$ and to belong to the monoclinic $P21$ space group, with unit cell parameters $a = 10.2725(2)$ Å, $b = 15.2009(3)$ Å, $c = 23.7310(4)$ Å, $\alpha = \gamma = 90°$, and $\beta = 95.8960(10)°$. The unit cell revealed the presence of two distinct conformers with different biphenyl torsional angles of 25.7° and 34.8° (Figure 5.12b). Unlike tetraesters **TE-5** and **TE-6**, which yielded close-packed crystal structures, extended analogue **TE-9** produced crystals in which 14% of the volume is available for the inclusion of guests.[23, 24]

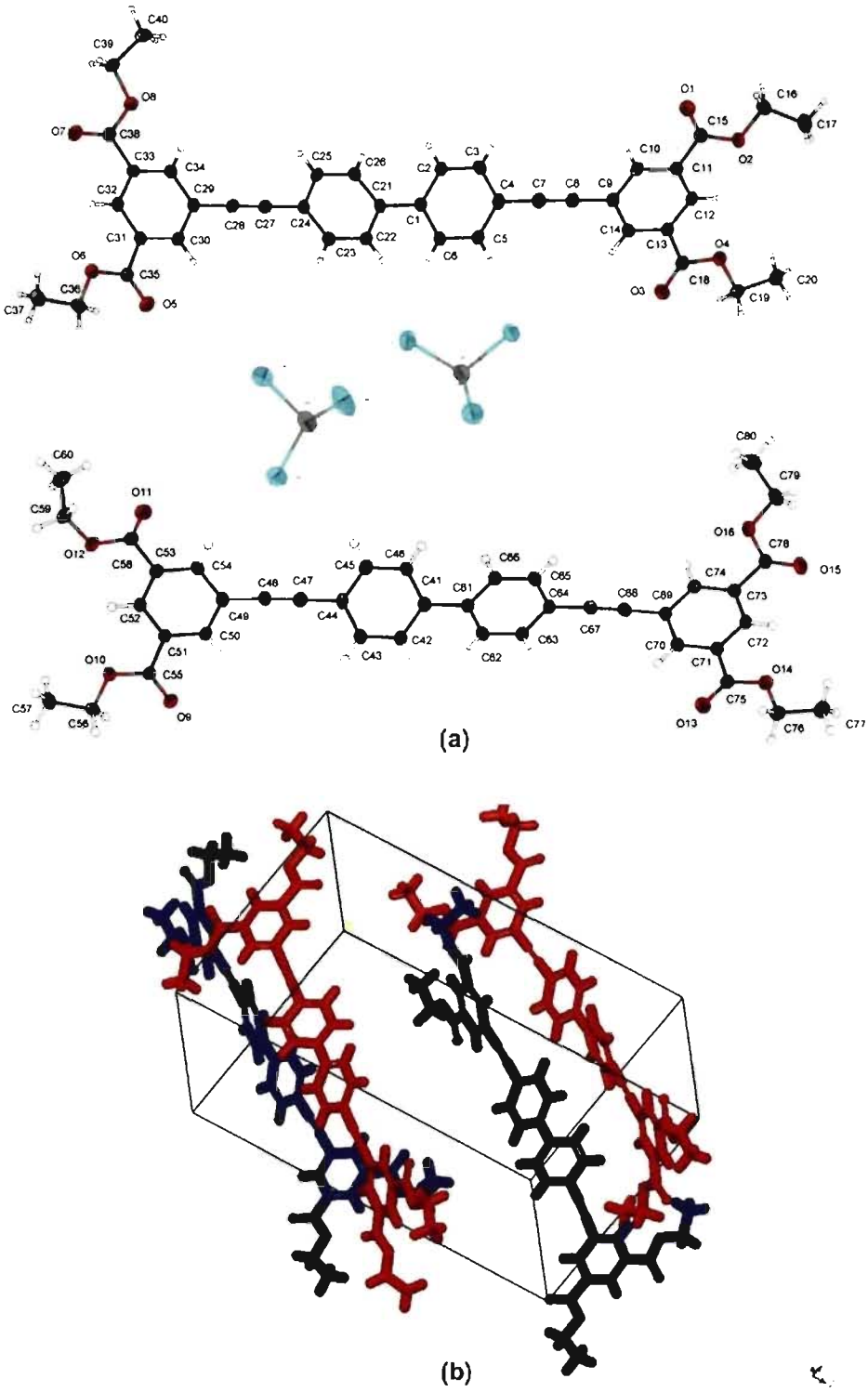

Figure 5.12 (a) ORTEP view of the structure of crystals of tetraester **TE-9** grown from hexane/$CHCl_3$, with the numbering scheme adopted. Ellipsoids are drawn at the 30% probability level. (b) Unit cell showing two conformers with different torsional angles (red and blue). Guest molecules of $CHCl_3$ are removed for clarity.

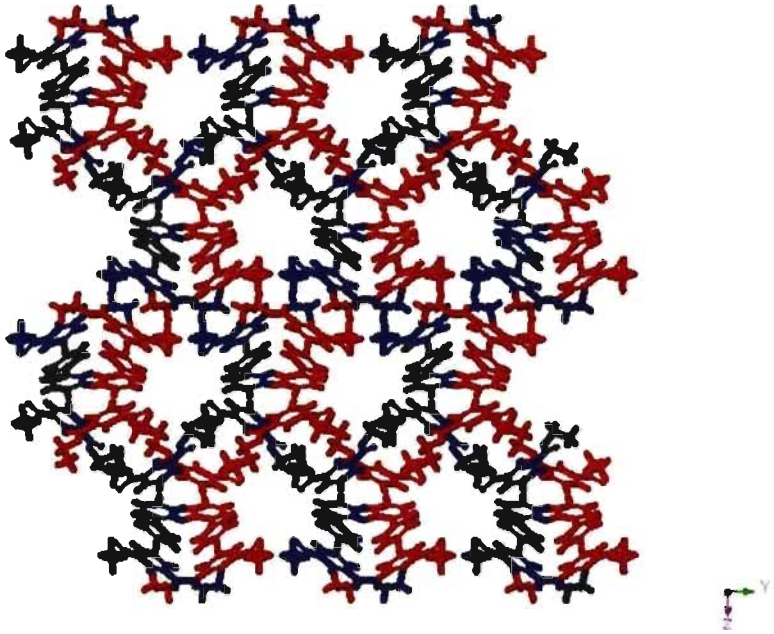

(a)

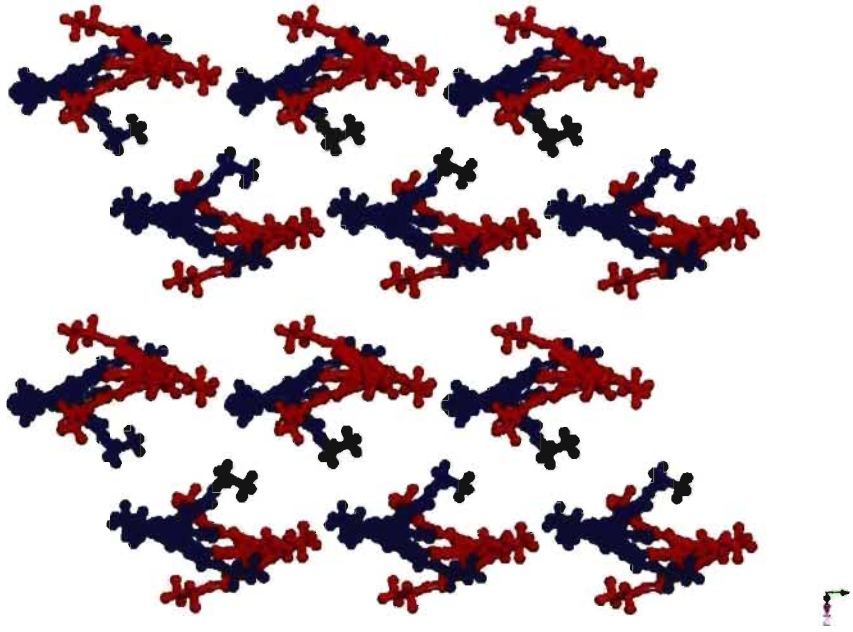

(b)

Figure 5.13 Structure of crystals of tetraester **TE-9** grown from hexane/$CHCl_3$. (a) View along the *a* axis showing the crossed layers composed of a single conformer (red or blue). (b) View of the crystal structure showing cross-linked molecules. Guest molecules of chloroform are omitted for clarity.

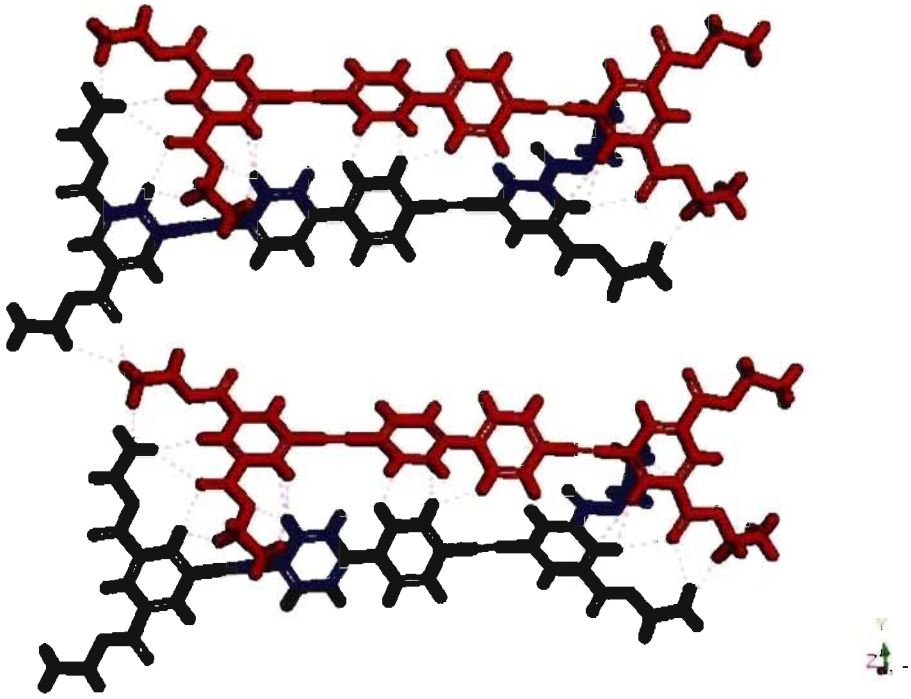

Figure 5.14 View along the *c* axis showing interactions between neighboring conformers of tecton **TE-9**. Short contacts are represented by broken lines.

As shown in Figure 5.13, crystals of tetraester **TE-9** are composed of interwoven layers, each containing a single conformer. Figure 5.14 shows that the molecules in adjacent layers interact with their neighboring conformers by forming a number of close contacts, with average H···H and O···H distances of 2.718 and 2.703 Å. The special hydrogen-bonding pattern proposed in the model of 2D adsorption (Figure 5.11) is not observed in 3D.

Comparison of the observed 3D structure of tetraester **TE-9** with the proposed 2D nanopattern formed by adsorption on HOPG does not reveal impressive parallels. It is reassuring that tetraester **TE-6** and extended analogue **TE-9** both favor square 2D networks in which the molecular components are packed with their long axes perpendicular.

However, this similarity is partly fortuitous, because expansion of the network has occurred at the expense of a lower density of coverage. This may help explain the reluctance of extended tetraester **TE-9** to form large domains, as well as its inability to crystallize in 3D without including molecules of solvent, or without forming interwoven layers. All these observations suggest that compound **TE-9** is not endowed with a high level of ability to form periodic structures, either in 2D or 3D.

5.3.7 2D Nanopatterns Formed by Tetraester TE-7

Tetraester **TE-7** is identical to compound **TE-6**, except that the isophthalate units are linked to a diethynylnaphthyl core instead of to a diethynylphenyl core. The molecular length remains the same, so comparison of the 2D nanopatterns produced by adsorption on HOPG can be investigated by STM to shed light on the role of the core in controlling adsorption. The observed STM images are provided in Figures 5.15 and 5.16. The structure can be interpreted as the square network favored by analogues **TE-6** and **TE-9**; however, the domains are small and do not have the impressive long-range uniformity seen in the case of tetraester **TE-6**.

The schematic representation in Figure 5.16a highlights the square pattern formed by adsorbed tetraester **TE-7**. Figure 5.16b shows that various cavities in the nanopattern have different sizes and shapes. These differences are a logical consequence of the particular molecular core present in compound **TE-7**. Specifically, the molecular models in Figures 5.17 and 5.18 indicate how different cavities (highlighted in gray) can arise from the

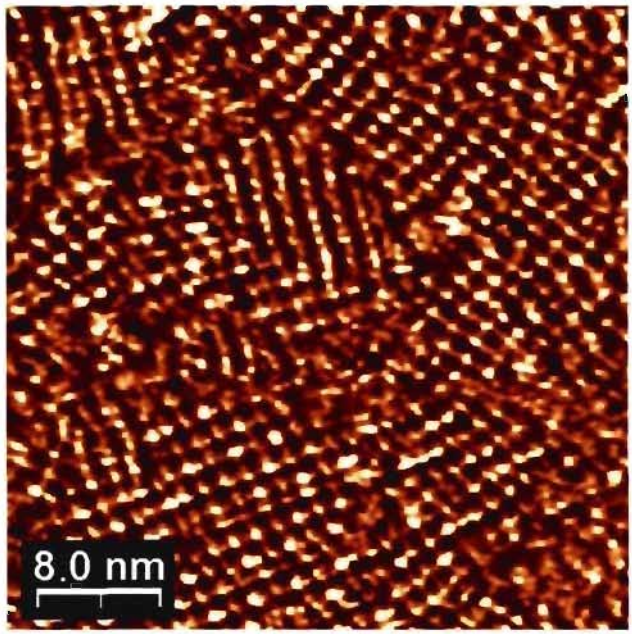

(a)

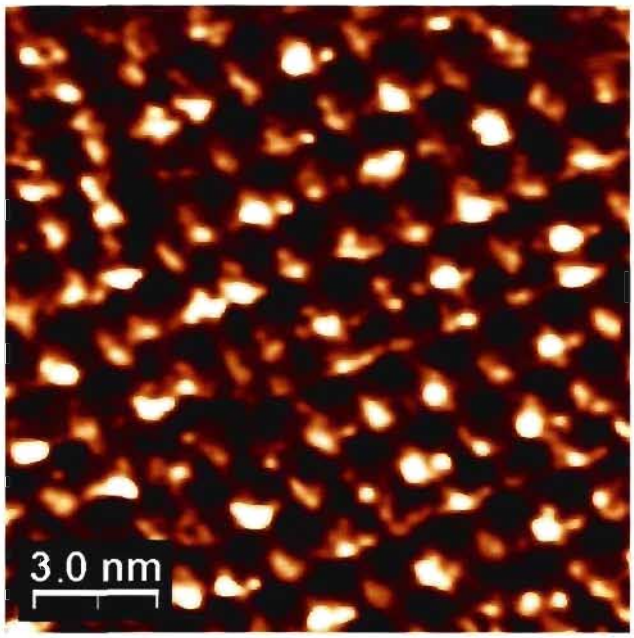

(b)

Figure 5.15 STM images of 2D nanopatterns formed by the adsorption of tetraester **TE-7** on HOPG (deposition from heptanoic acid, with V_{bias} = -1.5 V and I_{set} = 50 pA). (a) Large-scale image showing different domains. (b) Higher-resolution image showing inhomogeneous structures.

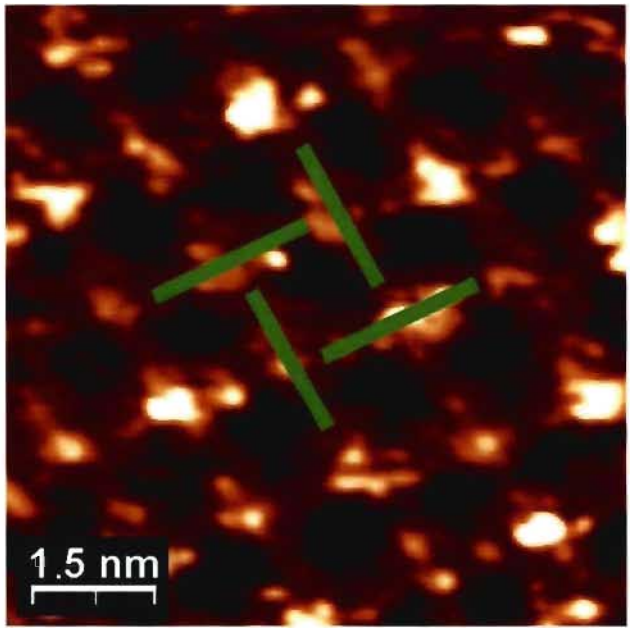

(a)

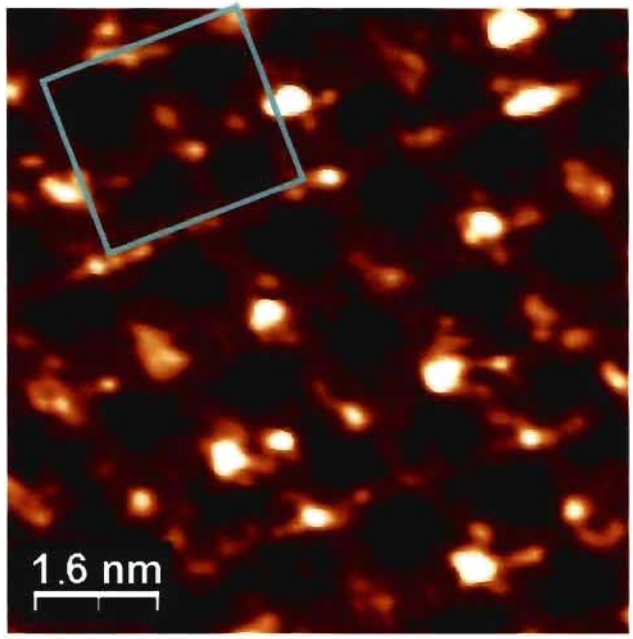

(b)

Figure 5.16 Enlarged STM images of 2D nanopatterns formed by the adsorption of tetraester **TE-7** on HOPG. (a) Schematic representation of the square network, with green bars representing individual molecules. (b) Cavities in the square networks with different shapes and sizes (highlighted in light blue).

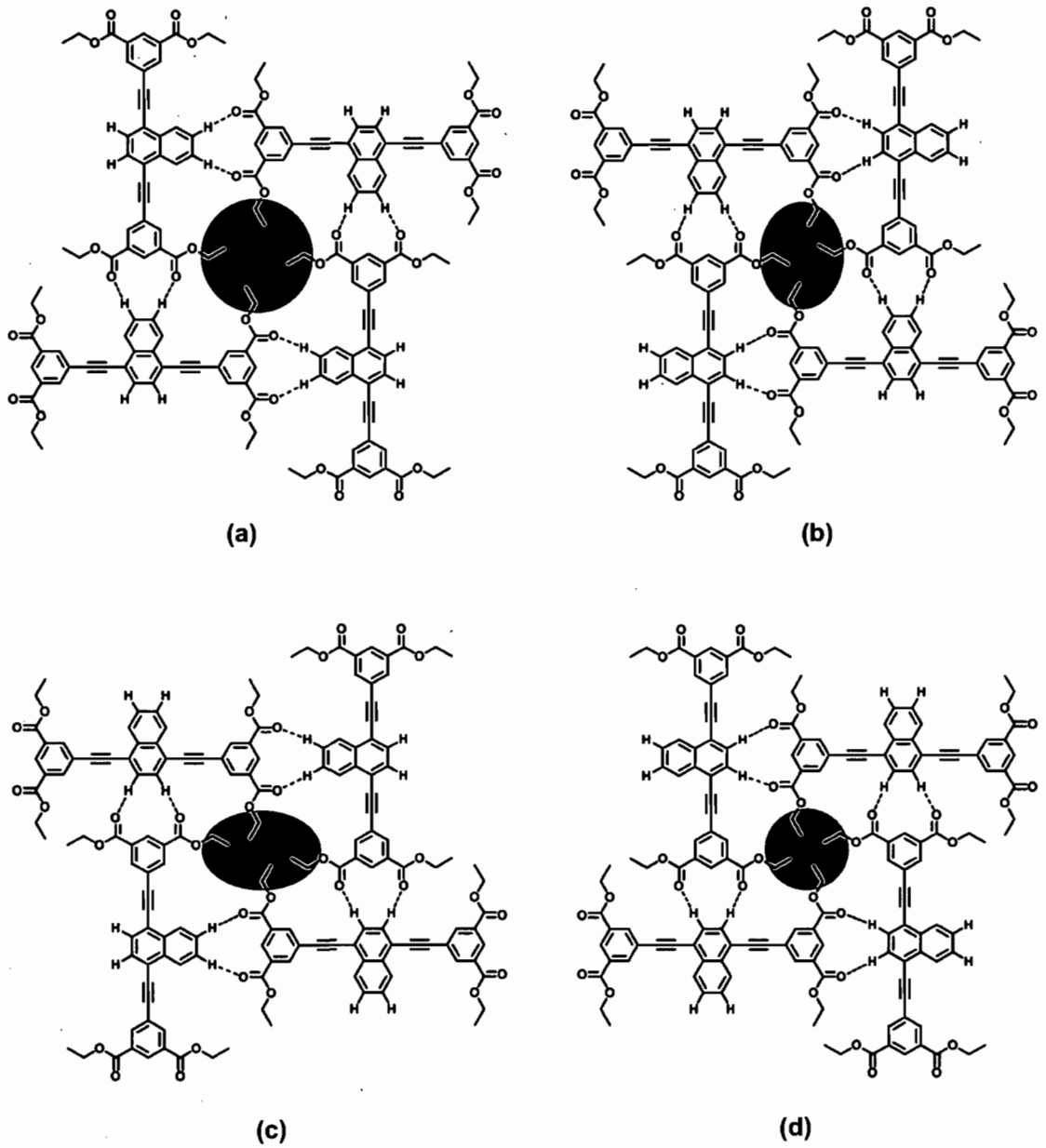

Figure 5.17 Proposed molecular models showing four possible hydrogen-bonded square networks formed by adsorbed tetraester **TE-7**, with cavities of different shapes and sizes highlighted in gray. C-H···O hydrogen bonds are represented by broken lines.

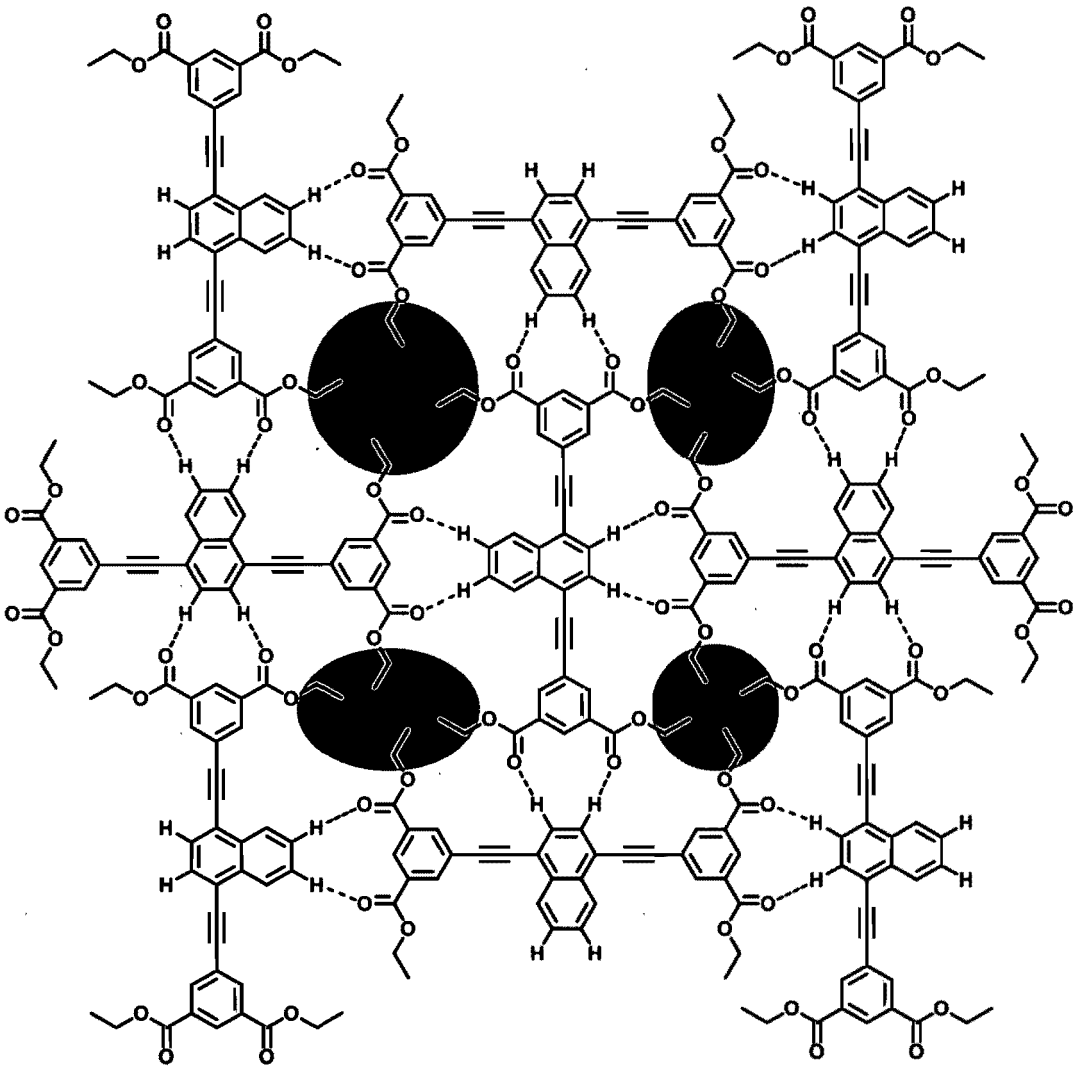

Figure 5.18 Tentative molecular model showing a combination of four possible square networks formed by adsorbed tetraester **TE-7**, with cavities highlighted in gray.

asymmetry of the naphthalene core with respect to the long molecular axis. Molecular models in Figure 5.17 suggest that tetraester **TE-7** can in fact produce four possible square networks, depending on the relative orientations of the naphthyl groups. Models (a) and (b) show motifs held together by C–H···O hydrogen bonds formed between carbonyl oxygen atoms and naphthalene C–H bonds only at the 2,3- or 6,7-positions, respectively. In contrast, model (c) or (d) shows that two of the naphthalene groups in the tetrameric

aggregate can use C-H bonds at the 2,3-positions, and the other two naphthalene groups can use C-H bonds at the 6,7-positions. Juxtaposition of the four possible square networks, as shown in Figure 5.18, can reproduce the irregular nanopattern highlighted in Figure 5.16b. This analysis provides strong support for our interpretation of the adsorption of tetraesters **TE-6**, **TE-9**, and **TE-7** on HOPG.

5.3.8 2D Nanopatterns Formed by Tetraester TE-8

Tetraesters **TE-8**, **TE-7**, and **TE-6** form a set of three closely analogous structures in which two isophthalate units are linked to conjugated linear cores of constant length derived from 9,10-diethynylanthracene, 1,4-diethynylnaphthalene, and 1,4-diethynylbenzene, respectively. The high affinity of anthracene for adsorption on various substrates, such as graphite and silver,[25-28] suggests that compound **TE-8** is predisposed to form an ordered 2D network. Because analogues **TE-6** and **TE-7** have already shown to produce square networks, we expected anthracene **TE-8** to behave similarly. As planned, it proved to be adsorbed on HOPG under our standard conditions to give well-resolved nanopatterns; unexpectedly, however, it generated linear chains with 2D chirality and not the anticipated square networks. STM images are provided in Figures 5.19-5.20.

Figure 5.19a shows multiple well-ordered domains with non-specific orientations, indicating that tetraester **TE-8** does not adopt a preferred orientation with respect to the underlying HOPG. Figure 5.19b shows well-ordered monolayers composed of linear chains. The bright protrusions correspond to individual molecules of compound **TE-8**. Figure

5.20a shows 2D nanopatterns with two distinct domains (A and B). The brightest contrast in each chain corresponds to the anthracene cores of tetraester **TE-8** due to its higher electron density, and ethyl groups fill the darker rows between adjacent chains.

As shown in Figures 5.20c and 5.20d, higher-resolution STM images of domains A and B with superimposed CPK models showed them to be mirror images. The unit cells for the enantiomorphous domains were found to be chiral, with parameters a = ~1.15 nm, b = ~2.46 nm, and γ = ~78°. In each model, the molecules that make up the chains correspond to the two conformations denoted by λ and δ in Figure 5.20b, which are enantiomorphic in 2D. In the gas phase, tetraester **TE-8** undergoes rapid rotation around the ethynylene linkers. In a closely analogous compound, 1,4-bis[(5-tert-butyl-3-formyl-4-hydroxyphenyl)ethynyl]benzene, the barrier to rotation around the ethynylene spoke was calculated to be only 0.037 eV.[29] In contrast, the adsorbed molecules are confined by the substrate, and packing appears to be optimized when the tetraester adopts the chiral λ and δ structures shown in Figure 5.20b, and when homochiral chains are created from either λ or δ. These preferences may reflect the peculiar structure of tetraester **TE-8**, which incorporates a long molecular axis but also has a thick core derived from anthracene. The favored orientation of the ester groups presumably allows space between adjacent molecules in the 2D assembly to be filled effectively. Similar 2D chirality arising from surface-confined conformations has been observed previously in porphyrin derivatives[30-33] and in other adsorbed species.[29, 34]

Figure 5.21c shows that a single enantiomer of tecton **TE-8** generates a homochiral linear chain by forming C–H···O hydrogen bonds between carbonyl oxygen atoms and

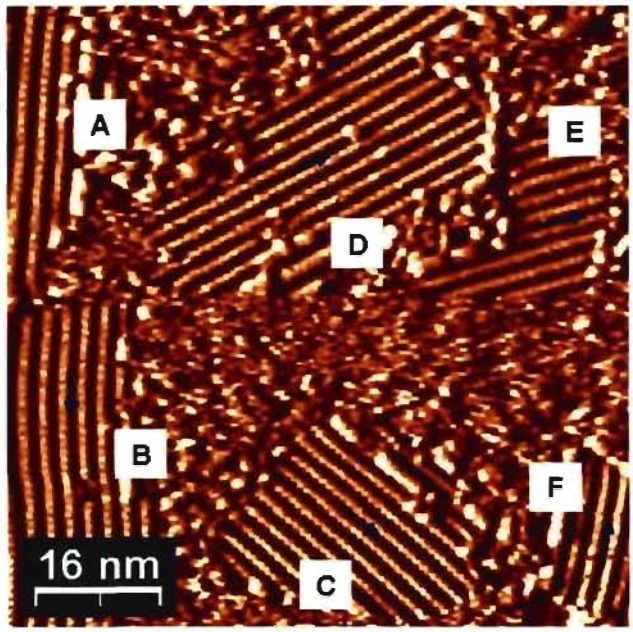

(a)

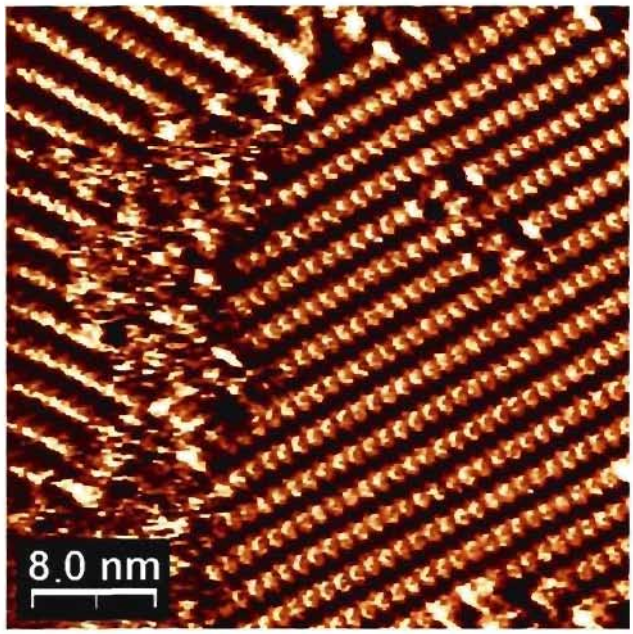

(b)

Figure 5.19 STM images of 2D nanopatterns produced by the adsorption of tetraester **TE-8** on HOPG (deposition from heptanoic acid, with V_{bias} = -1.5 V and I_{set} = 50 pA). (a) Large-scale image (over an area of 80 nm × 80 nm) showing six domains labeled A-F with diverse orientations relative to HOPG (shown with blue arrows). (b) Higher-resolution image showing distinct linear chains.

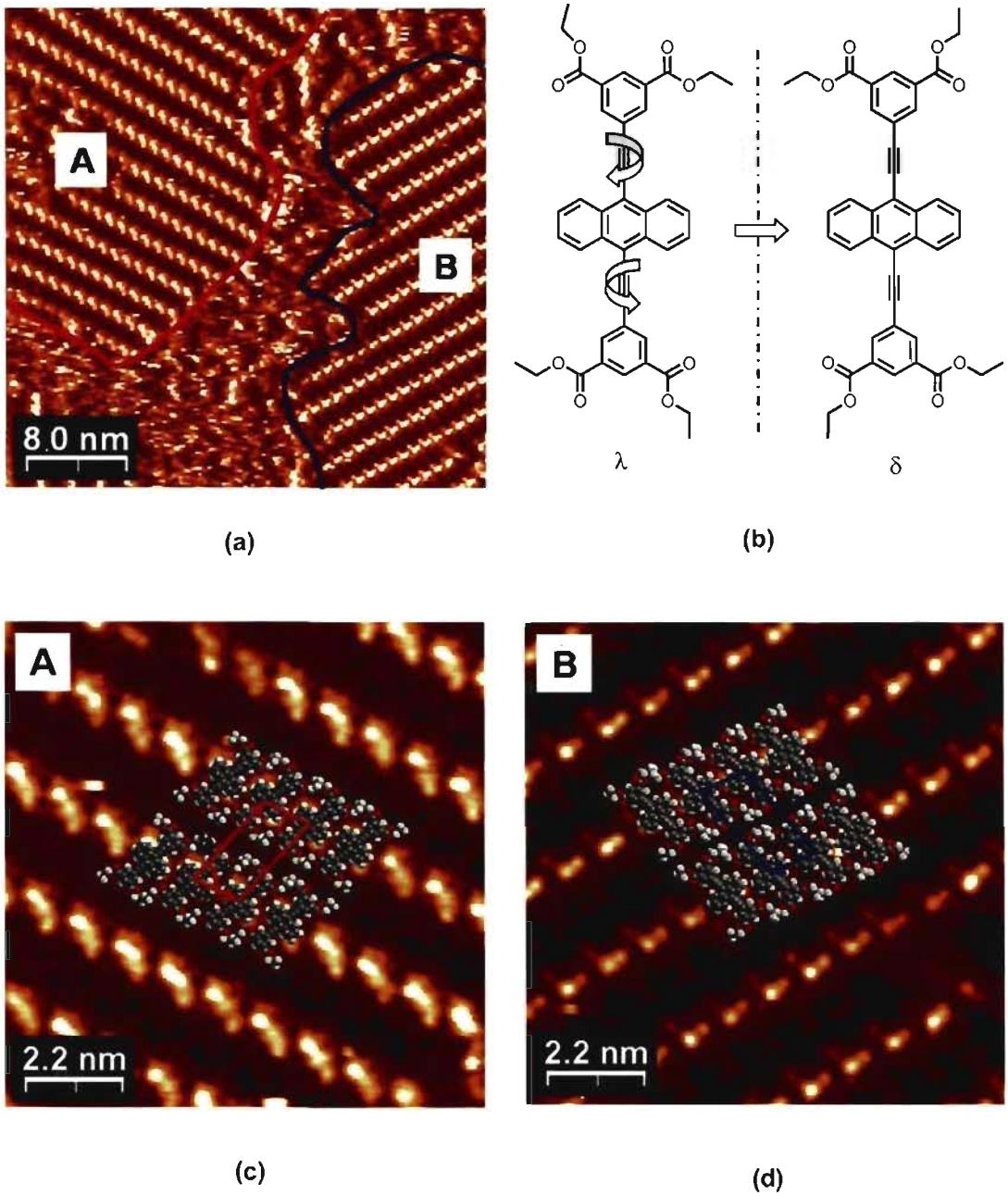

Figure 5.20 STM images of 2D nanopatterns formed by the adsorption of tetraester **TE-8** on HOPG (deposition from heptanoic acid, with V_{bias} = -1.5 V and I_{set} = 100 pA). (a) Large-scale image showing two distinct domains (A and B). (b) Molecular structures of 2D enantiomers of tetraester **TE-8** (λ and δ). (c) (d) Enlarged STM images of domains A and B, respectively, with superimposed CPK models showing 2D chirality. The unit cells are highlighted in red and blue.

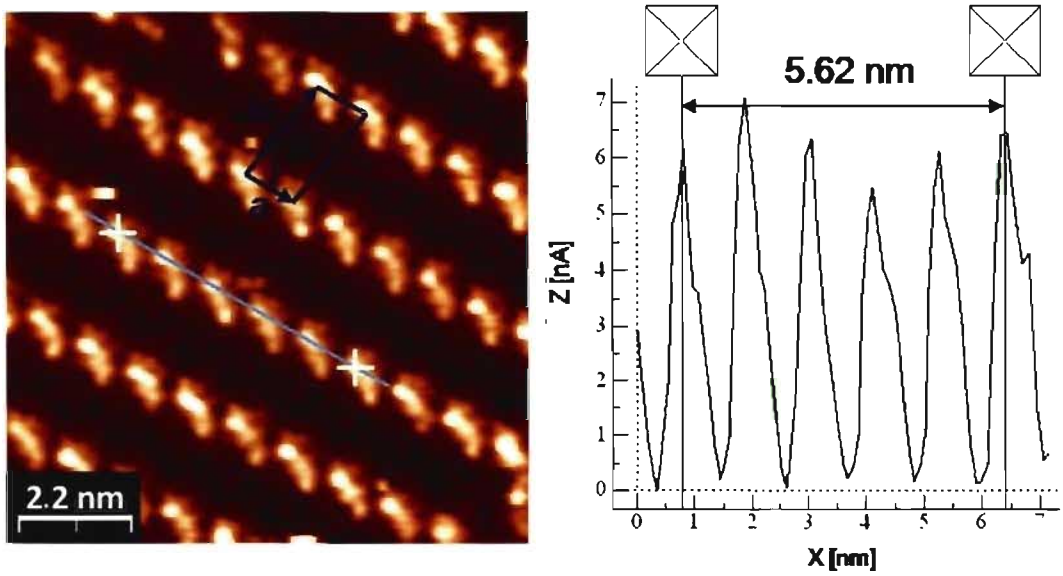

(a)

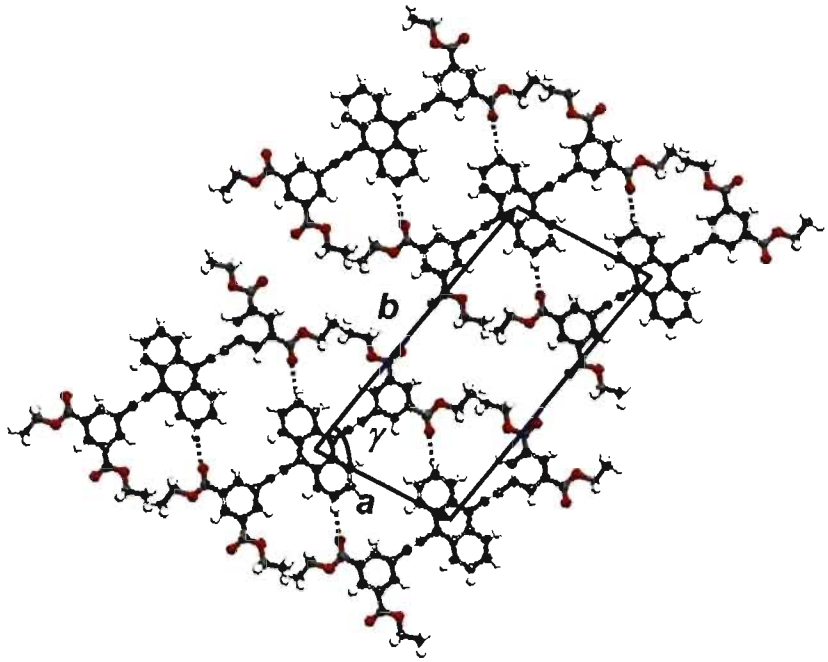

(c)

Figure 5.21 (a) STM image of the 2D nanopatterns produced by the adsorption of tetraester **TE-8**. The unit cell is highlighted in blue. (b) Profile of molecules aligned in a chain. (c) Proposed molecular model of hydrogen-bonded chains formed by tetraester **TE-8**. The unit cell is highlighted in blue. Hydrogen bonds are represented by broken lines.

aromatic C–H bonds. Assuming that the H···O distance is 2.42 Å, the unit cell parameters are calculated to be a = ~1.16 nm, b = ~2.38 nm, and γ = ~78°, which are consistent with the observed values shown in Figure 5.21a, as determined by a surface profile of adjacent molecules within a chain (Figure 5.21b). In this way, the proposed hydrogen-bonding motif can be considered to be supported by experimental evidence. Furthermore, a similar hydrogen-bonding motif was also found in the 3D structure of tetraester **TE-6** (Figure 5.9).

5.3.9 3D Crystal Structure of Tetraester TE-8

Additional information about the ability of tetraester **TE-8** to form ordered assemblies was obtained by solving its crystal structure. Suitable crystals were grown by allowing vapors of hexane to diffuse into a solution in chloroform, and their structure was determined by X-ray diffraction. Views of the structure are provided in Figures 5.22-5.23. The resulting crystals were found to have the composition **TE-8** • $CHCl_3$ and to belong to the P-1 space group, with unit cell parameters a = 9.019 (7) Å, b = 10.271 (12) Å, c = 13.319 (11) Å, α = 67.41(5)°, β = 73.35 (3)°, and γ = 64.22(4)°.

As expected, based on the nearly flat aromatic structure of tetraester **TE-8** and on the behavior of related compounds discussed above, the crystal is composed of sheets (Figure 5.23a). Within the sheets, each molecule interacts with four neighbors by forming close contacts with average distances less than 3.0 Å (Figure 5.23b). No C–H···O hydrogen bonds involving carbonyl oxygen atoms and aryl C–H bonds are present, as proposed to account for the observed 2D nanopatterns. Adjacent sheets are presumably associated by

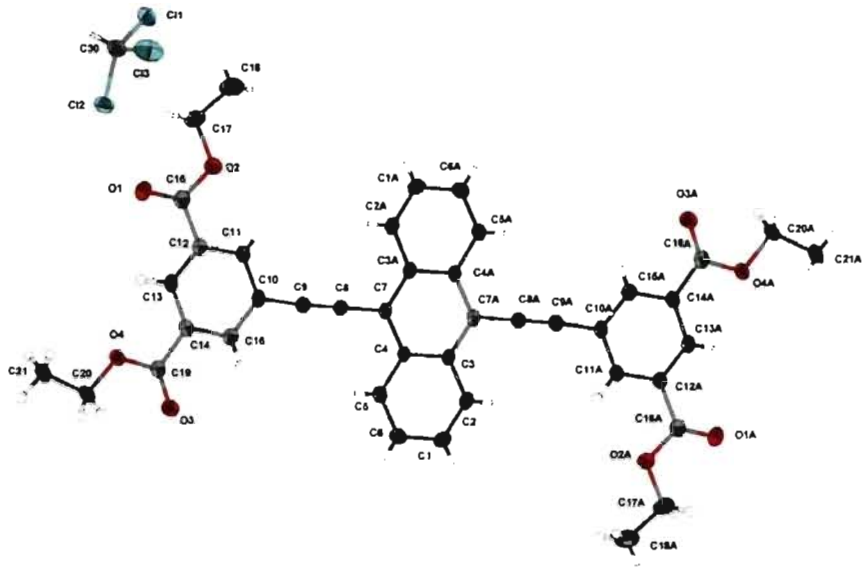

(a)

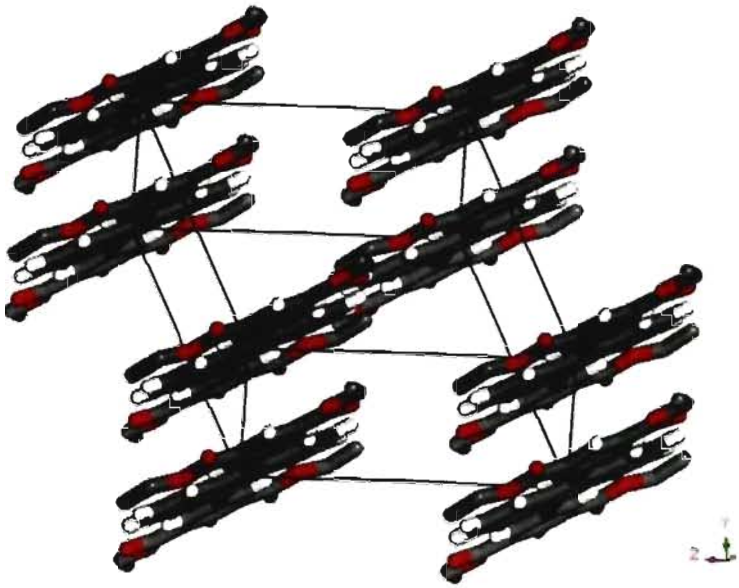

(b)

Figure 5.22 (a) ORTEP view of the structure of crystals of tetraester **TE-8** grown from hexane/$CHCl_3$, with the numbering scheme adopted. Ellipsoids are drawn at 30% probability level. Hydrogen atoms are represented by a sphere of arbitrary size. (b) View of the unit cell, with $CHCl_3$ removed for clarity.

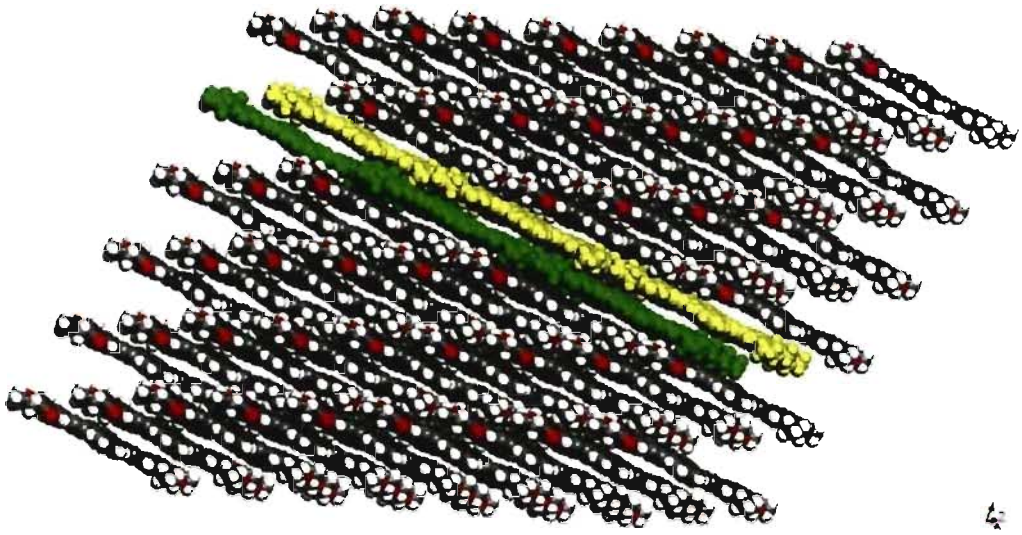

(a)

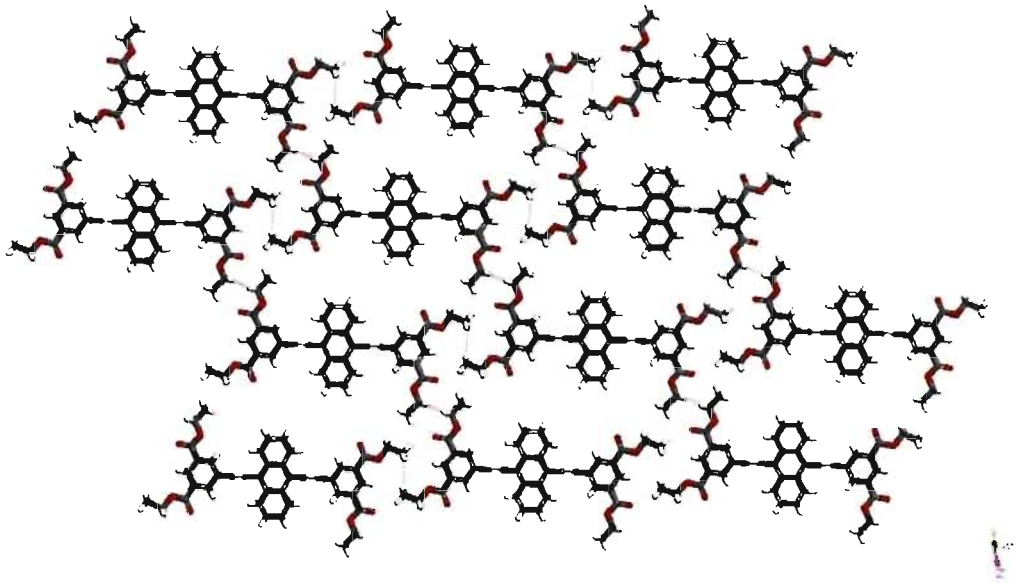

(b)

Figure 5.23 The structure of crystals of tetraester **TE-8** grown from hexane/$CHCl_3$. (a) View of the crystal structure showing stacked sheets, with two adjacent layers highlighted in yellow and green. (b) View of the structure showing closely packed molecules within a sheet. Close contacts are represented by broken lines.

π-π stacking, and the separation is approximately 3.5 Å.

The studies summarized above have revealed that tetraesters **TE-5**, **TE-6**, **TE-7**, **TE-8**, and **TE-9** are all readily adsorbed on HOPG and produce three distinct types of 2D nanopatterns, which have been called the butterfly network (**TE-5**), the square network (**TE-6**, **TE-7**, and **TE-9**), and the linear chain (**TE-8**). None of these particular preferences could have been predicted confidently in advance of carrying out STM studies; when viewed with hindsight, however, all the preferences reveal logical choices, and they show that the five tetraesters generate networks that accommodate particular features of their molecular structures. For example, either the square network or the linear chain would be unacceptable for tetraester **TE-5**, due to its short molecular length and the lack of a central aromatic ring that can participate in C–H···O hydrogen bonds. In addition, an open square network derived from anthracene-substituted tetraester **TE-8** would leave a significant fraction of the surface uncovered, whereas the alternative linear chain structure offers a more closely packed arrangement. In such ways, the tetraesters select periodic 2D structures that avoid significant shortcomings. It is noteworthy that the 2D structures generated by tetraester **TE-8** are chiral, although the molecule itself is achiral. This interesting phenomenon led us to rationally design new tectons to produce 2D chiral nanopatterns, thus leading to the STM studies reported in Chapter 6.

5.3.10 Competitive Adsorption of Tetraesters on HOPG

As a group, the tetraesters all showed good affinity for HOPG and produced well-resolved images when studied by STM. To further evaluate their relative ability to be adsorbed on HOPG, competition experiments were carried out using mixtures of tetraesters **TE-5**, **TE-6**, and **TE-8**. STM images were recorded under our standard conditions after deposition of a mixture of two tetraesters on HOPG. The resulting images are shown in Figures 5.24-5.26.

Figure 5.24 shows STM images of a 1:1 mixture of tetraesters **TE-6** (diethynylbenzene spacer) and **TE-8** (diethynylanthracene spacer) adsorbed on HOPG. Both images display a few domains composed of crystalline phases (**I** and **II**), as well as some amorphous phases. Phase **I** produces larger domains and corresponds to square networks built only from tetraester **TE-6**. Phase **II** yields smaller domains and corresponds to linear chains formed by tetraester **TE-8**. It is noteworthy that tetraester **TE-6** dominates the 2D crystallization when co-deposited with tetraester **TE-8**, which has a potentially significant advantage derived from the inherently strong affinity of the anthracene core for HOPG. We suggest that the high density of C–H···O hydrogen bonds makes square networks more stable than linear chains. If so, the behavior of tetraesters **TE-6** and **TE-8** provides an example of a system in which interadsorbate interactions play a more decisive role than adsorbate-surface interactions in determining what 2D nanopattern ultimately emerges.

When equimolar mixtures of tetraesters **TE-5** and **TE-8** were co-deposited (Figure 5.25), only compound **TE-8** was adsorbed. Even in large-scale images covering an area of

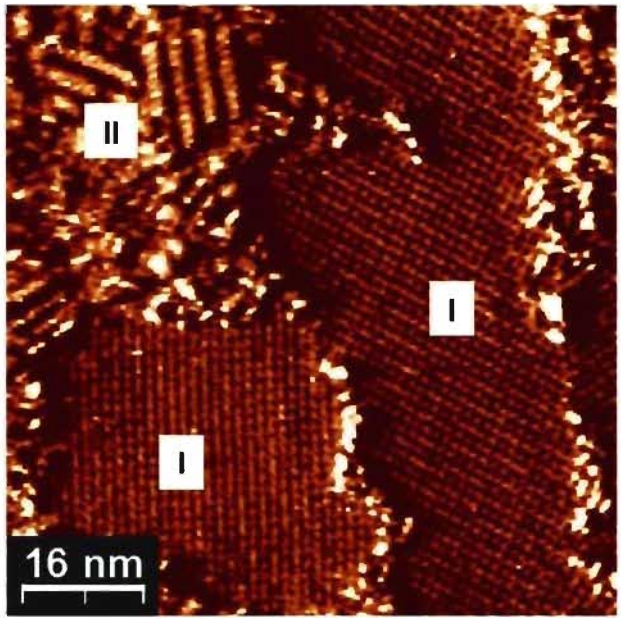

(a)

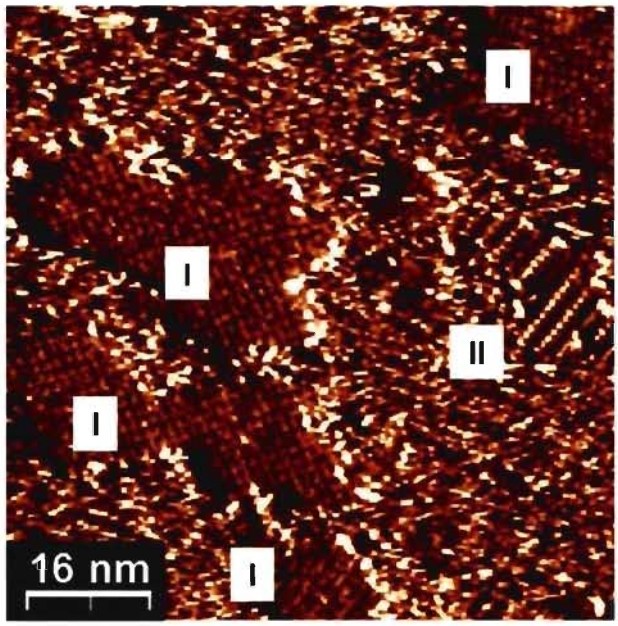

(b)

Figure 5.24 STM images showing the competitive adsorption of equimolar mixtures of tetraesters **TE-6** and **TE-8** (deposition from heptanoic acid, V_{bias} = -1.5 V and I_{set} = 100 pA). Ordered phase I corresponds to square networks built from compound **TE-6**, and phase II corresponds to linear chains formed by compound **TE-8**.

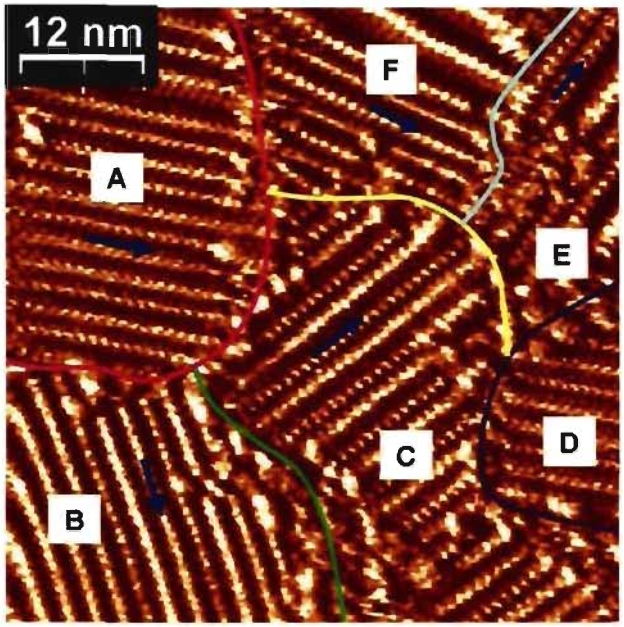

(a)

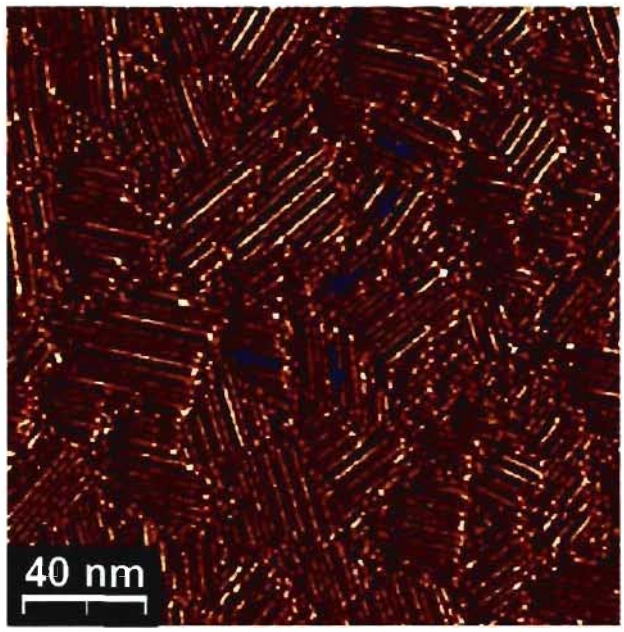

(b)

Figure 5.25 STM images showing the competitive adsorption of equimolar mixtures of tetraesters **TE-5** and **TE-8** (deposition from heptanoic acid, V_{bias} = -1.5 V and I_{set} = 100 pA). (a) Image over an area of 60 nm × 60 nm, with six domains labelled A-F, the boundary of domains highlighted in color, and non-specific orientations indicated by blue arrow. (b) Large-scale image showing an area of 200 nm × 200 nm.

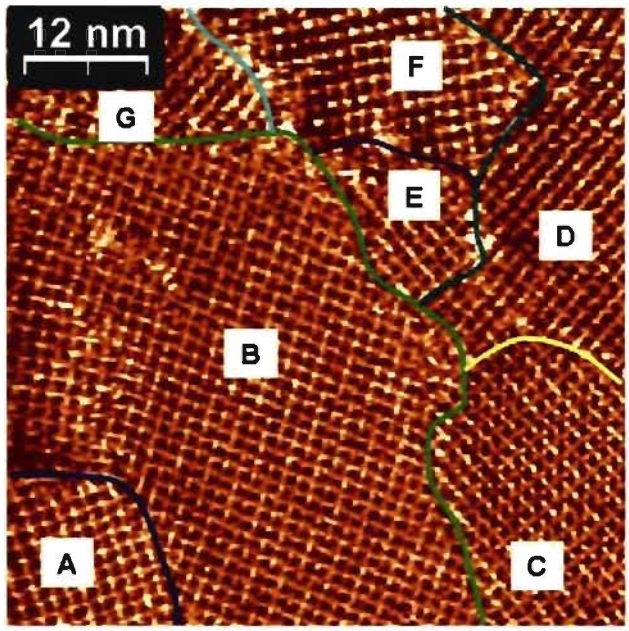

(a)

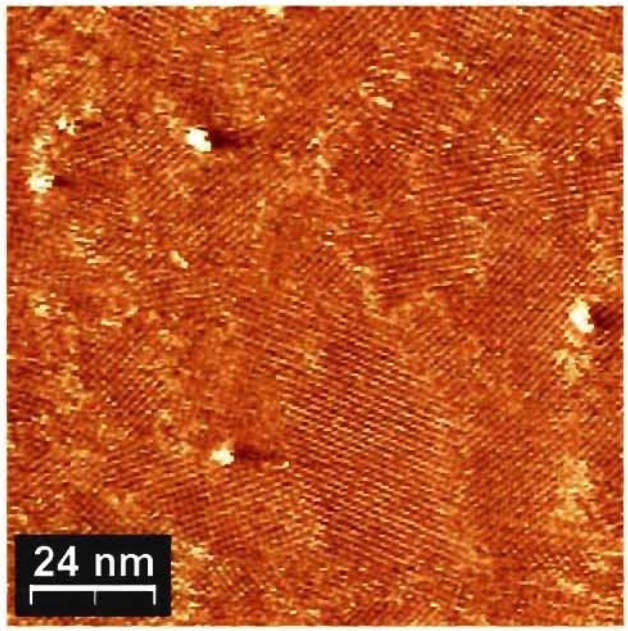

(b)

Figure 5.26 STM images showing the competitive adsorption of equimolar mixtures of **TE-5** and **TE-6** (deposition from heptanoic acid, V_{bias} = -1.5 V and I_{set} = 100 pA). (a) Image of an area of 60 nm × 60 nm, showing multiple domains of square networks, labelled A-G, with the boundary of the domains highlighted in color. (b) Large-scale image of an area of 120 nm × 120 nm, showing well-ordered networks.

200 nm × 200 nm, as shown in Figure 5.25b, only multiple domains consisting uniquely of tetraester **TE-8** are observed, and there are no traces of tetraester **TE-5**. The ability of tetraester **TE-8** to win this competition so overwhelmingly reflects the high affinity of its anthracene core for adsorption on HOPG. Similarly, in a competition involving a 1:1 mixture of tetraesters **TE-5** and **TE-6**, only compound **TE-6** was adsorbed, producing well-ordered square networks over a large area of 120 nm × 120 nm (Figure 5.26).

Competitive adsorption has been found to depend on the interplay of kinetic and thermodynamic factors.[35] The composition of the monolayer at equilibrium is related to the difference in free energy of the adsorbed components. The free energy associated with adsorption and monolayer formation involves contributions from interadsorbate interactions and adsorbate-surface interactions.[35] The success of tetraester **TE-6** (diethynylbenzene spacer) in the competitions outlined above appears to reflect contributions from both sources. Its extended planar structure assures strong adsorption on HOPG, and its ability to form a square network that is efficiently packed and stabilized by multiple C-H···O hydrogen bonds provides further energetic benefits. Together, these features allow tetraester **TE-6** to beat shorter analogue **TE-5** and to compete successfully with anthracene-substituted analogue **TE-8**.

5.4 Summary

In this chapter, we have presented the results of a systematic study of a family of five tetraesters **TE-5** to **TE-9** focusing on their 3D assembly, as determined by X-ray diffraction,

and on their 2D assembly on the surface of HOPG, as determined by STM at the liquid-solid interface. The five compounds have similar molecular structures, including largely planar linear conjugated cores grafted to isophthalate groups. Differences within the series have allowed us to probe the effects of systematic structural changes, including increased molecular length and width.

An increase in length, as shown by the behavior of tetraesters **TE-5** (ethyne core), **TE-6** (diethynylbenzene core), and **TE-9** (diethynylbiphenyl core), led to a change in 2D nanopatterns from the butterfly structure of compound **TE-5** to the square structures of the longer analogues. In all three cases, aromatic C-H···O hydrogen bonds appear to be crucial in directing the formation of well-ordered 2D nanopatterns.

In addition, altering the width of the cores proved to have a substantial influence on 2D assembly. Tetraester **TE-8** (anthracene core) produced linear chains different from the square networks generated by analogues **TE-6** (benzene core) and **TE-7** (naphthalene core). A noteworthy observation is that the linear chains generated by achiral tetraester **TE-8** showed 2D chirality when adsorbed on HOPG.

Given that the packing of the various tetraesters in 2D must accommodate the ethyl groups, it is reasonable to expect other esters to assemble in different ways. The effect of changing the ester groups is described in Chapter 6.

Comparison of the 2D and 3D crystallization of the family of tetraesters rarely revealed closely analogous structures. We attribute the observed differences to an important degree of conformational flexibility in the ester groups and to a lack of strong directional interactions able to position adjacent molecules in predictable ways. Nevertheless, certain

fundamental structural preferences are retained in both 2D and 3D, such as the tendency to form relatively closely packed sheets.

The results of competitive adsorption of mixtures of tetraesters **TE-5**, **TE-6,** and **TE-8** demonstrated that compound **TE-6** has a special ability to be adsorbed on HOPG, thereby underscoring the importance of inter-adsorbate interactions, such as hydrogen bonds, relative to adsorbate-surface interactions. This observation provides an encouraging sign that properly designed molecules can engage in strong inter-adsorbate interactions and can thereby create particular 2D nanopatterns that are controlled more by the adsorbate than by the underlying surface.

References

1. Plass, K. E.; Kim, K.; Matzger, A. J. *J. Am. Chem. Soc.* **2004**, *126*, 9042-9053.
2. Mamdouh, W.; Uji-i, H.; Dulcey, A. E.; Percec, V.; De Feyter, S.; De Schryver, F. C. *Langmuir* **2004**, *20*, 7678-7685.
3. De Feyter, S.; Gesquière, A.; Wurst, K.; Amabilino, D. B.; Veciana, J.; De Schryver, F. C. *Angew. Chem. Int. Ed.* **2001**, *40*, 3217-3220.
4. Samorì, P.; Yin, X.; Tchebotareva, N.; Wang, Z.; Pakula, T.; Jäckel, F.; Watson, M. D.; Venturini, A.; Müllen, K.; Rabe, J. P. *J. Am. Chem. Soc.* **2004**, *126*, 3567-3575.
5. Mu, Z.; Yang, X.; Wang, Z.; Zhang, X. *Langmuir* **2004**, *20*, 8892-8896.
6. Abdel-Mottaleb, M. M. S.; De Feyter, S.; Gesquière, A.; Sieffert, M.; Klapper, M.; Müllen, K.; De Schryver, F. C. *Nano Lett.* **2001**, *1*, 353-359.
7. Mamdouh, W.; Uji-i, H.; Gesquière, A.; De Feyter, S.; Amabilino, D. B.; Abdel-Mottaleb, M. M. S.; Veciana, J.; De Schryver, F. C. *Langmuir* **2004**, *20*, 9628-9635.
8. Tao, F.; Bernasek, S. L. *Chem. Rev.* **2007**, *107*, 1408-1453.
9. Love, J. C.; Estroff, L. A.; Kriebel, J. K.; Nuzzo, R. G.; Whitesides, G. M. *Chem. Rev.* **2005**, *105*, 1103-1170.
10. Park, J. S.; Wilson, J. N.; Hardastle, K. I.; Bunz, U. H. F.; Srinivasarao, M. *J. Am. Chem. Soc.* **2006**, *128*, 7714-7715.
11. Liu, L.; Liu, Z.; Xu, W.; Xu, H.; Zhang, D.; Zhu, D. *Tetrahedron* **2005**, *61*, 3813-3817.
12. Ōki, M.; Nakanishi, H. *Bull. Chem. Soc. Jpn.* **1970**, *43*, 2558-2566.

13. Scheiner, S.; Kar, T.; Gu, Y.-L. *J. Bio. Chem.* **2001**, *276*, 9832-9837.

14. Meadows, E. S.; De Wall, S. L.; Barbour, L. J.; Fronczek, F. R.; Kim, M.-S.; Gokel, G. W. *J. Am. Chem. Soc.* **2000**, *122*, 3325–3335.

15. Kuduva, S. S.; Craig, D. C.; Nangia, A.; Desiraju, G. R. *J. Am. Chem. Soc.* **1999**, *121*, 1936-1944.

16. Desiraju, G. R. *Acc. Chem. Res.* **1996**, *29*, 441–449.

17. Hobza, P.; Havlas, Z. *Chem. Rev.* **2000**, *100*, 4253-4264.

18. Venkatesan, V.; Fujii, A.; Ebata, T.; Mikami, N. *J. Phys. Chem. A* **2005**, *109*, 915-921.

19. Vishweshwar, P.; Nangia, A.; Lynch, V. M. *J. Org. Chem.* **2002**, *67*, 556-565.

20. Desiraju, G. R. *Acc. Chem. Res.* **2002**, *35*, 565-573.

21. Scheiner, S.; Kar, T.; Pattanayak, J. *J. Am. Chem. Soc.* **2002**, *124*, 13257-13264.

22. Stepanow, S.; Lin, N.; Vidal, F.; Landa, A.; Ruben, M.; Barth, J. V.; Kern, K. *Nano Lett.* **2005**, *5*, 901-904.

23. The percentage of volume accessible to guests is estimated by a standard method. In this method, the accessible volume is defined by the volume that can be occupied by a spherical probe of radius r constrained to move in a way that its center must remain at a distance no less than r from the closest point on the van der Waals surface of the ordered network. The accessible volume is calculated by using the PLATON program,[24] which uses a default value of 1.20 Å for the radius of the probe. This value is an appropriate model for small guests such as water. The van der Waals radii used to define surfaces for these calculations are as follows: C: 1.70 Å, H: 1.20 Å, N: 1.55 Å, and O: 1.52 Å. If V is the volume of the unit cell and V_g is the guest-accessible volume per unit cell as calculated by PLATON, then the percentage of the volume accessible to guests is given by $100V_g/V$. Although this volume is typically occupied at least in part by included guests, it can be considered to provide a measure of potential porosity.

24. Spek, A. L. PLATON, A Multipurpose Crystallographic Tool; Utrecht University: Utrecht, The Netherlands, 2001. van der Sluis, P.; Spek, A. L. *Acta Crystallogr.* **1990**, *A46*, 194-201.

25. Wei, Y.-H.; Kannappan, K.; Flynn, G. W.; Zimmt, M. B. *J. Am. Chem. Soc.* **2004**, *126*, 5318-5322.

26. Böhringer, M.; Schneider, W.-D.; Berndt, R. *Surf. Sci.* **1998**, *408*, 72-85.

27. Shimooka, T.; Yoshimoto, S.; Wakisaka, M.; Inukai, J.; Itaya, K. *Langmuir* **2004**, *17*, 6380-6385.

28. Wei, Y.; Tong, W.; Zimmt, M. B. *J. Am. Chem. Soc.* **2008**, *130*, 3399-3405.

29. Weigelt, S.; Busse, C.; Petersen, L.; Rauls, E.; Hammer, B.; Bothelf, K. V.; Besenbacher, F.; Linderoth, T. R. *Nature Mater.* **2006**, *5*, 112-117.

30. Jung, T. A.; Schlittler, R. R.; Gimzewski, J. K. *Nature* **1997**, *386*, 696-698.

31. Moresco, F.; Meyer, G.; Rieder, K.-H. *Phys. Rev. Lett.* **2001**, *86*, 672-675.

32. Loppacher, C.; Guggisberg, M.; Meyer, E.; Bammerlin, M.; Lüthi, R.; Schlittler, R.; Gimzewski, J. K.; Tang, H.; Joachim, C. *Phys. Rev. Lett.* **2003**, *90*, 066107.

33. Qiu, X. H.; Nazin, G. V.; Ho, W. *Phys. Rev. Lett.* **2004**, *93*, 196806.

34. Busse, C.; Weigelt, S.; Petersen, L.; Lægsgaard, E.; Besenbacher, F.; Linderoth, T. R. *J. Phys. Chem. B* **2007,** *111,* 5850-5860.

35. Backer, R. T.; Mougous, J. D.; Brackley, A.; Patrick, D. L. *Langmuir* **1999**, *15*, 4884-4891.

CHAPTER 6

Chiral 2D Nanopatterns Created by Derivatives of Isophthalic Acid

6.1 Introduction

Molecular chirality is of central importance in many areas of science and technology, including biology and medicine.[1,2] In the pharmaceutical industry, for example, chiral drugs must typically be made with high enantiomeric purity due to potential side effects of the other enantiomer.[3,4] Enantiomers can often be resolved by classical methods of crystallization,[5-10] and single enantiomers can increasingly be made directly by asymmetric synthesis. Pasteur was the first to conduct chiral resolution when he discovered optical activity by the manual separation of left-handed and right-handed crystals of derivatives of tartaric acid in 1849.[11]

Chirality in 3D is therefore a familiar concept in chemistry. With the invention and development of scanning tunneling microscopy (STM), it has become straightforward to image individual molecules confined to surfaces. With the restraints imposed by confinement on surfaces, chirality can be exhibited by molecules that are achiral in three-dimensional space. Increasingly, surface scientists are familiar with analyzing the conformation and chirality of adsorbed molecules on surfaces.[12-15] Generalizations about 2D chirality created by adsorption and supramolecular self-assembly on surfaces are summarized below.

When adsorbed on surfaces, enantiopure molecules (*R* or *S*) normally produce only one specific arrangement.[16-22] A typical example is tartaric acid,[16] whose *R*,*R* and *S*,*S* enantiomers are both assembled into parallel rows by adsorption on Cu(100). The alignment of individual molecules in each row is switched to the mirror orientation in the enantiomeric assembly, thereby creating visibly chiral surface nanopatterns.[16]

The adsorption of racemic mixtures on surfaces frequently leads to spontaneous separation of enantiomers to form enantiomorphous domains.[12, 13, 23-25] Such a process is called spontaneous resolution. In 3D, however, the formation of these conglomerates is an exception rather than a rule. Most racemic mixtures are known to crystallize as racemates with the unit cell composed of an equal number of molecules with opposite chirality.[26-28] It was originally proposed by Stewart and Arnett that 2D confinement enhances chiral discrimination between enantiomers.[24] A typical example is 5,6,11,12-tetraphenylnaphthacene (rubrene),[25] which has a chiral and nonplanar core due to intramolecular steric hindrance. STM investigations have shown that adsorption of racemates of rubrene on Au(111) can produce supramolecular decagons with spontaneous chiral resolution of the racemate into disjointed homochiral complex architectures.[25] Heptahelicene, which has a chiral helical structure, is an exception. When adsorbed on Cu (111), it does not undergo 2D spontaneous resolution into enantiomers, but instead it produces domains consisting of the racemate rather than individual enantiomers.[29]

Achiral or prochiral molecules have been found to create either spontaneously separated enantiomorphic (homochiral) domains or racemic (heterochiral) domains based on the confinement of surfaces and the loss of symmetry.[30-33] A typical example is achiral succinic acid which produced two enantiomorphous bisuccinate mirror domains on Cu(100). Interestingly, a small amount of enantiopure tartaric acid (2 mol %) can drive the racemic succinic acid layer toward a homochiral system.[30]

As discussed in Chapter 5, tetraester **TE-8** was found unexpectedly to generate 2D homochiral nanopatterns on HOPG. In this chapter, four related achiral compounds, **TE-10**,

TA-10, TE-11, and **TA-11**, were purposefully designed to create 2D chirality by adsorption on HOPG (Scheme 6.1). As expected, tetraesters **TE-10** and **TE-11** were found to produce enantiomeric domains. Surprisingly, tetraacid **TA-10** generated both homochiral and racemic domains, which were able to merge into each other smoothly. Unexpectedly, tetraacid **TA-11**

Scheme 6.1 Chemical structures of compounds **TE-10**, **TA-10**, **TE-11**, and **TA-11**.

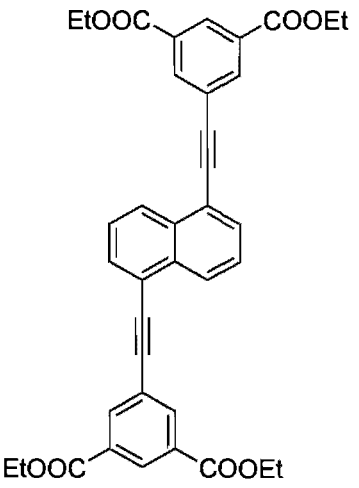

TE-10

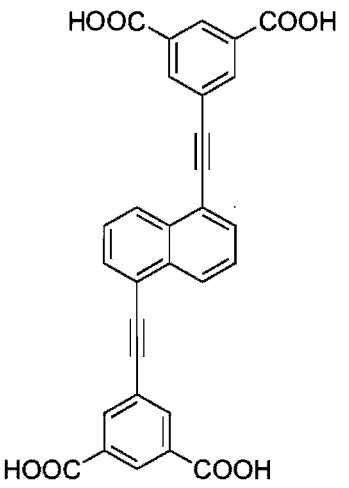

TA-10

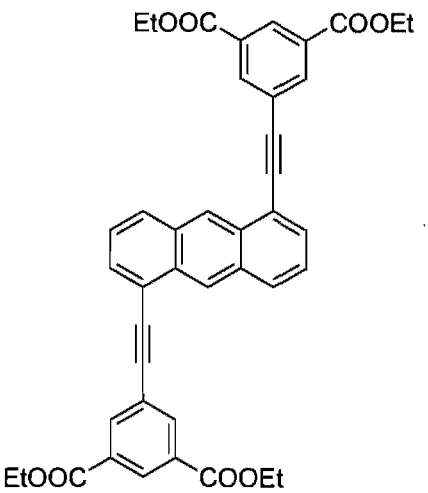

TE-11

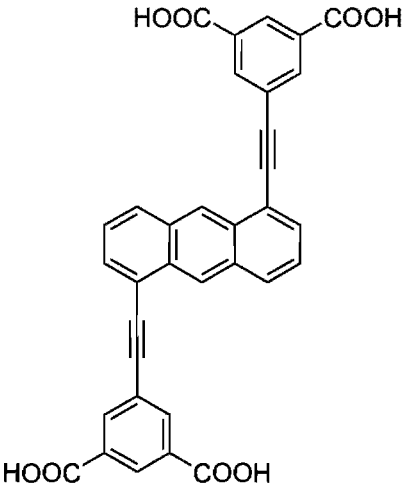

TA-11

was found to form a new racemic polymorph instead of homochiral domains.

6.2 Design and Synthesis of Compounds Expected to Show 2D Chirality

The above-mentioned molecules were systematically designed to have 2D chirality by changing the symmetry of the core with respect to the long molecular axis. Once adsorbed, these molecules cannot be superimposed on their mirror images due to surface confinement. In this chapter, we will present STM investigations of their 2D chirality when adsorbed on HOPG.

6.2.1 Synthesis of Compounds TE-10 and TA-10

Tetraester **TE-10** and analogous tetraacid **TA-10** were synthesized as shown in Scheme 6.2. Commercially available 1,5-diaminonaphthalene was diazotized under standard conditions and converted into the known 1,5-diiodonaphthalene (**25**)[34] in 85% yield. Diiodide **25** was then coupled with (trimethylsilyl)acetylene in the presence of catalytic dichlorobis(triphenylphosphine)palladium(II) and copper(I) iodide to provide intermediate **26**[34] in 90% yield. Intermediate **26** was deprotected to give 1,5-diethynylnaphthalene (**27**)[34] in 76% yield, and Sonogashira coupling with diethyl 5-iodobenzene-1,3-dicarboxylate (**17**) provided tetraester **TE-10** in 87% yield. The corresponding tetraacid **TA-10** was then prepared in 82% yield by hydrolysis and subsequential acidification using concentrated HCl.

Scheme 6.2 Synthesis of compounds **TE-10** and **TA-10.**

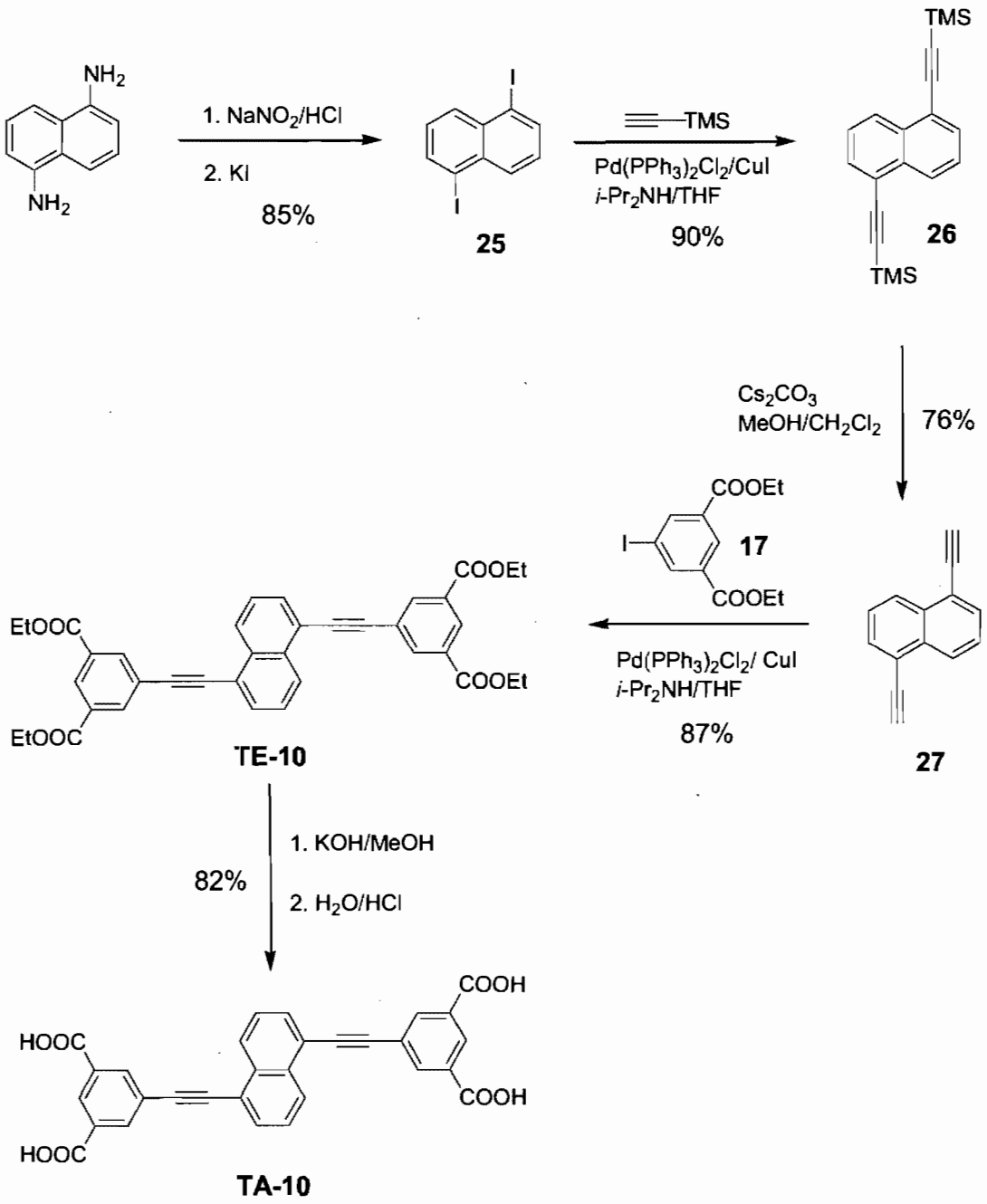

Scheme 6.3 Synthesis of tectons **TE-11** and **TA-11**

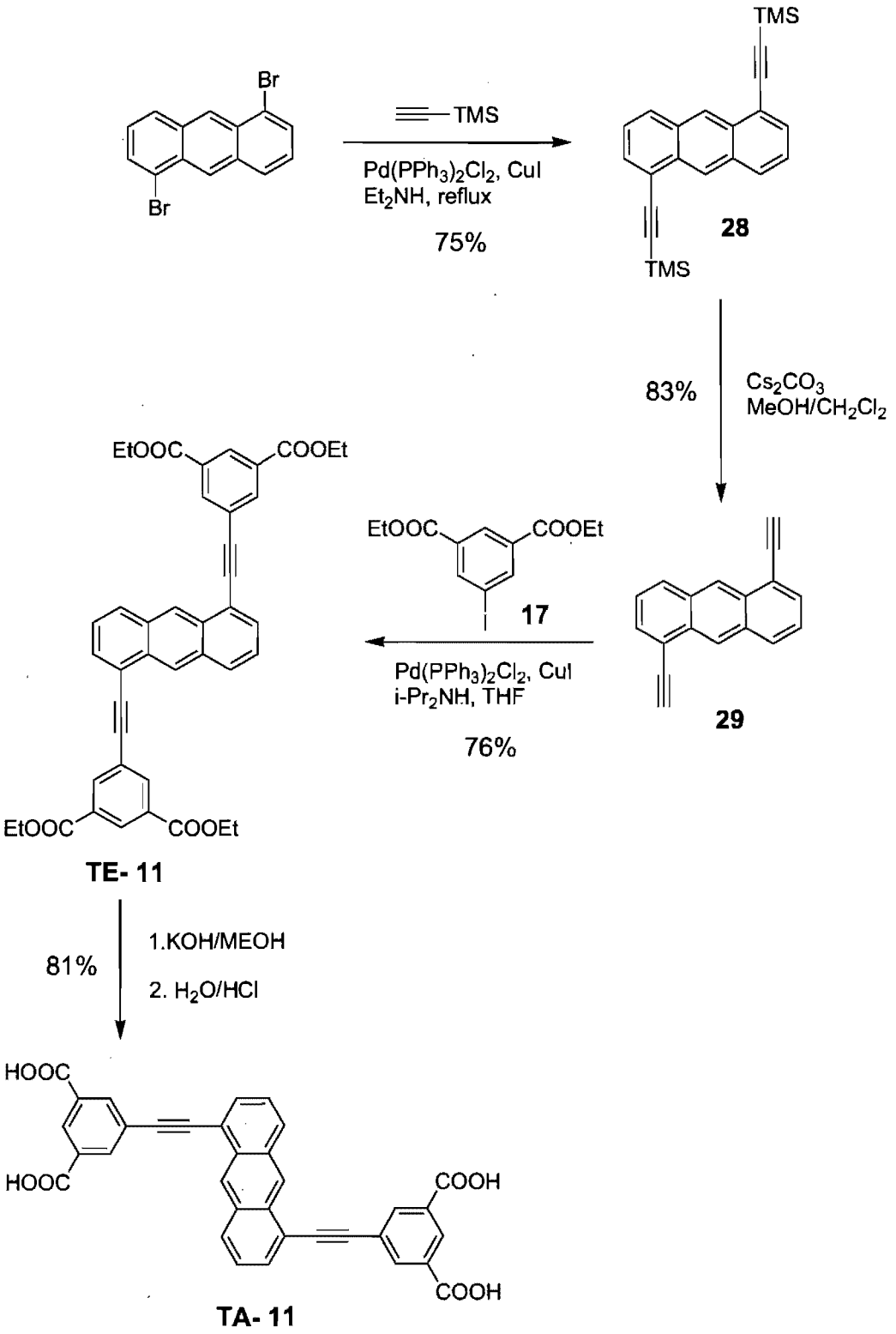

6.2.2 Synthesis of Compounds TE-11 and TA-11

The syntheses of tetraester **TE-11** and tetraacid **TA-11** are illustrated in Scheme 6.3. Sonogashira coupling of commercially available 1,5-dibromoanthracene with (trimethylsilyl)acetylene in the presence of catalytic dichlorobis(triphenylphosphine)palladium(II) and copper(I) iodide provided intermediate **28**[35] in 75% yield, which was then deprotected to give 1,5-diethynylanthracene (**29**)[35] in 83% yield. Sonogashira coupling of compound **29** with diethyl 5-iodobenzene-1,3-dicarboxylate (**17**) produced tetraester **TE-11** in 76% yield, and subsequent hydrolysis and acidification with concentrated HCl gave tetraacid **TA-11** in 81% yield.

6.3 2D Chiral Nanopatterns Formed by Tetraester TE-10

As shown in Chapter 5, tetraesters **TE-6**, **TE-7,** and **TE-9,** with different cores of phenyl, naphthalene, and biphenyl, respectively, produce similar square networks characterized by a perpendicular orientation of the principal molecular axes of neighboring molecules and by C–H···O hydrogen bonds between carbonyl oxygen atoms and aromatic C–H bonds. Cavities of the square networks formed by tecton **TE-7** are not homogenous but rather have variable sizes and shapes resulting from different orientations of the naphthalene core with respect to the long molecular axis. In the case of tetraester **TE-9**, however, large-scale periodicity was not observed, possibly because the increased molecular size reduced mobility on the surface and retarded assembly driven by hydrogen

bonding.

Scheme 6.4 2D enantiomers of tetraester **TE-10.**

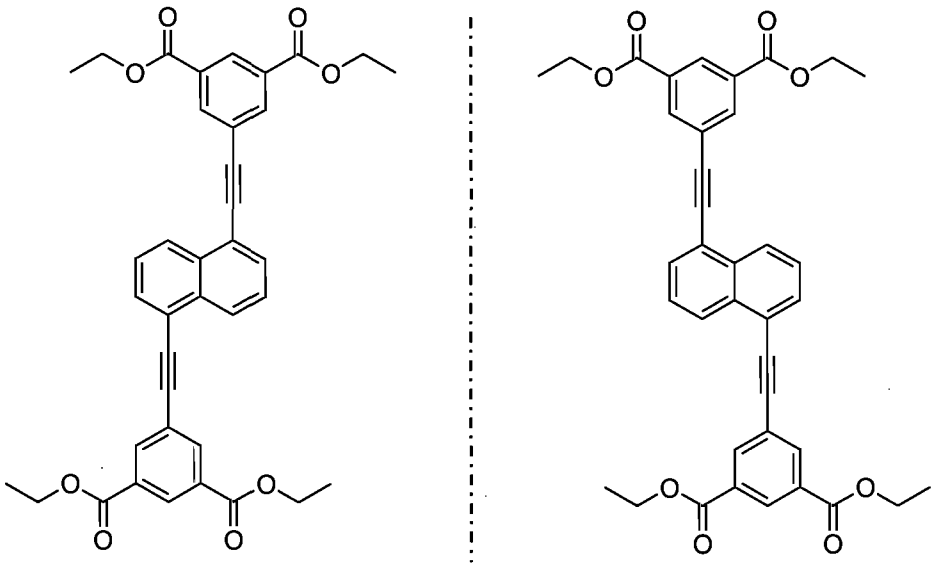

Based on these previous studies, the 2D nanopatterns formed by adsorption of isomeric naphthyl-substituted tetraester **TE-10** were expected to be of great interest, because this compound can be adsorbed to create surface enantiomers as shown in Scheme 6.4. In this illustration, a particular s-*trans* geometry is shown for all four ester groups, but alternative structures are also possible. Clearly, the two adsorbates shown in Scheme 6.4 cannot be superimposed in 2D. The adsorption of tetraester **TE-10** on HOPG was investigated by STM under conditions similar to those used in the study of analogous esters. The resulting images are shown in Figures 6.1-6.2.

Figure 6.1a shows well-ordered 2D nanopatterns composed of many individual domains. The area highlighted in yellow is enlarged in Figure 6.1b, where two domains are

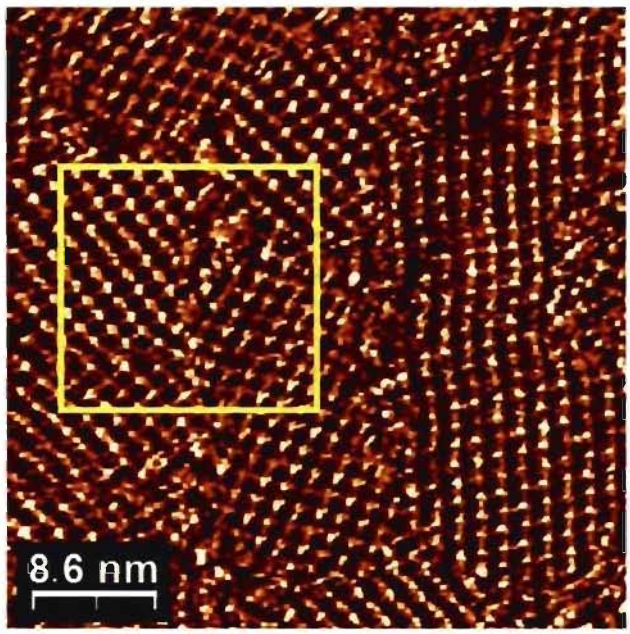

(a)

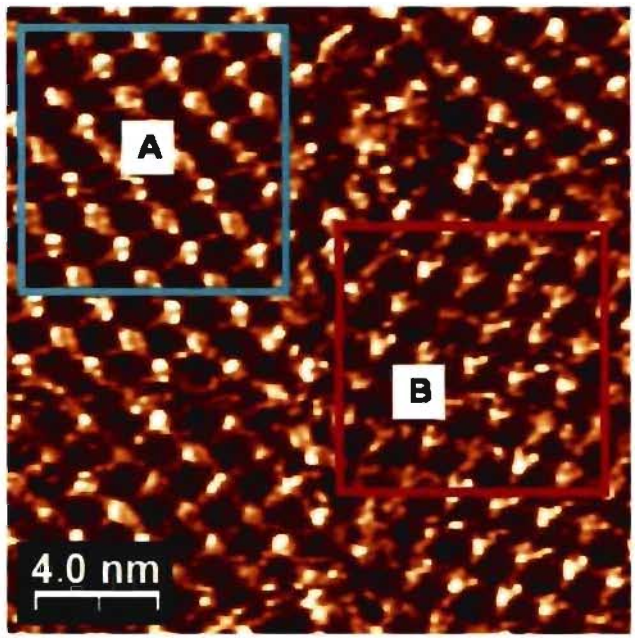

(b)

Figure 6.1 STM images of the 2D nanopatterns formed by the adsorption of tetraester **TE-10** on HOPG (deposition from heptanoic acid, with V_{bias} = -1.5 V and I_{set} = 100 pA). (a) Well-ordered monolayers composed of multiple domains in non-specific orientations with respect to the underlying graphite. (b) An enlarged image of the area highlighted in yellow in Figure 6.1a.

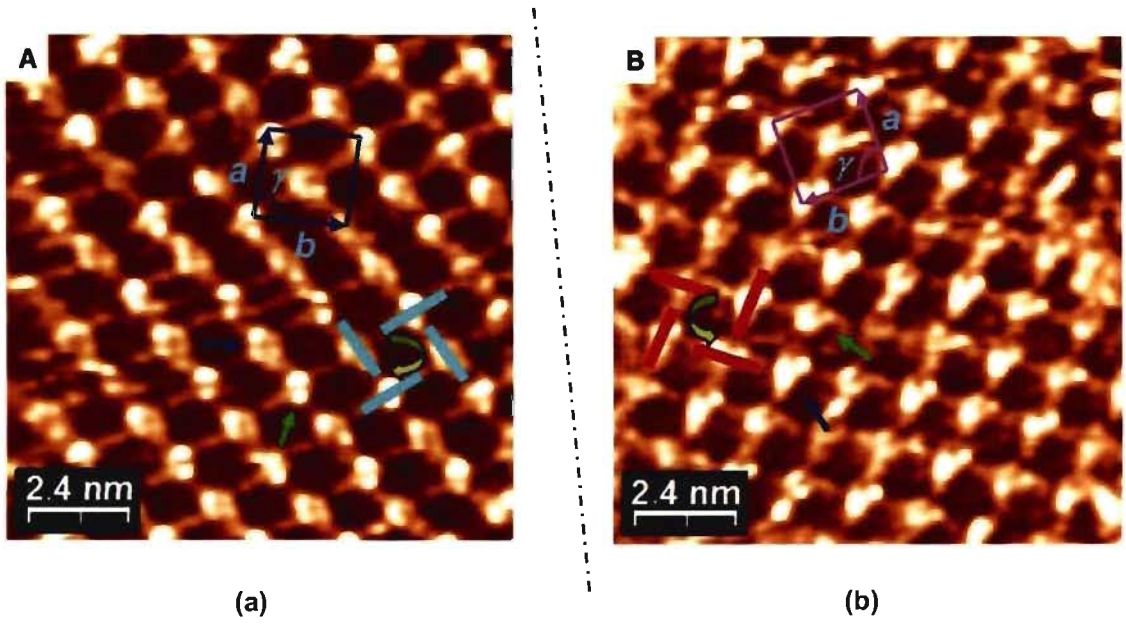

Figure 6.2 STM images of two homochiral domains formed by tetraester **TE-10**. Two types of bright spots are highlighted with blue and green arrows. (a) Square structures in clockwise orientation, with a schematic representation in light blue, and the unit cell highlighted in blue. (b) Square structures in a counter-clockwise direction, with a schematic representation in red, and the unit cell highlighted in pink.

labeled A and B, respectively. It is clear from first inspection that tetraester **TE-10** builds up square structures similar to those discussed in Chapter 5. Because compound **TE-10** is a 2D chiral molecule, we were interested in examining the structures in detail to see whether compound **TE-10** can form homochiral or heterochiral domains consisting of the two surface enantiomers. To analyze the structures of domains A and B in Figure 6.1b, they are further enlarged in Figure 6.2. The two unit cells highlighted in blue and pink are found to be chiral, with parameters $a = b = \sim 2.16$ nm, and $\gamma = \sim 90°$. The bright spots corresponding to individual molecules show two distinct features. Those such as the ones identified by green arrows are compact and well-resolved, with two arms clearly distinguished and offset

with respect to the naphthalene core. The others, highlighted by blue arrows, are more diffuse. This can be ascribed to lateral movement of the molecules, thus making them appear larger than the fixed molecules (green arrows); however, the molecular long axis can still be seen. According to STM studies reported by other groups, molecules adsorbed on surfaces can show distinct dynamic features, such as rotations in the course of imaging.[36-38] In our case, the lateral displacement of molecules identified by blue arrows can be induced by the STM tip,[39] in particular when the scan orientation is perpendicular to the molecular long axis. As a result, the two types of molecules are considered to be perpendicular to each other, with each end-group pointing to the center of the neighbors. The schematic representation in Figure 6.2a shows that four adjacent molecules in light blue form a square structure arranged in clockwise direction. In contrast, Figure 6.2b shows four neighboring molecules (in red) assembled into a square network arranged in anticlockwise direction. As a result, domains A and B are enantiomorphous with respect to the black axis (dotted line in Figure 6.2).

The proposed molecular models in Figure 6.3 illustrate the formation of two cyclic hydrogen-bonded square structures composed of opposite 2D enantiomers. The central naphthalene cores are highlighted in light blue and red to distinguish the two perpendicular orientations of tetraester **TE-10**, which correspond to the bright features in the STM images. Like the square structures formed from the tetraesters discussed in Chapter 5, the square motif formed by tetraester **TE-10** is proposed to be held together by C–H···O hydrogen bonds between carbonyl oxygen atoms and naphthalene C–H bonds at the 2,3- and 6,7-positions. Asuuming that the average H···O distance is 2.42 Å, the parameters of the

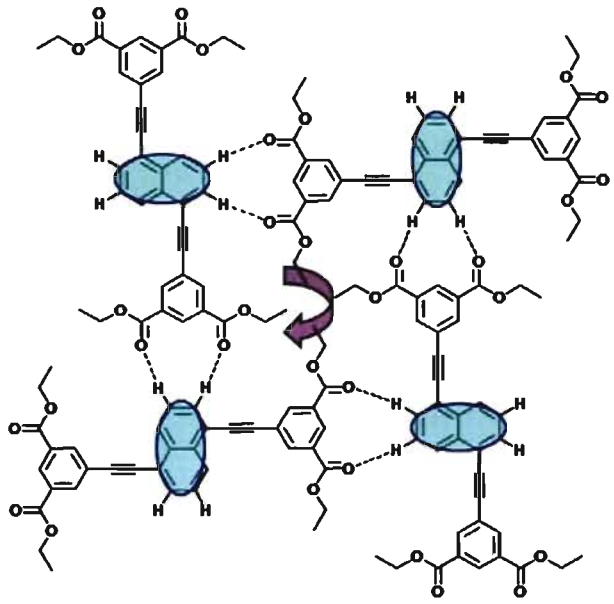

(a)

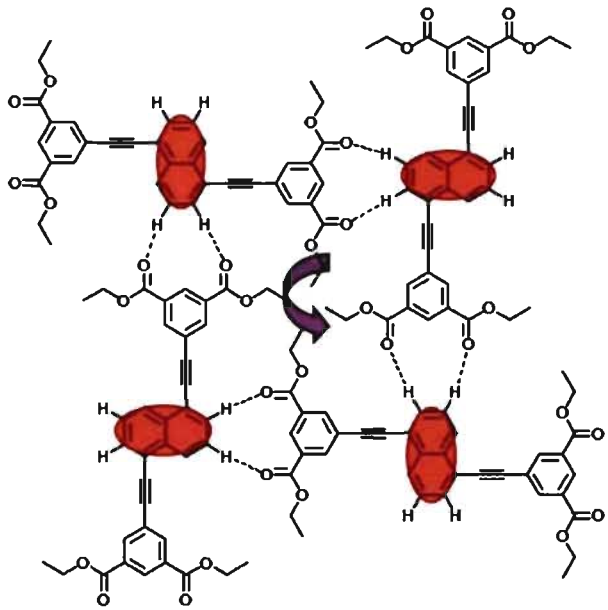

(b)

Figure 6.3 Proposed molecular models of hydrogen-bonded square networks with 2D chirality produced by tetraester **TE-10**. Hydrogen bonds are represented by broken lines. (a) Square structure arranged in clockwise orientation. (b) Square structure arranged in anticlockwise orientation.

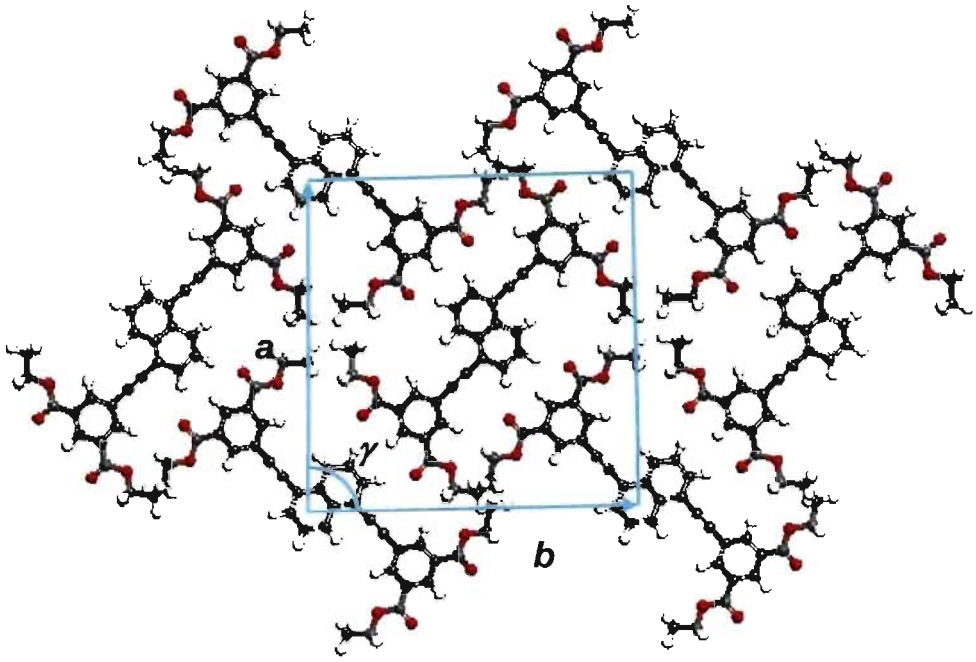

Figure 6.4 Proposed 2D arrangement of tecton **TE-10** adsorbed on graphite. The unit cell is highlighted in light blue.

unit cell shown in Figure 6.4 are therefore calculated to be $a = b = \sim 2.09$ nm and $\gamma = \sim 90°$, which are consistent with those obtained by analysis of the image shown in Figure 6.2.

The 2D nanopatterns formed by the four tetraesters **TE-6**, **TE-7**, **TE-9**, and **TE-10** establish that the compounds show consistent behavior and always maintain a basic square structure in which neighbors are oriented perpendicularly, even when the cores or the molecular symmetry are different. We suggest that three main factors help to preserve this robust hydrogen-bonded supramolecular architecture: 1) The aromatic cores provide hydrogen atoms needed to form C–H···O hydrogen bonds with nearby carboxylate moieties; 2) the topology of the tetraesters, including the length of the molecule and the size of its core, keeps the cavities defined by the square networks acceptably small; and 3) the ethyl groups of the esters are suitably accommodated within the cavities and can help stabilize

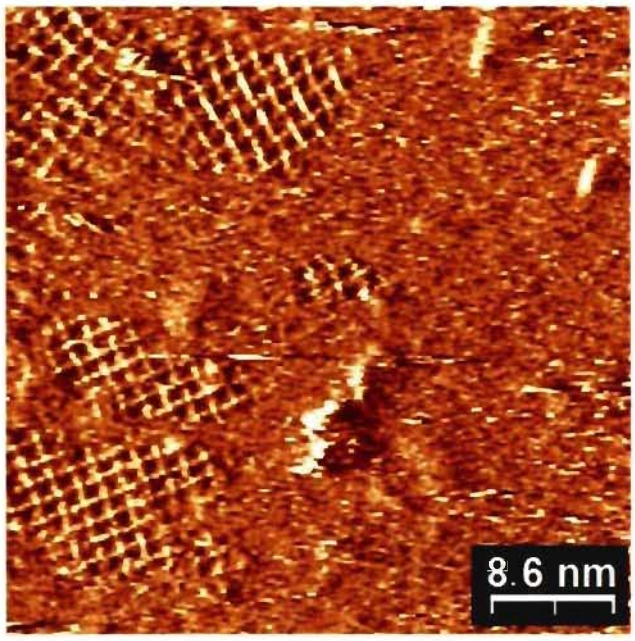

(a)

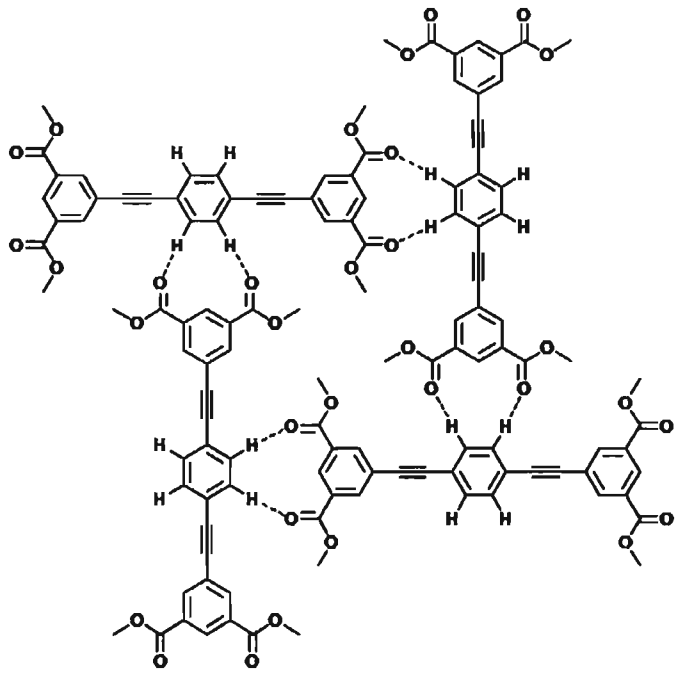

(b)

Figure 6.5 (a) An STM image of 2D nanopatterns produced by depositing the tetramethyl analogue of tetraethyl ester **TE-6** on HOPG under standard conditions (heptanoic acid, with V_{bias} = -1.5 V and I_{set} = 50 pA). (b) Proposed molecular model showing the hydrogen-bonded square structure, with four methyl groups accommodated in the central cavity without filling it.

the networks by the formation of van der Waals interactions.

To test these hypotheses, we examined the adsorption of analogues in which the ester groups were altered. The required compounds were synthesized by the same procedure used to make tetraester **TE-6**.[40] As shown in Figure 6.5, when tetraethyl ester **TE-6** was replaced by its tetramethyl analogue, only a few locally ordered square nanopatterns could be found, probably because the four methyl groups are too far away from each other to yield significant van der Waals stabilization. When the tetraethyl ester was replaced by its tetrapropyl ester, no well-defined 2D nanopatterns at all were observed by STM, presumably because four propyl groups cannot be accommodated in the central cavity of the square networks.

During our work, we have consistently made an effort to compare molecular assembly on surfaces with that observed in 3D crystals. Unfortunately, we have not yet succeeded in crystallizing tetraester **TE-10**.

6.4 2D Chiral Nanopatterns Formed by Tecton TA-10

The ability of extended tecton **TA-10** to create 2D chiral nanopatterns has been investigated by STM under conditions similar to those used in the study of tecton **TA-7**, which was found to form both parallel and Kagomé networks on HOPG (Figures 4.11-4.12). Analogue **TA-10** was designed to have the same naphthalene core, but with lower symmetry with respect to the long molecular axis. Molecular models proposed in Scheme 6.5 indicate that tecton **TA-10** can exist as 2D enantiomers. As a result, tecton

TA-10 was expected to produce surface nanopatterns showing 2D chirality. We were eager to discover whether it maintains a structure similar to that of analogue **TA-7** or whether it forms a new architecture. STM images of its adsorption are provided in Figures 6.6-6.8.

Scheme 6.5 2D enantiomers of tecton **TA-10**.

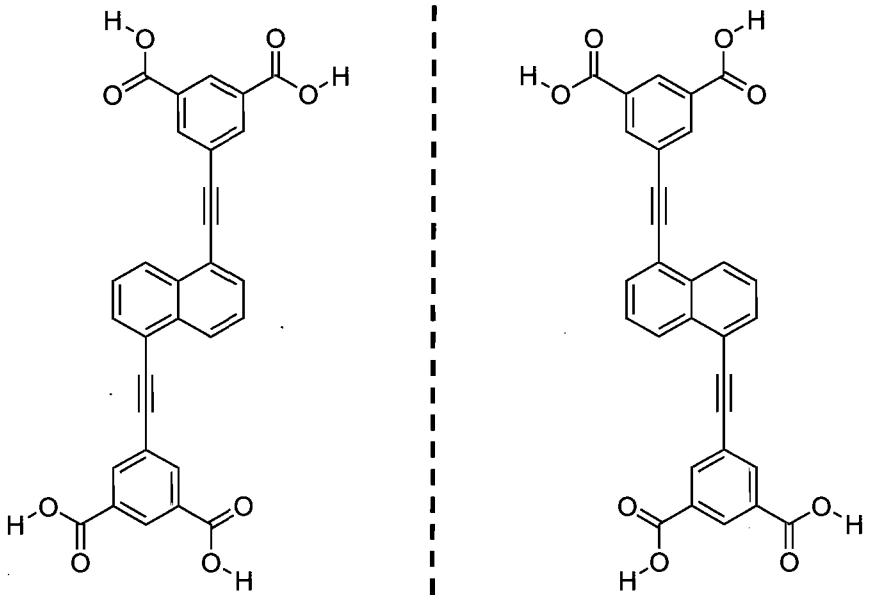

Figure 6.6a shows an STM image of well-ordered nanopatterns built from tecton **TA-10**, showing two distinct phases A and B, which are found to switch into each other smoothly without any interruption. Phase B seems to be the parallel structure as discussed in Chapter 4; however, phase A shows an entirely new pattern. Figure 6.6b shows an enlarged image of phase A, displaying a zigzag pattern composed of rows of dimers. Molecular resolution of tecton **TA-10** provides evidence for an asymmetric shape, which reflects the offset way in which the sticky sites are grafted to the naphthalene core. Models in Figure 6.7a highlight the parallel and zigzag arrays, which can transform

smoothly into each other without creating disrupted domain boundaries. The unit cells are determined to be a = ~2.06 nm, b = ~2.10 nm, and γ = ~50° for the parallel network, and a = ~2.07 nm, b = ~2.98 nm, and γ = ~87° for the zigzag network. The molecular density of surface coverage is calculated to be ~0.38 and ~0.40 molecule/nm^2 for the parallel and zigzag networks, respectively, which helps explain how the two motifs can coexist.

Proposed molecular models in Figure 6.7b show that hydrogen bonds between –COOH groups within dimers, as well as between adjacent rows, govern the formation of the zigzag pattern. Assuming that the average H···O distance is 2.05 Å, the parameters of the unit cell shown in Figure 6.7b are therefore calculated to be a = ~2.19 nm, b = ~3.05 nm, and γ = ~90° , which are close to those obtained by analysis of the image shown in Figure 6.7a. It is important to note that this model requires that the dimers consist of paired 2D enantiomers of tecton **TA-10**. Such racemic 2D networks have rarely been reported in the literature. An example is provided by heptahelicene,[29] which was shown by Ernst and co-workers to be adsorbed on Cu(111) as enantiomorphous domains of racemic composition.

As established in Chapter 4, parallel networks dominate the 2D nanopatterns formed by tectons **TA-5** and **TA-8** (with isophthalic acid units linked by an acetylenic spacer and a 9,10-diethynylanthracene spacer, respectively), and they are also observed in the adsorption of tecton **TA-7** (1,4-diethynylnaphthalene spacer). Because tecton **TA-10** (1,5-diethynylnaphthalene spacer) is a member of this family of tetraacids, it was not surprising to find that it also produces parallel networks, but the simultaneous formation of zigzag networks composed of racemic dimers was unexpected. We therefore subjected

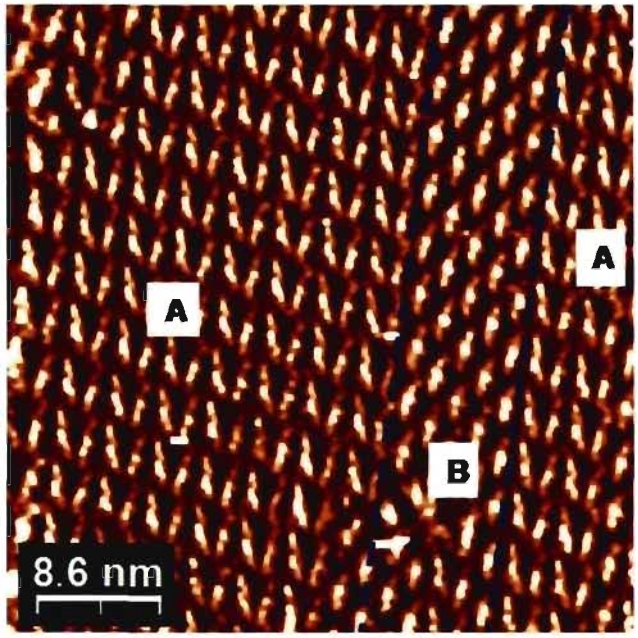

(a)

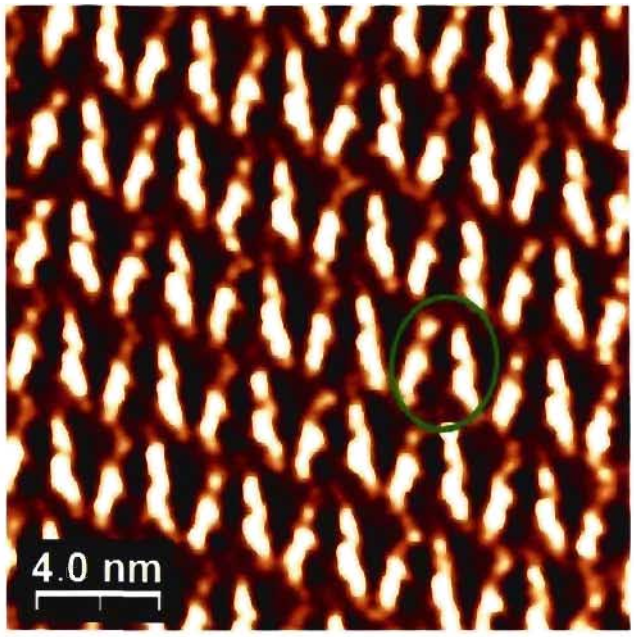

(b)

Figure 6.6 STM images of 2D nanopatterns on HOPG built from tecton **TA-10** by deposition from heptanoic acid (V_{bias} = -1.5 V and I_{set} = 100 pA). (a) Two different phases A and B can merge fluidly into each other without any interruption. (b) Well-ordered patterns constructed from pairs of tectons that form regular zigzag rows. One such pair is highlighted in green.

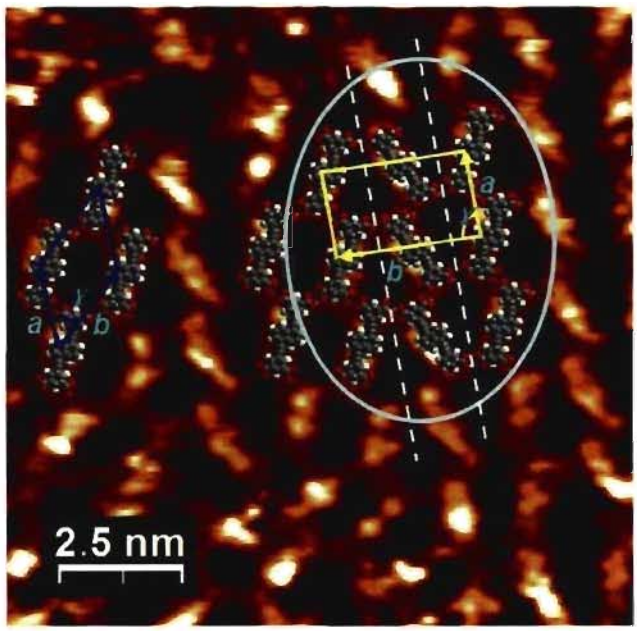

(a)

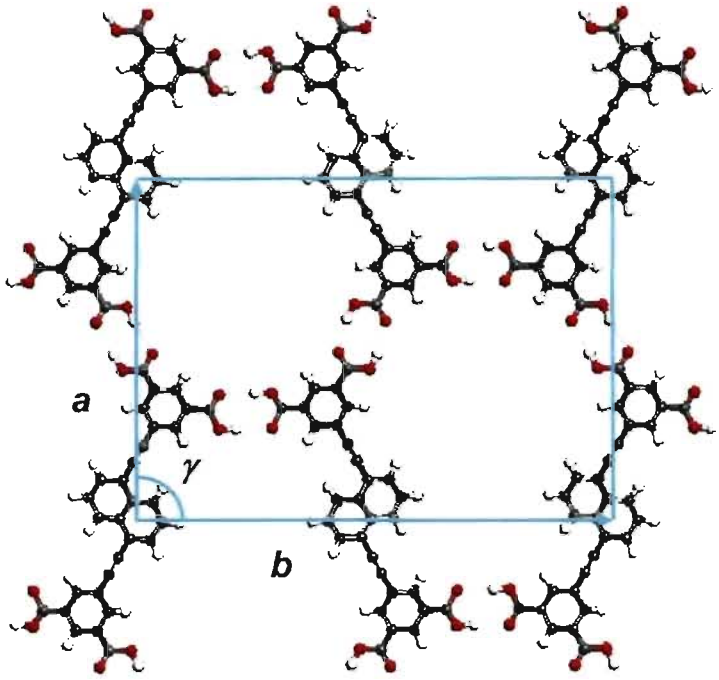

(b)

Figure 6.7 (a) An STM image with superimposed space-filling models showing the parallel and racemic zigzag phases formed by tecton **TA-10**. (b) Proposed molecular model showing hydrogen-bonded racemic dimers and their connections with neighbors. The unit cell is highlighted in light blue.

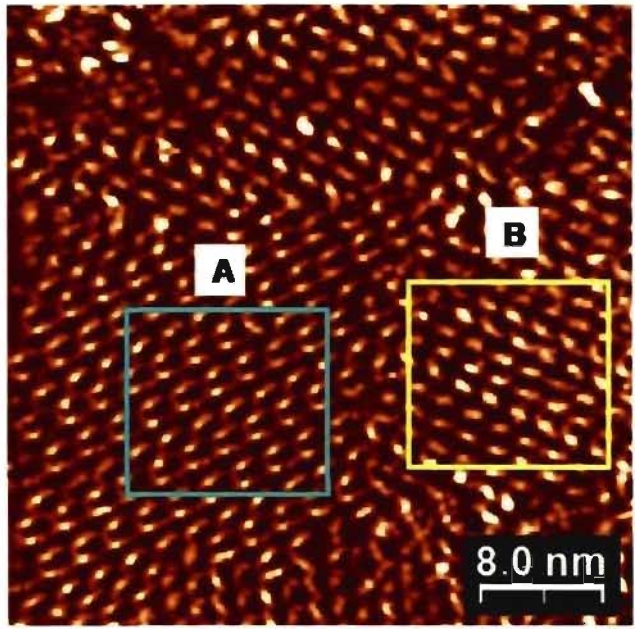

(a)

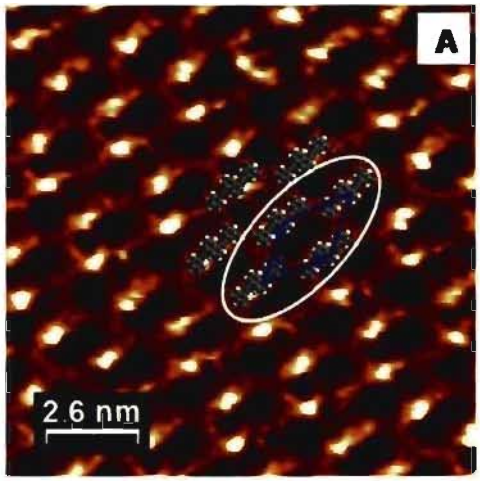

(b)

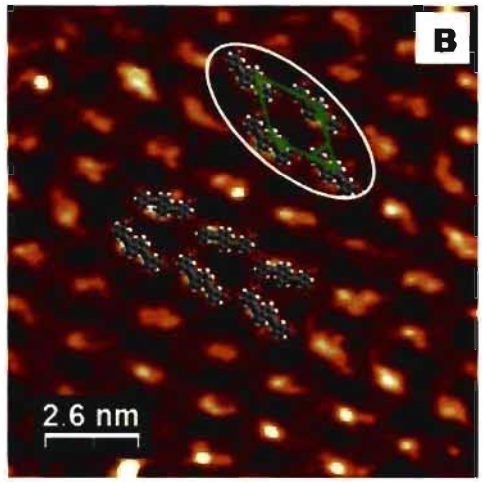

(c)

Figure 6.8 STM images of 2D chiral nanopatterns formed by the adsorption of tecton **TA-10** on HOPG (deposition from heptanoic acid, with V_{bias} = -1.5 V and I_{set} = 100 pA). (a) Image showing multiple domains. Area A (blue) consists of an essentially homogeneous parallel structure, whereas area B (yellow) mixes the parallel structure and zigzag structure. (b) Enlarged image of area A, with the unit cell highlighted in blue. (c) Enlarged image of area B, with the unit cell of the parallel structure highlighted in green. Superimposed CPK models show the parallel structure and racemic zigzag structure.

STM images of the 2D nanopatterns to more thorough analysis. Figure 6.8a shows multiple domains, some consisting largely of the parallel architecture (such as area A) and others containing the racemic zigzag architecture as well (such as area B). Areas A and B are enlarged in Figures 6.8b and 6.8c, respectively, with superimposed CPK models. Nanopatterns in area A display an essentially homogenous parallel structure. Both the parallel and racemic zigzag structures can be seen in area B. It is important to note that the unit cells proposed for the parallel network are probably chiral, as illustrated by molecular models in Figure 6.9, and the hydrogen-bonded parallel networks are chiral and composed of a single 2D enantiomer. Nevertheless, because the asymmetric shape

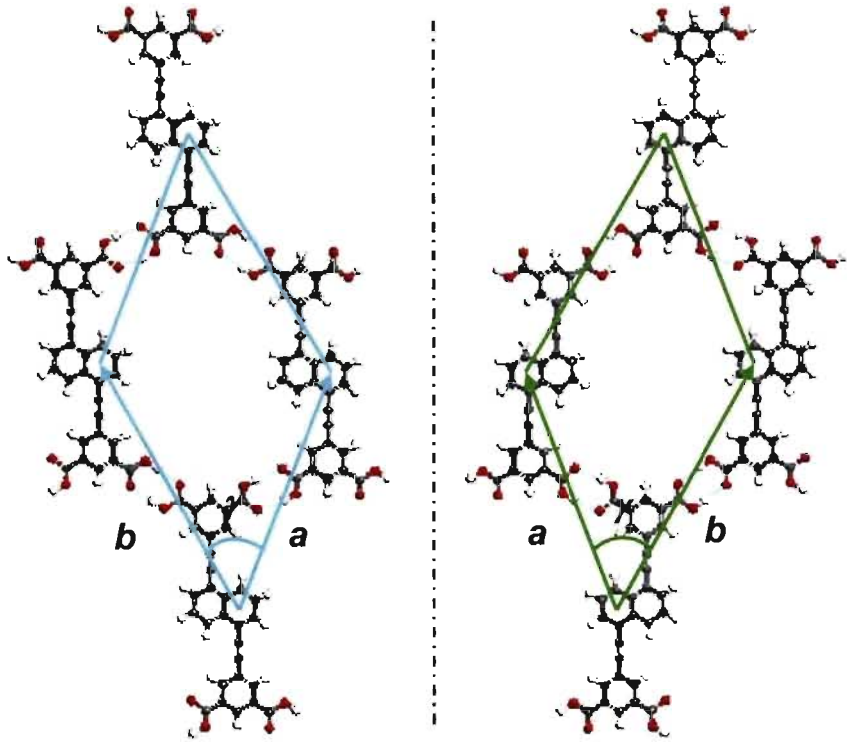

Figure 6.9 Proposed molecular models of the 2D chiral hydrogen-bonded parallel structure produced by tecton **TA-10**. Hydrogen bonds are represented by broken lines. The unit cells are highlighted in light blue and green, respectively.

reflecting the offset of two arms with respect to the naphthalene core cannot be seen as clearly as that in the racemic zigzag phases, the images alone do not provide firm proof that the parallel networks are homochiral. Assuming that the average H···O distanceis 2.05 Å, the parameters of the unit cells shown in Figure 6.9 are thereby calculated to be a = ~1.99 nm, b = ~2.15 nm, and γ = ~50°, which are consistent with the observed values shown in Figure 6.7a.

Based on combined analysis of STM images and models, we conclude that both homochiral and heterochiral 2D nanopatterns (parallel and zigzag motifs, respectively) are formed by the adsorption of achiral molecule **TA-10** on HOPG. This phenomenon of the coexistence of homochiral and heterochiral domains has rarely been observed, and the adsorption of 2D chiral molecules on surfaces normally shows a clear preference for either homochiral structures or heterochiral structures, with homochiral structures being more frequently encountered. It is noteworthy that the homochiral and heterochiral patterns produced by tecton **TA-10** can merge into each other smoothly without any interruption, and a molecule at the edge of a homochiral parallel domain can form a pair with its 2D enantiomer to initiate a transition into the racemic zigzag motif. Both patterns are predicted to have closely similar hydrogen-bonding energies because all four -COOH groups are fully engaged in hydrogen bonding.

6.5 2D Chiral Nanopatterns Formed by Tetraester TE-11

Tetraester **TE-11** (with two diethyl isophthalate units linked by a 1,5-diethynylanthracene spacer) was designed to be a 2D chiral isomer of tecton **TE-8**

(diethyl isophthalate units linked by a 9,10-diethynylanthracene spacer). Although not obviously chiral, isomer **TE-8** was found to form homochiral 2D nanopatterns on HOPG, due to the adoption of chiral conformations through surface confinement of carboethoxy groups that prevents their free rotation in adsorbed molecules (see Chapter 5). We expected tetraester **TE-11** to produce 2D chiral nanopatterns different from those formed by isomer **TE-8**, as a result of changing the symmetry of the molecular core. Scheme 6.6 shows 2D surface enantiomers produced by tetraester **TE-11**, based on an arbitrary conformation of the carboethoxy substituents. An STM investigation of compound **TE-11** was performed under conditions similar to those used in the study of isomer **TE-8**, and STM images are provided in Figures 6.10-6.12.

The images in Figures 6.10a and 6.10b show well-ordered monolayers built from tetraester **TE-11** over a very large area (150 × 150 nm^2). Clearly, the entire nanopatterns in each image are composed of homogenous parallel tapes in a single orientation. Higher-resolution images in Figures 6.10c and 6.10d reveal the parallel tapes in detail. As shown in Figure 6.11, STM images with superimposed space-filling models suggest that each parallel tape is composed of single 2D enantiomers of tetraester **TE-11** packed side-by-side. The bright features are attributed to the π-conjugated molecular backbone, particularly the anthracene core. The blue arrow represents molecular alignment within the tapes. Enantiomorphous homochiral tape domains were found to coexist in the same image (Figure 6.12a). As shown in Figures 6.12b and 6.12c, the unit cells for the enantiomorphous domains were found to be chiral, with parameters a = ~1.06 nm, b = ~2. 37 nm, and γ = ~85°. The two chiral arrangements can be distinguished by the different orientations of the long

molecular axis (as shown in white arrows), which is used instead of the orientation of the anthracene core due to its relatively lower resolution.

Scheme 6.6 Proposed 2D enantiomers of tetraester **TE-11**, with an arbitrary conformation of the carboethoxy groups similar to the one favored by isomer **TE-8**.

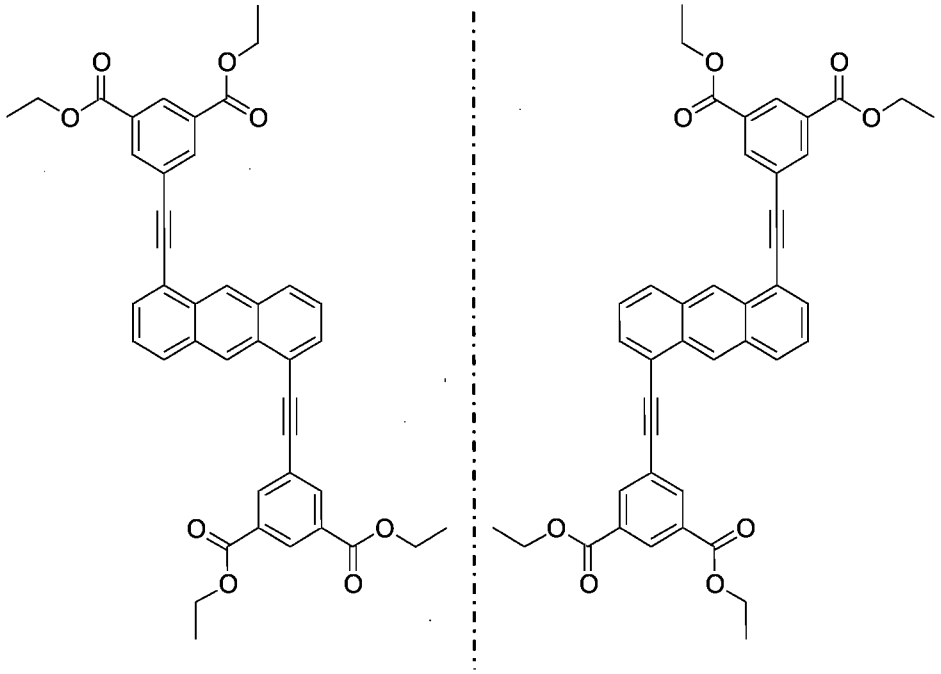

The chiral tapes can be illustrated by the proposed molecular models in Figure 6.13. In these models, the individual molecules of tetraester **TE-11** adopt conformations identical to those illustrated in Scheme 6.6 and analogous to those proposed to be favored in the adsorption of isomer **TE-8**. We suggest that the favored conformations are determined in part by the need to optimize 2D packing. C-H···O hydrogen bonds are proposed to be generated between carbonyl oxygen atoms and aryl C-H bonds, with a typical H···O distance of ~2.40 Å. This distance would place neighboring molecules at a separation of ~1 nm (Figure 6.13b). The unit cell parameters are therefore determined to be a = ~0.99 nm, b = ~2. 38 nm, and γ = ~86°, which are consistent with those determined by analysis of the STM imagess shown in Figure 6.12.

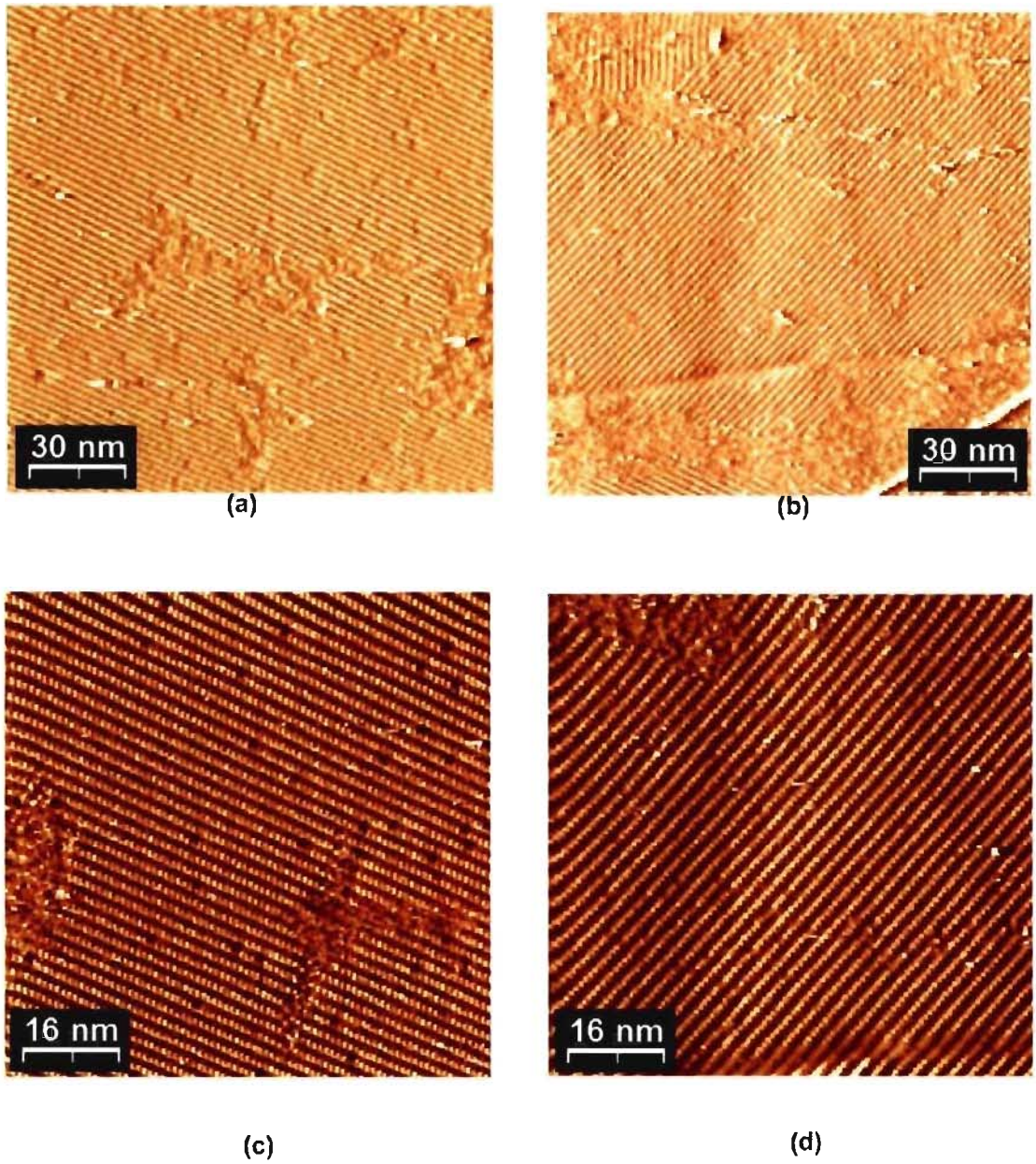

Figure 6.10 STM images of 2D nanopatterns formed by the adsorption of tetraester **TE-11** on HOPG (deposition from heptanoic acid, with V_{bias} = -1.5 V and I_{set} = 100 pA). (a, b) Large-scale ordered monolayers over an area of 150 × 150 nm^2. (c, d) Higher-resolution images showing parallel tapes.

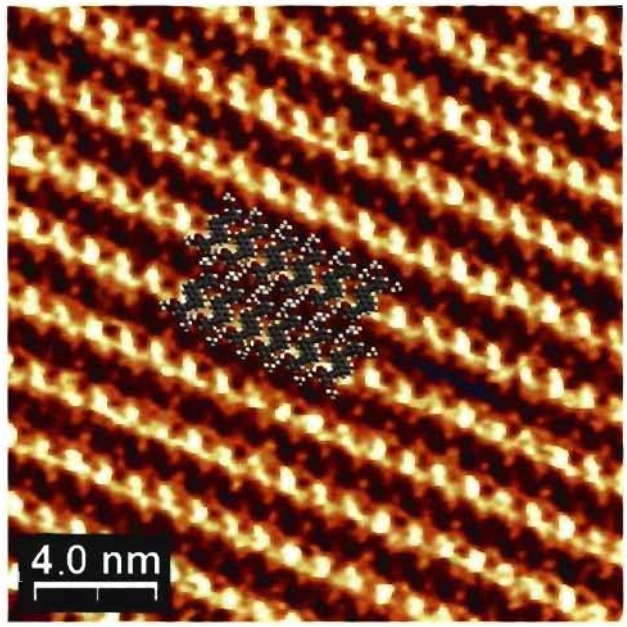

(a)

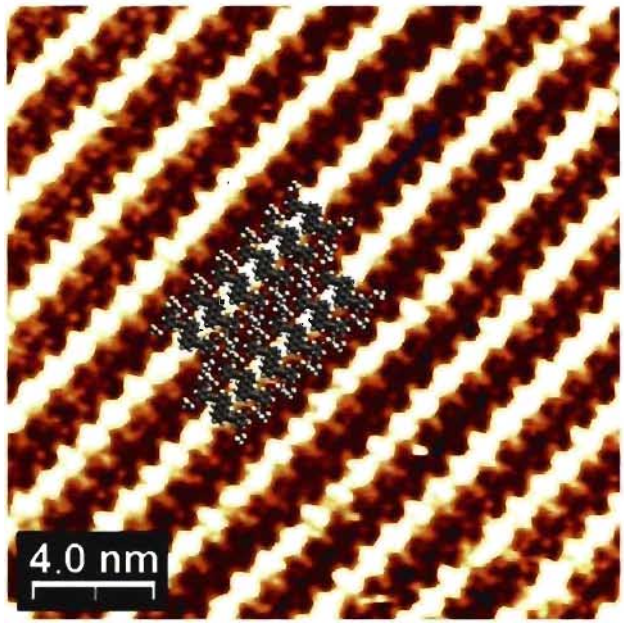

(b)

Figure 6.11 Higher-resolution STM images of 2D chiral nanopatterns formed by the adsorption of tetraester **TE-11** as enantiopure tapes, with superimposed CPK models. The images show parallel tapes aligned in different orientations (represented by blue arrows).

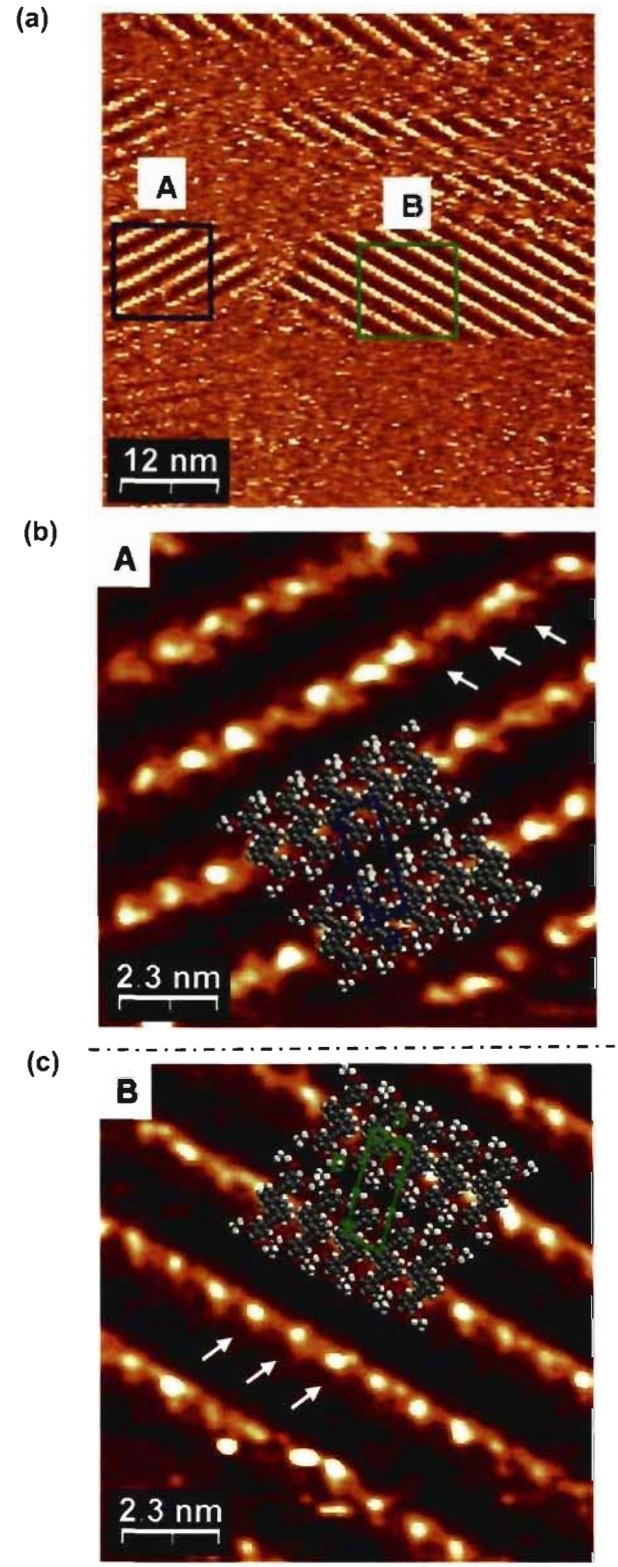

Figure 6.12 STM images of 2D nanopatterns created by the adsorption of tetraester **TE-11** on HOPG. (a) Large-scale image showing two homochiral domains A and B, highlighted in blue and green, respectively. (b) (c) Enlarged images of areas A and B, respectively, with superimposed CPK models. The unit cells are highlighted in blue and green. The white arrows in each image represent different orientations of the long molecular axis.

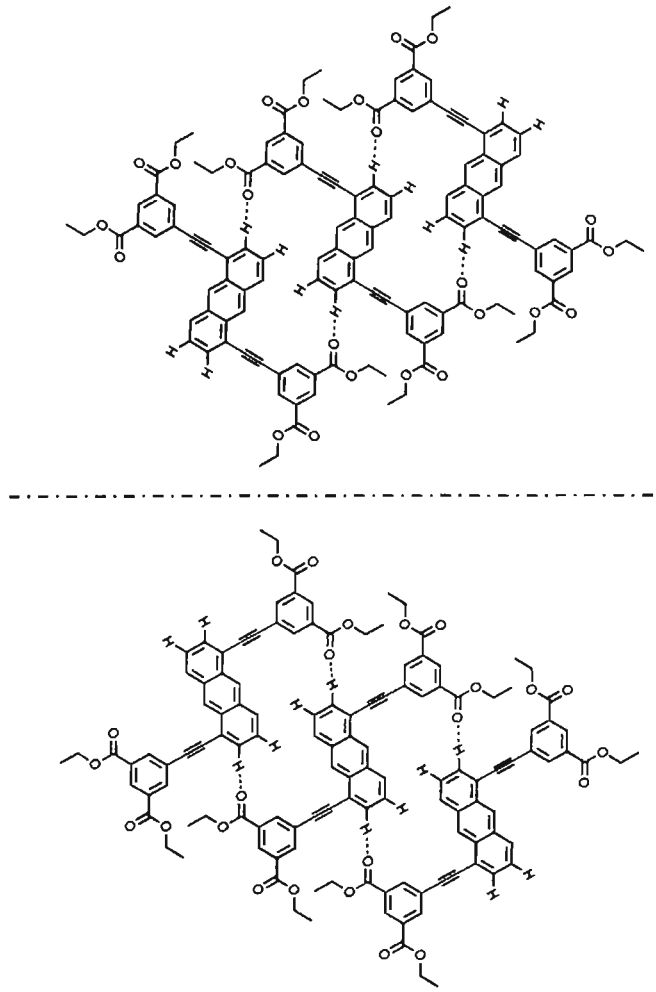

Figure 6.13 (a) Proposed molecular models of hydrogen-bonded tapes composed of opposite 2D enantiomers of tetraester **TE-11**. Hydrogen bonds are represented by broken lines. (b) Proposed 2D arrangement of one enantioner of **TE-11**. The unit cell is highlighted in light blue.

6.6 2D Nanopatterns Formed by Tecton TA-11

The formation of 2D chiral nanopatterns from asymmetric tecton **TA-11** (with two isophthalic acid units linked by a 1,5-diethynylanthracene spacer) was investigated by STM under conditions similar to those used in our previous study of symmetric isomer **TA-8** (isophthalic acid units linked by a 9,10-diethynylanthracene spacer), which was shown to favor an achiral hydrogen-bonded parallel structure. Tecton **TA-11** was expected to produce 2D chiral nanopatterns different from those formed by tecton **TA-10** (isophthalic acid units linked by a 1,5-diethynylnaphthalene spacer), due to anthracene replacing the naphthalene core. Molecular models proposed in Scheme 6.7 indicate that tecton **TA-11** can exist as 2D enantiomers. STM images of the adsorption of tecton **TA-11** on HOPG are provided in Figures 6.14-6.15.

Figure 6.14a shows well-ordered nanopatterns with areas of defects. Figure 6.14b shows different domains composed of nanopatterns arranged primarily in the same orientation, as highlighted in red. However, a small domain highlighted in blue appears to be organized differently from the other domains. As shown in Figure 6.15a and 6.15b, enlarged STM images of the two typical nanopatterns with superimposed molecular models suggest that each domain is composed of single 2D enantiomers of tecton **TA-11** packed side-by-side. The two unit cells are found to be chiral, with parameters $a = b = \sim 1.83$ nm and $\gamma = \sim 82°$. The bright protrusions corresponding to individual molecules show distinct orientations of alignment in each homochiral domain.

To interpret the formation of the homochiral rhombic structure, molecular models composed of single 2D eantiomers are proposed in Figure 6.15c and 6.15d. Neither model

Scheme 6.7 2D enantiomers of tecton **TA-11**.

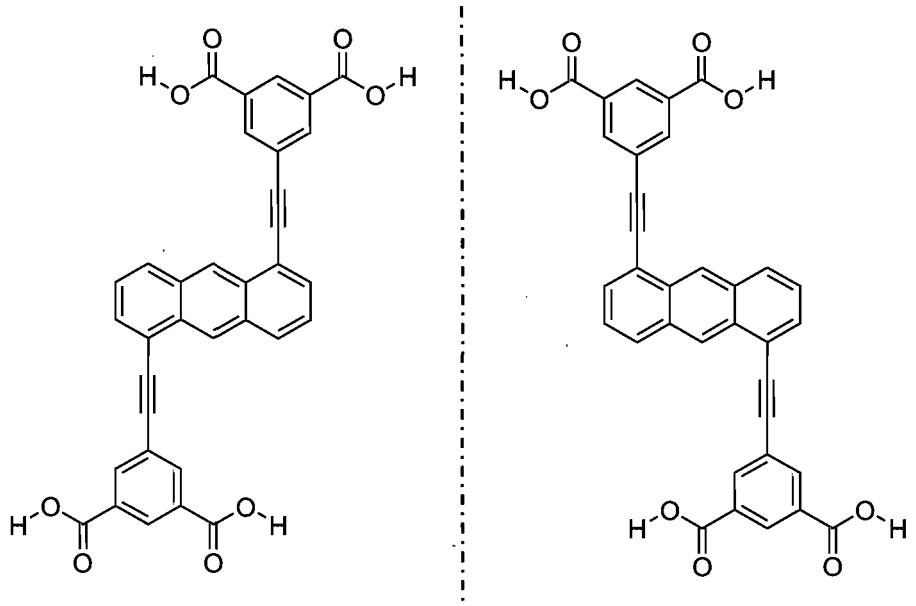

invokes normal O–H···O hydrogen bonding of the type seen in assemblies of related tetraacids discussed in Chapter 4. Instead, we suggest that the observed nanopattern can be considered to be built from linear tapes that are associated by C–H···O hydrogen bonds between carbonyl oxygen atoms and aryl C–H bonds. These hydrogen bonds are assumed to have normal lengths of approximately 2.42 Å. The model shows a rhombic structure composed of a single 2D enantiomer shown in Scheme 6.7, with unit cell parameters $a = b = \sim 1.76$ nm and $\gamma = \sim 80°$, which are consistent with those observed in STM images. No prominent interactions can be found between adjacent tapes, unless the adjacent tapes are displaced to allow normal O–H···O hydrogen bonding to be formed between –COOH groups. As shown in Figure 6.16, such a displacement drives the unit cell parameters to be $a = 1.76$, $b = \sim 1.82$ nm, and $\gamma = \sim 63°$. Molecular density of packing is thereby increased slightly from 0.328 molecule/ nm^2 (Figure 6.15c) to 0.351 molecule/nm^2. Such an unusual

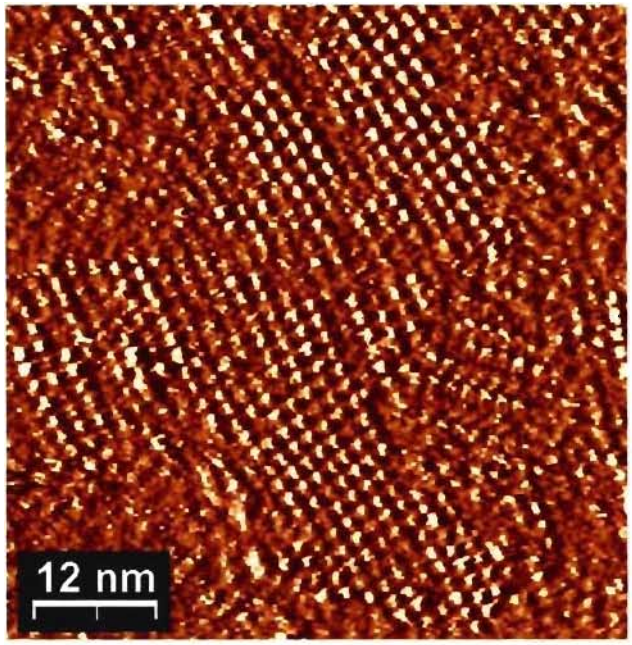

(a)

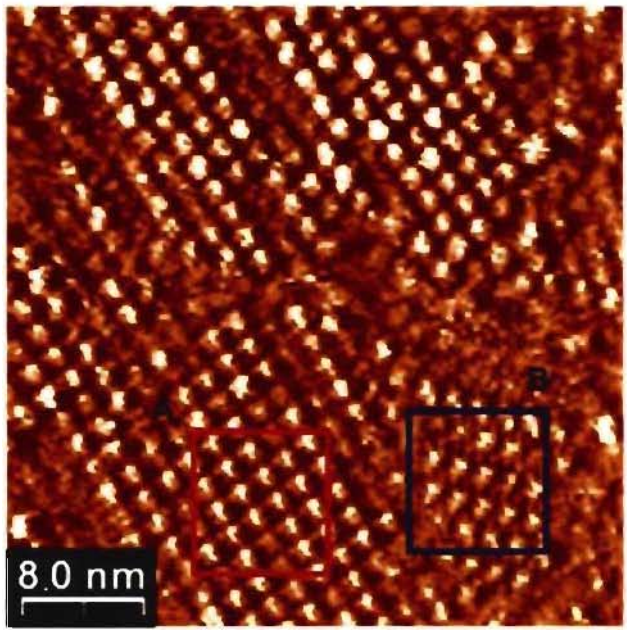

(b)

Figure 6.14 STM images of 2D nanopatterns formed by the adsorption of tecton **TA-11** on HOPG (deposition from heptanoic acid, with V_{bias} = -1.5 V and I_{set} = 100 pA). (a) Large-scale image showing ordered arrays with areas of defects. (b) Higher-resolution image showing well-ordered patterns highlighted in red. A small domain showing a different orientation is highlighted in blue.

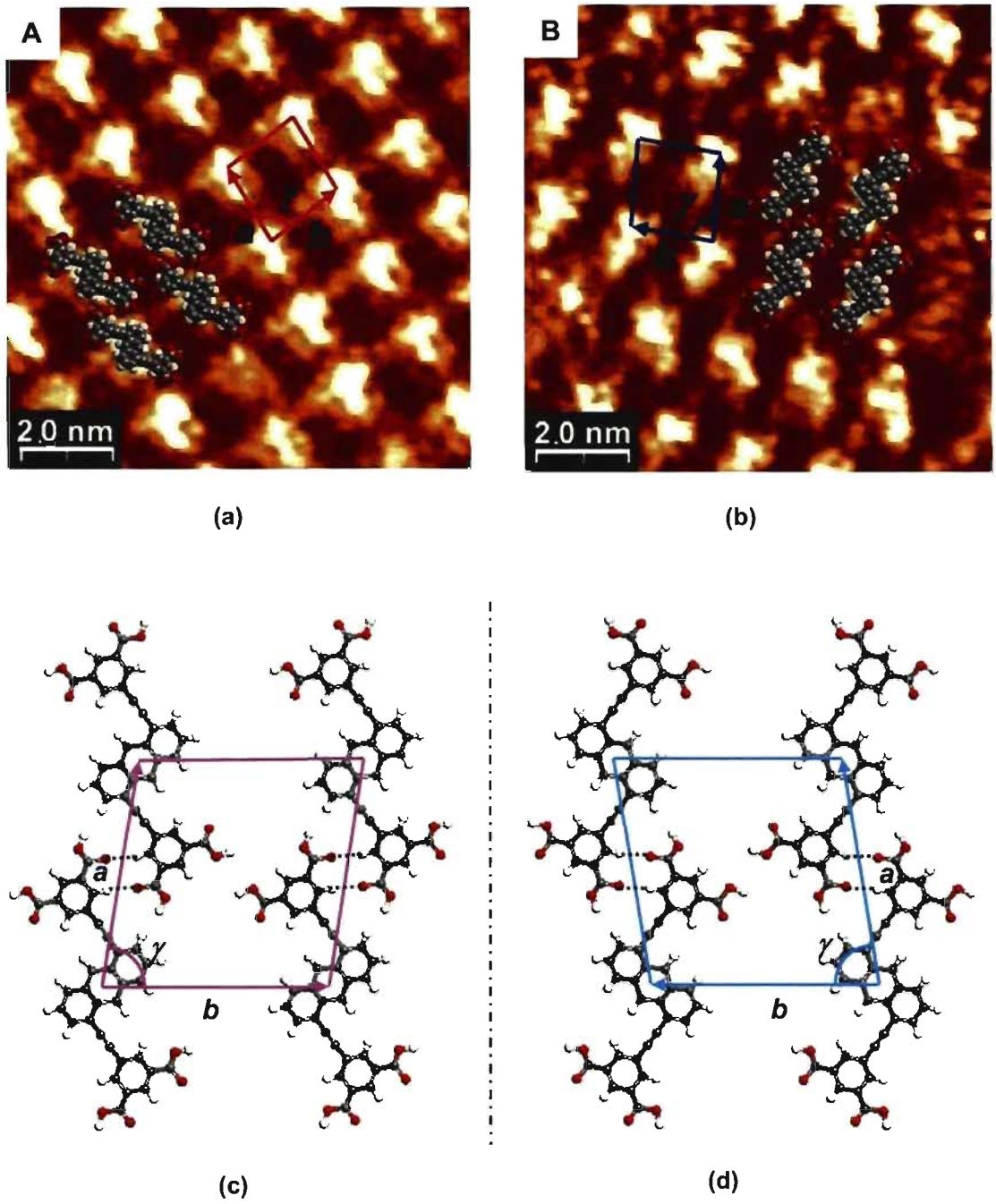

Figure 6.15 (a, b) Enlarged STM images of 2D enantiomorphous domains with superimposed molecular models, showing a rhombic structure formed by tecton **TA-11**. The unit cell is highlighted in red and blue, respectively. (c, d) Proposed molecular models suggest the formation of linear tapes composed of single 2D enantiomers of tecton **TA-11**. Hydrogen bonds are represented by broken lines. The unit cells are highlighted in pink and light blue, respectively.

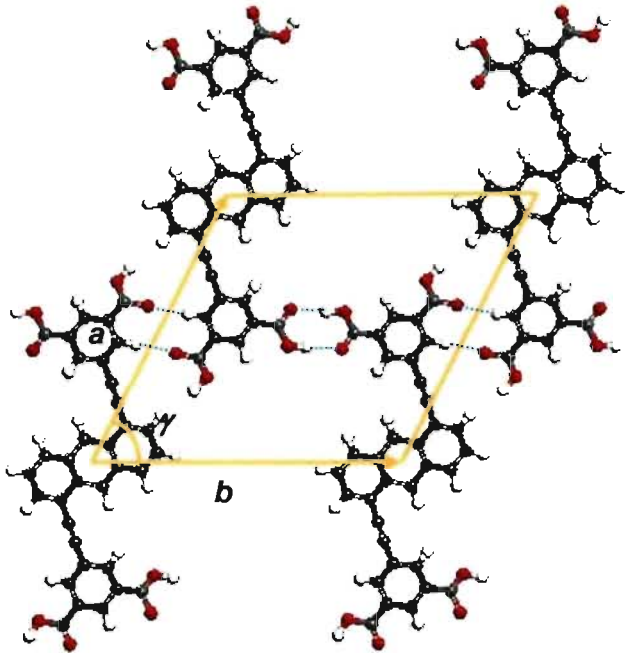

Figure 6.16 An optimized molecular model for 2D arrangement of tecton **TA-11**. Hydrogen bonds are represented by broken lines. The unit cell is highlighted in yellow.

rhombic network formed by tecton **TA-11** with a smaller number of hydrogen bonds can be partially ascribed to strong interactions between the adsorbed molecules and the underlying graphite, as represented by the case of tecton **DAT-3** in Chapter 3.

Detailed comparison of the adsorption of tecton **TA-11** and related compounds may provide deeper understanding of various factors that can affect molecular self-assembly on surfaces. Analogue **TA-10**, which has a core containing naphthalene in place of anthracene, forms both a homochiral parallel network and a racemic zigzag network. As a result, we suggest that the formation of the unusual rhombic nanopattern by tecton **TA-11** originates in part from the increased importance of adsorbate-substrate interactions. The analogous tetraester **TE-11,** which has $-COOC_2H_5$ substituents in place of the -COOH groups of tecton **TA-11**, forms densely-packed enantiomorphous tapes but adopts a different C–H···O

hydrogen bonding motif, resulting in part from the steric effects of the four ester groups. These observations suggest that attaining a higher density of coverage is a priority for compounds with anthracene cores. In the light of the behavior of tetracid **TA-11**, it is therefore surprising that isomer **TA-8**, which has a 9,10-substituted anthracene core, produces parallel hydrogen-bonded networks instead of the more compact but less hydrogen-bonded structure favored by compound **TA-11**. We suggest that this difference arises because the zigzag shape of **TA-11** permits unusual C–H···O hydrogen bonds to be formed without causing steric repulsion involving the anthracene core. Such an arrangement is difficult for tecton **TA-8**, which has two long arms located symmetrically with respect to the anthracene core. Clearly, molecular geometry plays an important role in determining the formation of the ultimate nanopatterns.

We conclude that adsorption of the family of tetraesters and tetraacids of the type we have studied is controlled by a large number of potentially significant factors, despite the relative structural simplicity of the adsorbates. These factors include the overall molecular topology (as it affects packing within the adsorbed layer), hydrogen bonding within the layer, and the strength of adsorbate-surface interactions. We suggest that when adsorbate-surface interactions are modest, hydrogen bonding can place a prominent role in determining what nanopatterns are favored, at least when the networks are not excessively open. In contrast, when adsorbate-surface interactions are strong, patterns that increase the density of coverage can be favored even when they incorporate hydrogen bonding that is far from optimal. Because of these multiple factors and their complex competition, it is not yet possible to create 2D molecular nanopatterns in a completely predictable way.

6.7 Summary

In this chapter, we have presented the results of STM investigations of a series of related compounds designed to create chiral 2D nanopatterns by adsorption on HOPG. All the compounds have asymmetric π-conjugated cores grafted to two isophthalic acid units or corresponding esters. Chiral tetraester **TE-10** (naphthalene core) was found to generate square nanopatterns composed of homochiral domains. As expected, chiral tetraester **TE-11** (anthracene core) also produced enantiomorphic domains, but they consisted of parallel tapes. The difference in 2D assembly is presumably related to the size of the cores and their affinity for HOPG, with anthracene favoring a higher density of coverage at the expense of inter-adsorbate hydrogen bonding.

Chiral tetraacid **TA-10** (naphthalene core) was found to create two types of extensively hydrogen-bonded structures, a homochiral parallel network and a heterochiral zigzag network. Most interestingly, the two motifs are closely related, and adjacent domains can merge into each other smoothly, without any interruption in hydrogen bonding. Surprisingly, analogous tetraacid **TA-11** (anthracene core) yielded enantiomorphous rhombic nanopatterns more typically observed in the deposition of related tetraesters, which cannot engage in strong inter-adsorbate hydrogen bonding. We attribute the contrasting behaviors of tetraacids **TA-10** and **TA-11** to the strong ability of the anthracene core to dominate adsorption and favor closer packing, even at the expense of effective inter-adsorbate hydrogen bonding.

References

1. Cline, D. B. *Physical Origin of Homochirality in Life*; AIP: Woodbury, New York, **1996**, 17-49.
2. Sgekdon, R. A. *Chirotechnology*; Dekker, New York/Basel, **1993**, 39-72.
3. Jirage, K. B.; Martin, C. R. *Trends Biotechnol.* **1999**, *17*, 197-221.
4. Caner, H.; Groner, E.; Levy, L. *Drug Discovery Today* **2004**, *9*, 105-116.
5. Stefan, R. I; van Staden, J. F.; Aboul-Enein, H. Y. *Electroanalysis* **1999**, *11*, 1233-1245.
6. Crosby, J. *Tetrahedron* **1991**, *47*, 4789-4796.
7. Jacques, J. Collet, A.; Wilen, S. H. *Enantiomers, Racemates, and Resolutions*; John Wiley & Sons, New York, **1981**, 328-342.
8. Valente, E. J.; Smith, T. N.; Harris, M. E. *Chirality* **2001**, *13*, 244-250.
9. Liao, J.; Sun, X. X.; Cui, X.; Yu, K. B.; Zhu, J.; Deng, J. G. *Chem.-Eur. J.* **2003**, *9*, 2611-2615.
10. Olszewska, T.; Milewska, M. J.; Gdaniec, M.; Maluszyńska, H.; Poloński, T. *J. Org. Chem.* **2001**, *66*, 501-506.
11. Pasteur, L. *Ann. Chim. Phys.* **1848**, *24*, 442-459.
12. Jung, T. A.; Schlittler, R. R.; Gimzewski, J. K. *Nature* **1997**, *386*, 696-698.
13. Lopinski, G. P.; Moffatt, D. J.; Wayner, D. D. M.; Wolkow, R. A. *Nature* **1998**, *392*, 909-911.
14. Böhringer, M.; Morgenstern, K.; Schneider, W.-D.; Berndt, R. *Angew. Chem. Int. Ed.* **1999**, *38*, 821-823.
15. Fang, H.; Giancarlo, L. C.; Flynn, G. W. *J. Phys. Chem.* **1998**, *102*, 7311-7315.

16. Lorenzo, M. O.; Baddeley, C. J.; Muryn, C.; Raval, R. *Nature* **2000**, *404*, 376-379.

17. Kuhnle, A.; Lindertoh, T. R.; Hammer, B.; Besenbacher, F. *Nature* **2002**, *415*, 891-893.

18. Steven, F.; Dyer, D. J.; Walba, D. M. *Angew. Chem. Int. Ed.* **1996**, *35*, 900-901.

19. De Feyter, S.; Gesquiere, A.; Abdel-Mottaleb, M. M.; Grim, P. C. M.; De Schryver, F. C.; Meiners, C.; Sieffert, M. *Acc. Chem. Res.* **2000**, *33*, 520-531.

20. De Feyter, S.; Gesquiere, A.; De Schryver, F. D.; Meiners, C.; Sueffert, M.; Müllen, K. *Langmuir* **2000**, *16*, 9887-9894.

21. De Feyter, S.; Grim, P. C. M.; Rucker, M.; Vanoppen, P.; Meiners, C.; Sieffert, M.; Valiyaveettil, S.; Müllen, K.; De Schryver, F. C. *Angew. Chem. Int. Ed.* **1998**, *37*, 1223-1226.

22. Jonkheijm, P.; Miura, A.; Zdanowska, M.; Hoeben, F. J. M.; De Feyter, S.; Schenning, A. P. H. J.; De Schryver, F. C.; Meijer, E. W. *Angew. Chem. Int. Ed.* **2004**, *43*, 74-78.

23. De Feyter, S.; Gesquiere, A.; Wurst, K.; Amabilino, D. B.; Veciana, J.; De Schryver, F. C. *Angew. Chem. Int. Ed.* **2001**, *40*, 3217-3220.

24. Böhringer, M.; Schneider, W.-D.; Berndt, R. *Angew. Chem. Int. Ed.* **2000**, *39*, 792-795.

25. Blüm, M.-C.; Ćavar, E.; Pivetta, M.; Patthey, F.; Schneider, W.-D. *Angew. Chem. Int. Ed.* **2005**, *44*, 5334-5337.

26. Yokota, M.; Doki, N.; Shimizu, K. *Cryst. Growth Des.* **2006**, *6*, 1588-1590.

27. Okamoto, Y.; Ikai, T. *Chem. Soc. Rev.* **2008**, *37*, 2593-2608.

28. Paci, I.; Szleifer, I.; Ratner, M. A. *J. Am. Chem. Soc.* **2007**, *129*, 3545-3555.

29. Fasel, R.; Parschau, M.; Ernst, K.–H. *Nature* **2006**, *439*, 449-452.

30. Parschau, M.; Romer, S.; Ernst, K.–H. *J. Am. Chem. Soc.* **2004**, *126*, 15398-15399.

31. Hibino, M.; Sumi, A.; Tsuchiya, H.; Hatta, I. *J. Phys. Chem. B* **1998**, *102*, 4544-4547.

32. Fang, H.; Giancarlo, L. C.; Flynn, G. W. *J. Phys. Chem. B* **1998**, *102*, 7311-7315.

33. Yablon, D. G.; Giancarlo, L. C.; Flynn, G. W. *J. Phys. Chem. B* **2000**, *104*, 7627-7635.

34. Rodriguez, J. G.; Tejedor, J. L. *J. Org. Chem.* **2002**, *67*, 7631-7640.

35. Rein, R. ; Gross, M.; Solladie, N. *Chem. Commun.* **2004**, 1992-1993.

36. Gimzewski, J. K. ; Joachim, C. ; Schlittler, R.; Langlais, V. *Science* **1998**, *281*, 531-533.

37. Griessl, S. J. H.; Lackinger, M.; Jamitzky, F.; Markert, T.; Hietschold, M.; Heckl, W. M. *Langmuir* **2004**, *20*, 9403-9407.

38. Lei, S.; Tahara, K.; Feng, X.; Furukawa, S.; De Schryver, F. C.; Müllen, K.; Tobe, Y.; De Feyter, S. *J. Am. Chem. Soc.* **2008**, 7119-7129.

39. Griessl, S. J. H.; Lackinger, M.; Jamitzky, F.; Markert, T.; Hietschold, M.; Heckl, W. M. *J. Phys. Chem. B* **2004**, *108*, 11556-11560.

40. The tetramethyl and tetrapropyl analogues of tetraethyl ester **TE-6** were synthesized by the same procedure as that used for preparing **TE-6**. Tetramethyl 5,5'-(1,4-phenylenedi-2,1-ethynediyl)bis(1,3-benzenedicarboxylate): mp > 230 °C; IR (KBr) 2953, 1729, 1246 cm^{-1}; ^1H NMR (400 MHz, $CDCl_3$) δ 8.64 (t, ^4J = 1.6 Hz, 2H), 8.36 (d, ^4J = 1.6 Hz, 4H), 7.56 (s, 4H), 3.98 (s, 12H); HRMS (ESI) calcd for $C_{30}H_{22}O_8$ + H *m/e* 510.4909, found 510.4913. Tetrapropyl 5,5'-(1,4-phenylenedi-2,1-ethynediyl)bis(1,3-benzene dicarboxylate): mp 115 °C; IR (KBr) 2971, 1717, 1244 cm^{-1}; ^1H NMR (400 MHz, $CDCl_3$) δ 8.64 (t, ^4J = 1.6 Hz, 2H), 8.36 (d, ^4J = 1.6 Hz, 4H), 7.57 (s, 4H), 4.34 (t, ^3J = 7 Hz, 8H), 1.83 (sextet, ^3J = 7 Hz, 8H), 1.06 (t, ^3J = 7 Hz, 12H); ^{13}C NMR (100 MHz, $CDCl_3$) δ 165.58, 136.76, 132.17, 131.78, 130.67, 124.32, 123.31, 91.03, 89.97, 67.57, 22.48, 10.90; HRMS (ESI) calcd for $C_{38}H_{38}O_8$ + H *m/e* 622.7035, found 622.7031.

CHAPTER 7

Conclusions and Future Work

7.1 Key Determinants of 2D Molecular Nanopatterning

Crystal engineering has seen explosive growth in recent years. A key strategy has been to build crystals using molecular self-assembly directed by reliable non-covalent interactions such as hydrogen bonds. The building blocks employed in this strategy, which have been called tectons, have well-defined geometries attached to multiple functional groups that control intermolecular association. In this dissertation, such a strategy was systematically explored for the first time as a way to nanopattern surfaces. Tectons were designed to have inherently strong affinity for adsorption on HOPG by incorporating largely planar conjugated aromatic cores. To favor strong inter-adsorbate interactions, these cores were grafted to various sticky sites, including diaminotriazine groups (Chapter 3) and isophthalic acid units (Chapters 4 and 6). For comparison, adsorption of the corresponding isophthalate esters was also examined (Chapter 5 and 6). An integrated study of the association of these compounds was carried out, featuring analysis by STM of 2D nanopatterns adsorbed on HOPG, augmented by extensive studies of 3D association by X-ray crystallography.

A recent theoretical study[1] has suggested that adsorption on graphite is determined by the following three types of interactions, shown in order of increasing importance: 1) long-range repulsive π-π interactions (0.10-0.30 eV) between the adsorbed molecules and graphite; 2) medium-range attractive π-π^* interactions (0.30-0.60 eV) between the functional groups and graphite; 3) short-range hydrogen-bonding interactions between functional groups (0.60-0.80 eV). The final structure of the adsorbate on graphite will

reflect the relative contributions of these interactions.

In the work summarized in this thesis, we have found that 2D nanopatterns formed by the adsorption of well-defined tectons on HOPG depend on several key factors, including molecular length, core size, molecular geometry, and the ability of functional groups to engage in hydrogen bonds. Our observations are in general agreement with the theoretical analyses discussed above. Key factors are analyzed below in greater detail.

7.1.1 Effect of Molecular Length

A particular feature of our study is the systematic comparison of the adsorption of series of molecules in which length varies, but in which the sticky sites remain the same and the cores are of the same general type. This is exemplified in Chapter 3 by the study of tecton **DAT-1** (two diaminotriazine groups linked by a diphenylacetylene spacer) and its elongated analogue **DAT-2** (two diaminotriazine groups linked by a 1,4-(diphenylethynyl)phenyl spacer). Both compounds generated well-ordered nanopatterns on HOPG, suggesting good affinity for the surface. Elongated tecton **DAT-2** behaved in part as expected, and the adsorbed molecules formed chains held together by hydrogen bonding according to the characteristic face-to-face motif preferred by DAT groups. However, adjacent chains were neither close-packed nor hydrogen bonded. We suggest that a fully hydrogen-bonded 2D network constructed from compound **DAT-2** would be too open to offer a suitable density of coverage, but not open enough to accommodate adsorbed molecules of the solvent, heptanoic acid. Shorter analogue **DAT-1**

was observed to achieve a higher density of packing by forming a monolayer in which half of the molecules are twisted out of the plane. The observed structure represents a compromise that increases coverage at the expense of making inter-adsorbate hydrogen bonding weaker. These examples demonstrate clearly that the hydrogen bonding of DAT groups is not strong enough to dictate what nanopattern emerges, and the existence of multiple hydrogen-bonding motifs available to DAT groups further complicates the effort to maintain a consistent architecture as the length is increased. Subtle effects of adsorbate-substrate interactions therefore appear to play an important role in determining what nanopattern is ultimately observed. As a result, the observed patterns are different in molecules of different length and affinity for HOPG, despite the underlying similarity of their structures.

Chapter 4 examines the association of tectons in which two isophthalic acid groups are attached to cores of different length. In BTA, the groups are attached directly to create a derivative of biphenyl, whereas in tectons **TA-5** and **TA-6** the groups are separated by ethynyl and 1,4-diethynylphenyl spacers, respectively. The resulting series of compounds BTA, **TA-5**, and **TA-6** therefore have long planar molecular cores of different length. Compounds of this type are designed to associate by normal cyclic hydrogen bonding of pairs of -COOH groups, leading either to parallel networks or Kagomé networks. All three compounds behaved as planned. The shortest analogue, BTA, was found to form the parallel network, while the longest analogue, **TA-6,** generated the Kagomé network. Of particular interest is the behavior of intermediate tecton **TA-5,** which produced hybrid structures composed of both parallel and Kagomé networks. The two motifs are closely

matched in energy and can merge into each other without creating discontinuities, thus resulting in frustrated 2D crystallization and the formation of molecularly resolved images of glasses. Co-adsorption of mixtures of tectons **TA-5** and **TA-6** on HOPG also proved to produce 2D molecular glasses. Again, the observed nanopatterns change with molecular length, when other parameters remain largely constant. Clearly, changes in length simultaneously change the heat of adsorption and thereby alter the balance between inter-adsorbate and adsorbate-substrate interactions, and we recognize the impossibility of examining the effect of length alone. Scaling 2D architectures by scaling the length of the individual subunits is likely to prove very challenging. It is helpful that tetraacids BTA, **TA-5**, and **TA-6** all maintained consistent patterns of interadsorbate hydrogen bonding, unlike the more promiscuous DAT series.

Similarly, as revealed in Chapter 5, the related tetraesters **TE-9**, **TE-10**, and **TE-11** differ primarily in length, but they were found to generate three different types of structures: the butterfly structure (**TE-9**), square structure (**TE-10**), and rhombic structure (**TE-11**). In all three cases, weak aromatic C–H···O hydrogen bonds appear to be present in the observed 2D nanopatterns, but the absence of stronger hydrogen bonds eliminates a potentially powerful directing effect that might have imposed greater similarity among the observed nanopatterns. The structural divergence of compounds **TE-9**, **TE-10**, and **TE-11** confirms a basic guideline of molecular tectonics, which requires the use of strong directional interactions to impose a particular order on association in 2D or 3D.

Effects of molecular length on 2D nanopatterns have been widely discussed by De Feyter and co-workers, but they have focused only on the length of long-chain alkyl

substituents.[2,3] For tectons without alkyl substituents, designed to have the same functional groups attached to similar cores, molecular length has proven to be a key determinant in the formation of well-ordered 2D nanopatterns. Clearly, the change of length influences the adsorbate-substrate interactions, alters the relative importance of interadsorbate interactions, and may have subtle indirect effects that determine which hydrogen bonding motifs are favored.

7.1.2 Effect of Core Size

Another feature of our study is the systematic comparison of the adsorption of series of molecules in which the length and sticky sites remain constant, but in which the aromatic character of the cores is varied. This is exemplified in Chapter 4 by the study of tetraacids **TA-6**, **TA-7,** and **TA-8**, which have conjugated linear cores incorporating benzene, naphthalene, and anthracene, respectively. Tecton **TA-6** was found to generate the Kagomé network, tecton **TA-8** formed the parallel network, and tecton **TA-7** produced both parallel and Kagomé networks in different areas, although the parallel network was clearly the dominant structure and formed larger domains. Chapter 5 presents a parallel study of the corresponding tetraesters **TE-6** (benzene in core), **TE-7** (naphthalene in core), and **TE-8** (anthracene in core). Compound **TE-8** produced linear tapes, unlike the square networks generated by analogues **TE-6** and **TE-7**. In all three cases, aromatic C–H···O hydrogen bonds are considered to help direct the association of adjacent tectons.

Both series of examples summarized above show that the architectures of 2D

nanopatterns depend on the nature of the core, when length and interadsorbate interactions are held constant. Alteration of the core influences the importance of adsorbate-substrate interactions, thus leading to the formation of different nanopatterns. With increasing aromatic character of the core, from benzene to naphthalene to anthracene, we expect increased affinity for HOPG and a tendency to favor closely packed straightforward structures, such as linear tapes, which increase the percentage of surface that is covered. In such cases, adsorbate-surface interactions increase at the expense of directional interadsorbate interactions. Other structures, such as the square nanopatterns formed by tetraesters **TE-6** and **TE-8**, incorporate hydrogen bonds that impose special constraints on packing and thereby reduce surface coverage in exchange for stronger inter-adsorbate interactions.

7.1.3 Effect of 2D Chirality

The compounds presented in Chapter 7 were specifically designed to have 2D chirality and to create enantiomorphous domains on the surface of HOPG. Tetraesters **TE-10** and **TE-11**, which have cores of 1,5-disubstituted naphthalene and 1,5-disubstituted anthracene, respectively, behaved as planned by generating enantiomorphous domains. Compound **TE-10** (naphthalene core) yielded a square network, and compound **TE-11** (anthracene core) produced linear tapes. These observations are consistent with the principles summarized above: 1) The observed nanopatterns are altered by changes in the aromatic character of the core, despite contstant molecular length and functionalization; and 2)

increased aromatic character tends to favor more closely packed structures that offer a higher density of coverage. Similarly, nanopatterns formed by the related 2D chiral tetraacids **TA-10** (naphthalene) and **TA-11** (anthracene) were different in ways consistent with the two principles underscored above.

The alteration of molecular geometry and symmetry to introduce 2D chirality may not change the adsorbate-substrate interactions, but it reliably alters the types of nanopatterns generated. In particular, it introduces the possibility of creating homochiral and heterochiral domains by adsorption. Molecular geometry is well known to be able to change 2D nanopatterns substantially, as shown by De Feyter and co-workers,[4,5] who examined derivatives of dehydrobenzo[12]annulene. One with a rhombic core formed Kagomé networks on HOPG, whereas one with a triangular core produced honeycomb structures. However, no previous studies have examined systematic alterations of molecular symmetry as an efficient way to generate completely different molecular nanopatterns, as well as to create 2D chirality purposefully.

7.1.4 Effect of Functional Groups

The studies summarized above provide solid proof that 2D nanopatterns produced by the adsorption of molecules with the same length and the same core can differ radically, depending on the functional groups that are present on the periphery. These groups can have important effects both on the heat of adsorption (adsorbate-substrate interactions) and on inter-adsorbate interactions. For example, compounds **DAT-1**, **TA-5**, and **TE-5,** which

all have the same diphenylethyne core, generated linear tapes, hybrid structures composed of both parallel and Kagomé networks, and butterfly structures, respectively. Similarly, compounds **DAT-2**, **TA-6**, and **TE-6**, which all have a core of 1,4-bis(phenylethynyl)benzene, produced linear tapes, Kagomé networks, and square structures, respectively. Furthermore, related pairs of compounds including **TA-7/TE-7**, **TA-8/TE-8**, **TA-10/TE-10**, and **TA-11/TE-11**, which have the same core grafted with either tetraacids or tetraesters, were found to produce entirely different nanopatterns on HOPG.

For tectons having the same core, the long-range π-π interactions between the adsorbed tectons and graphite, as presented previously, should be similar. The diversity of 2D nanopatterns can therefore be considered to originate from the medium-range attractive π-π^* interactions between the functional groups and graphite, as well as the hydrogen-bonding interactions of functional groups, which are crucial for directing molecular self-assembly.

7.2 Comparison of 2D and 3D Crystallization

Another characteristic feature of our work is the extensive integration of studies of 2D assembly based on analysis of STM images, with comparative examination of 3D structures, based on X-ray crystallography. As shown in Chapters 3 and 5, compounds with DAT groups (**DAT-1**, **DAT-2**, and **DAT-3**) and tetraesters (**TE-5**, **TE-6**, **TE-8**, and **TE-9**) have been crystallized, and the structures of their 2D and 3D assemblies have been

compared. Curiously, the corresponding tetraacids proved to be exceedingly difficult to crystallize. Comparisons of the 2D and 3D structures have provided deeper understanding of the ability of intermolecular interactions to control assembly in 2D and 3D. Generally, the compounds we have studied tend to crystallize as layered structures, which is a reflection of their extended flat geometries. In the case of compounds with DAT groups, the individual sheets proved to be extensively hydrogen bonded, with characteristic intermolecular N–H···N hydrogen bonding according to established motifs preferred by DAT groups. In the case of the tetraesters, the layers were found to be closely packed, with various weak C–H···O hydrogen bonds.

The structures observed in 2D and 3D rarely showed extensive homology, but certain important features are nevertheless shared. For example, similar face-to-face hydrogen-bonding motifs formed by DAT groups are found in both 2D and 3D structures of tecton **DAT-2**. In general, aromatic C–H···O hydrogen bonds appear to help direct the formation of 2D nanopatterns by the tetraesters, and they have also been seen in the 3D structure of compounds **TE-6** and **TE-8**. By comparing the 2D and 3D structures of the family of tetraesters, we have also revealed the importance of the specific conformations adopted by the ester groups, and we have confirmed that there are no strong directional interactions able to position adjacent molecules in predictable ways. This observation confirms the importance of using strong intermolecular interactions in engineering molecular assemblies, both in 2D and in 3D.

7.3 Future Work

Our previous work has used a powerful combination of synthesis, X-ray diffraction, STM, and computation to probe how 3D and 2D crystallization responds to systematic structural alterations. It is clear that directional interactions between adsorbed tectons can be even more important than diffuse interactions with the surface in determining the outcome of 2D nanopatterns. Our future work will focus on two challenging problems: 1) Performing nanolithography based on molecular masking and 2) controlling molecular organization in films thicker than monolayers, with significant 3D topography. Preliminary work summarized in this thesis has revealed that planar compounds with multiple DAT groups, such as **DAT-1**, have a strong affinity for HOPG and can form well-ordered structures in which molecules are adsorbed both parallel to the surface and inclined to it. This introduces an intriguing element of 3D topography that we intend to amplify by working with nonplanar analogues (represented by tectons **12-13**). These compounds are also ideal for binding curved surfaces such as those of carbon nanotubes or nanoparticles.

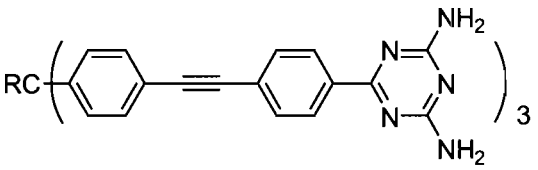

12

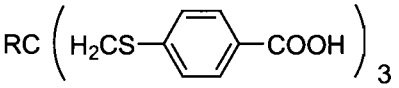

13

In addition, the strong inter-adsorbate interactions of these tectons and related compounds may allow them to adhere to normally inactive surfaces and to thereby act as priming layers that facilitate the subsequent adsorption of compounds of lower affinity.

References

1. Rochefort, A.; Wuest, J. D. *Langmuir* **2008**, *25*, 210-215.

2. Tahara, K.; Furukawa, S.; Uji-i, H.; Uchino, T.; Ichikawa, T.; Zhang, J.; Mamdouh, W.; Sonoda, M.; De Schryver, F. C.; De Feyter, S.; Tobe, Y. *J. Am. Chem. Soc.* **2006**, *128*, 16613-16625.

3. Lei, S.; Tahara, K.; Feng, X.; Furukawa, S.; De Schryver, F. C.; Müllen, K.; Tobe, Y.; De Feyter, S. *J. Am. Chem. Soc.* **2008**, *130*, 7119-7129.

4. Furukawa, S.; Uji-i, H.; Ichikawa, T.; Sonoda, M.; De Schryver, F. C.; Tobe, Y.; De Feyter, S. *J. Am. Chem. Soc.* **2006**, *128*, 3502-3503.

5. Tahara, K.; Johnson, C. A.; Fujita, T.; Sonoda, M.; De Schryver, F. C.; De Feyter, S.; Haley, M. M. ; Tobe, Y. *Langmuir* **2007**, *23*, 10190-10197.

6. Zhang, W.; Moore, J. S. *Angew. Chem. Int. Ed.* **2006**, *45*, 4416-4439.

7. Li, Y.; Zhao J.; Yin, X.; Yin, G. *ChemPhysChem* **2006**, *7*, 2593-2600.

8. Moore, J. S. *Acc. Chem. Res.* **1997**, *30*, 402-413.

9. Ge, P.-H.; Fu, W.; Herrmann, W. A.; Herdtweck, E.; Campana, C.; Adams, R. D.; Bunz, U. H. F. *Angew. Chem. Int. Ed.* **2000**, *39*, 3607-3610.

10. Shetty, A. S.; Fischer, P. R.; Stork, K. F.; Bohn, P. W.; Moore, J. S. *J. Am. Chem. Soc.* **1996**, *118*, 9409-9414.

11. Venkataraman, D.; Lee, S.; Zhang, J.; Moore, J. S. *Nature* **1994**, *371*, 591-593.

12. Miljanić, O. Š.; Vollhardt, K. P. C.; Whitener, G. D. *Synlett* **2003**, *1*, 29-34.

13. Li, H.; Huang, W.; Guo, Z.; Guduru, R.; Sun, Y.-P. *J. Phys. Chem. B* **2005**, *109*,

11886-11892.

14. Guldi, D. M. *Chem. Commun.* **2000**, 321-327.

CHAPTER 8

Experimental Section

8.1 General Information

All reagents and solvents were purchased from commercial sources and used without further purification unless otherwise indicated. Anhydrous and oxygen-free solvents were obtained by passing them through columns packed with activated alumina and supported copper catalyst (Glass Contour, Irvine, CA). Reactions requiring oxygen-free conditions were carried out under prepurified nitrogen, which was further dried by passing it through a $CaSO_4$ column.

Melting points were measured with a Thomas-Hoover capillary melting point apparatus (Arthur H. Thomas Co., Philadelphia, PA) and were uncorrected. Infrared spectra were recorded on a Perkin-Elmer 1600 series FTIR spectrophotometer using potassium bromide discs (KBr) or as neat liquid samples. Proton (^1H) and carbon (^{13}C) NMR spectra were recorded on a Bruker AV-400 instrument (400 MHz, 100.5 MHz). Chemical shifts (δ) were measured in parts per million (ppm) with reference to an internal standard, which was either tetramethylsilane (TMS) or dimethyl sulfoxide (DMSO, δH 2.49, δC 39.5). Coupling constants (*J*) are expressed in Hz. The abbreviations used for the description of multiplicities of the peaks are: s = singlet, d = doublet, t = triplet, q = quartet, bs = broadened singlet, dd = doublet of doublets, m = multiplet. High-resolution mass spectra (HRMS) were measured at the Centre régional de spectrométrie de masse du Département de Chimie de l'Université de Montréal. Elemental analyses were performed by the Laboratoire d'analyse élémentaire at the Université de Montréal. Flash chromatography was accomplished according to the standard procedure using Kieselgel 60 (230-400 mesh) silica gel.

X-ray crystallographic analyses were carried out on a Bruker AXS diffractometer using Cu Kα radiation produced from a FR591 rotating anode generator equipped with MONTEL 200 or HELIOS optics. The lattice parameters were optimized from a least-squares calculation on carefully centered reflections. Lattice determination and data collection were carried out using SMART Version 5.630 software.[1] Data reduction was performed using SAINT Version 7.01 software.[2] The structure refinement was performed using SHELXL.[3] The data were corrected for adsorption using the SADABS program within the SHELXTL 6.14 software package.[4,5]

8.2 Experimental Details

8.2.1 STM Studies

All experiments were performed at room temperature (20 - 25 °C) using a JEOL- 5200 SPM instrument equipped with a narrow scanner. Heptanoic acid was purchased from Aldrich and used as received. Platinum/iridium STM tips (Pt/Ir, 80%/20%, diameter = 0.2 mm) were prepared by mechanical cutting with a wire cutter. Prior to imaging, target tectons were suspended in heptanoic acid in amounts equivalent to concentrations of approximately 10^{-4} M. For a typical experiment, the freshly cleaved surface of HOPG (Structure Probe, Inc., SPI-1 grade) was first imaged to determine the quality of the Pt/Ir tip and the smoothness of the graphite surface. Once this was determined, a droplet (~ 1 μL) of a suspension containing the target compound was applied. The STM investigations were then carried out at the liquid-solid interface in the constant-height mode. STM imaging was

performed by changing the tunneling parameters (voltage applied to the tip and the average tunneling current). Raw STM images were processed using a JEOL software package (WinSPM DPS software Version 2.01, R. B. Leane, JEOL Ltd.) and a freeware (WSxM 4.0 Develop 8.21, Nanotec Electronica S. L., © August 2005). There was no need for further correction or calibration, as shown by the ability to obtain reproducible structural parameters in multiple experiments, including scans of TMA and HOPG itself. Molecular modeling was performed using the software Materials Studio (v4.3.0.0, Accelrys Software Inc., © 2008).

8.2.2 Synthesis of Bis(4-cyanophenyl)acetylene (6)[6,7]

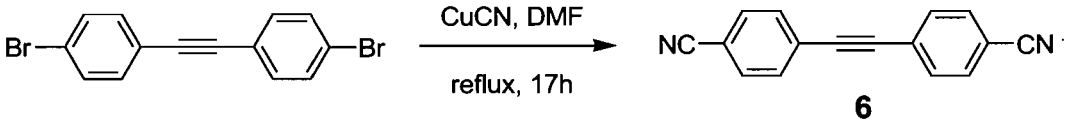

6

Commercially available bis(4-bromophenyl)acetylene (2.10 g, 6.25 mmol) was combined with CuCN (1.68 g, 18.7 mmol in dry DMF (10 mL), and the mixture was heated at reflux under N_2 for 17 h. The mixture was then cooled to room temperature and poured into water (50 mL). The resulting precipitate was collected by filtration and washed with a 3:1 mixture of water/ethylenediamine and then with water. The residue was suspended in CH_2Cl_2, and the organic phase was washed several times with a mixture of water and ethylenediamine. The organic phase was then washed with water, 1 M HCl, and brine, and it was subsequently dried over $MgSO_4$ and filtered. Volatiles were then removed by evaporation under reduced pressure. The crude product was purified by flash

chromatography (1:1 hexane/CH_2Cl_2) to give bis(4-cyanophenyl)-acetylene[6,7] (**6**; 1.06 g, 4.64 mmol, 74%) as a colorless solid: ^{1}H NMR (400 MHz, $CDCl_3$) δ 7.62 (d, ^3J = 8 Hz, 4H), 7.67 (d, ^3J = 8 Hz, 4H); ^{13}C NMR (100 MHz, $CDCl_3$) δ 92.0, 112.8, 118.7, 127.5, 132.6, 132.7.

8.2.3 Synthesis of DAT-1

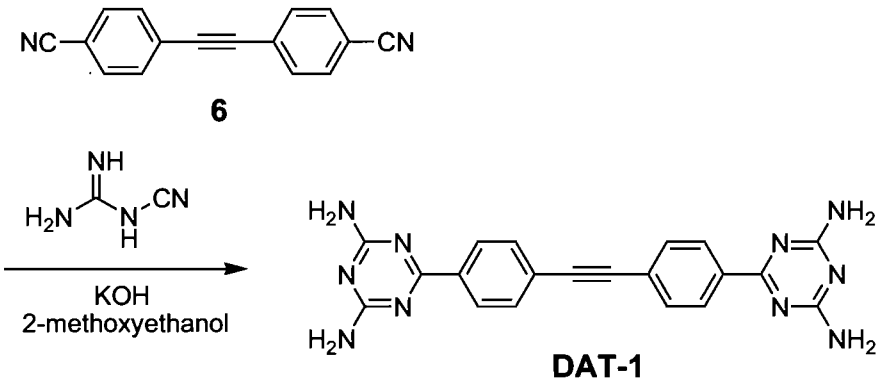

A mixture of bis(4-cyanophenyl)acetylene (**6**; 1.00 g, 4.38 mmol), dicyandiamide (1.47 g, 17.5 mmol), and potassium hydroxide (0.50 g, 8.9 mmol) in 2-methoxyethanol (15 mL) was heated at reflux for 20 h. The mixture was cooled to room temperature and diluted with water. The resulting precipitate was collected by filtration, washed with hot water, ethanol, and methanol, and dried in vacuum. The crude product was then recrystallized from DMSO/water to give 4,4'-bis(diaminotriazinyl)diphenylacetylene (**DAT-1**; 1.22 g, 3.18 mmol, 70%) as a colorless solid: mp > 250 °C; IR (KBr) 3499, 1618, 1396 cm^{-1}; ^{1}H NMR (400 MHz, DMSO-d_6) δ 6.81 (bs, 8H), 7.68 (d, ^3J = 8.2 Hz, 4H), 8.30 (d, ^3J = 8.2 Hz, 4H); ^{13}C NMR (100 MHz, DMSO-d_6) δ 91.8, 125.3, 128.8, 132.2, 138.3, 168.3, 170.2; HRMS (APCI) calcd for $C_{20}H_{16}N_{10}$+H *m/z* 397.1632, found 397.1640.

8.2.4 Synthesis of 1,4-Bis[(4-cyanophenyl)ethynyl]benzene (7)[8]

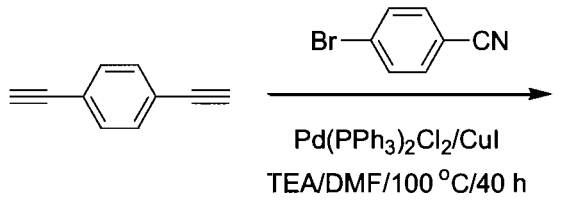

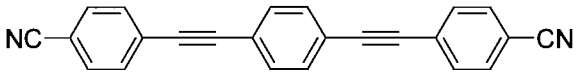

7

A mixture of triethylamine (TEA; 50 mL) and DMF (50 mL) was degassed by bubbling N_2 through it for 30 min. 4-Bromobenzonitrile (1.82 g, 10.0 mmol) was added, followed by dichlorobis(triphenylphosphine)palladium(II) (110 mg, 0.158 mmol) and copper(I) iodide (35.2 mg, 0.184 mmol). The mixture was stirred at room temperature for 3 h, and then a solution of 1,4-diethynylbenzene (694 mg, 5.50 mmol) in DMF (5 mL) was added dropwise. The resulting mixture was stirred at room temperature for 30 min and then at 100 °C for 40 h. Volatiles were then removed by evaporation under reduced pressure. Ethyl acetate (100 mL) was added to the residue, and a yellow solid precipitated immediately. The solid was separated by filtration, washed with H_2O, ethyl acetate, and hexane, and dried in vacuum. The crude product was recrystallized from DMSO to provide pure 1,4-bis[(4-cyanophenyl)ethynyl]benzene[8] (**7**; 1.15 g, 3.52 mmol, 90%) as a yellow-brown solid mp > 230 °C; IR (KBr) 2233, 1601 cm^{-1} ; ^1H NMR (400 MHz, DMSO-d_6) 7.92 (d, ^3J = 8 Hz, 4H), 7.77 (d, ^3J = 8 Hz, 4H), δ 7.69 (s, 4H); ^{13}C NMR (100 MHz, DMSO-d_6) δ 133.53, 133.12, 132.91, 127.65, 123.18, 119.26, 112.14, 93.46, 87.15; HRMS (ESI) calcd for $C_{24}H_{12}N_2$ + Ag *m/e* 435.0051, found 435.0045.

8.2.5 Synthesis of DAT-2

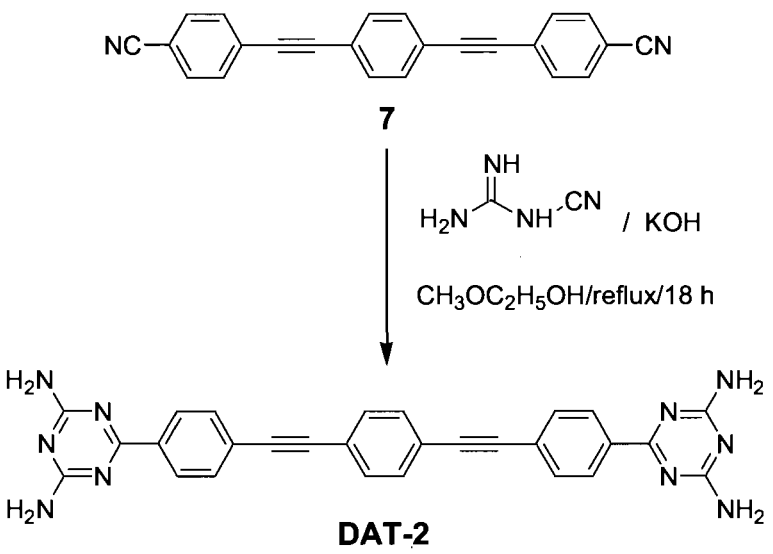

Dicyandiamide (230 mg, 2.73 mmol) and KOH (217 mg, 3.86 mmol) were added to 2-methoxyethanol (20 mL). The mixture was heated at 50 °C and stirred until the solids were dissolved. 1,4-Bis[(4-cyanophenyl)ethynyl]benzene (**7**; 250 mg, 0.761 mmol) was added to the solution. The resulting mixture was stirred at reflux for 18 h. The precipitated yellow solid was collected by filtration, washed with H_2O and ethyl ether, and dried in vacuum to provide **DAT-2** (223 mg, 0.449 mmol, 78%) as light yellow solid: mp > 250 °C; IR (KBr) 3315, 1604, 1399 cm^{-1}; ^1H NMR (400 MHz, DMSO-d_6) δ 8.30 (d, ^3J = 8 Hz, 4H), 7.68 (d, ^3J = 8 Hz, 4H), 7.65 (s, 4H), 6.83 (bs, 8H); ^{13}C NMR (100 MHz, DMSO-d_6) δ 170.24, 168.28, 138.30, 132.67, 132.22, 128.80, 125.27, 123.34, 92.18, 91.53; HRMS (ESI) calcd for $C_{28}H_{20}N_{10}$ + H *m/e* 497.1950, found 497.1945.

8.2.6 Synthesis of 1,4-Bis(dodecyloxy)-2,5-diiodobenzene (9)[9]

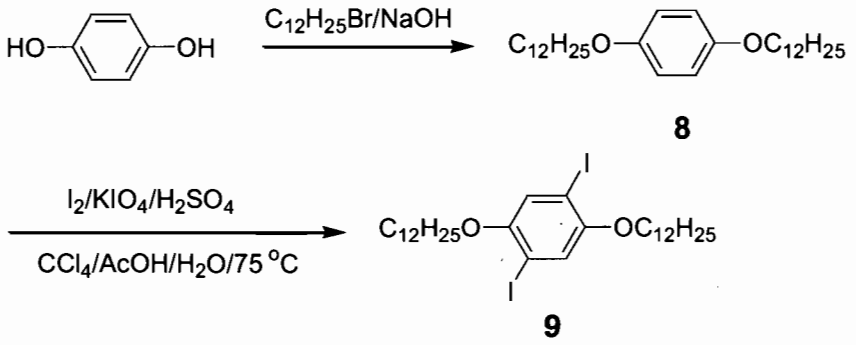

1,4-Hydroquinone (1.1 g, 10 mmol) was dissolved in DMF (20 mL), followed by the addition of 1-bromododecane (5.2 g, 20 mmol) and sodium hydroxide (2.4 g, 60 mmol). The resulting mixture was heated at 120 °C for 12 h. The mixture was then cooled to room temperature and diluted with H_2O (100 mL). The resulting solution was neutralized to pH ~7 with concentrated aqueous HCl (10 N). The precipitated solid was collected by filtration and washed successively with hexane and ethyl ether to provide 1,4-bis(dodecyloxy)benzene[9] (**8**; 3.89 g, 8.71 mmol, 87%) as a colorless waxy solid: ^{1}H NMR (400 MHz, $CDCl_3$) δ 6.81 (s, 4H), 3.89 (t, ^3J = 6.4 Hz, 4H), 1.75 (m, 4H), 1.26 (m, 36H), 0.88 (t, ^3J = 6.8 Hz, 6H); ^{13}C NMR (100 MHz, $CDCl_3$) δ 153.60, 115.78, 69.06, 32.34, 30.08, 30.03, 30.05, 30.01, 29.84, 29.82, 29.77, 26.48, 23.11, 14.54.

1,4-Bis(dodecyloxy)benzene (**8**; 2.26 g, 5.06 mmol) was dissolved in glacial acetic acid (20 mL). To the solution were added iodine (1.16 g, 4.57 mmol) and potassium iodate (654 mg, 3.06 mmol), and then a small amount of sulfuric acid (0.8 mL), H_2O (3 mL), and CCl_4 (4 mL) were added. The resulting mixture was heated at 75 °C for 3 h. A solution of sodium thiosulfate (10 mL, 2 N) was then added to consume unreacted iodine. The

resulting solution was extracted with dichloromethane (200 mL). The organic phase was washed with aqueous sodium hydroxide (5%) and H_2O, and it was then dried over $MgSO_4$. Volatiles were removed by evaporation under reduced pressure, and the residue was purified by recrystallization from ethanol to give pure 1,4-bis(dodecyloxy)-2,5-diiodobenzene[9] (**9**; 2.85 g, 4.08 mmol, 81%) as a colorless solid: ^{1}H NMR (400 MHz, $CDCl_3$) δ 7.17 (s, 2H), 3.92 (t, ^3J = 6.4 Hz, 4H), 1.79 (m, 4H), 1.26 (m, 36H), 0.88 (t, ^3J = 8 Hz, 6H); ^{13}C NMR (100 MHz, $CDCl_3$) δ 153.27, 123.19, 86.72, 70.77, 32.34, 30.08, 30.06, 30.00, 29.98, 29.78, 29.70, 29.56, 26.44, 23.11, 14.55.

8.2.7 Synthesis of 1,4-Bis(dodecyloxy)-2,5-diethynylbenzene (11)[10,11]

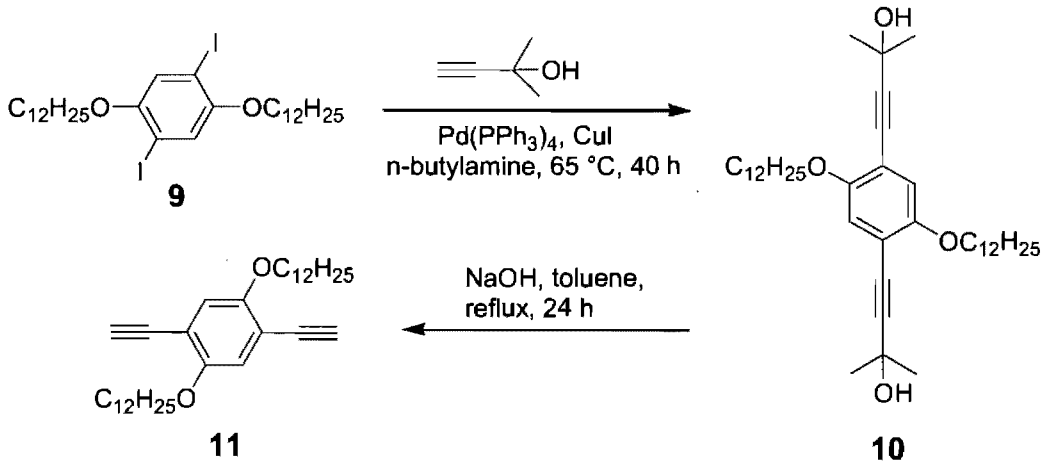

1,4-Bis(dodecyloxy)-2,5-diiodobenzene (**9**; 1.05 g, 1.50 mmol) was added to n-butylamine (100 mL), which was degassed by bubbling dry N_2 through it for 30 min, followed by the addition of tetrakis(triphenylphosphine)palladium (110 mg, 0.0752 mmol), copper(I) iodide (30 mg, 0.15 mmol), and 2-methyl-3-butyn-2-ol (252 mg, 2.99 mmol). The resulting mixture was stirred at 60 ~ 65 °C for 40 h. Removal of volatiles by evaporation under reduced pressure left a residue, which was further purified by flash

chromatography on silica (5:1 hexane/ethyl acetate) to give intermediate **10**[10,11] (720 mg, 1.17 mmol, 80%) as a yellow solid: ^{1}H NMR (400 MHz, $CDCl_3$) δ 6.84 (s, 2H), 3.92 (t, ^3J = 6.4 Hz, 4H), 1.78 (m, 4H), 1.62 (s, 6H), 1.26 (m, 36H), 0.88 (t, ^3J = 7.2 Hz, 6H); ^{13}C NMR (100 MHz, $CDCl_3$) δ 153.93, 117.35, 113.68, 99.46, 78.83, 69.82, 66.14, 32.32, 31.84, 30.17, 30.08, 30.06, 30.05, 29.82, 29.76, 29.65, 26.43, 23.10, 14.53.

Intermediate **10** (424 mg, 0.694 mmol) was dissolved in toluene (80 mL), followed by the addition of sodium hydroxide (4.2 g, 0.11 mol). The resulting mixture was stirred at reflux for 24 h. Volatiles were removed under reduced pressure to give a residue, which was then purified by flash chromatography on silica (6:1 hexane/ethyl acetate) to provide 1,4-bis(dodecyloxy)-2,5-diethynylbenzene[10,11] (**11**; 308 mg, 0.0606 mmol, 90%) as a colorless solid: mp 103°C; IR (KBr) 3280, 1580, 1255 cm^{-1}; ^{1}H NMR (400 MHz, $CDCl_3$) δ 6.95 (s, 2H), 3.96 (t, ^3J = 6.4 Hz, 4H), 3.33 (s, 2H), 1.79 (m, 4H), 1.26 (m, 36H), 0.88 (t, ^3J = 7.2 Hz, 6H); ^{13}C NMR (100 MHz, $CDCl_3$) δ 154.37, 118.11, 113.63, 82.80, 80.18, 70.04, 32.33, 30.07, 30.06, 29.99, 29.98, 29.76, 29.74, 29.52, 26.30, 23.10, 14.53.

8.2.8 Synthesis of DAT-3

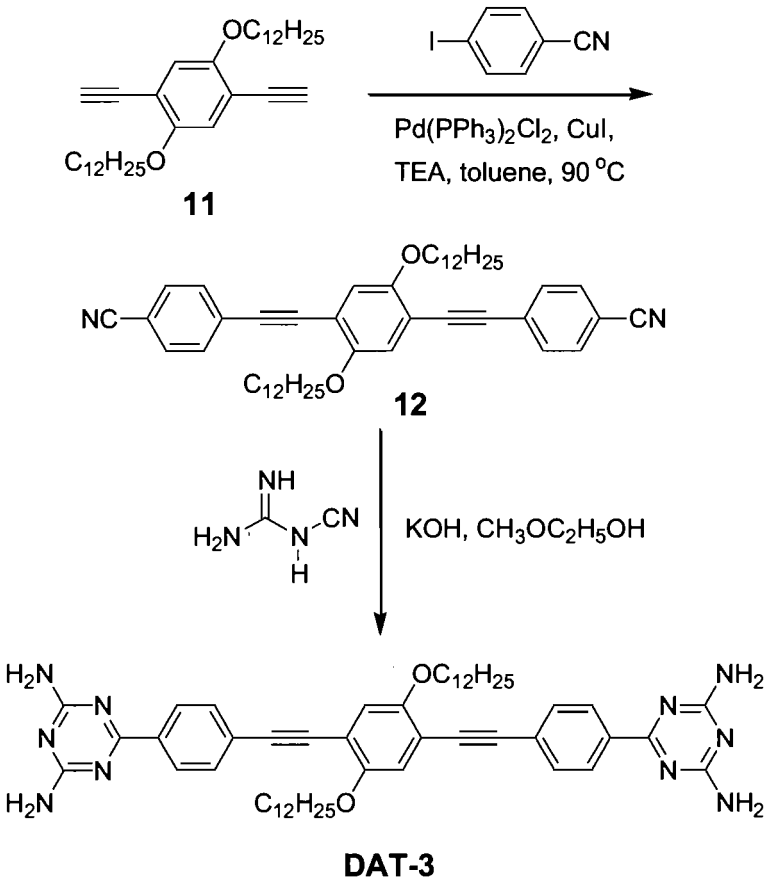

A mixture of dry triethylamine (15 mL) and toluene (30 mL) was degassed by bubbling dry N_2 through it for 30 min. 1,4-Bis(dodecyloxy)-2,5-diethynylbenzene (**11**; 220 mg, 0.445 mmol) was added to the mixture, followed by 4-iodo-benzonitrile (224 mg, 0.981 mmol), bis(triphenylphosphine)palladium(II) dichloride (19 mg, 0.026 mmol), and copper(I) iodide (25 mg, 0.13 mmol). The resulting mixture was stirred at room temperature for 15 min and was then heated at 90 °C for 20 h. Removal of volatiles by evaporation under reduced pressure left a residue, which was purified by flash chromatography on silica (7:1 hexane/ethyl acetate) to give dinitrile **12** (150 mg, 0.215 mmol, 65%) as a yellow solid.

Without further purification, dinitrile **12** (150 mg, 0.215 mmol) was added to 2-methoxyethanol (15 mL), followed by the addition of dicyandiamide (66 mg, 0.78 mmol) and potassium hydroxide (63 mg, 1.1 mmol). The resulting mixture was stirred at reflux for 18 h. The mixture was cooled to room temperature and diluted with H_2O (30 mL). The precipitated solid was collected by filtration, washed with H_2O and ethyl acetate, and dried in vacuum to provide **DAT-3** (204 mg, 0.236 mmol, 78%) as a bright yellow solid: mp 215 °C; IR (KBr) 2922, 1544, 1396 cm^{-1}; ^1H NMR (400 MHz, DMSO-d_6) δ 8.29 (d, ^3J = 8 Hz, 4H), 7.60 (d, ^3J = 8 Hz, 4H), 7.21 (s, 2H), 6.79 (s, 8H), 4.07 (t, ^3J = 6.2 Hz, 4H), 1.15 (m, 40H), 0.80 (t, ^3J = 7.2 Hz, 6H); ^{13}C NMR (100 MHz, DMSO-d_6) δ 170.92, 167.14, 153.71, 135.20, 131.55, 126.64, 128.35, 114.73, 113.53, 95.41, 88.01, 67.92, 32.30, 31.61, 30.26, 28.92, 27.77, 24.71, 23.64, 22.80, 15.82, 15.14, 14.41; HRMS (ESI) calcd for $C_{52}H_{68}N_{10}O_2$ + H *m/e* 865.5601, found 865.5599. Anal. Calcd for $C_{52}H_{68}N_{10}O_2$: N, 16.19; C, 72.19; H, 7.92. Found: N, 16.04; C, 72.08; H, 7.60.

8.2.9 Synthesis of 1,3,5-Triethynylbenzene (14)[12,13]

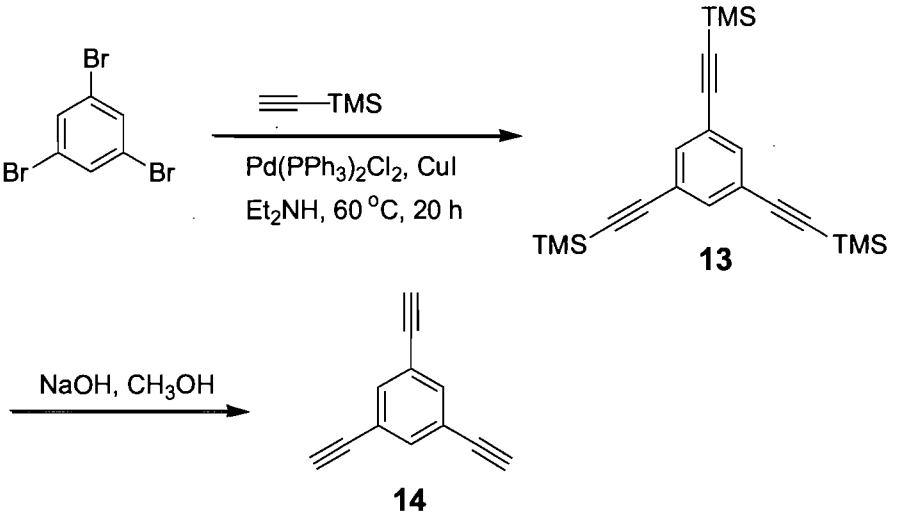

1,3,5-Tribromobenzene (2.1 g, 6.7 mmol) was dissolved in diethylamine (60 mL). The

mixture was degassed by bubbling dry N_2 through it for 30 min, and then dichlorobis(triphenylphosphine)palladium(II) (110 mg, 0.163 mmol) and copper(I) iodide (26 mg, 0.14 mmol) were added. The mixture was stirred at room temperature for 15 min, and then (trimethylsilyl)acetylene (2.78 g, 28.3 mmol) was added dropwise. The resulting mixture was heated at 50 °C for 20 h. The formed precipitate was filtered off and washed with ethyl ether. The combined filtrates were evaporated under reduced pressure to leave a residue, which was purified by flash chromatography on a column (Al_2O_3, hexane) to give 1,3,5-tris[(2-trimethylsilyl)ethynyl]benzene[12,13] (**13**; 2.26 g, 6.16 mmol, 92%) as a colorless solid: ^{1}H NMR (400 MHz, $CDCl_3$) δ 7.52 (s, 3H), 0.26 (s, 27H); ^{13}C NMR (100 MHz, $CDCl_3$) δ 135.32, 124.04, 103.54, 95.99, 0.23.

1,3,5-Tris[(2-trimethylsilyl)ethynyl]benzene (**13**; 2.6 g, 7.1 mmol) was dissolved in methanol (50 mL), followed by the addition of an aqueous solution of sodium hydroxide (0.1 N, 30 mL). The resulting mixture was stirred at room temperature for 1 h. Removal of methanol by evaporation under reduced pressure left a residue that was extracted with ethyl ether. The organic phase was separated, washed with H_2O, and then dried over $MgSO_4$. Volatiles were removed by evaporation under reduced pressure to provide 1,3,5-triethynylbenzene[12,13] (**14**; 1.06 g, 7.06 mmol, 98%) as a beige solid: ^{1}H NMR (400 MHz, $CDCl_3$) δ 7.60 (s, 3H), 3.14 (s, 3H); ^{13}C NMR (100 MHz, $CDCl_3$) δ 136.07, 123.32, 82.07, 79.16.

8.2.10 Synthesis of 1,3,5-Tris[2-(4-cyanophenyl)ethynyl]benzene (15)[14]

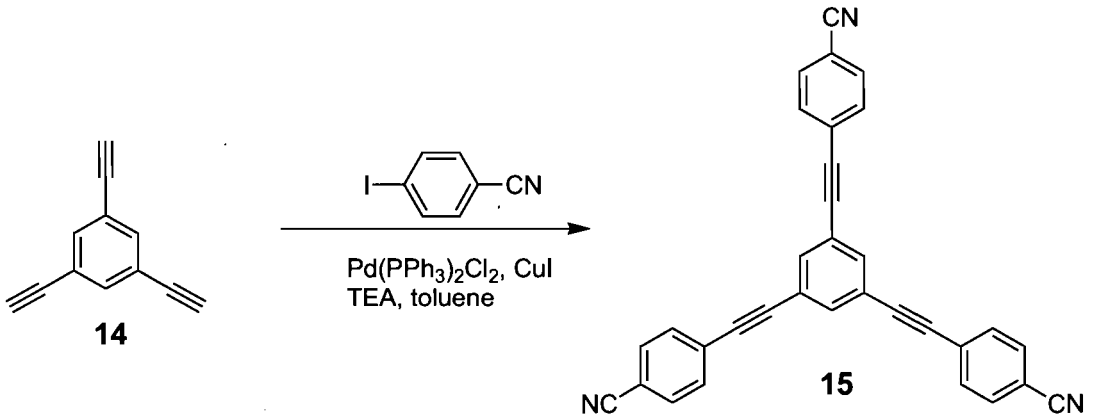

A mixture of toluene (40 mL) and triethylamine (20 mL) was degassed by bubbling dry N_2 through it for 30 min. 4-Iodobenzonitrile (1.07 g, 4.67 mmol) was added, followed by bis(triphenylphosphine)palladium(II) dichloride (57 mg, 0.081 mmol) and copper(I) iodide (25 mg, 0.13 mmol). The resulting mixture was stirred at room temperature for 15 min, and then a solution of 1,3,5-triethynylbenzene (**14**; 200 mg, 1.33 mmol) in dry toluene (5 mL) was added dropwise. The mixture was heated at 90 °C for 24 h, cooled, and then filtered. Volatiles were removed from the filtrate by evaporated under reduced pressure. The residue was dissolved in a small amount of dichloromethane and precipitated by the addition of hexane. The resulting solid was separated by filtration, washed with H_2O, hexane, and ethyl ether, and then dried in vacuum to give 1,3,5-tris[2-(4-cyanophenyl)ethynyl]benzene[14] (**15**; 390 mg, 1.40 mmol, 65%) as a beige solid: ^{1}H NMR (400 MHz, DMSO-d_6) δ 7.91 (d, ^3J = 8 Hz, 6H), 7.85 (s, 3H), 7.74 (d, ^3J = 8 Hz, 6H); ^{13}C NMR (100 MHz, DMSO-d_6) δ 135.67, 133.51, 133.18, 127.33, 123.93, 119.21, 112.31, 91.75, 90.44.

8.2.11 Synthesis of DAT-4

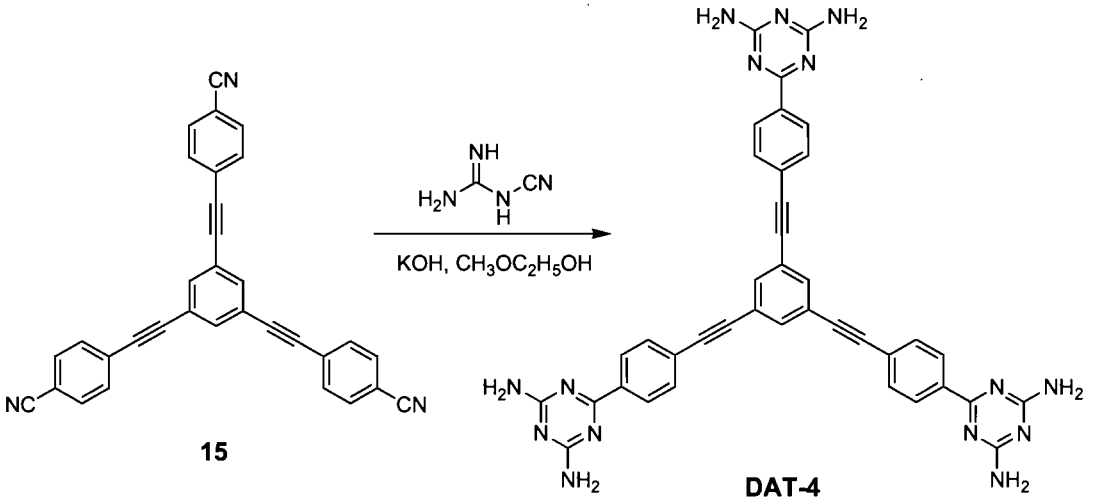

1,3,5-Tris[2-(4-cyanophenyl)ethynyl]benzene (**15**; 193 mg, 0.427 mmol) was added to 2-methoxyethanol (15 mL), followed by dicyandiamide (150 mg, 1.79 mmol) and potassium hydroxide (135 mg, 2.41 mmol). The resulting mixture was stirred and heated at reflux for 20 h. The mixture was cooled to room temperature and diluted with water. The resulting precipitate was collected by filtration, washed with hot water, hexane, and ethyl ether, and dried in vacuum to provide **DAT-4** (226 mg, 0.320 mmol, 75%) as a light yellow solid: mp > 250 °C; IR (KBr) 3192, 1579, 1396 cm^{-1}; ^1H NMR (400 MHz, DMSO-d_6) δ 8.31 (d, ^3J = 8 Hz, 6H), 7.84 (s, 3H), 7.71 (d, ^3J = 8 Hz, 6H), 6.83 (bs, 12H); ^{13}C NMR (100 MHz, DMSO-d_6) δ 170.21, 168.27, 138.53, 134.96, 132.36, 128.80, 124.98, 124.51, 91.68, 89.97; HRMS (ESI) calcd for $C_{39}H_{28}N_{15}$ + H *m/e* calcd. 706.2640, found 706.2647.

8.2.12 Synthesis of 3,3',5,5'-Biphenyltetracarboxylic acid (BTA)[15,16]

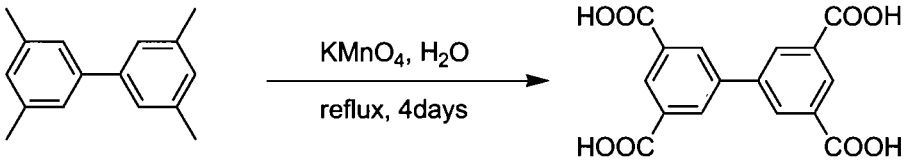

BTA

A mixture of 3,3',5,5'-tetramethylbiphenyl (1.0 g, 2.9 mmol), potassium permanganate (6.0 g, 23 mmol), and H_2O (200 mL) was stirred at reflux for 4 days. The unreacted 3,3',5,5'-tetramethylbiphenyl was removed by filtration. The filtrate was acidified to pH ~2 with a solution of HCl (3 N), affording a colorless precipitate. The precipitate was then washed with water and ethyl ether and was dried in vacuum to provide 3,3',5,5'-biphenyltetracarboxylic acid[15,16] (BTA; 558 mg, 1.69 mmol, 59%) as a colorless solid: ^{1}H NMR (400 MHz, DMSO-d_6) δ 13.5 (bs, 4H), 8.51 (s, 2H), 8.43 (s, 4H); ^{13}C NMR (100 MHz, DMSO-d_6) δ 167.18, 140.10, 133.20, 132.28, 130.91; HRMS (ESI) calcd for $C_{16}H_{10}O_8$ –H *m/e* 329.0297, found 329.0303.

8.2.13 Synthesis of Diethyl 5-Iodo-1,3-benzenedicarboxylate (17)[17]

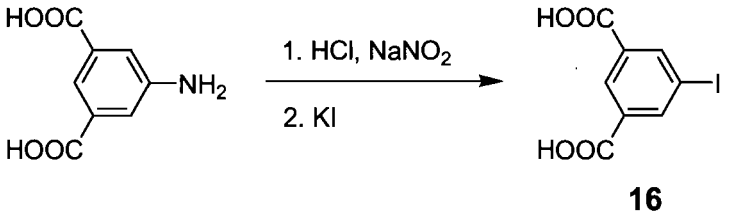

16

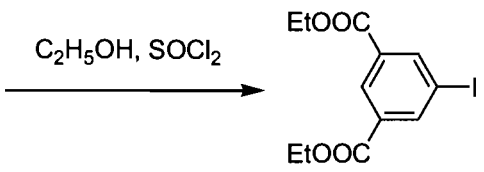

17

5-Aminophthalic acid (7.0 g, 39 mmol) was suspended in H_2O (20 mL) at 0 ~ 5 °C, followed by the addition of diluted HCl (100 mL, 1N) and sodium nitrite (2.8 g, 40 mmol). The resulting mixture was stirred at room temperature for 1 h to complete diazotization. A small amount of sulfamic acid (~100 mg) was added to remove excess nitrite. A solution of potassium iodide (25.5 g, 0.154 mol) dissolved in H_2O (15 mL) was added slowly, and then the mixture was stirred overnight at room temperature. The resulting solid was collected by filtration, washed with H_2O, and dried in vacuum to give 5-iodoisophthalic acid[17] (**16**; 8.26 g, 28.3 mmol, 73%) as a pink solid: ^{1}H NMR (400 MHz, DMSO-d_6) δ 13.5 (bs, 2H), 8.41 (s, 3H); ^{13}C NMR (100 MHz, DMSO-d_6) δ 166.11, 142.28, 133.96, 129.99, 95.64.

5-Iodoisophthalic acid (**16**; 5.0 g, 17 mmol) was added to absolute ethanol (50 mL), followed by slow addition of thionyl chloride (9.84 g, 82.7 mmol) at 0 °C. The resulting mixture was stirred at reflux for overnight. Ethanol was distilled out, and the crude residue was dissolved in ethyl acetate, affording a solution which was then washed with water and dried over anhydrous $MgSO_4$. Removal of the solvent by evaporation under reduced pressure left a residue that was further purified by flash chromatography on silica (6:1 hexane/ethyl acetate) to provide diethyl 5-iodo-1,3-benzenedicarboxylate[17] (**17**; 5.05 g, 14.5 mmol, 85%) as a colorless solid: ^{1}H NMR (400 MHz, DMSO-d_6) δ 8.64 (t, ^4J = 1.6 Hz, 1H), 8.54 (d, ^4J = 1.6 Hz, 2H), 4.42 (q, ^3J = 7.2 Hz, 4H), 1.43 (t, ^3J = 7.2 Hz, 6H); ^{13}C NMR (100 MHz, DMSO-d_6) δ 164.77, 142.71, 132.92, 130.21, 93.79, 62.15, 14.70.

8.2.14 Synthesis of Diethyl 5-Ethynyl-1,3-benzenedicarboxylate (18)[17]

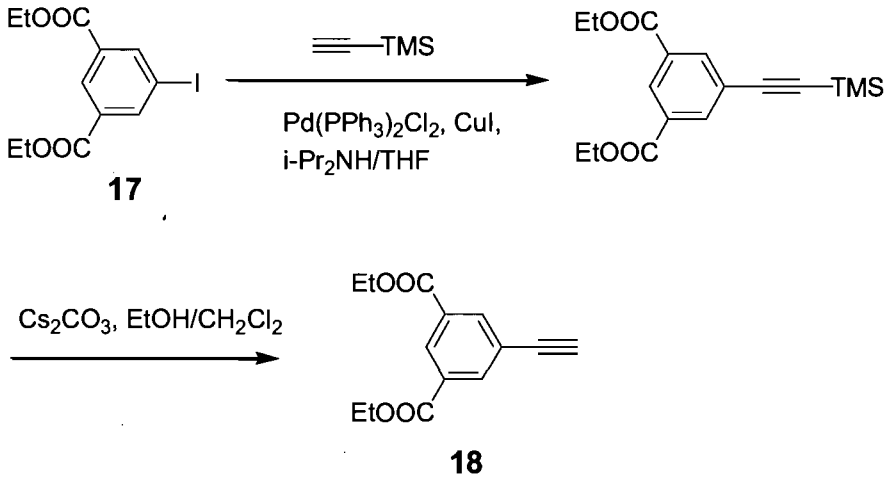

A mixture of dry THF (20 mL) and di-isopropylamine (10 mL) was degassed by bubbling dry N_2 through it for 30 min. Diethyl 5-iodo-1,3-benzenedicarboxylate (**17**; 1.52 g, 4.31 mmol) was added, followed by bis(triphenylphosphine)palladium(II) dichloride (161 mg, 0.229 mmol) and copper(I) iodide (87 mg, 0.46 mmol). The mixture was stirred at room temperature for 15 min, and then a solution of (trimethylsilyl)acetylene (417 mg, 4.25 mmol) in dry THF (5 mL) was added. The resulting mixture was stirred overnight at room temperature and was then filtered. Volatiles were removed from the filtrate by evaporation under reduced pressure. The residue was purified by flash chromatography on silica (7:1 hexane/ethyl acetate) to give crystalline diethyl 5-[2-(trimethylsilyl)ethynyl]-1,3-benzenedicarboxylate[17] (1.29 g, 4.08 mmol, 95%) as colorless needles: ^{1}H NMR (400 MHz, $CDCl_3$) δ 8.57 (t, ^4J = 1.6 Hz, 1H), 8.25 (d, ^4J = 1.6 Hz, 2H), 4.38 (q, ^3J = 7.2 Hz, 4H), 1.40 (t, ^3J = 7.2 Hz, 6H), 0.25 (s, 9H); ^{13}C NMR (100 MHz, $CDCl_3$) δ 165.56, 137.19, 131.66, 130.75, 124.57, 103.40, 97.00, 62.04, 14.83, 0.32.

Diethyl 5-(2-(trimethylsilyl)ethynyl]-1,3-benzenedicarboxylate (901 mg, 2.83 mmol)

was dissolved in a mixture of EtOH (5 mL) and CH_2Cl_2 (5 mL), and cesium carbonate (1.02 g, 5.29 mmol) was then added. The resulting mixture was stirred vigorously at room temperature for 2 h. Removal of the solvents by evaporation under reduced pressure left a residue, which was dissolved in CH_2Cl_2, washed with water, and then dried over anhydrous $MgSO_4$. Removal of solvent by evaporation under reduced pressure provided diethyl 5-ethynyl-1,3-benzenedicarboxylate[17] (**18**; 495 mg, 2.01 mmol, 71%) as a pale yellow solid: ^{1}H NMR (400 MHz, $CDCl_3$) δ 8.64 (t, ^4J = 1.2 Hz, 1H), 8.31 (d, ^4J = 1.2 Hz, 2H), 4.42 (q, ^3J = 7.2 Hz, 4H), 3.20 (s, 1H), 1.42 (t, ^3J = 7.2 Hz, 6H); ^{13}C NMR (100 MHz, $CDCl_3$) δ 165.38, 137.29, 131.67, 131.00, 132.41, 82.07, 79.46, 62.00, 14.67.

8.2.15 Synthesis of TE-5[18]

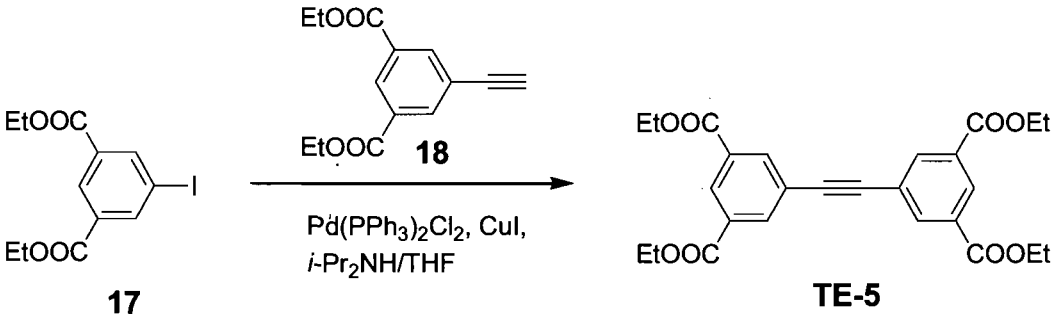

A mixture of dry THF (20 mL) and di-isopropylamine (10 mL) was degassed by bubbling dry N_2 through it for 30 min. Diethyl 5-iodo-1,3-benzenedicarboxylate (**17**; 315 mg, 0.905 mmol) was added, followed by bis(triphenylphosphine)palladium(II) dichloride (37.5 mg, 0.0534 mmol) and copper(I) iodide (28.7 mg, 0.151 mmol). The mixture was stirred at 25 °C for 15 min, and then a solution of diethyl 5-ethynyl-1,3-benzenedicarboxylate (**18**; 200 mg, 0.812 mmol) in dry THF (5 mL) was

added dropwise. The resulting mixture was stirred overnight at 25 °C. Volatiles were removed by evaporation under reduced pressure, and the residue was purified by flash chromatography on silica (5:1 hexane/ethyl acetate) to provide pure tetraethyl 5,5'-(1,2-ethynediyl)bis(1,3-benzenedicarboxylate)[18] (**TE-5**; 310 mg, 0.665 mmol, 82%) as a pale yellow solid: mp 172 °C; IR (KBr) 2984, 1733, 1722, 1241 cm^{-1}; ^1H NMR (400 MHz, $CDCl_3$) δ 8.68 (t, ^4J = 1.6 Hz, 2H), 8.40 (d, ^4J = 1.6 Hz, 4H), 4.45 (q, ^3J = 7.2 Hz, 8H), 1.45 (t, ^3J = 7.2 Hz, 12H); ^{13}C NMR (100 MHz, $CDCl_3$) δ 165.46, 136.87, 131.83, 130.94, 123.88, 89.50, 62.06, 14.72; HRMS (ESI) calcd for $C_{26}H_{26}O_8$ + H *m/e* 467.1700, found 467.1688. Anal. Calcd for $C_{26}H_{26}O_8$: C, 66.94; H, 5.62. Found: C, 66.81; H, 5.72.

8.2.16 Synthesis of TA-5[18]

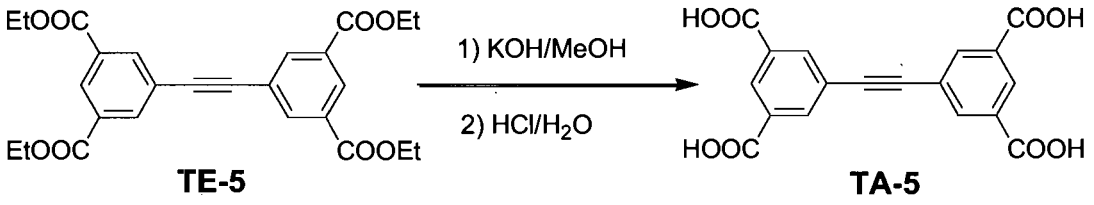

TE-5 **TA-5**

Tetraethyl 5,5'-(1,2-ethynediyl)bis(1,3-benzenedicarboxylate) (**TE-5**; 200 mg, 0.429 mmol), methanol (2 mL), and solid potassium hydroxide (240 mg, 4.28 mmol) were added to a 15 mL pressure tube containing a stirring bar. The tube was closed, and the mixture was stirred and heated at 80 °C for 3 h. Water (10 mL) was then added to dissolve solids, and the resulting solution was acidified to pH 1-2 with concentrated aqueous HCl (10 N). The precipitated solid was separated by filtration and washed successively with water and dichloromethane to give pure 5,5'-(1,2-ethynediyl)bis(1,3-benzenedicarboxylic acid)[18]

TA-5; 122 mg, 0.345 mmol, 81%) as a beige solid: mp > 225 °C ; IR (KBr) 3100 (br), 1703 cm^{-1}; ^1H NMR (400 MHz, DMSO-d_6) δ 8.46 (s, 2H), 8.33 (s, 4H), 13.50 (bs, 4H); ^{13}C NMR (100 MHz, DMSO-d_6) δ 166.67, 136.73, 132.88, 130.99, 123.70, 89.79; HRMS (ESI) calcd for $C_{18}H_{10}O_8$ - H *m/e* 353.0303, found 353.0305.

8.2.17 Synthesis of TE-6[18]

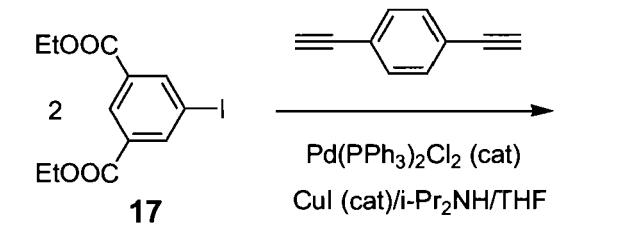

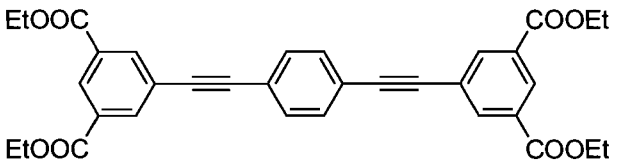

TE-6

A mixture of dry THF (20 mL) and di-isopropylamine (10 mL) was degassed by bubbling dry N_2 through it for 30 min. Diethyl 5-iodo-1,3-benzenedicarboxylate (**17**; 1.50 g, 4.31 mmol) was added, followed by bis(triphenylphosphine)palladium(II) dichloride (105 mg, 0.150 mmol) and copper(I) iodide (57.0 mg, 0.299 mmol). The mixture was stirred at room temperature for 15 min, and then a solution of 1,4-diethynylbenzene (252 mg, 2.00 mmol) in dry THF (5 mL) was added dropwise. The mixture was stirred overnight under N_2 at room temperature. The resulting solid was separated by filtration and dissolved in dichloromethane, and the organic phase was washed with water and dried over anhydrous $MgSO_4$. Removal of volatiles by evaporation under reduced pressure left a residue of pure

tetraethyl 5,5'-(1,4-phenylenedi-2,1-ethynediyl)bis(1,3-benzenedicarboxylate)[18] (**TE-6**; 986 mg, 1.74 mmol, 87%) as a pale yellow solid: mp 202 °C; IR (KBr) 2985, 1716, 1238 cm^{-1}; ^1H NMR (400 MHz, $CDCl_3$) δ 8.66 (s, 2H), 8.39 (s, 4H), 7.58 (s, 4H), 4.44 (q, ^3J = 7.1 Hz, 8H), 1.46 (t, ^3J = 7.1 Hz, 12H); ^{13}C NMR (100 MHz, $CDCl_3$) δ 165.54, 136.79, 132.17, 131.75, 130.65, 124.32, 123.32, 91.03, 89.96, 62.03, 14.73; HRMS (ESI) calcd for $C_{34}H_{30}O_8$ + H *m/e* 567.2013, found 567.2004. Anal. Calcd for $C_{34}H_{30}O_8$: C, 72.07; H, 5.34. Found: C, 72.12; H, 5.44.

8.2.18 Synthesis of TA-6[18]

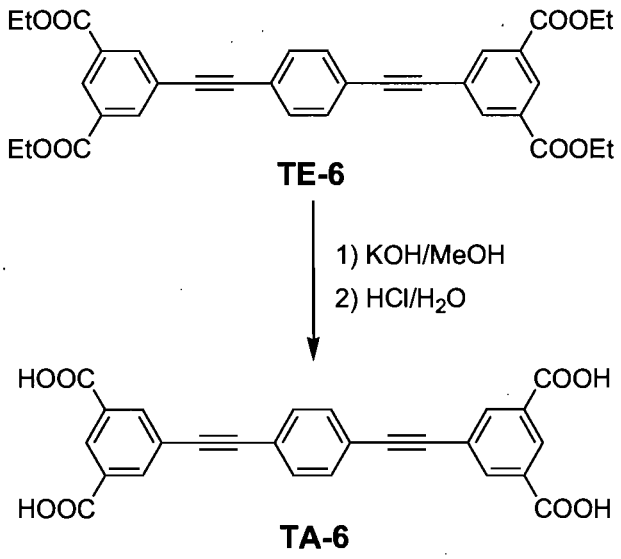

Tetraethyl 5,5'-(1,4-phenylenedi-2,1-ethynediyl)bis(1,3-benzenedicarboxyate) (**TE-6**; 286 mg, 0.505 mmol), methanol (5 mL), and solid potassium hydroxide (256 mg, 4.56 mmol) were added to a 15 mL pressure tube containing a stirring bar. The tube was closed, and the mixture was stirred and heated at 80 °C for 3 h. Water (10 mL) was then added to dissolve solids, and the resulting solution was acidified to pH 1-2 with concentrated

aqueous HCl (10 N). The precipitated solid was separated by filtration and washed successively with water and dichloromethane to give pure 5,5'-(1,4-phenylenedi-2,1-ethynediyl)bis(1,3- benzenedicarboxylic acid)[18] (**TA-6**; 180 mg, 0.396 mmol, 78%) as a beige solid: mp > 230 °C; IR (KBr) 3100 (br), 1700 cm^{-1}; ^1H NMR (400 MHz, DMSO-d_6) δ 13.53 (bs, 4H), 8.46 (s, 2H), 8.27 (s, 4H), 7.71 (s, 4H); ^{13}C NMR (100 MHz, DMSO-d_6) δ 165.79, 135.57, 132.15, 131.94, 129.93, 123.01, 122.30, 90.35, 89.57; HRMS (ESI) calcd for $C_{26}H_{14}O_8$ - H *m/e* 453.0616, found 454.0626.

8.2.19 Synthesis of 1,4-Diethynylnaphthalene (20)[19]

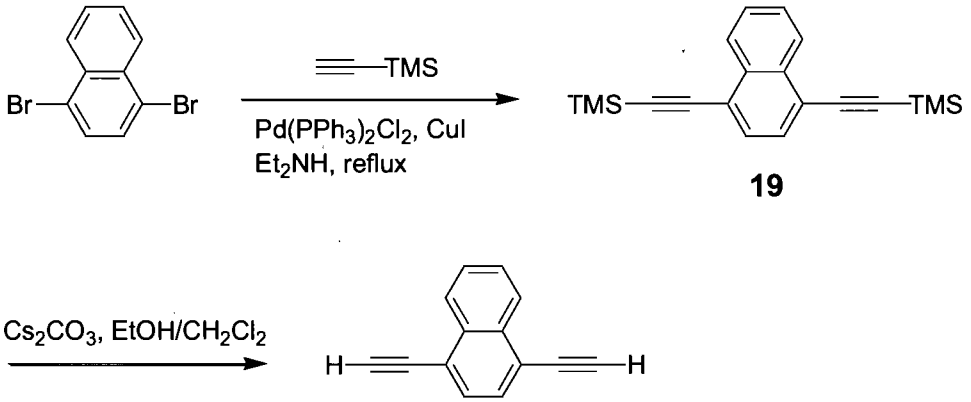

Diethylamine (50 mL) was degassed by bubbling dry N_2 through it for 30 min. 1,4-Dibromonaphthalene (2.28 g, 8.04 mmol) was added, followed by bis(triphenylphosphine)palladium(II) dichloride (280 mg, 0.399 mmol) and copper(I) iodide (152 mg, 0.798 mmol). The mixture was stirred at room temperature for 15 min, and then (trimethylsilyl)acetylene (3.14 g, 32.0 mmol) was added. The resulting mixture was heated and stirred at reflux overnight. Volatiles were removed by evaporation under

reduced pressure, and the residue was purified by flash chromatography on silica (1:20 benzene/hexane) to give 1,4-bis[2-(trimethylsilyl)ethynyl]naphthalene[19] (**19**; 2.13 g, 6.64 mmol, 85%) as a pale yellow solid: ^{1}H NMR (400 MHz, $CDCl_3$) δ 8.34 (m, 2H), 7.62 (s, 2H), 7.60 (m, 2H), 0.33 (s, 18H); ^{13}C NMR (100 MHz, $CDCl_3$) δ 133.49, 130.39, 127.66, 126.96, 121.94, 103.20, 101.79, 0.45.

1,4-Bis[2-(trimethylsilyl)ethynyl]naphthalene (**19**; 1.81 g, 5.62 mmol) was dissolved in a mixture of dichloromethane (10 mL) and ethanol (10 mL), and then cesium carbonate (2.72 g, 14.1 mmol) was added. The resulting mixture was stirred at room temperature for 2 h. After filtration, volatiles were removed by evaporation under reduced pressure to leave a solid, which was dissolved in dichloromethane. The organic phase was washed with water and dried over anhydrous $MgSO_4$. Removal of volatiles by evaporation under reduced pressure provided 1,4-diethynylnaphthalene[19] (**20**; 863 mg, 4.90 mmol, 87%) as a tan crystalline solid: ^{1}H NMR (400 MHz, $CDCl_3$) δ 8.42 (m, 2H), 7.71 (s, 2H), 7.66 (m, 2H), 3.60 (s, 2H); ^{13}C NMR (100 MHz, $CDCl_3$) δ 133.60, 130.75, 127.91, 126.87, 121.38, 84.11, 81.86.

8.2.20 Synthesis of TE-7

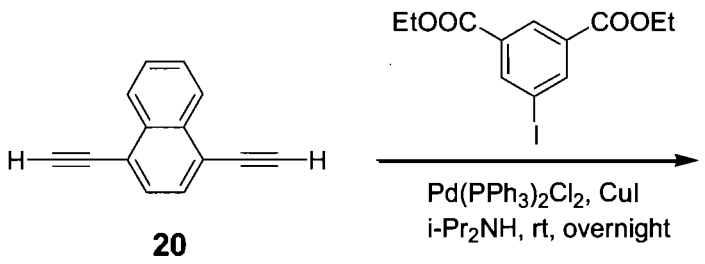

20

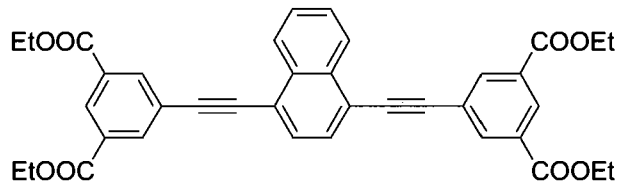

TE-7

A mixture of dry THF (30 mL) and di-isopropylamine (15 mL) was degassed by bubbling dry N_2 through it for 30 min. Diethyl 5-iodo-1,3-benzenedicarboxylate (2.10 g, 6.03 mmol) was added, followed by bis(triphenylphosphine)palladium(II) dichloride (120 mg, 0.171 mmol) and copper(I) iodide (57 mg, 0.30 mmol). The mixture was stirred at room temperature for 15 min, and then a solution of 1,4-diethynylnaphthalene (**20**; 590 mg, 3.35 mmol) in dry THF (5 mL) was added dropwise. The mixture was stirred overnight at room temperature. Removal of volatiles by evaporation under reduced pressure left a residue, which was then purified by flash chromatography (1:20 hexane/$CHCl_3$) to provide **TE-7** (1.63 g, 2.10 mmol, 80%) as a yellow solid: mp 141 °C; IR (KBr) 2980, 1723, 1187 cm^{-1}; ^1H NMR (400 MHz, $CDCl_3$) δ 8.66 (s, 2H), 8.46 (s, 4H), 8.46 (m, 2H), 7.77 (s, 2H), 7.70 (m, 2H), 4.45 (q, ^3J = 7.2 Hz, 8H), 1.46 (t, ^3J = 7.2 Hz, 12H); ^{13}C NMR (100 MHz, $CDCl_3$) δ 165.56, 136.81, 133.34, 131.81, 130.68, 130.47, 128.06, 126.98, 124.45, 121.72, 94.56, 89.52, 62.08, 14.75; HRMS (ESI) calcd for $C_{38}H_{32}O_8$ + H *m/e* 617.2161, found 617.2169.

8.2.21 Synthesis of TA-7

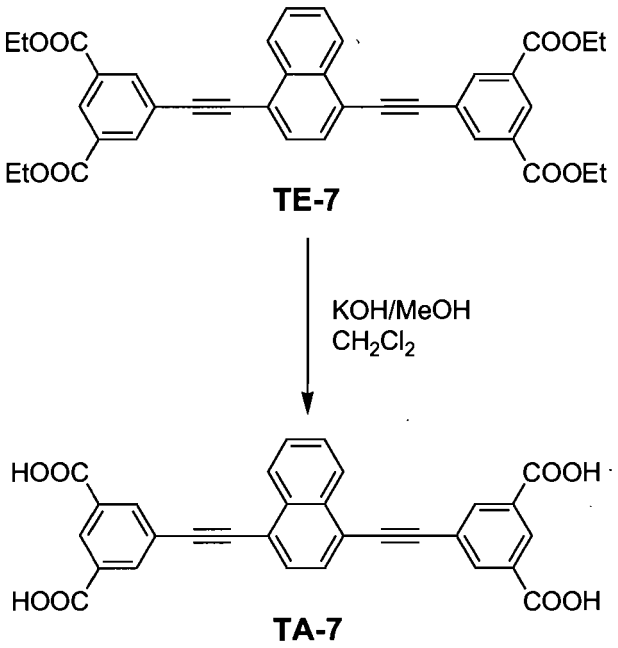

Tetraethyl 5,5'-(1,4-naphthalenedi-2,1-ethynediyl)bis(1,3-benzenedicarboxylate) (**TE-7**; 301 mg, 0.485 mmol), methanol (4 mL), dichloromethane (2 mL), and solid potassium hydroxide (256 mg, 4.56 mmol) were added to a 15 mL pressure tube containing a stirring bar. The tube was closed, and the mixture was stirred and heated at 80 °C for 3 h. Water (10 mL) was then added to dissolve solids, and the resulting solution was acidified to pH 1-2 with concentrated aqueous HCl (10 N). The precipitated solid was separated by filtration and washed successively with water and dichloromethane to give 5,5'-(1,4-naphthalenedi-2,1-ethynediyl)bis(1,3-benzenedicarboxylic acid) (**TA-7**; 178 mg, 0.354 mmol, 73%) as a light yellow solid: mp > 250 °C; IR (KBr) 3077, 1699, 1275 cm^{-1}; ^1H NMR (400 MHz, DMSO-d_6) δ 13.6 (bs, 4H), 8.49 (s, 2H), 8.49 (m, 2H), 8.40 (s, 4H), 7.94 (s, 2H), 7.82 (m, 2H); ^{13}C NMR (100 MHz, DMSO-d_6) δ 166.79, 136.56, 133.15, 133.04, 131.37, 130.96, 129.18, 127.16, 123.93, 121.44, 95.27, 89.35; HRMS (ESI) calcd for $C_{30}H_{16}O_8$ + H *m/e* 505.0923, found 505.0918.

8.2.22 Synthesis of 9,10-Diethynylanthracene (22)[19,20]

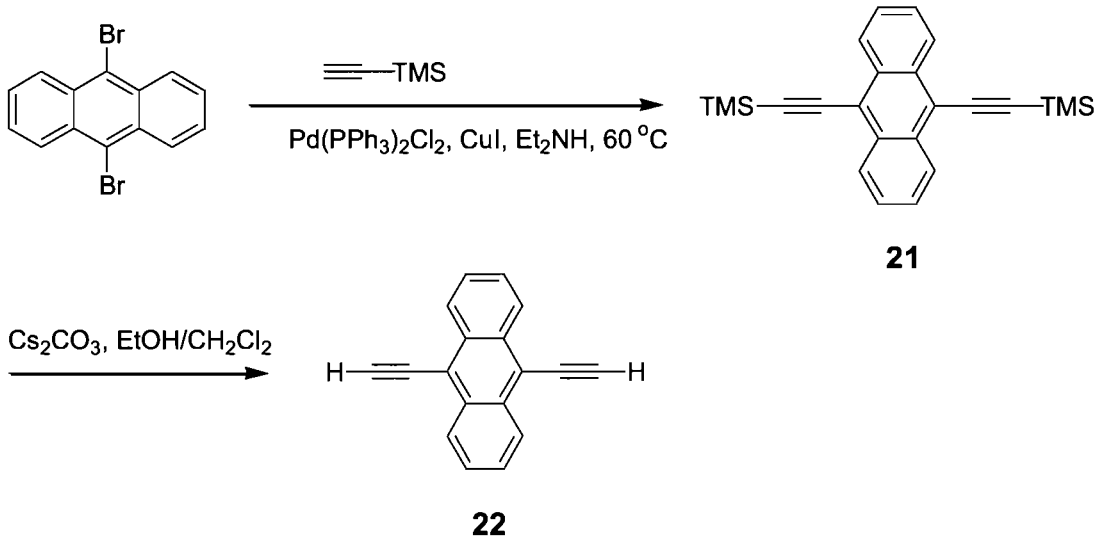

Diethylamine (100 mL) was degassed by bubbling dry N_2 through it for 30 min. 9,10-Dibromoanthracene (2.38 g, 7.14 mmol) was added, followed by bis(triphenylphosphine)palladium (II) dichloride (208 mg, 0.296 mmol) and copper(I) iodide (116 mg, 0.609 mmol). The mixture was stirred at room temperature for 15 min, and then (trimethylsilyl)acetylene (2.79 g, 28.5 mmol) was added. The resulting mixture was heated and stirred overnight at 60 °C under N_2. Volatiles were removed under reduced pressure. The residue was purified by flash chromatography on silica (1:9 benzene/hexane) to give 9,10-bis[2-(trimethylsilyl)ethynyl]anthracene[19] (**21**; 3.26 g, 5.48 mmol, 76%) as a yellow solid: ^{1}H NMR (400 MHz, $CDCl_3$) δ 8.57 (m, 4H), 7.60 (m, 4H), 0.42 (s, 18H); ^{13}C NMR (100 MHz, $CDCl_3$) δ 132.65, 127.61, 127.27, 118.85, 108.58, 101.89, 0.62.

9,10-Bis[2-(trimethylsilyl)ethynyl])anthracene (**21**; 743 mg, 2.00 mmol) was dissolved in a mixture of dichloromethane (10 mL) and ethanol (10 mL), and then cesium carbonate (783 mg, 4.06 mmol) was added. The resulting mixture was stirred at room temperature for 2 h. After filtration, volatiles were removed by evaporation under reduced pressure to leave

a solid, which was dissolved in dichloromethane. The organic phase was washed with water and dried over anhydrous $MgSO_4$. Removal of volatiles by evaporation under reduced pressure provided 9,10-diethynylanthracene[20] (**22**; 384 mg, 1.70 mmol, 85%) as a red dark crystalline solid: ^1H NMR (400 MHz, $CDCl_3$) δ 8.61 (m, 4H), 7.63 (m, 4H), 4.08 (s, 2H); ^{13}C NMR (100 MHz, $CDCl_3$) δ 132.87, 127.45, 127.08, 118.21, 90.28, 80.61.

8.2.23 Synthesis of TE-8

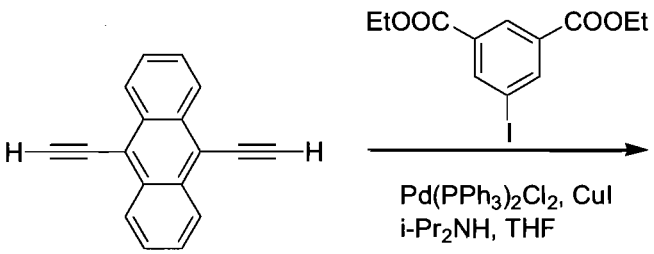

22

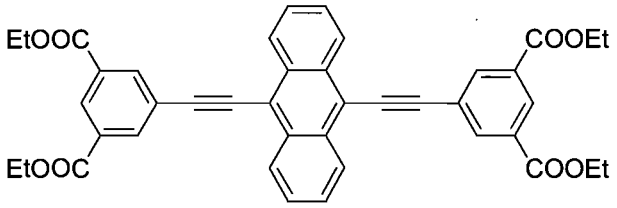

TE-8

A mixture of dry THF (30 mL) and di-isopropylamine (15 mL) was degassed by bubbling dry N_2 through it for 30 min. Diethyl 5-iodo-1,3-benzenedicarboxylate (776 mg, 2.23 mmol) was added, followed by bis(triphenylphosphine)palladium(II) dichloride (40 mg, 0.057 mmol) and copper(I) iodide (30 mg, 0.16 mmol). The mixture was stirred at room temperature for 15 min, and then a solution of 9,10-diethynylanthracene (**22**; 228 mg, 1.01 mmol) in dry THF (5 mL) was added dropwise. The mixture was stirred overnight at room temperature. The resulting solid was separated by filtration and dissolved in chloroform.

The solution was washed with water and then dried over anhydrous $MgSO_4$. Removal of volatiles by evaporation under reduced pressure provided **TE-8** (582 mg, 0.874 mmol, 88%) as a red solid: mp > 250 °C; IR (KBr) 2950, 1720, 1318, 1221 cm^{-1}; ^1H NMR (400 MHz, $CDCl_3$) δ 8.72 (m, 4H), 8.71 (t, ^4J = 1.6 Hz, 2H), 8.59 (d, ^4J = 1.6 Hz, 4H), 7.72(m, 4H), 4.49 (q, ^3J = 7.2 Hz, 8H), 1.48 (t, ^3J = 7.2 Hz, 12H); ^{13}C NMR (100 MHz, $CDCl_3$) δ 165.25, 136.39, 132.20, 131.53, 130.35, 127.27, 127.17, 124.27, 118.22, 100.49, 88.09, 61.76, 14.39; HRMS (ESI) calcd for $C_{42}H_{34}O_8$ + H *m/e* 667.2332, found 667.2326. Anal. Calcd for $C_{42}H_{34}O_8$: C, 75.66; H, 5.14. Found: C, 75.64; H, 4.68.

8.2.24 Synthesis of TA-8

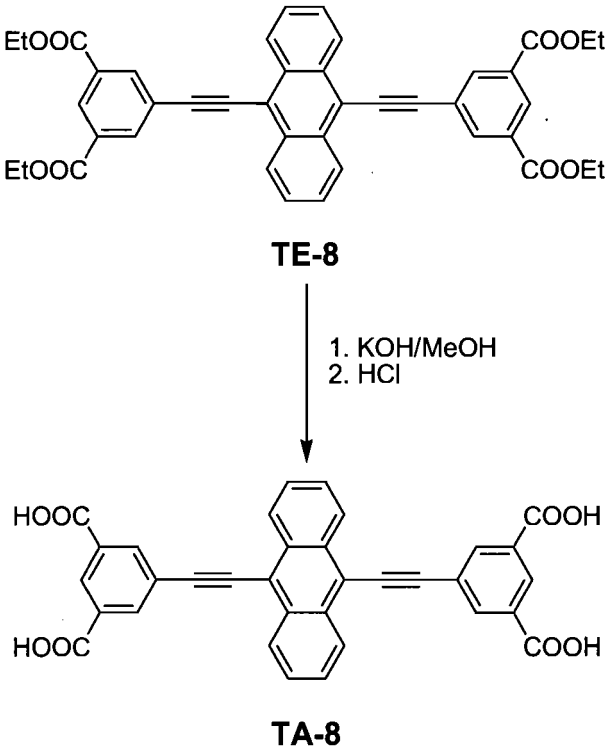

Diethyl 5,5'-(9,10-anthracenedi-2,1-ethynediyl)bis(1,3-benzenedicarboxylate) (**TE-8**; 251 mg, 0.375 mmol), methanol (4 mL), and solid potassium hydroxide (101 mg, 1.80 mmol)

were added to a 15 mL pressure tube containing a stirring bar. The tube was closed, and the mixture was stirred and heated at 80 °C for 3 h. Water (10 mL) was then added to dissolve solids, and the resulting solution was acidified to pH 1-2 with concentrated aqueous HCl (10 N). The precipitated solid was separated by filtration and washed successively with water and dichloromethane to give 5,5'-(1,4-anthracenedi-2,1-ethynediyl)bis(1,3-benzene dicarboxylic acid) (**TA-8**; 145 mg, 0.263 mmol, 70%) as a light yellow solid: mp > 250 °C; IR (KBr) 3429, 1698, 1207 cm-1; ^{1}H NMR (400 MHz, DMSO-d_6) δ 13.5 (bs, 4H), 8.74 (m, 4H), 8.56 (d, ^4J = 1.6 Hz, 4H), 8.53 (t, ^4J = 1.6 Hz, 2H), 7.85 (m, 4H); ^{13}C NMR (100 MHz, DMSO-d_6) δ 166.80, 136.71, 133.08, 132.33, 129.01, 127.72, 127.62, 124.12, 118.31, 101.80, 88.06; HRMS (ESI) calcd for $C_{34}H_{18}O_8$ + H *m/e* 555.1080, found 555.1074.

8.2.25 Synthesis of 4,4'-Diethynylbiphenyl (24) [21,22]

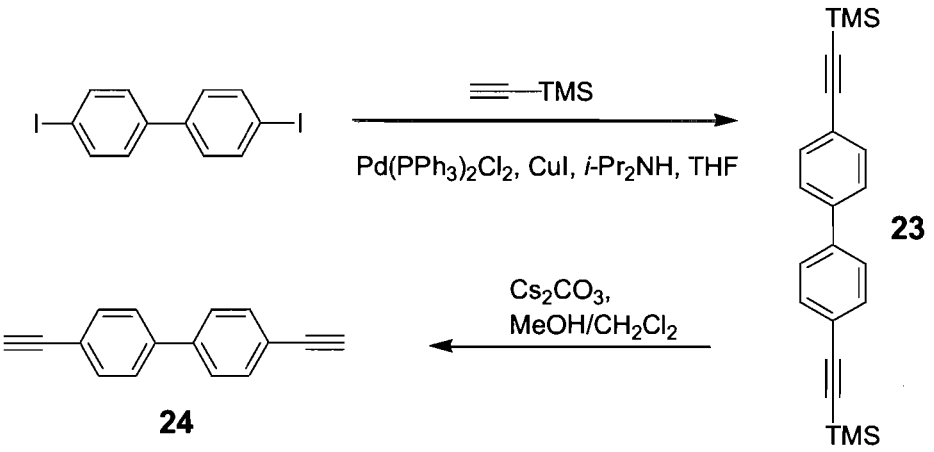

A mixture of dry THF (70 mL) and di-isopropylamine (20 mL) was degassed by bubbling dry N_2 through it for 30 min. 4,4'-Diiodobiphenyl (2.48 g, 6.11 mmol) was added, followed by bis(triphenylphosphine)palladium(II) dichloride (215 mg, 0.306 mmol) and copper(I) iodide (118 mg, 0.620 mmol). The mixture was stirred at room temperature for

15 min, and then a solution of (trimethylsilyl)acetylene (1.32 g, 13.4 mmol) in dry THF (5 mL) was added dropwise. The resulting mixture was stirred overnight at room temperature. Volatiles were removed by evaporation under reduced pressure. The residue was purified by flash chromatography on silica (40:1 hexane/ethyl acetate) to give 4,4'-bis[2-(trimethylsilyl)ethynyl]biphenyl[21] (**23**; 1.79 g, 5.19 mmol, 85%) as a yellow crystalline solid: ^{1}H NMR (400 MHz, $CDCl_3$) δ 7.57 (d, ^3J = 8 Hz, 4H), 7.54 (d, ^3J = 8 Hz, 4H), 0.34 (s, 18H); ^{13}C NMR (100 MHz, $CDCl_3$) δ 140.58, 132.89, 127.16, 122.88, 105.34, 95.65, 0.48.

4,4'-Bis[2-(trimethylsilyl)ethynyl]biphenyl (**23**; 1.59 g, 4.59 mmol) was dissolved in a mixture of dichloromethane (10 mL) and ethanol (10 mL), followed by cesium carbonate (1.67 g, 8.66 mmol). The resulting mixture was stirred at room temperature for 2.5 h. After filtration, volatiles were removed under reduced pressure to leave a residue, which was then dissolved in dichloromethane. The organic phase was washed with water and dried over anhydrous $MgSO_4$. Removal of volatiles by evaporation under reduced pressure provided 4,4'-diethynylbiphenyl[22] (**24**; 800 mg, 3.96 mmol, 86%) as a pale yellow crystalline solid: ^{1}H NMR (400 MHz, $CDCl_3$) δ 7.57 (d, ^3J = 8 Hz, 4H), 7.54 (d, ^3J = 8 Hz, 4H), 3.14 (s, 2H); ^{13}C NMR (100 MHz, $CDCl_3$) δ 140.94, 133.07, 127.33, 121.90, 83.81, 78.55.

8.2.26 Synthesis of TE-9

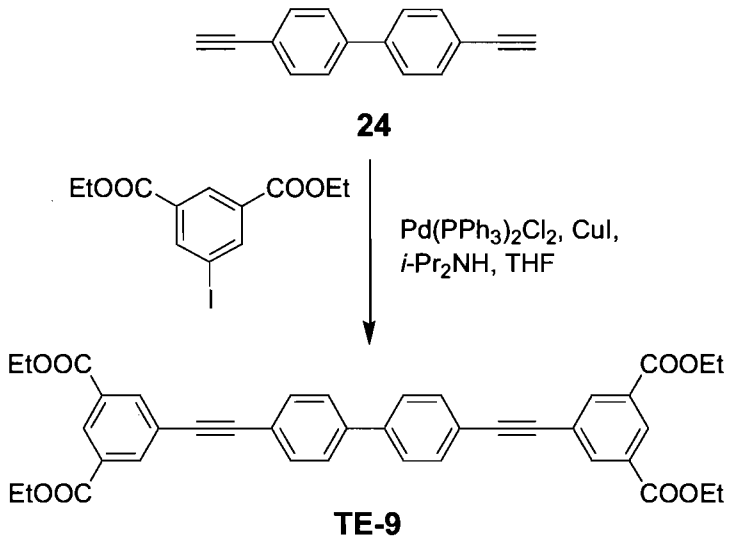

A mixture of dry THF (30 mL) and di-isopropylamine (15 mL) was degassed by bubbling dry N_2 through it for 30 min. Diethyl 5-iodo-1,3-benzenedicarboxylate (1.75 g, 5.03 mmol) was added, followed by bis(triphenylphosphine)palladium(II) dichloride (93 mg, 0.13 mmol) and copper(I) iodide (52 mg, 0.27 mmol). The mixture was stirred at room temperature for 15 min, and then a solution of 4,4'-diethynybiphenyl (**24**; 513 mg, 2.54 mmol) in dry THF (10 mL) was added dropwise. The resulting mixture was stirred overnight at room temperature and was then filtered. Hexane was added to the filtrate to form a precipitate, which was then separated by filtration and washed successively with water and hexane to give **TE-9** (800 mg, 1.25 mmol, 49%) as a yellow solid: mp 153 °C; IR (KBr) 3422, 2980, 1725, 1242 cm^{-1}; ^1H NMR (400 MHz, $CDCl_3$) δ 8.64 (t, ^4J = 1.6 Hz, 2H), 8.38 (d, ^4J = 1.6 Hz, 4H), 7.64 (s, 8H), 4.44 (q, ^3J = 8 Hz, 8H), 1.44 (t, ^3J = 8 Hz, 12H); ^{13}C NMR (100 MHz, $CDCl_3$) δ 165.60, 140.85, 136.78, 132.70, 131.72, 130.48, 127.42, 124.58, 122.34, 91.33, 88.93, 62.01, 14.74; HRMS (ESI) calcd for $C_{40}H_{34}O_8$ + H *m/e* 643.2306, found 643.2326.

8.2.27 Synthesis of 1,5-Diethynylnaphthalene (27)[23]

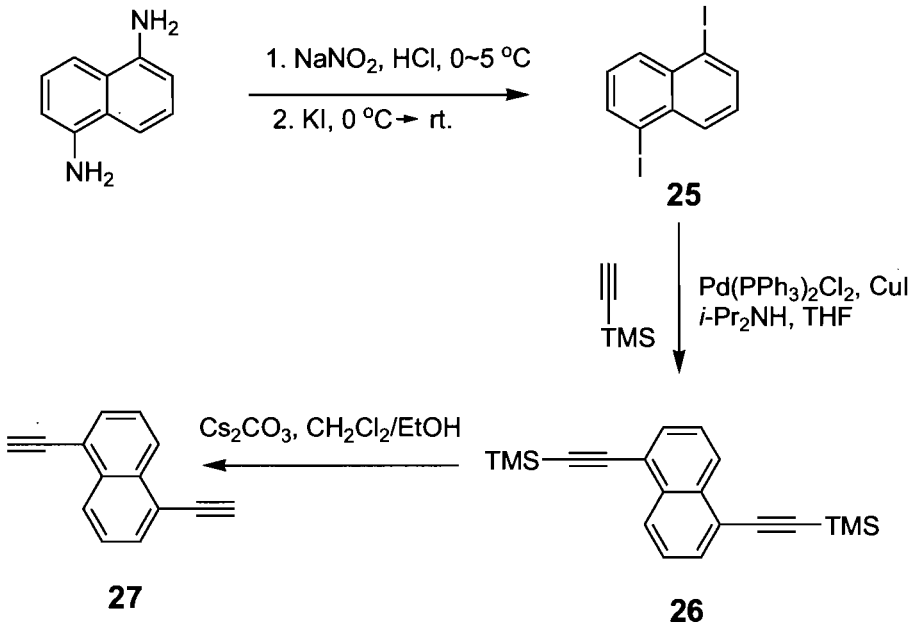

1,5-Diaminonaphthalene (5.20 g, 32.9 mmol) was suspended in H_2O (20 mL) at 0 ~ 5 °C, and then dilute HCl (100 mL, 1N) and sodium nitrite (4.53 g, 66.7 mmol) were added. The resulting mixture was stirred at room temperature for 1 h to complete diazotization. A small amount of sulfamic acid (~100 mg) was added to remove excess nitrite. A solution of potassium iodide (42.1 g, 0.252 mol) in H_2O (15 mL) was added slowly, and then the mixture was stirred overnight at room temperature. The resulting solid was collected by filtration, washed with water, and dried in vacuum to give 1,5-diiodonaphthalene[23] (**25**; 10.6 g, 27.9 mmol, 85%) as a tan crystalline solid.

A mixture of dry THF (50 mL) and di-isopropylamine (25 mL) was degassed by bubbling dry N_2 through it for 30 min. 1,5-Diiodonaphthalene (**25**; 1.91 g, 5.03 mmol) was added, followed by bis(triphenylphosphine)palladium(II) dichloride (179 mg, 0.254 mmol) and copper(I) iodide (97 mg, 0.51 mmol). The mixture was stirred at room

temperature for 15 min. A solution of (trimethylsilyl)acetylene (2.03 g, 20.7 mmol) in dry THF (5 mL) was added dropwise. The resulting mixture was stirred overnight at room temperature. Removal of volatiles by evaporation under reduced pressure left a residue, which was then purified by flash chromatography on silica (20:1 hexane/benzene) to give 1,5-bis[2-(trimethylsilyl)ethynyl]naphthalene[23] (**26**; 1.45 g, 4.52 mmol, 90 %) as a nearly colorless crystalline solid: ^{1}H NMR (400 MHz, $CDCl_3$) δ 8.41 (d, ^3J = 8 Hz, 2H), 7.80 (d, ^3J = 8 Hz, 2H), 7.56 (t, ^3J = 8 Hz, 2H), 0.41 (s, 18H); ^{13}C NMR (100 MHz, $CDCl_3$) δ 133.58, 131.81, 127.69, 126.50, 121.63, 103.29, 100.35, 0.55.

1,5-Bis[2-(trimethylsilyl)ethynyl]naphthalene (**26**; 475 mg, 1.48 mmol) was dissolved in a mixture of CH_2Cl_2 (5 mL) and EtOH (5 mL), and then cesium carbonate (1.46 g, 7.57 mmol) was added. The resulting mixture was stirred vigorously at room temperature for 2.5 h. After filtration, volatiles were removed from the filtrate by evaporation under reduced pressure to leave a solid which was dissolved in CH_2Cl_2. The organic phase was washed with water and dried over anhydrous $MgSO_4$. Removal of volatiles by evaporation under reduced pressure provided 1,5-diethynylnaphthalene[23] (**27**; 198 mg, 1.13 mmol, 76 %) as a pale yellow crystalline solid: ^{1}H NMR (400 MHz, $CDCl_3$) δ 8.37 (d, ^3J = 8 Hz, 2H), 7.76 (d, ^3J = 8 Hz, 2H), 7.50 (t, ^3J = 8 Hz, 2H), 3.48 (s, 2H); ^{13}C NMR (100 MHz, $CDCl_3$) δ 133.66, 132.25, 127.79, 126.57, 120.69, 82.91, 81.89.

8.2.28 Synthesis of TE-10

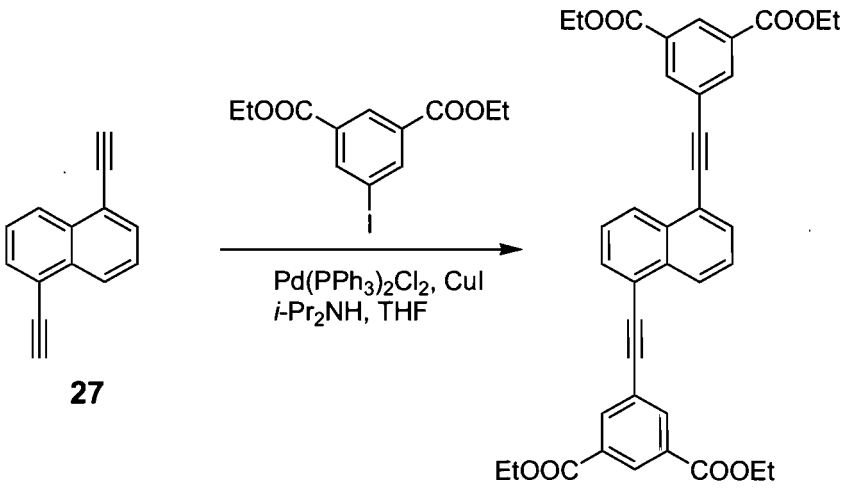

27 **TE-10**

A mixture of dry THF (20 mL) and di-isopropylamine (10 mL) was degassed by bubbling dry N_2 through it for 30 min. Diethyl 5-iodo-1,3-benzenedicarboxylate (455 mg, 2.58 mmol) was added, followed by bis(triphenylphosphine)palladium (II) dichloride (48 mg, 0.069 mmol) and copper(I) iodide (32 mg, 0.17 mmol). The mixture was stirred at room temperature for 15 min, and then a solution of 1,5-diethynylnaphthalene (**27**; 190 mg, 1.08 mmol) in dry THF (10 mL) was added dropwise. The resulting mixture was stirred overnight at room temperature. The precipitated solid was separated by filtration and washed successively with water and acetone to give **TE-10** (580 mg, 0.938 mmol, 87 %) as a yellow solid: mp 190 °C; IR (KBr) 3424, 2977, 1727, 1240 cm^{-1}; ^1H NMR (400 MHz, $CDCl_3$) δ 8.67 (t, ^4J = 1.2 Hz, 2H), 8.50 (d, ^3J = 8 Hz, 2H), 8.47 (d, ^4J = 1.2 Hz, 4H), 7.87 (d, ^3J = 8 Hz, 2H), 7.63 (t, ^3J = 8 Hz, 2H); ^{13}C NMR (100 MHz, $CDCl_3$) δ 165.61, 136.81, 133.43, 131.92, 131.81, 130.61, 127.87, 126.81, 124.56, 121.15, 93.19, 89.39, 62.08, 14.76; HRMS (ESI) calcd for $C_{38}H_{32}O_8$ + H *m/e* 617.2175, found 617.2165.

8.2.29 Synthesis of TA-10

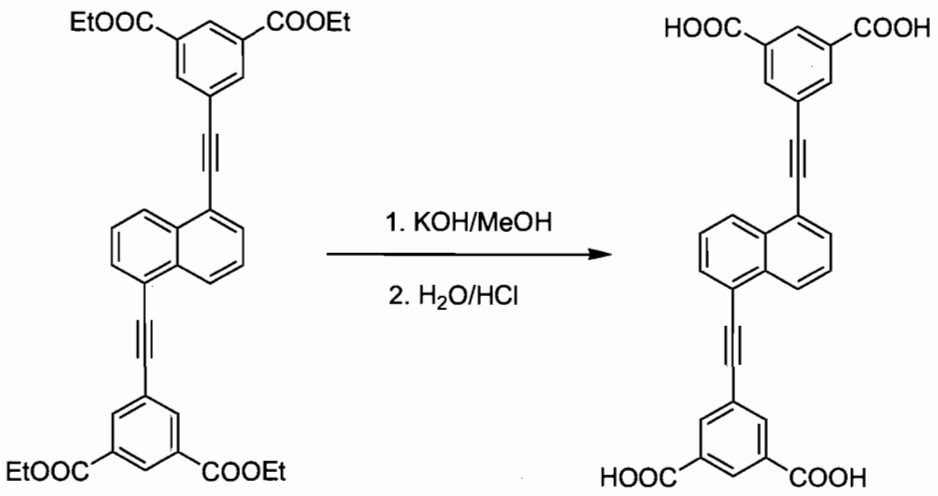

TE-10 **TA-10**

TE-10 (312 mg, 0.505 mmol), methanol (5 mL), and solid potassium hydroxide (256 mg, 4.56 mmol) were added to a 15 mL pressure tube containing a stirring bar. The tube was closed, and the mixture was stirred and heated at 80 ℃ for 3 h. Water (10 mL) was then added to dissolve solids, and the resulting solution was acidified to pH 1-2 with concentrated aqueous HCl (10 N). The precipitated solid was separated by filtration and washed successively with water and dichloromethane to give pure **TA-10** (208 mg, 0.414 mmol, 82 %) as a pale yellow solid: mp > 250 °C; IR (KBr) 3085, 1713, 1190 cm^{-1}; ^1H NMR (400 MHz, DMSO-d_6) δ 13.56 (bs, 4H), 8.53 (d, ^3J = 8 Hz, 2H), 8.49 (s, 2H), 8.41 (s, 4H), 8.02 (d, ^3J = 8 Hz, 2H), 7.77 (t, ^3J = 8 Hz, 2H); ^{13}C NMR (100 MHz, DMSO-d_6) δ 166.74, 136.60, 133.14, 132.97, 132.81, 130.84, 128.20, 128.05, 124.11, 120.80, 93.77, 89.31; HRMS (ESI) calcd for $C_{30}H_{16}O_8$ − H *m/e* 503.0767, found 503.0776.

8.2.30 Synthesis of 1,5-Diethynylanthracene (29)[24]

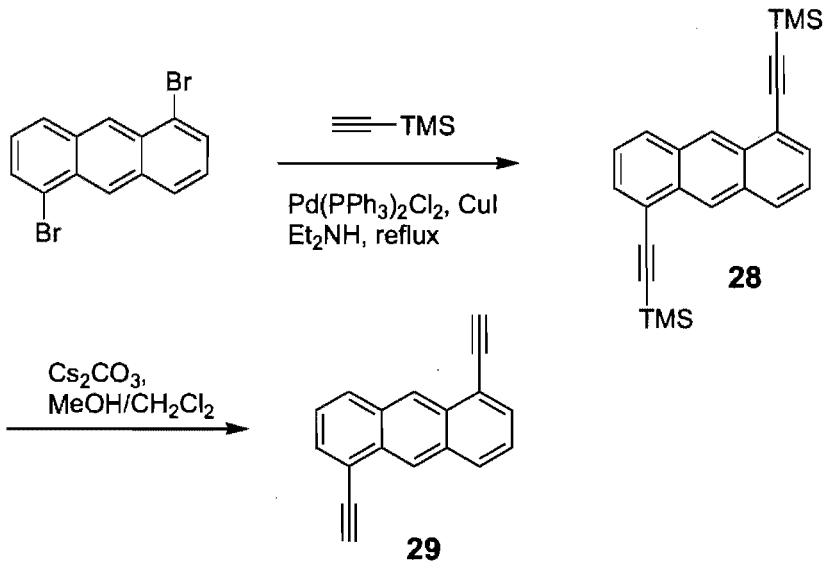

Diethylamine (100 mL) was degassed by bubbling dry N_2 through it for 30 min. 9,10-Dibromoanthracene (1.48 g, 4.46 mmol) was added, followed by bis(triphenylphosphine)palladium(II) dichloride (153 mg, 0.218 mmol) and copper(I) iodide (93 mg, 0.49 mmol). The mixture was stirred at room temperature for 15 min, and then (trimethylsilyl)acetylene (1.75 g, 17.9 mmol) was added. The resulting mixture was heated and stirred overnight at 60 °C under N_2. Volatiles were removed under reduced pressure. The residue was purified by flash chromatography on silica (1:10 benzene/hexane) to give 1,5-bis[2-(trimethylsilyl)ethynyl]anthracene[24] (**28**; 1.86 g, 3.35 mmol, 75%) as a yellow crystalline solid: ^{1}H NMR (400 MHz, $CDCl_3$) δ 8.94 (s, 2H), 8.10 (d, ^3J = 8 Hz, 2H), 7.80 (d, ^3J = 8 Hz, 2H), 7.48 (t, ^3J = 8 Hz, 2H), 0.47 (s, 18H); ^{13}C NMR (100 MHz, $CDCl_3$) δ 131.94, 131.73, 131.49, 130.30, 126.22, 125.42, 121.17, 103.65, 100.60, 0.63.

1,5-Bis[2-(trimethylsilyl)ethynyl]anthracene (**28**; 650 mg, 1.17 mmol) was dissolved in a mixture of dichloromethane (10 mL) and methanol (10 mL), and then cesium

carbonate (452 mg, 2.34 mmol) was added. The resulting mixture was stirred at room temperature overnight. After filtration, volatiles were removed from the filtrate by evaporation under reduced pressure to leave a solid, which was then dissolved in dichloromethane. The organic phase was washed with water and dried over anhydrous $MgSO_4$. Removal of volatiles by evaporation under reduced pressure provided 1,5-diethynylanthracene[24] (**29**; 220 mg, 0.972 mmol, 83%) as a red dark crystalline solid: ^{1}H NMR (400 MHz, $CDCl_3$) δ 8.91 (s, 2H), 8.07 (d, ^3J = 8 Hz, 2H), 7.77 (d, ^3J = 8 Hz, 2H), 7.43 (dd, ^3J = 8 Hz, ^4J = 1.6 Hz, 2H), 3.59 (s, 2H); ^{13}C NMR (100 MHz, $CDCl_3$) δ 132.01, 131.98, 131.79, 130.47, 126.05, 125.41, 120.20, 82.99, 82.23.

8.2.31 Synthesis of TE-11

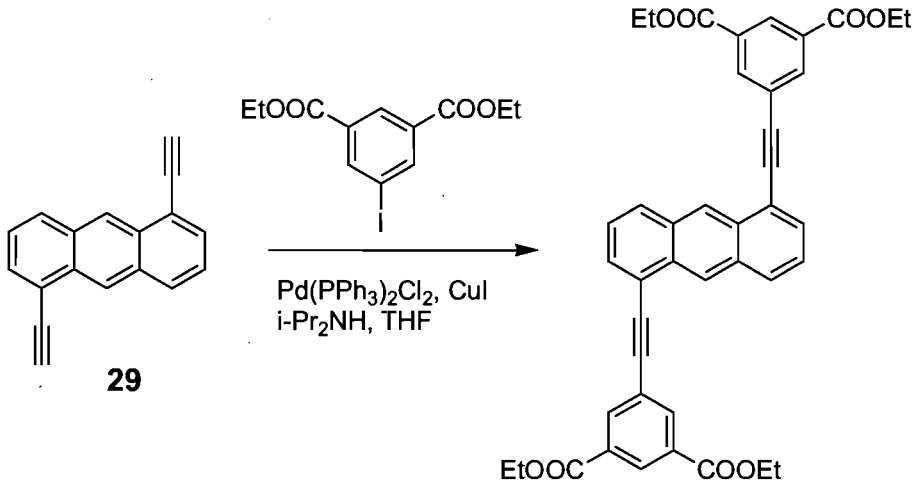

29 **TE-11**

A mixture of dry THF (30 mL) and di-isopropylamine (15 mL) was degassed by bubbling dry N_2 through it for 30 min. Diethyl 5-iodo-1,3-benzenedicarboxylate (873 mg, 2.51 mmol) was added, followed by bis(triphenylphosphine)palladium(II) dichloride (44 mg,

0.057 mmol) and copper(I) iodide (43 mg, 0.23 mmol). The mixture was stirred at room temperature for 15 min, and then a solution of 1,5-diethynylanthracene (**29**; 287 mg, 1.14 mmol) in dry THF (5 mL) was added dropwise. The mixture was stirred overnight at room temperature. The resulting solid was separated by filtration and dissolved in chloroform, and the organic phase was washed with water and dried over anhydrous $MgSO_4$. Removal of volatiles by evaporation under reduced pressure left a residue of tetraethyl 5,5'-(1,5-anthracenedi-2,1-ethynediyl)bis(1,3-benzenedicarboxylate) (**TE-11**; 501 mg, 0.755 mmol, 76%) as a bright yellow solid: mp 220 °C; IR (KBr) 3422, 2981, 1727, 1241 cm^{-1}; ^1H NMR (400 MHz, $CDCl_3$) δ 9.01 (s, 2H), 8.70 (s, 2H), 8.55 (s, 4H), 8.19 (d, ^3J = 8 Hz, 2H), 7.87 (d, ^3J = 8 Hz, 2H), 7.54 (t, ^3J = 8 Hz, 2H), 4.50 (q, ^3J = 7.2 Hz, 8H), 1.49 (t, ^3J = 7.2 Hz, 12H); ^{13}C NMR (100 MHz, $CDCl_3$) δ 165.28, 136.52, 136.60, 131.69, 131.45, 131.40, 131.19, 130.22, 125.78, 125.13, 124.33, 120.23, 92.87, 89.38, 61.70, 14.37; HRMS (ESI) calcd for $C_{42}H_{34}O_8$ + H *m/e* 667.2332, found 667.2326.

8.2.32 Synthesis of TA-11

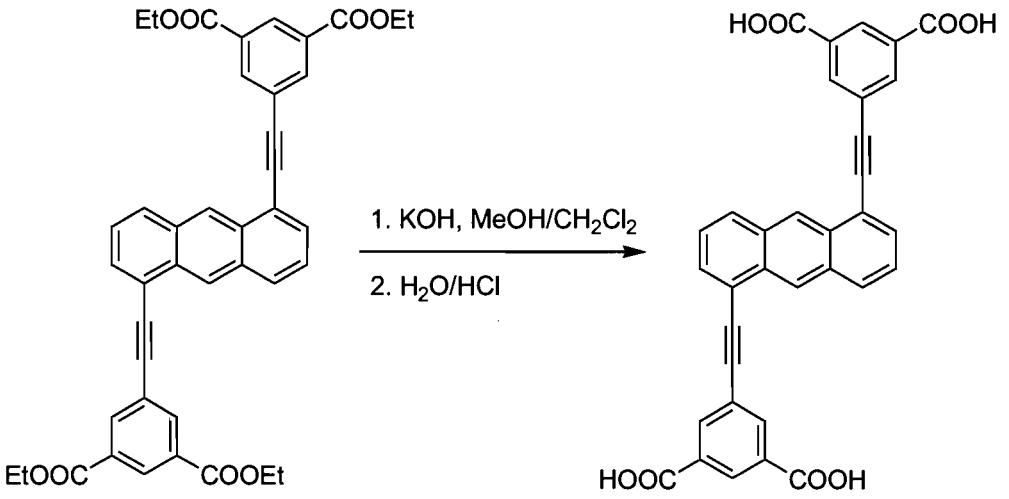

TE-11 **TA-11**

Tetraethyl 5,5'-(1,5-anthracenedi-2,1-ethynediyl)bis(1,3-benzenedicarboxylate) (**TE-11**; 200 mg, 0.300 mmol), methanol (4 mL), dichloromethane (2 mL), and solid potassium hydroxide (84 mg, 1.5 mmol) were added to a 15 mL pressure tube containing a stirring bar. The tube was closed, and the mixture was stirred and heated at 80 °C overnight. Water (10 mL) was then added to dissolve the solids, and the resulting solution was acidified to pH 1-2 with concentrated aqueous HCl (10 N). The precipitated solid was separated by filtration and washed successively with water and dichloromethane to give 5,5'-(1,4-anthracenedi-2,1-ethynediyl)bis(1,3-benzenedicarboxylic acid) (**TA-11**; 162 mg, 0.304 mmol, 81%) as a light yellow solid: mp > 250 °C; IR (KBr) 3080, 1717, 1202 cm^{-1}; ^1H NMR (400 MHz, DMSO-d_6) δ 9.14 (s, 2H), 8.51 (d, ^4J = 1.6 Hz, 4H), 8.50 (t, ^4J = 1.6 Hz, 2H), 8.46 (d, ^3J = 8 Hz, 2H), 8.02 (d, ^3J = 8 Hz, 2H), 7.64 (t, ^3J = 8 Hz, 2H); ^{13}C NMR (100 MHz, DMSO-d_6) δ 166.83, 136.73, 132.91, 132.81, 132.14, 131.39, 131.23, 130.78, 126.50, 126.27, 124.33, 120.11, 93.76, 89.76; HRMS (ESI) calcd for $C_{34}H_{18}O_8$ - H *m/e* 553.0923, found 553.0929.

References

1. SMART (2003). Version 5.630. Bruker Molecular Analysis Research Tools. Bruker AXS Inc., Madison, WI 53719-1173.
2. SAINT (2004). Release 7.01; Integration Software for Single-Crystal Data. Bruker AXS Inc., Madison, WI 53719-1173.
3. G. M. Sheldrick, SHELXS-97, Program for the Solution of Crystal Structures and SHELXL-97, Program for the Refinement of Crystal Structures, Universität Göttingen: Germany, 1997.
4. Sheldrick, G. M. (2004). SADABS, Bruker Area Detector Absorption Correction. Bruker AXS Inc., Madison, WI 53719-1173.
5. SHELXTL (1997) Release 6.14; The Complete Software Package for Single Crystal Structure Determination. Bruker AXS Inc., Madison, WI 53719-1173.
6. Zhang, W.; Kraft, S.; Moore, J. S. *J. Am. Chem. Soc.* **2004**, *126*, 329-335.
7. Dixon, S.; Whitby, R. J. *Tetrahedron Lett.* **2006**, *47*, 8147-8150.
8. Nguyen, P.; Yuan, Z.; Agocs, L.; Lesley, G.; Marder, T. B. *Inorg. Chim. Acta* **1994**, *220*, 289-296.
9. Li, G.; Wang, X.; Wang, F. *Tetrahedron Lett.* **2006**, *47*, 723-725.
10. Ziessel, R.; Diring, S. *Tetrahedron Lett.* **2006**, *47*, 4687-4692.
11. Khatyr, A.; Ziessel, R. *J. Org. Chem.* **2000**, *65*, 3126-3134.
12. Weber, E.; Hecker, M.; Koepp, E.; Orlia, W.; Czugler, M.; Csoregh, I. *J. Chem. Soc. Perkin Trans. II* **1988**, *7*, 1251-1257.
13. Suresh, P.; Srimurugan, S.; Babu, B.; Pati, H. N. *Tetrahedron Asym.* **2007**, *18*,

2820-2827.

14. Yamaguchi, Y.; Ochi, T.; Miyamura, S.; Tanaka, T. ; Kobayashi, S. ; Wakamiya, T. ; Matsubara, Y.; Yoshida, Z. *J. Am. Chem. Soc.* **2006**, *128*, 4504-4505.

15. Mazik, M.; Koenig, A. *J. Org. Chem.* **2006**, *71*, 7854-7857.

16. Coles, S. J.; Holmes, R.; Hursthouse, M. B.; Price, D. *J. Acta Cryst.* **2002**, *E58*, o626-o628.

17. Aujard, I.; Baltaze, J.-P.; Baudin, J.-B.; Cogne, E.; Ferrage, F.; Jullien, L.; Perez, E.; Prevost, V.; Qian, L. M.; Ruel, O. *J. Am. Chem. Soc.* **2001**, *123*, 8177-8188.

18. Zhou, H.; Dang, H.; Yi, J.-H.; Nanci, A.; Rochefort, A.; Wuest, J. D. *J. Am. Chem. Soc.* **2007**, *129*, 13774-13775.

19. Khan, M. S.; Al-Mandhary, M. R. A.; Al-Suti, M. K.; Al-Battashi, F. R.; Al-Saadi, S.; Ahrens, B.; Bjernemose, J. K.; Mahon, M. F. *Dalton Trans.* **2004**, *15*, 2377-2385.

20. Zhao, Z.; Yu, S.; Xu, L.; Wang, H.; Lu, P. *Tetrahedron* **2007**, *63*, 7809-7815.

21. Park, J. S.; Wilson, J. N.; Hardastle, K. I.; Bunz, U. H. F.; Srinivasarao, M. *J. Am. Chem. Soc.* **2006**, *128*, 7714-7715.

22. Liu, L.; Liu, Z.; Xu, W.; Xu, H.; Zhang, D.; Zhu, D. *Tetrahedron* **2005**, *61*, 3813-3817.

23. Rodriguez, J. G.; Tejedor, J. L. *J. Org. Chem.* **2002**, *67*, 7631-7640.

24. Rein, R.; Gross, M.; Solladie, N. *Chem. Commun.* **2004**, *17*, 1992-1993.